Electrohydrodynamic Driven Airflows for Microelectronics Thermal Management

by

Abdulmajeed A. Ramadhan

Submitted in accordance with the requirements for the degree of
Doctor of Philosophy

The University of Leeds
School of Mechanical Engineering
Institute of Thermofluids

July, 2018

The candidate confirms that the work submitted is his own and that appropriate credit has been given where reference has been made to the work of others. This copy has been supplied on the understanding that it is copyright material and that no quotation from the thesis may be published without proper acknowledgement.

The right of Abdulmajeed A. Ramadhan to be identified as Author of this work has been asserted by him in accordance with the Copyright, Designs and Patents Act 1988.

This thesis is dedicated

*To the memory of my dear **father**, who was a constant source of support and motivation for me before he passed away.*

*To my beloved **mother**, for her endless love that makes many things possible.*

*To my darling **wife**, who has supported me in all my endeavors.*

*To my gorgeous **sons**, Harith, Atheer and Rami, who always fill my life with fun.*

ACKNOWLEDGEMENTS

First and foremost, I would like to express my sincere gratitude and appreciation to my supervisors, Professor Harvey Thompson, Dr Jon Summers, and Professor Nik Kapur, for their constant support, guidance and motivation throughout the research.

Special appreciation and thanks must go to Dr Jon, not only for his invaluable academic advice but for his kind support and being a big brother to me through all difficult circumstances that I have encountered over the years of research.

I would also like to thank my scholarship sponsors, the Higher Committee for Education Development in Iraq (HCED), for the financial support and providing me this opportunity.

I would also like to extend my gratitude to the all of the faculty and staff in the school of Mechanical Engineering for their kind cooperation and to my colleagues and friends for their support.

A special thanks goes to the IT support team at the University of Leeds for providing the High Performance Computing facility (POLARIS) used to solve the powerful numerical jobs of this thesis.

My sincere appreciation goes to my brother and best friend, Dr. Ghalib Ibrahim, for his extensive support and being by my side through all the good times and bad.

Finally, words cannot express my gratitude and heartfelt appreciation to my beloved parents, dear brothers and sisters, and my wonderful wife, for believing in me and their continued support and encouragement.

ABSTRACT

The increasing demand for effective and compact thermal solutions for the next generation of thin and high-power density consumer electronics is challenging the capability of miniature mechanical systems to meet the required cooling performance. Due to their attractive and unique advantages with no moving parts, design flexibility, small-scale structure, low height profile, silent operation, and effective flow generation, electrohydrodynamic (EHD) air movers are well positioned to become a key emerging cooling technology as alternative to conventional rotary fans. In its general objective, this thesis aims to investigate the benefits and highlight the features of EHD air movers as a thermal management cooling solution in advanced and small-scale microelectronics, supporting all previous efforts in this direction.

Due to the strong influence of the geometric parameters of EHD devices on the corona discharge process and the resulting EHD flow, numerical modelling represents a powerful tool to design and optimize EHD devices, especially of complex and small-scale structures, where the capability of experimental investigations is limited or challenging. This study presents an accurate and validated numerical method to solve the coupled equations of electrostatics, charge transport and fluid flow for the two-dimensional (2D) modelling of EHD airflow induced through a wire-to-plane/grid channel configuration, and is the first to develop a three-dimensional model (3D) that couples the EHD flows with conjugate heat transfer modelling.

Based on thermal management requirements and from a design perspective, a comprehensive investigation and analysis into the influence of geometric parameters on the efficiency of EHD wire-to-grid blowers is performed and optimal configurations are proposed for a range of heights from 9 to 15 mm. Results reveal that using fine emitter wires is more efficient than thicker ones, and the grounded electrode locations affect significantly the electric field distribution and the blower efficiency. It is also found that using the grid as a further collector increases the blower performance, with higher flow production, lower operating voltage and reduced blower size.

Further numerical developments are devoted to optimize the configuration of miniature wire-to-plane EHD blowers for heights up to 10 mm, which is the most preferred geometry for integration in the cooling systems of thin electronic applications. For ranges of fixed operating power and voltage, the efficient optimized electrode gaps are predicted and defined by simple expressions. The influence of channel sidewall on the EHD flow rate and velocity profile are investigated and the results show that the 2D modelling is valid to effectively predict flow rates produced by wide and short EHD blowers compared to that obtained by 3D simulations.

A combined EHD air blower that enables a reduction in the level of applied voltage and a control of flow production is developed. Performance comparisons against commercial rotary blowers demonstrate that the optimized miniature EHD blowers are more competitive for cooling miniaturized and extended heated surfaces based on blower size, flow rate with uniform velocity profile, and power consumption.

A novel design of an EHD system integrated with compact heat sinks is presented as a thermal management cooling solution for advanced and thin consumer applications. Results of a parametric study demonstrate that the EHD system offers flexible structure design with the ability to reduce the height and increase the width as required, providing a unique feature to be installed in low-profile laptops. Moreover, compared to traditional cooling systems used in the current standard low power laptops, the proposed EHD system offers promising cooling performance with higher thermal design power (TDP), reduced thermal solution volume and lower height profile.

TABLE OF CONTENTS

LIST OF TABLES

LIST OF FIGURES

TABLE OF NOTATIONS

Symbol	Description with unit
A_b	Exposed base surface area of fin channels ($= (N_f - 1)\, S_f\, L_f$), (m^2)
A_f	Heat transfer area per fin ($= 2\, H_f\, L_f$), (m^2)
A_s	Heat exchange surface area, (m^2)
A_w	Surface area of the corona wire, (m^2)
b	Collecting surface length in wire-to-plane EHD channel configuration, (m)
b_P	Maximum effective length for the case of constant power, (m)
b_V	Maximum effective length for the case of constant applied voltage, (m)
c_p	Specific heat capacity of air, (J/kg.K)
d	Diameter of corona wire electrode, (m)
d_P	Actual distance between corona wire and the edge of collecting surface, (m)
D	Charge diffusion coefficient of ions, (m^2/s)
E	Electric field, (V/m)
E_e	Electric field strength at corona electrode surface, (V/m)
E_0	Electric field strength necessary to air breakdown, (V/m)
$\vec{E}$	Electric field intensity vector
Es	Electric source number
Esl	Electric slip number
f	Roughness factor of the wire surface
F	The body or Coulomb force, (N/m^3)
G	Electrode gap (or distance between the electrodes), (m)
G_P	Optimal electrode gap at constant power, (m)
G_V	Optimal electrode gap at constant applied voltage, (m)
G_w	Electrode gap between emitter wire and heat sink, (m)
h	EHD blower height, (m)
h_a	Average convection heat transfer coefficient, ($W/m^2.K$)
h_F	Fan height, (m)
H_f	Fin height, (m)
H_h	Heat sink height, (m)
I_c	Ion current, (A)
$\vec{J}$	Electric current density vector
k_a	Thermal conductivity of air, (W/m.K)
k_s	Thermal conductivity of heat sink (or solid), (W/m.K)
L	EHD blower length, (m)
L_d	Length of dielectric wall, (m)
L_f	Fin length, (m)
L_h	Heat sink length, (m)
$\dot{m}$	Mass flow rate, (kg/s)
n_w	Number of integrated emitter wires

Symbol	Description with unit
N_{f}	Number of fins
N_{w}	Number of collecting grid wires
Nu	Nusselt number
P	Static pressure, (Pa)
P_{elec}	Electrical power, (W)
P_{m}	Mechanical power, (W)
P_{o}	Power consumed by the fan, (W)
P_{s}	Electrostatic pressure, (Pa)
Pr	Prandtl number
q	Space charge density, (C/m^3)
q_{i}	Initial applied value of space charge density, (C/m^3)
q_{J}	Heat source due to Joule heating effect, (W)
q_{o}	Heat dissipation power applied to the heat sink base, (W)
Q	Flow rate, (l/min or CFM)
Q_{t}	Total heat dissipated from the heat sink, (W)
r	Radius from the centre of the corona wire within the ionization region, (m)
R_{e}	Actual corona electrode radius, (m)
Re_{E}	Electric Reynolds number
R_0	External radius of the ionization layer, (m)
R_{b}	Thermal conduction resistance across the heat sink base, ($^{\mathrm{o}}$C/W)
R_{hs}	Thermal resistance of heat sink, ($^{\mathrm{o}}$C/W)
R_{th}	Total thermal resistance of heat sink, ($^{\mathrm{o}}$C/W)
Re	Reynolds number
S_{f}	Fin spacing, (m)
S_{w}	Spacing between grid wires, (m)
t_{b}	Heat sink base thickness, (m)
t_{f}	Fin thickness, (m)
T	Temperature, (K or $^{\mathrm{o}}$C)
T_{a}	Ambient temperature, (K)
T_{b}	Maximum temperature at heat sink base, (K)
T_{s}	Average heat sink surface temperature, (K)
u_{c}	Average air velocity at fin channel inlet, (m/s)
u_{o}	Average air velocity at blower outlet, (m/s)
$\vec{U}$	Velocity vector of the airflow
V	Electric potential, (V)
V_{e}	Voltage applied to corona electrode, (V)
V_0	Voltage on the external boundary of the ionization boundary, (V)
w	EHD blower width, (m)
W_{h}	Heat sink width, (m)
X	Collecting surface location in wire-to-grid EHD channel configuration, (m)

Greek Letters

Symbol	Description with unit
δ	Air density factor
ε	Permittivity of air, (C/V.m)
ε_0	Permittivity of free space, ($= 8.854 \times 10^{-12}$ C/V.m)
ε_r	The relative permittivity of air ($= 1$)
η	Electro-mechanical efficiency
η_f	Efficiency of the fins
θ	Effective drifting angle, (^{o})
μ	Dynamic viscosity of air, (N.s/m^2)
μ_p	Positive air ion mobility in the electric field, (m^2/V.s)
ν	Kinematic viscosity of air, (m^2/s)
ν_i	velocity of ions, (m/s)
ρ	Density of air, (kg/m^3)
σ	Electrical conductivity of air, (S/m)
ϕ	Fan diameter, (m)
ω	Fan rotational speed, (rad/s)

TABLE OF ABBREVIATIONS

Abbreviation	Description
2D	Two Dimensional
3D	Three Dimensional
AC	Alternating Current
CCFL	Cold Cathode Florescent Lamp
CFD	Computational Fluid Dynamics
CIV	Corona Inception Voltage
CL	Collector Length
CPU	Central Processing Unit
ECL	Effective Collector Length
ESP(s)	Electrostatic Precipitator(s)
DC	Direct Current
EFA(s)	Electrostatic Fluid Accelerator(s)
EHD	Electrohydrodynamic(s)
Eq.	Equation
et al.	Latin et alia (and others)
FEM	Finite Element Method
GN	Grid with Number of wires
GPU	Graphics Processing Unit
HVPS	High Voltage Power Supply
ITRS	International Technology Roadmap for Semiconductors
NG	No Grid
NCS	No Collecting Surface
PCB(s)	Printed Circuit Board(s)
PDE(s)	Partial Differential Equation(s)
PIV	Particle Image Velocimetry
P-Q	Pressure-Flow Rate
SIA	Semiconductor Industry Association
STP	Standard Temperature and Pressure
TDP	Thermal Design Power
TIM	Thermal Interface Material
WG	With Grid

THESIS RELATED PUBLICATIONS

Journal Papers

(1) Ramadhan, A.A., N. Kapur, J.L. Summers, and H.M. Thompson, "***Numerical Modelling of Electrohydrodynamic Airflow Induced in a Wire-to-grid Channel***". Journal of Electrostatics, 2017. **87**: p. 123–139.

(2) Ramadhan, A.A., N. Kapur, J.L. Summers, and H.M. Thompson, "***Numerical Analysis and Optimization of Miniature Electrohydrodynamic Air Blowers***". IEEE Transactions on Plasma Science, 2017. **45**(11): p. 3007–3018.

(3) Ramadhan, A.A., N. Kapur, J.L. Summers, and H.M. Thompson, "***Performance and Flow Characteristics of Miniature EHD Air Blowers for Thermal Management Applications***". Journal of Electrostatics, 2018. **93**: p. 31–42.

(4) Ramadhan, A.A., N. Kapur, J.L. Summers, and H.M. Thompson, "***Numerical Development of EHD Cooling Systems for Laptop Applications***". Applied Thermal Engineering. 2018. **139**: p. 144–156.

CHAPTER 1

Introduction

1.1 Motivation

Efficient dissipation of heat generated from microelectronic components represents one of the major thermal management challenges for engineers and designers of modern microelectronic applications. During operation of electronic devices, high-performance chips can generate significant levels of heat and cause high temperatures, leading to reduced device performance and being a major factor of producing thermo-mechanical stresses on printed circuit boards (PCBs) [1]. Effective cooling systems are required to maintain the temperatures of electronic components within safe operating limits and avoid overheating and subsequent device failure. Development in cooling technologies has received increasing attention due to the rapid advancement in the microelectronics industry, which has been associated with increasing the processing performance of the integrated circuits in parallel with reducing their size.

Over the last five decades, the semiconductor industry has significantly been developed following Moore's law [2], which states that the number of transistors in an integrated circuit doubles approximately every two years, resulting in a smaller transistor size and greater power density [3]. Since the transistor feature size became below 90 nanometres, early estimates of scaling trends indicated that the chip power density (in W/cm^2) may increase more than 13 times as the transistor size decreases to 15 nanometres, causing an exponential growth in the associated power density on microelectronic chips [4]. Recent years have shown significant advancements in semiconductor industry when Samsung Electronics has started mass production of new system-on-chip with transistor size of 10 nanometres [5], while the IBM research group is inching the way into a 5 nanometre node chip [6].

Figure 1.1 shows that the number of transistors per chip has doubled about every two years since the 1970s, and the current transistor density has exceeded 10^9 transistors per die with an expectation to be around 10^{11} by 2020, while the heat

generation associated with chip's electrons speeds (Clock speeds) have steadily increased. Indeed, as the transistor size decreases, the movement of electrons through smaller scales of silicon circuits becomes faster, increasing their ability to generate higher heat in the chips [7]. However, although the electrons speeds were limited to generate more heat since around 2004, the current heat generation rates still represent significant issue as the demand for small-scale and high-power density devices is increasing, while the capability of conventional thermal solutions is limited. Traditionally, forced-air cooling induced by rotary fans is the preferred and popular cooling method for most microelectronic devices due to its low cost, availability and simplicity. However, the increasing performance of microelectronics has led not only to a higher heat generation but to smaller and thinner devices, where the performance of traditional mechanical solutions for effective cooling is reduced under the miniaturization condition. Based on these considerations, the need for effective thermal management cooling solutions for the future microelectronics remains critical and at the centre of attention of academic research communities, engineering designers and industrial companies.

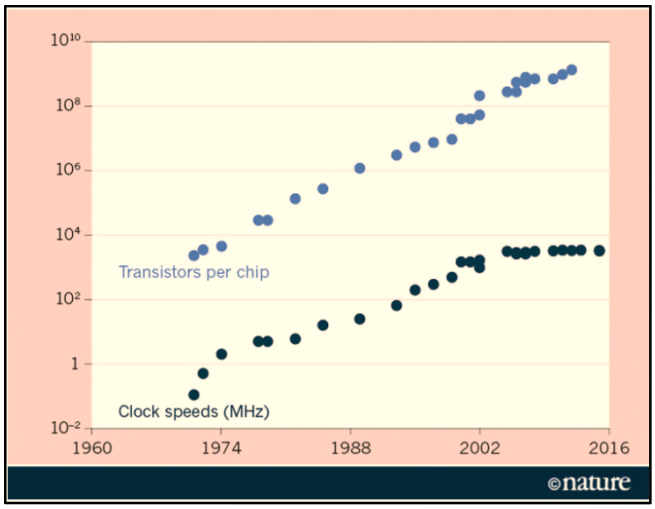

Figure 1.1 Trends of transistor density (transistor per chip) following Moore's law, and the associated electrons' clock speed for microelectronics over the past five decades including the current one. Figure adapted from Nature (2016) [7].

The work in this thesis is motivated due to the essential need for efficient and compact thermal modules for microelectronics that meet the thermal management requirements in terms of flexibility, reliability, cooling performance and acoustic

levels. Electrohydrodynamic (EHD) flow is one of the emerging airside cooling technologies that have great potential to extend the restricted capabilities of miniaturized traditional mechanical fans, such as reduced performance and installation size, in modern and ultra-thin microelectronic applications. With the advantage of no moving parts, EHD air blowers offer silent operation, good reliability, uniform velocity profile, wide range of flexibility in both scale and design, and promising cooling performance on small and thin applications [8].

As the development and optimization of the traditional air cooling methods has reached a high degree of maturity, it is important to open the improvement door for emerging airside cooling technologies to meet the current and future requirements of advanced microelectronic applications. The present study explores and investigates the application of EHD air blowers based on thermal management considerations in terms of modelling analysis, design development and optimization, performance and flow characteristics, and integration with heat sinks, for convective heat transfer in miniaturized consumer microelectronics such as laptop computers or future high-end Internet of Things devices.

1.2 Electrohydodynamic (EHD) Airflow for Thermal Management

1.2.1 Introduction to EHD air movers

Electrohydrodynamic (EHD) air movers (also known as Electrostatic Fluid Accelerators) are simple devices that provide a means of generating air motion by a gas discharge across two electrodes without the need for moving parts. In the EHD airflow approach, electrical energy is converted into kinetic energy of the moving air stream by applying a high voltage electric field between a sharp corona electrode and a grounded collecting surface in the air. When a sufficiently high electric field gradient is created at the corona electrode, the surrounding air molecules are ionized. The resultant charged ions are then accelerated under the effect of electrostatic forces towards the collector electrode, transferring their momentum and energy into the surrounding air particles and inducing air movement known as an ionic wind (also referred to as a corona or an electric wind). A simple schematic diagram of an EHD airflow induced by a positively charged corona wire is shown in **Figure 1.2**.

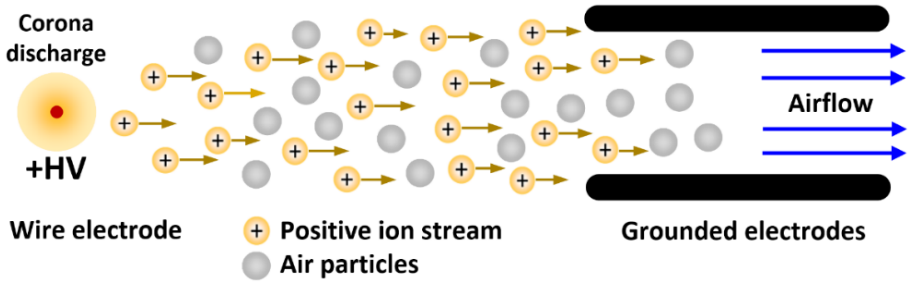

Figure 1.2 Schematic diagram of an EHD airflow induced by a positive corona discharge.

EHD air pumps can be designed using various-scale structures of electrode configurations, offering a wide range of flexibility that enables installation in small spaces, where the application of conventional mechanical air movers is limited. With the absence of moving solid parts, EHD devices have extremely low weight and operate with no vibration or lubrication requirements, offering stable and silent operation. The mechanism of EHD driven flow provides the capability to change the flow magnitude and direction during operation for effective local cooling.

Unlike traditional air movers, ionic wind can be induced through narrow channels with high speeds and low levels of flow pressure losses and operating power, offering promising cooling performance and electrical to mechanical transduction efficiency. EHD devices have been effectively used for forced convection heat transfer in confined and open space applications, either as air blowers in the cooling system, or for cooling hot spots regions, where a stable airflow jet is desired. Moreover, EHD driven airflow provides another feature when it acts as a secondary flow in the presence of external bulk flow to mix flows and disrupt the thermal boundary layer for heat transfer enhancements.

Apart from the use in the heat transfer field, significant research into EHD phenomena has been presented in numerous studies for their application in electrostatic precipitators (ESPs), where the contaminated particles are collected from a flowing fluid under the effect of electrostatic charge [9-14]. Corona discharge has also been examined in different applications such as acoustic transduction [15-17], dehumidification (electrostatic fog-liquefiers) [18-20], and air sterilization [21, 22].

In its general and specific features, EHD flow technology is considered an attractive viable air cooling solution and has great potential to become an alternative to conventional rotary fans, meeting the thermal management requirements in a class of microelectronics cooling. The next sections present the main advantages and disadvantages of EHD based air cooling in comparison with traditional mechanical air movers.

1.3 EHD Airflow Characteristics

1.3.1 Advantages of EHD air movers

1.3.1.1 Design flexibility

Unlike rotary fans, EHD blowers can be designed and fabricated in various sizes, shapes and geometries, depending on the application, to generate a steady flow or create an impinging jet of air for local hot spot cooling whether in free or confined space flow fields. In addition, corona electrodes can be applied with tips/needles, wires, and edges of razors, and be arrayed into different configurations (single or multi-electrodes), while collector electrodes can be set as round or flat geometries, as well as adopted as a heat exchange surface.

1.3.1.2 Device size

EHD cooling systems can be installed and fitted in a small physical space of thin profile and small-scale applications, where mechanical fans encounter technical hurdles. Due to the absence of moving parts, EHD pumps can be designed in very small thicknesses and fabricated for micro-scale microelectronic applications. Moreover, using the collector electrode as a thermal exchange surface offers reduced EHD device size and weight and also leads to effective heat transfer with reduced boundary layer thickness.

Table 1.1 presents a comparison between a rotary fan and an EHD pump based on a cooling device size to dissipate an amount of heat at approximately 40 ^{o}C temperature difference. It shows that the EHD pump volume required to remove about 1.4 W of heat is 38 mm^3, compared to 720 mm^3 needed for a rotary fan to dissipate nearly the same amount of heat [8]. This example indicates the

effectiveness of the EHD technology to dissipate heat in small spaces of applications with higher transduction efficiency compared to a mechanical fan.

Table 1.1 Comparison between an EHD pump and a rotary fan based on cooling device size required to dissipate heat at approximately the same temperature difference [8].

Technology	**ΔT (°C)**	**Device volume (mm^3)**	**Heat dissipation (W)**	**Efficiency(*) (CFM/W)**
EHD pump [23]	38.3	38	1.57	5.04
Rotary fan	40.0	720	1.29	0.57

(*) Produced flow rate in cubic feet per minute (CFM) per consumed power in watts.

1.3.1.3 Low acoustic level

EHD devices can be considered silent air cooling systems due to the absence of vibration and acoustic noise during operation caused by rotating or moving parts. Additionally, based on the operating theory of corona discharge and ionic wind, no changes in the electric field and the pressure waves occur during the operation, offering a stable and silent condition for EHD technology [24]. This advantage is independent of geometry, applied voltage and scaling laws of EHD devices.

1.3.1.4 Velocity profile

In the case of air flow in a channel, EHD driven flow offers an improved velocity profile compared to that achieved due to rotary fans. **Figure 1.3** shows the idealized velocity profiles of both EHD and fan flows between two parallel plates. In conventional fans, a classic parabolic air velocity profile is formed due to viscous effects and pressure differential flow from a fan, resulting in relatively inefficient heat removal at the solid-fluid boundary. EHD flow offers non-parabolic profile with higher velocity close to the channel walls because of the local Coulomb forces that move fluid molecules are installed inside the channel. Therefore, the airflow induced by EHD blowers can provide better and flatter flow profile, which greatly can reduce the boundary layer thickness and effectively enhance the heat transfer [25].

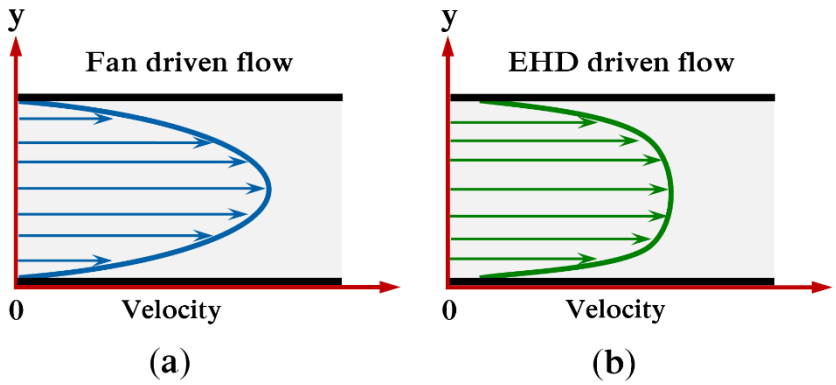

Figure 1.3 Idealized laminar airflow velocity profile between two parallel plates generated by (a) pressure differential flow due to fan, and (b) corona-driven air pump [25].

1.3.1.5 Boundary layer modification

In addition to their function of generating primary flows, EHD air movers can be used to induce secondary flows in the presence of the bulk flow for improved heat transfer rates. The EHD secondary flow can boost and/or mix airflows, causing active disturbances and reductions in the fluid and thermal boundary layers and, thereby, leading to better heat transfer enhancements [26], as shown in **Figure 1.4**. Furthermore, when the collector electrode of an EHD device is used as a thermal exchange surface, additional momentum can be provided to the air particles within the boundary layer region, reducing its thickness and enhancing heat removal [25].

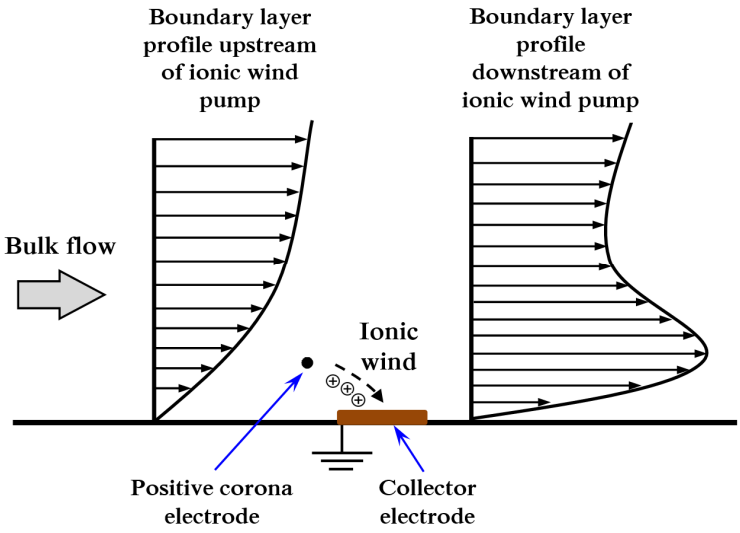

Figure 1.4 Schematic diagram of the boundary layer modification of external bulk flow on a flat surface due to the secondary flow of ionic wind induced by EHD pump [27].

1.3.1.6 Dynamic airflow pattern

A unique feature of EHD air movers is their ability to provide various dynamic airflow patterns by changing the distribution of applied voltage at the collector electrode, as shown in **Figure 1.5**. This feature can be employed to control flow in local cooling of electronics with the ability to change the trajectory and level of ionic wind velocity using the same applied voltage [28]. Moreover, applying different voltages at corona electrodes in multi-stage arrangement also offers flow-control for localized and hot spot cooling in thermal management applications.

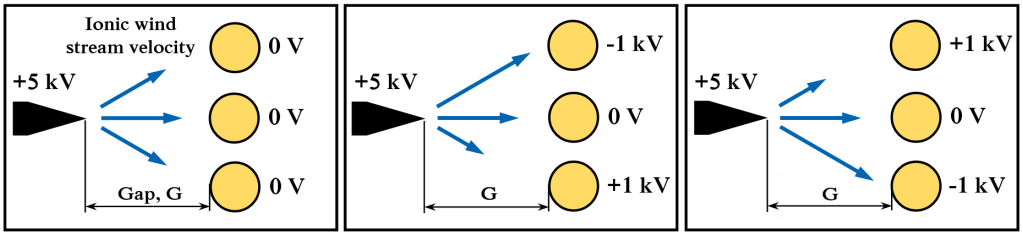

Figure 1.5 Dynamic EHD airflow pattern controlled by varying collector voltage distribution. Arrow length refers to the velocity magnitude of ionic wind [28].

1.3.2 Disadvantages of EHD air movers

Though EHD technology offers many unique features and attractive advantages for cooling systems in advanced electronic devices, several associated drawbacks due to corona discharge phenomenon represent challenges in the practical implementation. The following points highlight and explain these disadvantages and describe suggested solutions to tackle them or reduce their effects on the performance of EHD devices.

1.3.2.1 Ozone generation

Ozone generation (O_3) is one of the main disadvantages of EHD flow technology, and is a normal by-product and direct result of corona discharge. At a given electrode gap and ambient conditions, the ozone production rate in an EHD device depends on the polarity type (positive or negative), level of applied voltage, and corona electrode configuration. A large amount of ozone, as an undesirable

result, can affect and damage the environment, and be hazardous to human health at certain levels. According to the National Ambient Air Quality Standards, the maximum allowable safe concentration of ozone for an 8-hour daily exposure is less than 0.1 parts per million (ppm) [29].

However, a number of studies reported that ozone produced due to corona discharge can be reduced by using a positive corona rather than negative one [30-32]. Typically, ozone formation increases proportionally with applied potential and current density [33]. Therefore, using a high aspect ratio between the EHD electrodes can reduce the corona onset voltage, which is the magnitude of voltage required for discharge to occur, and thereby decrease the ozone production [23, 34]. This aspect also can be considered with using very fine smooth and round corona electrodes, small electrode gaps, and multi-stages of EHD flow generators [30, 33].

In their numerical modelling validated against experiments, Chen and Davidson [34] demonstrated that the rate of ozone production due to positive discharge increases linearly with the current density at a given wire radius and gas temperature. Based on this fact, they found that at a fixed current density per wire length of 0.4 A/m^2, the ozone generation rate can be decreased by 62% (from 15.3 to 5.8 ppm) by reducing corona wire radius from 200 to 100 μm, and by 44% using a wire of 100 μm-radius and increasing gas temperature from 300 to 500 K. Results also showed that using very fine corona wire with 20 μm-diameter can keep the ozone generation rate at a low level of 0.089 ppm, under the same given current density and at 300 K.

In practical applications, using ozone destructive materials such as ozone catalysts in the EHD devices is required, which enable mitigation of ozone production by converting O_3 into oxygen [35].

1.3.2.2 Electrode degradation

The degradation of the emitter electrode during the operation of corona discharge represents a significant challenge to provide an adequate lifetime of EHD devices. Electrode degradation mainly occurs as a result of surface oxidation and metal sputtering in a high electric field, leading to corona electrode failure. This in

turn can considerably reduce device longevity and lead to unstable voltage operation over time [25].

However, the proper selection of materials for the emitter electrode, which is the most prone to degradation, and avoiding all materials that have a high tendency to erode and decay over time can improve the electrode resistance to degradation. Previous investigations demonstrated that emitter electrodes made from silicon and silicon dioxide materials have significantly lower corrosion compared to metals under the effect of corona discharge [36].

Furthermore, it was experimentally found that coating corona electrodes with palladium (Pd), which has a high resistance to corrosion and good electrical and thermal conductivities, can reduce electrode degradation and increase the device lifetime by 3.5 times longer than that without coating [37]. Moreover, using positive corona electrodes offers less oxidization and corrosion, improving EHD device lifetime and providing a stable operation [38, 39].

1.3.2.3 The need for a high voltage source

The need to minimize the high voltage required to initiate corona discharge (usually on the order of kilovolts) while improving pumping performance remains a research focus. Typically, ionic wind velocity increases proportionally with increasing applied voltage and discharge currents (or input power) at a given electrode gap. Indeed, the need for compact high voltage converters required for operating EHD cooling systems in microelectronic applications is one of the integration and practical challenges [25]. However, it was reported that both the onset and operating voltages of positive polarity can be reduced at a given electrode gap by using a very fine tip curvature emitter due to the higher electric field created [40], or decreasing the electrode gap at a given operating current [27]. Moreover, using multi-stage EHD wind generators can significantly improve the flow generation at certain low operating voltages [25, 41].

1.3.2.4 The influence of environmental factors

The environmental factors such as air humidity and dust particles can affect the operation of corona discharge. For the positive discharge, the increase in air relative humidity increases the corona onset voltage to certain limits before it tends to decrease as the relative humidity increases [42]. For a negative corona, the increase in air humidity decreases the electric field strength, corona current and ion mobility of air, leading to a lower air breakdown than that proposed by Peek's equation [43].

The accumulation of dust particles, which is a shared problem between rotary fans and EHD pumps, can occur on the EHD device due to the movement of charged particles towards the surface of opposite polarity under the effect of electric field and electrostatic forces. The collection of dust particle mainly occurs on the collector electrode and causes increased electrical resistance and reduced ion current, resulting in an increased thermal resistance of the heat exchange surface (heat sink) and drop in the performance and longevity of EHD devices [25, 44].

In their experimental and numerical study, Jewell-Larsen et al. [44] presented the first concerns regarding the dust accumulation on EHD cooling systems. Although no advice was given in their conclusions on how to reduce dust accumulation, the study, however, determined the locations on the collecting surface where the majority of the dust particles are collected, and offered a simulation model for investigating and optimizing the longevity of EHD devices. Practically, using a pre-filter is one of the available options to protect the EHD cooling device from the accumulation of dust particles during operation.

1.3.2.5 Low pressure head

Typically, the flow rate produced by EHD devices mainly depends on the amount of kinetic energy and momentum imparted to the air molecules due to collision with charged ions traveling across the electrodes and not by mechanical moving solid parts like in rotary fans. Therefore, the pressure head of EHD pumps is low compared to that created by fan blades, with a reduced ionic acceleration to overcome pressure restriction caused by converging or long channels [45]. However,

using cascading designs with multi-stages of EHD pumps can significantly improve airflow rate production and lead to a higher cooling performance [25, 41].

1.4 Thermal Management Cooling Solutions

1.4.1 Overview

The recent years have shown a dramatic growth in the microelectronics industry in terms of circuit component density, microfabrication processes, functional complexity and operating power, including a wide range of modern applications from mobile devices to powerful server units. According to recent reports of the Semiconductor Industry Association (SIA) [46], the global semiconductors market shows that the sale trends are increasingly growing and the demand for high-performance portable microelectronic devices is accelerating.

On the other hand, however, reports released by the International Technology Roadmap for Semiconductors (ITRS) [3] have indicated that the current and future trends of thermal design power of microelectronics are steadily increasing and the associated high heat fluxes require improved cooling methods for efficient heat dissipation. Furthermore, the heat generated from the advanced integrated circuits is non-uniform, causing high local power densities (hot spots) and limiting the thermal solution system as well as the performance and reliability of devices. Based on these trends, the design and development of the future consumer microelectronics relies critically on the availability of innovative and compact thermal solutions beyond the capabilities of the traditional cooling systems.

The response of thermal industries has led to significant developments in thermal management cooling technologies for effective heat removal and lower levels of power consumption, acoustic noise and manufacturing cost. Although elaborate cooling systems such as on-chip liquid cooling [47], Aquasar (IBM) [48], dielectric liquid immersion technology [49], and other types of liquid cooling have been developed and successfully proven for higher thermal dissipation rates than that are possible by air cooling, cost limitations still prevent their large scale adoption.

Due to the higher heat conductivity and capacity of liquid compared to air, liquid cooling technologies are considered very effective methods to remove extremely high heat fluxes (above 100 W/cm^2). However, the implementation of these approaches for consumer microelectronics is complex and requires high levels of manufacturing quality to avoid leakage problems, resulting in costly devices compared to air cooled methods. Among the wide range of thermal management applications, the adoption of liquid cooling approaches has been largely confined to high performance computing systems such as servers and data centers, where the cost is elastic and the dissipation of enormous generated heat fluxes is required [50, 51].

Passive thermal solutions such as heat transport technologies; including phase-change heat pipes, liquid and spray coolers, and vapour chambers, are also efficiently used in high heat flux applications to transport thermal energy from hot spot regions to heat exchangers, where the heat can be dissipated from the system. For years, heat pipes have been developed and commonly used with rotary fans and heat sinks as effective cooling systems for microelectronic devices such as laptops and computer servers. However, although heat pipes have effective heat transfer with very low thermal resistance, their implementation becomes critical as the microelectronic device and the cooling system become smaller and thinner, causing performance limitations [52], practical fabrication challenges and increases in cost [53]. Other emerging heat transport technologies such as microchannels [54-56] and droplet manipulation [57], offer higher heat transfer than traditional heat sinks and have shown significant performance on localized dissipation of high heat flux and hot spot cooling applications. However, the manufacturing cost and the relatively high pumping power required to overcome the increased pressure losses make their application still limited in consumer microelectronics [8].

Among other cooling technologies, air cooling using fans remains the most popular thermal management solution, especially in portable microelectronic and consumer products. This is attributed to their design flexibility and relatively low cost of manufacturing and implementation as well as the capability to dissipate the generated heat to the ambient environment, which is ultimately a required feature for most devices. Classic assemblies of heat sink and rotary fan have been successfully used for cooling macro-scale electronic applications such as desktop computers and

servers. However, this option is no longer viable for thin and small-scale microelectronics, where both the device thickness and the ability to increase the thermal exchange area are limited.

Typically, the cooling system of most thin microelectronic devices such as laptops involves using both passive and active cooling technologies to remove high heat fluxes to the ambient air. As illustrated in **Figure 1.6**, the heat is transported using an integrated heat spreader (most often simply a copper plate) from the CPU silicon die, where a high heat-flux density is generated, to a larger thermal conductive surface. Thermal interface materials (TIM) such as thermal greases, phase change materials and gels, act to provide passively efficient thermal exchange and high thermal conductivity in the interface between solid components. The heat is then moved via heat transport devices such as phase-change heat pipes to the heat exchange surface (heat sink), where the heat is actively dissipated out of the device using air mover devices such as centrifugal rotary blowers.

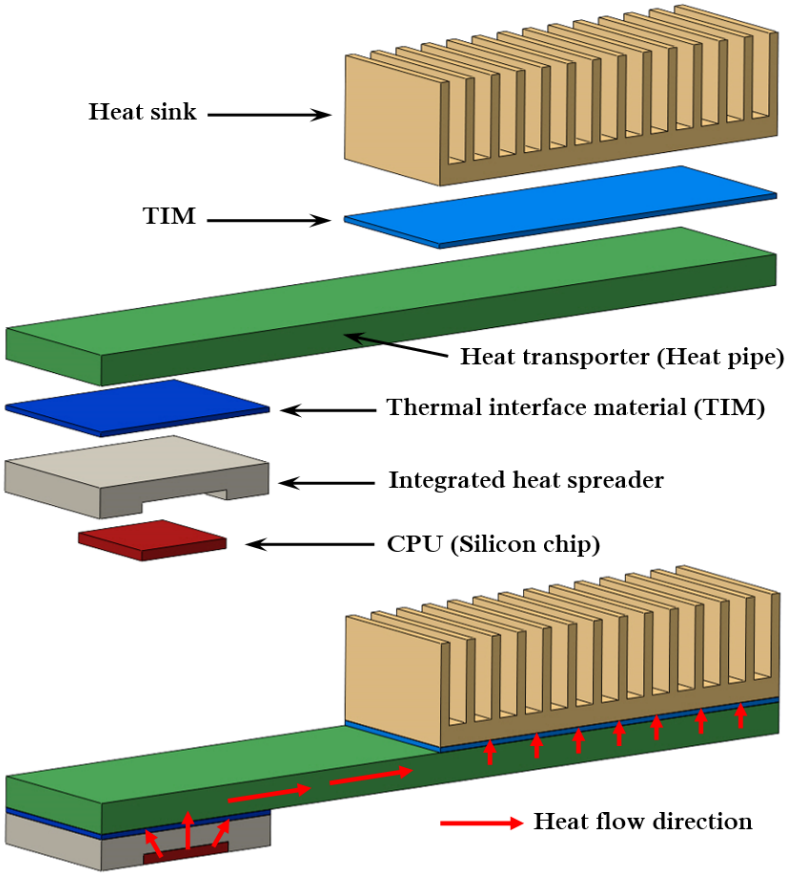

Figure 1.6 Traditional notebook thermal management cooling system, showing the heat flow direction from the heat source to the ambient air via the heat exchange surface.

In fact, the desired low thermal resistance, which is defined as the ability of a material to resist flow of heat (K/W), of the air-cooled heat sink mainly relies on the effective conduction heat transfer from the heat source to the heat sink fins, and the efficient heat dissipation via forced convection from fin surface to the ambient air. Basically, the efficient exchange of heat at the solid-fluid boundary layer of a forced-air cooled heat sink enables to achieve higher heat transfer rates and lower thermal resistance between the heated surfaces and the cooling air.

The total heat dissipated (in W) from the heat sink by the airflow is

$$Q_{\mathrm{t}} = h_{\mathrm{a}}\, A_{\mathrm{s}}\, (T_{\mathrm{s}} - T_{\mathrm{a}}) = \dot{m}\, c_{\mathrm{p}} (T_{\mathrm{out}} - T_{\mathrm{in}}) \tag{1.1}$$

where h_{a} is the convection heat transfer coefficient, A_{s} is the heat exchange surface area (m^2), T_{s} and T_{a} are the average heat sink surface and air temperatures (K), respectively, $\dot{m}$ is the mass flow rate (kg/s), c_{p} is the specific heat capacity of air (kJ/kg.K), and T_{out} and T_{in} are the average air temperatures at the exit and inlet of the heat sink (K), respectively.

The equation shows that the heat dissipation rate due to forced convection can be enhanced by increasing the heat exchange surface area at a given flow rate or increasing the mass flow rate at a given heat dissipation area. However, as the heat exchange area increases at a given heat sink size, a dense arrangement of the fins is required, leading to higher flow resistance losses and a reduced cooling performance. Likewise, extending the heat sink size requires further installation space for the cooling system and an increase in the number of associated fans.

On the other hand, increasing the heat transfer rate can also be achieved by improving the flow rate produced the rotary blower. However, this option remains limited under the miniaturization condition. This means that as the microelectronic device becomes thinner and smaller, increasing the size of the heat exchanger or the cooling airflow rate is restricted by the thickness and weight of the device, or the capability of the miniaturized rotary blower to produce sufficient flow rate.

Although today's industries offer miniaturized structures of fans and blowers with thicknesses in millimetres, further shrinkage in their size, which is practically

limited by the fan blade height and motor design, leads to less reliability, a reduction in the flow rate, and an increase in the power consumption and acoustic level due to the associated high rotational speed. The next section presents the main technical drawbacks and implementation challenges of mechanical centrifugal blowers under the condition of fan scaling laws, and discusses the possibilities of current emerging air cooling technologies such as synthetic jets and piezoelectric fans as alternatives to the traditional fans in thin and small-scale consumer microelectronics.

1.4.2 Airside cooling technologies

1.4.2.1 Conventional rotary fans

Rotary fans have been used for a long time as a successful cooling method to produce airflow used to dissipate thermal energy in microelectronic products and heat transfer applications. As the result of many years of development and optimization, mechanical fans represent by far the most popular method of active air production for forced convection cooling due to their efficiency in heat dissipation, low manufacturing cost and easy installation.

The performance of rotary fans is governed by scaling relationships that describe the change in the fan characteristics based on its geometric features, and given by [58],

$$\dot{V} \propto (\omega)^1 \, (\phi)^2 \, (h_{\mathrm{F}})^1 \tag{1.2}$$

$$\Delta P \propto (\rho)^1 \, (\omega)^2 \, (\phi)^2 \tag{1.3}$$

$$P_{\mathrm{o}} = \dot{V} \, \Delta P \propto (\rho)^1 \, (\omega)^3 \, (\phi)^4 \, (h_{\mathrm{F}})^1 \tag{1.4}$$

where $\dot{V}$ is the output flow rate of the fan, ΔP is the pressure rise, P_{o} is the power consumed by the fan, ρ is the air density, and ω, ϕ, and h_{F} are the fan rotational speed, diameter, and height, respectively.

These scaling laws obviously state that the flow rate and power consumption characteristics scale linearly with fan size while the pressure rise is invariant and independent of fan height, assuming fan electrical to mechanical transduction

efficiency is constant regardless of the change in fan dimensions. Indeed, the conventional scaling laws were determined and effectively proven for large scale fans operating at very high Reynolds numbers, where the inertia forces are dominant. However, as the fan becomes thinner and smaller for advanced microelectronic devices, the loss mechanisms become significant and the validity of the fan laws breaks down [59].

Based on fan diameter and rotational speed, it was demonstrated that the traditional fan laws are not effective at flows of low Reynolds numbers to predict the flow characteristics of miniature axial [60, 61] and centrifugal [62, 63] fans, where the viscous effects are considered. In addition, it was reported that as the fan becomes smaller and operates at low rotational speeds, the boundary layers created on the fan rotors in low flow regimes effectively block flow through the fan, reducing the produced flow rate, and causing significant losses on the fan performance and transduction efficiency [64].

A significant experimental study was conducted by Walsh et al. [59] to examine the validity of the fan scaling laws for profile heights at miniature scales using different sizes of centrifugal fans. They proved that the magnitudes of flow rate, pressure rise, and power consumption predicted by the conventional fan scaling laws does not exactly agree with those of the experiments. Based on this, they stated that it is not valid to apply fan scaling laws for flow rate and power consumption based on only blade profile height to determine fan pumping efficiency independently of fan diameter.

Figure 1.7 shows the fan aspect ratio, which is defined by fan blade height to fan diameter, as a function of the predicted performance trends relative to the fan scaling laws (represented by lines) and the measured performance (identified by dashed lines). Results reveal that the maximum flow coefficient, which is defined as $\dot{V}/h_{\mathrm{F}}\omega\phi^2$, lies in a range of aspect ratio between 0.07 and 0.16, but it is significantly reduced out of this range.

Therefore, as fan aspect ratio decreases (or the fan becomes smaller), both flow rate and pressure coefficient are significantly reduced at a constant rotational speed although an associated drop in power consumption can be achieved. Moreover, decreasing the fan diameter at a given blade profile leads to significant

losses in fan performance and efficiency because both flow rate and pressure change with the square of the diameter, as described by the scaling equations (1.2) and (1.3).

A further experimental study was presented by Walsh et al. [65] to investigate the levels of acoustic emission from miniature centrifugal fans and examine their agreement with those predicted by scaling laws. They found that the acoustic levels increase at low Reynolds number with reduced mass flow, and reported that the product of the Reynolds number, which is based on the maximum velocity and the rotor outer radius, and the aspect ratio squared $[(h_F/\phi)^2]$ should be greater than 30 to avoid unfavorable acoustic levels. In addition, as the fan becomes thinner and smaller, the design of miniature fan motors and rotors represents further challenges due to the manufacturing cost and the reliability against bearing failure [66].

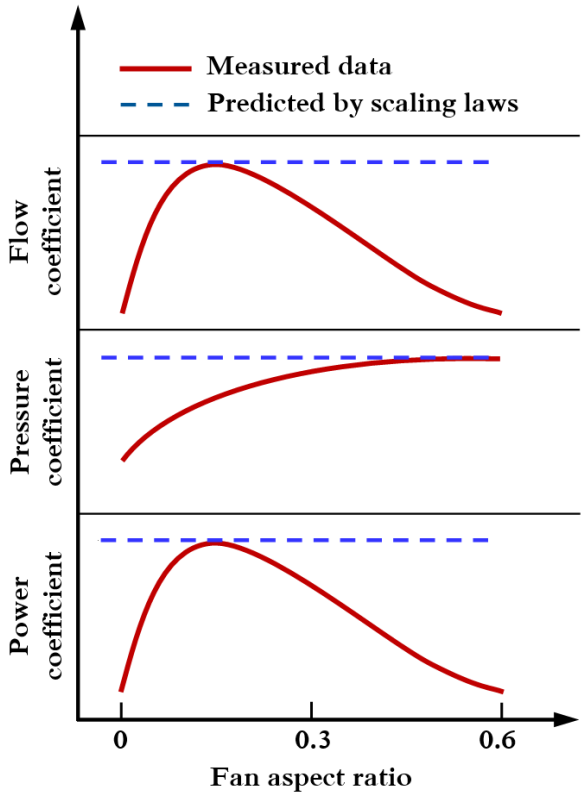

Figure 1.7 Fundamental limits of the miniaturized rotary fan under the scaling laws in terms of flow coefficient ($\dot{V}/h_F\omega\phi^2$), pressure coefficient ($\Delta P/\rho\omega^2\phi^2$), and power coefficient ($P_o/\rho\omega^3\phi^4 h_F$) at a constant rotational speed [8, 59].

In the case of centrifugal fans, which are usually used in thin microelectronic applications, the fan height is a limiting factor and must be fixed based on the device

thickness while the fan diameter can be selected to stay within the effective aspect ratio range, where the fan provides its highest flow rate. This restriction in turn may cause limitations in the flow rate produced by the fan and hinder its ability to dissipate the required amount of heat effectively from the heat exchange surface.

One of the ways to overcome this limitation is to increase the number of fans in the system in order to improve the flow rate and widen its outlet area for extended heat sinks. However, this requires a larger installation volume in the cooling system, increases the power consumption and the possibility of rotating mechanical parts to fail, and can lead to higher acoustic emissions due to frequency interference caused by multiple fans [67].

Therefore, for a given heat generated by the microelectronic device, further shrinkage in the fan size leads to reduced flow rates, less reliability, an increase in the power consumption, and ultimately, a reduction in the fan cooling performance. For these reasons, there is a critical need for alternative effective cooling solutions that meet the thermal management requirements for small form factor devices.

1.4.2.2 Synthetic jets

In their simple structure and operating mechanism, synthetic jets are considered to be one of the most innovative active cooling technologies proposed for the thermal management of microelectronics. Unlike conventional air jets produced with net mass flux, synthetic jets are zero-net-mass jets and can produce high momentum of unsteady turbulent impinging flow with no additional mass required to the system. A synthetic jet ejector mainly consists of a flexible membrane, an air cavity, and an orifice nozzle, as shown in **Figure 1.8**.

Basically, the airflow is produced by the synthetic jet device due to the movement pulse of a membrane, which induces flow to move back and forth, causing a periodic ejection and suction of air inside the cavity. Due to this mechanism, the surrounding air is sucked into the cavity and then forced to leave through the orifice nozzle, generating unsteady impinging jets with vortex rings formed near the opening [68].

One of the main applications of synthetic jets as ejectors is the operation in conjunction with a rotary fan to induce a secondary flow disturbance. Moreover, the

induced periodic jet can be effectively used in the presence of primary flow to control the surface temperature of heat sinks and integrated circuit components, or employed as impinging synthetic jet (primary flow) for hot spot cooling.

In the presence of steady primary flow produced by a fan, the unsteady flow jet and the formed periodic vortex structures can improve the turbulent flow and modify boundary layers for enhanced heat transfer rates [69]. This in turn leads to significant benefits related to the fan with lower rotating speeds, reduced operating power and acoustic noise, increasing the fan reliability and improving the overall cooling performance of the system. Synthetic jets can also play a significant role when they are placed upstream of the heat sink inlet to control and direct the incoming flow induced by a fan and reduce flow bypass, increasing the heat removal and enhancing the system efficiency [68].

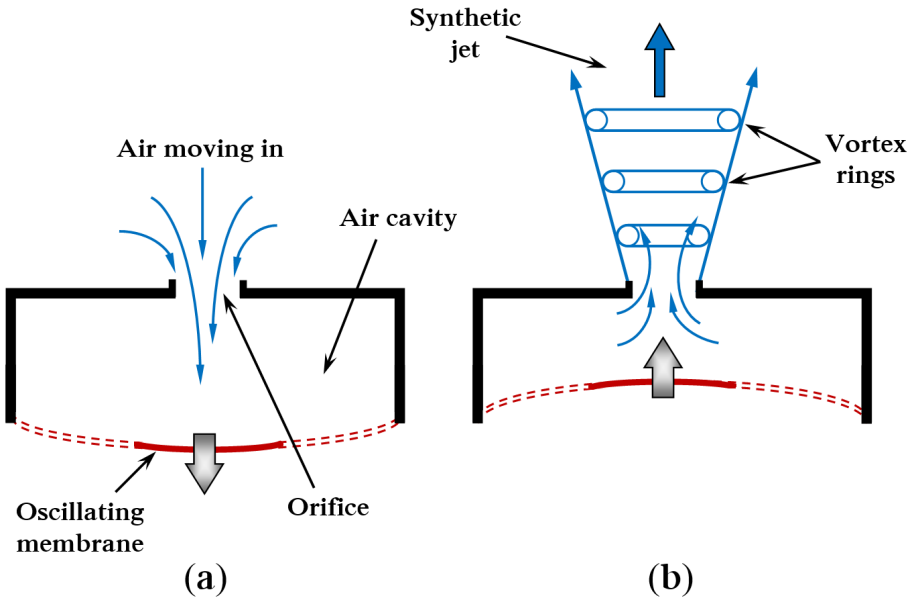

Figure 1.8 Schematic diagram of the synthetic jet operation mechanism; (a) entrance of air (b) generation of vortex rings and air jet [70].

Synthetic jet ejectors were investigated and suggested for cooling portable platforms [71, 72], and optimized based on performance for printed wiring boards (PWB) [73] and integrated heat sinks [74, 75]. However, although synthetic jets have many attractive features such as no rotating parts, low operating power and acoustic noise, high reliability, flexible shape, small size, and promising localized

cooling performance, their performance decreases as their scale is reduced, making their application is limited to cool only low-power consumer products [76]. Another serious disadvantage beyond the implementation of synthetic jets in confined spaces in the absence of an external net flux, is their re-ingestion of the air that has already ejected and passed over a heated surface, leading to a reduced cooling performance [77].

In general, synthetic jets are highly recommended to be used in conjunction with rotary fans for increased heat transfer rate in high performance applications such as servers and desktop computers, or for applications in open environments such as LED (light-emitting diode) cooling, where the long operating life of the cooling device is required and the large size that passively cooled can be reduced [8, 78, 79].

1.4.2.3 Piezoelectric fans

Piezoelectric fans (also known as piezo fans) are a solid state active air mover technology that has emerged as a viable cooling solution for the thermal management of microelectronic devices. It simply consists of a patch of piezoelectric material (piezo element) attached to a flexible cantilever blade, as shown in **Figure 1.9**. The operation mechanism of the piezoelectric fan depends on the contraction and expansion of the piezo element under alternating applied voltage, which occur with the same frequency as the input signal, causing oscillations at the free end of the blade. When the fan structure is driven at resonance, the oscillations and generated displacement at the blade tip become larger and cause a considerable airflow movement [80, 81].

With their inherent and attractive features of high reliability, no bearings or wearing parts, long operating life, small and simple structure, minimal noise emissions, low operating power, and efficient control of air and heat removal, piezo fans can meet the special thermal management requirements for microelectronics cooling [82]. Over recent years, the unique airflow patterns provided by single or multiple piezo fans have been developed and optimized to be used in integration with heat sinks for active cooling [83, 84], or for local cooling of microelectronic components [85, 86] and LED packages [87, 88].

Among other air cooling methods, piezoelectric fans have the highest energy conversion efficiency due to their extremely low operating power [8]. However, although increasing the resonance mode of the piezo fan can lead to higher flow rates, the associated increase in the power consumption and the acoustic level offsets this advantage [82]. Moreover, although these devices have recently shown effective cooling performance in miniature scale when integrated into a heat sink of a height of 3.5 mm [89], the low flow rate production, which degrades as the blade scale decreases, limits their practicable application in high-power consumer devices [8]. A recent review study indicated that the characteristics of piezoelectric fans are gaining greater acceptance in LED lighting applications, where the reliability, long lifetime and low power consumption are critical needs [90].

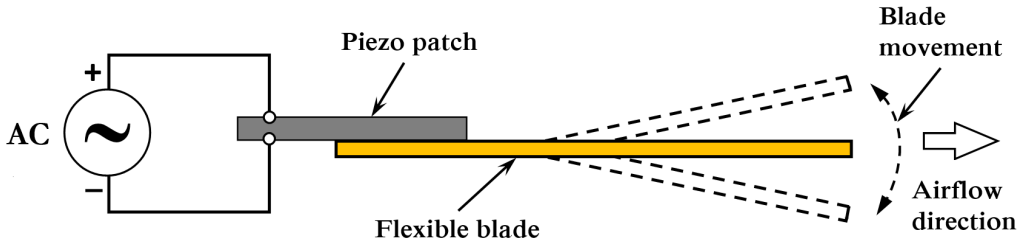

Figure 1.9 Schematic diagram of a piezoelectric fan vibrating under an applied AC voltage [82].

1.5 Chapter Summary

As alternative airside technologies are being developed to replace the rotary fans or overcome their limitations for modern high-power microelectronics, the balance between the advantages and disadvantages of each thermal solution dictates whether they will be adopted based on thermal management considerations. In the consumer applications, where the cost factor and the user comfort are considered, the response for efficient compact thermal modules that ensure the device functionality becomes challenging. Although the inherent advantages of both synthetic jets and piezoelectric fans make them competitive to rotary fans in terms of reliability, scale structure, lifetime, power consumption and noise levels, their modest flow rates produced at small-scales overshadows these considerations.

In their comprehensive review and analysis study, Wang et al. [8] recently compared the performance of a number of alternative air pumping methods against rotary fans for microelectronics cooling, including piezoelectric fans, synthetic jets and EHD air movers. They concluded that although piezoelectric fans and synthetic jets are potentially useful for cooling of localized hot-spots, they are generally unsuitable for consumer microelectronics due to their inability to generate sufficient cooling airflow rates. In contrast, they found that the EHD air movers have great potential to be used as a thermal management solution for microelectronics cooling, offering important advantages over rotary fans due to their flexibility, silent operation, reduced energy consumption, smaller volume requirements, and ability to generate sufficient flow rates that provide effective heat dissipation on small form factor microelectronics.

1.6 Objectives and Scope of Thesis

The performance of mechanical rotary fans required to provide efficient cooling for the next generation of thin and high-power density consumer microelectronics is expected to be increasingly problematical due to their limitations in small-scale applications. This has led to increased attention on alternative cooling solutions, such as the emerging EHD technology, to examine their capability in small form factor applications based on thermal management requirements. However, as is true of many other emerging technologies, EHD flow based cooling systems still require more investigation, development and design optimization in order to meet the required cooling performance in miniaturized electronics before they are commercially viable.

This thesis explores the benefits of using EHD flow technology as an alternative thermal management solution to mechanical cooling systems in practical small-scale microelectronics, and attempts to move its application a step forward towards a real-world implementation. The objectives of this thesis are broken into three main parts:

The first presents a validated numerical EHD flow model that solves the set of coupled-physics equations of electrostatics, charge transport, and fluid dynamics. Developed models that couple EHD flow and conjugate heat transfer modules and

enable heat dissipation predictions are an important part of modelling development in this thesis. As not all aspects of EHD processes can be observed or examined through experimental investigations and in order to save time and cost, numerical modelling represents an important tool to design and optimize EHD devices, provide accurate predictions of performance and efficiency, and investigate the influence of geometric parameters, offering wide scope for exploring the future design and optimization of EHD based thermal systems. In this light, this thesis contributes and presents the first developed three-dimensional (3D) numerical model to investigate EHD flow characteristics and the sidewall effects of EHD channels, and applies a conjugate heat transfer module for integrated EHD flow based cooled heat sinks, which to the best of the author's knowledge has not been developed before.

The second contribution presents a numerical investigation and comprehensive analysis into the development of EHD flow induced by a blower of wire-to-plane/grid configuration based on airflow rate, pressure generation, power conversion efficiency and device scaling. The investigation is devoted to study the influence of the fundamental design parameters of miniature EHD air blowers on pumping performance. The optimization of EHD blower design requires a delicate balance between the resultant flow production and the associated engineering challenges related to EHD process such as the high level of applied voltage. This thesis strives to provide a design optimization of EHD blowers that predict the efficient locations of EHD electrodes based on the effective levels of operating voltage and power. It also includes design considerations of size and power consumption and demonstrates the capability of applying low height and small-scale EHD air blowers for cooling thermal management applications such as consumer electronics.

The third part presents 3D numerical simulations to investigate the benefits of integrating EHD blower with a plate-fin heat sink and examines the cooling performance and benefits of integrating EHD systems into modern laptop computers. This thesis aims to evaluate the scope for integrated EHD air blowers to replace mechanical fans in low-profile electronic devices.

Although the undesired side effects of the corona discharge process such as ozone production and electrode degradation represent major disadvantages and challenging against EHD technology in the real implementation, they are beyond the scope of this thesis. However, the most influencing factors that have been reported towards ozone mitigation are considered in this work such as using a positive polarity and very fine corona electrode.

1.7 Thesis Outline

The remainder of this thesis is divided into six chapters.

Chapter 2 describes the fundamentals and theory of the corona discharge process, including the operating mechanism of EHD flow and the characteristics of positive and negative discharges. The chapter also presents a detailed review that covers the use of EHD flow in the field of heat transfer applications and thermal management considerations. A concise review over the modelling of EHD flow based heat transfer is also included at the end of the chapter.

Chapter 3 presents a detailed explanation of the EHD numerical modelling, including the governing equations, numerical method, and assumptions used for the space charge generation and fluid dynamics. Two- and three-dimensional numerical models are developed using the finite element method and appropriate boundary conditions for EHD driven flows induced in wire-to-grid/plane channels. The models are validated carefully against numerical and experimental data for the electrical and fluid dynamic characteristics.

Chapter 4 presents a comprehensive numerical analysis and developments on the EHD blowers of wire-to-grid configuration to investigate the influence of geometrical and design parameters on the EHD blower performance and conversion efficiency. Optimal design is predicted based on pumping performance and the effective levels of operating conditions.

Further numerical developments and design optimization are presented in Chapter 5 for miniature EHD blowers of wire-to-plane configuration based on thermal management considerations. Simple expressions are presented to predict the optimal design based on the blower height. The chapter includes 3D modelling of an

EHD blower to study the flow rate, static pressure, flow pattern, and sidewall effects on outlet velocity profile and magnitude. An optimized and combined EHD blower is proposed, and comparisons against commercial miniature rotary blowers based on pumping efficiency and blower size are presented.

Using the optimal designs predicted in previous chapter, Chapter 6 proposes a novel design of EHD cooling system and presents developed 3D numerical models to solve the coupled physics of EHD flow and conjugate heat transfer for EHD air blowers in integration with a heat exchanger of parallel-plates structure. For a range of operating conditions, a parametric study is undertaken to evaluate the impact of design parameters on the thermal performance of EHD system. The predicted maximum operating temperatures are compared with those allowed in the real implementation of fan-cooled laptops.

Finally, Chapter 7 summarises the main conclusions from the results presented in this thesis, and suggests future research directions.

CHAPTER 2

Fundamentals and State of the Art

2.1 Preface

Electrohydrodynamics (EHD) is a process of interactions between electric fields and fluids, resulting in a corona discharge and thereby a fluid movement. The mechanism of this process occurs in the air when a sufficiently high potential difference is applied across two electrodes. The first electrode has a high tip curvature of a very small radius such as needle or wire and is called the emitter or corona electrode, while the second electrode has a low tip curvature and an opposite polarity to the emitter electrode and is called the collector electrode. The sharp edge of the corona electrode is necessary to create the electric field gradient, which is responsible for ionizing air particles in close proximity to the corona electrode surface, and subsequently causes the corona discharge phenomenon.

Since the intensity of the electric field created at sharp points is greater and stronger than that created at blunt bodies, the voltage required to cause corona discharge at the corona electrode is lower compared to that of the collector electrode. This fact can be explained by the basic formula of the electric field intensity (E) of a sphere, given by Gauss's law:

$$E = \frac{\tilde{Q}}{4\pi\ \varepsilon_0\ R_e^2} \tag{2.1}$$

where $\tilde{Q}$ is the charge, R_e is the radius of electrode curvature, and ε_0 is permittivity of free space (constant). This basic formula shows that the electric field intensity increases as the radius decreases, and the electrode geometry has a significant effect on the corona discharge generation.

It is important to state that the space across the EHD electrodes is occupied by both positive ions and electrons that exist in the air due to the background radiation, which is mainly caused by the radioactive elements and cosmic rays. The existence of these electrons is active to create an initial concentration required for the ionization process and corona discharge [91].

2.2 Basic EHD Flow Principle

The operation of EHD flow induced by positive corona discharge, where a high voltage is applied between corona and collector electrodes, and the resultant ionic wind flow is shown in **Figure 2.1**. In general, when a sufficiently high voltage of a certain polarity is applied to a sharp edge of corona electrode, an electrical field is created and continues to increase until it exceeds the breakdown strength of the air. At this level, the particles of opposite charge are attracted and connected to the corona electrode, creating a conductive region around it. Due to the strong electric field and the increase in the conductive region, the absorbed charges are accelerated and lead to more liberation and ejection of charges from neutral particles. This operation is called the ionization phenomenon and occurs in a region called the ionization zone.

The rest of the charged particles are then attracted to the collector electrode, which has the opposite polarity of the corona electrode. During their motion, the charged ions collide with neutral air molecules and transfer a part of their momentum and energy to them, resulting in a bulk air movement towards the collector electrode called the ionic wind. When the ionized molecules reach the collector electrode, they return to be neutralized again. The space where the air molecules are propelled from the ionization layer into the collector electrode is called the drifting zone.

Both positive and negative corona can be generated depending on the voltage polarity applied at the corona electrode. Thus, positive corona can be generated by applying a high positive DC voltage at the high curvature emitting electrode, while the collector is grounded. Similarly, but conversely, when a corona electrode is subjected to a high negative DC voltage while the anode electrode is adopted as a

collector, a negative corona discharge is operated. Corona discharge can also be created by an AC sinusoidal or pulsed potential.

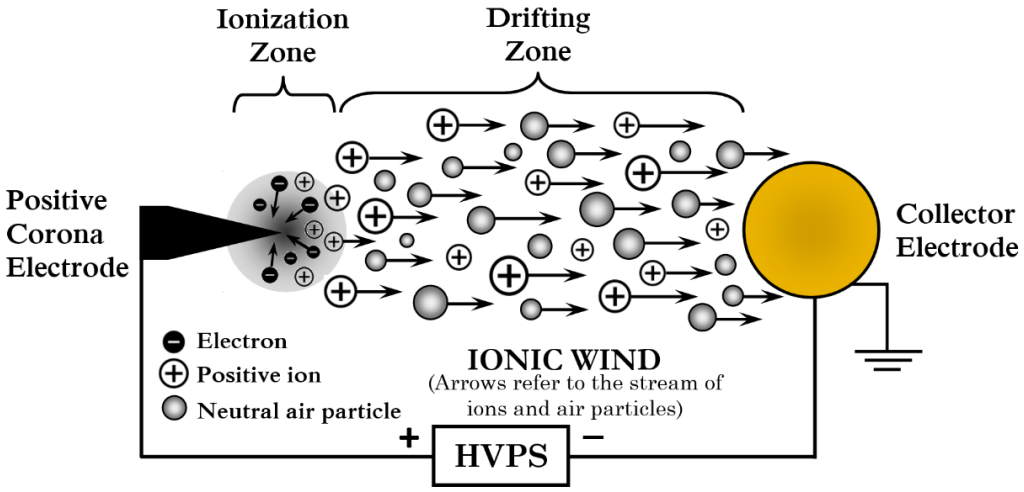

Figure 2.1 Schematic of positive corona discharge and the ionic wind induced by the movement of positive ions towards the collector electrode [8].

2.3 The Corona Discharge Process

2.3.1 Positive corona discharge

The positive corona discharge phenomenon and the related ionization process have been well understood and described in the literature [39, 92-96], and is illustrated in **Figure 2.2**. The process of positive corona discharge occurs when a high positive electric potential is applied to the corona electrode, while the collecting electrode is grounded, creating a gradient electric field across them. When this voltage increases and exceeds a certain value called corona inception (or onset) voltage (CIV), which is the high enough voltage required to create the electric field needed to ionize the air molecules, the corona discharge phenomenon begins to take effect. Below the CIV value, no discharge occurs and no current can be detected between the two electrodes.

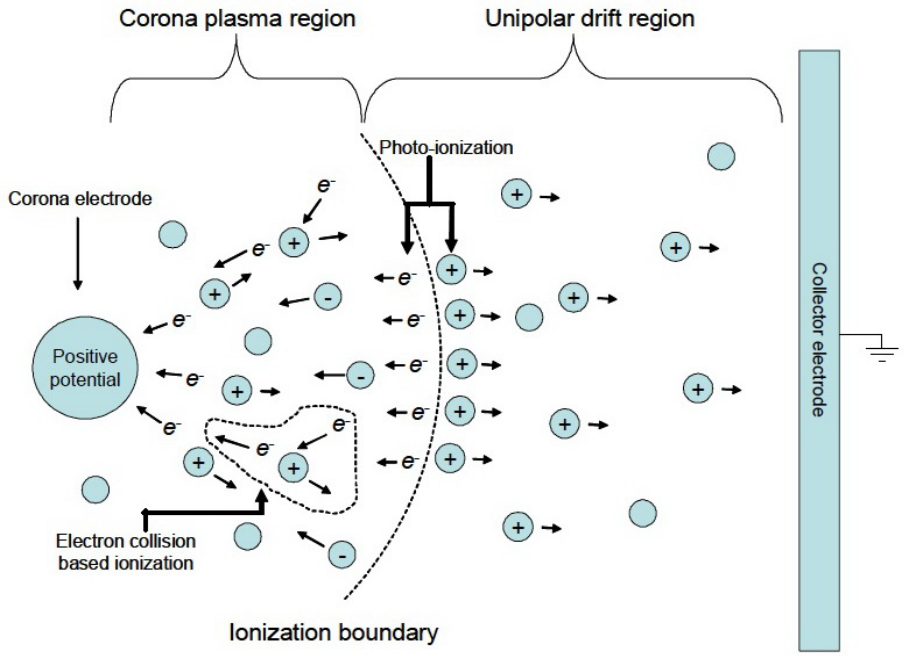

Figure 2.2 The process of positive corona discharge [96].

The created electric field must exceed the dielectric strength or the breakdown strength of the air in order to initiate a corona discharge. The dielectric strength of a material (expressed in V/m), is the level of electric field that the material can withstand before becoming electrically conductive. Thus, when the applied potential increases and exceeds the CIV, the electric field strength necessary for producing corona discharge is created. At this level, a space charge is formed due to the positive ions, and a low discharge current is created and flows across the drifting zone of the electrode space. The ion current then increases proportionally and exponentially with the electric field (or the applied voltage), following Ohm's law regime, as shown in **Figure 2.3**.

Thus, when the electric field intensity increases beyond this level, the free electrons that naturally exist in the air in the close vicinity are accelerated towards the corona electrode, and the bound electrons in the atomic orbitals of air molecules are liberated. These electrons and the resulting positive ions are then accelerated by Coulomb forces with enough kinetic energy to release more electrons from neutral air molecules during collisions. Due to a further increase in voltage, the velocity of charged molecules (positive ions) increases through their free path, leading to more collisions with the neutral molecules and greater production of new ions. As a result,

the ion current suddenly and rapidly increases with a high current density, reaching the breakdown voltage region across the electrode separation gap, where the electrical arcing and a spark-over occur.

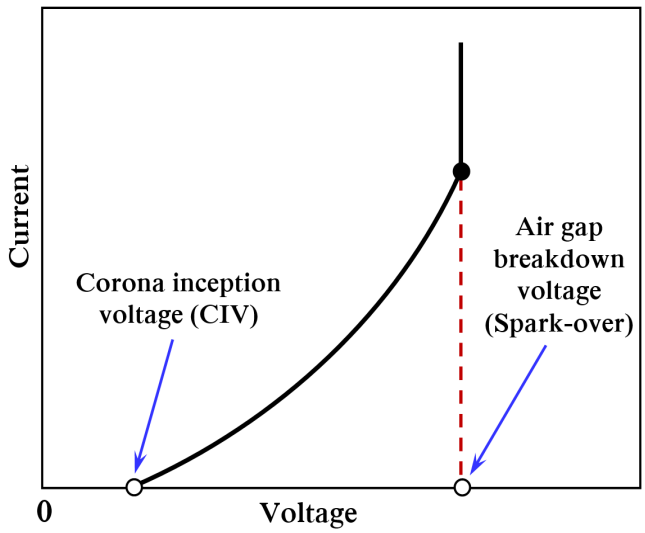

Figure 2.3 Corona current-voltage relationship.

The newly released electrons, in turn, lead to further breakdown, forming an electrically conductive region in a process called avalanche breakdown or the electron avalanche. This zone, where the conductive region is created and the electron avalanche occurs, is called the ionization (corona plasma) region. In addition, positive ions and free electrons are also produced due to the photo-ionization process when the photons eject electrons from air molecules.

It is important to mention that the ionization region ideally contains free electrons and positive ions, and is surrounded by a distinct layer called the ionization boundary (or surface), which is a complex interface where there is a delicate balance of repulsion and attraction processes caused by the Coulomb forces. In order to simplify the analysis in the ionization layer, Kaptsov's assumption [97] can be applied, which assumes that the electric field strength at the boundary between the ionization and drifting zones is constant, as will be explained in detail in Chapter 3.

Free electrons may recombine with positive ions, or form negative ions when they attach to electronegative air molecules, such as O_2. Both recombination and

electron attachment cause a reduction in the net ionization rate. However, due to the high energy of electrons that are close to the corona electrode, the net ionization is sustained there, but the processes of attachment and recombination dominate as the distance from the corona electrode surface increases, leading to a decrease in the net ionization rate. At the boundary of the ionization and plasma regions, both processes of attachment and recombination, and the rate of ionization become equal and in a balanced act.

During the process, free electrons and the produced negative ions are attracted towards the corona electrode, creating a secondary plasma (corona ionization), and leading to production of more positive ions. These positive ions are then repelled by the positive high voltage of the corona electrode and flow towards the negative collector electrode under the effect of Coulomb forces. During their path through the drifting region, which ideally consists of only positive ions and neutral air molecules, the unipolar ions transfer and exchange their momentum into neutral air molecules due to collisions between them, transforming the electric energy to the kinetic energy, and creating a bulk air flow (ionic wind). The ionization process cannot occur at the negative collector electrode due to its large tip curvature and the inefficient electric field intensity near it.

2.3.2 Negative corona discharge

As for positive corona, the ionization process for a DC negative corona has been well described [93, 96, 98-101] and can be shown in **Figure 2.4**. Generally, when a high negative potential is applied to the corona electrode and exceeds the corona onset, a high electric field is created and leads to a negative corona discharge. As in the positive corona case, the electron avalanche process is initiated due to the naturally occurring electrons in the air. However, unlike the positive corona process, photo-emission from the corona electrode surface has the primary responsibility to produce the secondary electrons in negative corona [101], and this production depends on the negative electrode material, indicating that the effect of material selection on negative corona discharge is higher compared to that for positive coronas [102]. The positive ions are then attracted towards the highly negative corona, creating a positive sheath of ions surrounding the corona electrode, where the ionization process occurs.

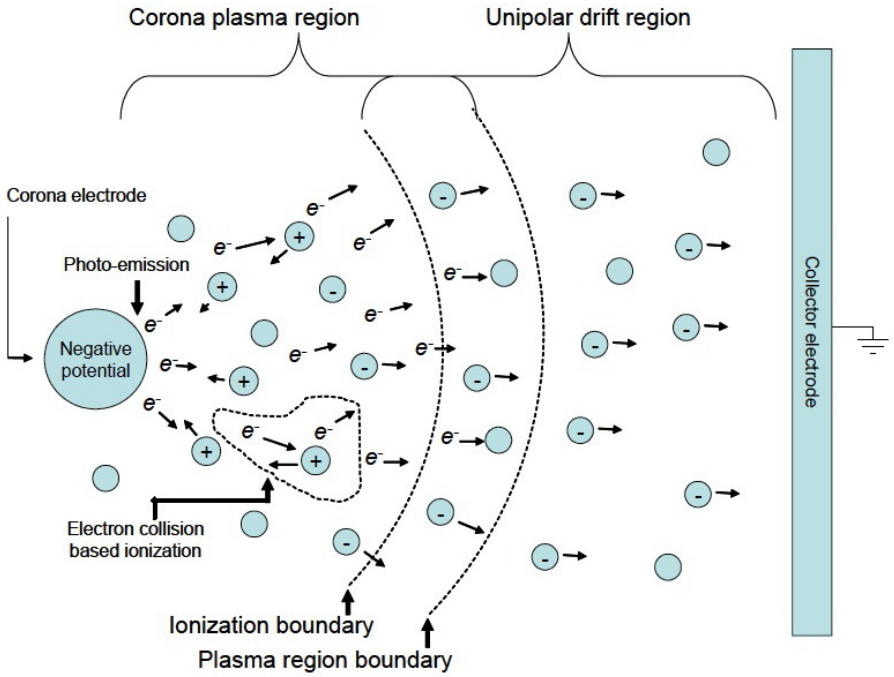

Figure 2.4 The process of negative corona discharge [96].

In the ionization region, the process of recombination and attachment of free electrons is lower than the production rate of free electrons due to electron collisions with air molecules. However, the rate of recombination and attachment of free electrons increases with increasing distance from the corona electrode, and be equal or greater than the ionization rate, forming the ionization layer. Due to the ionization process, free electrons are then repelled away from the negative corona by the repulsive force effect, and leave the ionization zone towards the positive collector.

Unlike positive corona, the free electrons bombard the neutral air molecules at the ionization region layer, creating certain chemical reactions and extending the plasma boundary outside the ionization region layer, where the chemical reactions occur. Due to this larger ionization region, the tendency of negative corona to produce ozone is higher than the positive one [96]. Ultimately, when the electrons are accelerated and moved towards the grounded collector, they collide with the neutral air molecules and transfer momentum, creating the ionic wind.

2.4 Characteristics of Positive and Negative Discharges

The main difference between positive and negative coronas is that the electrons travel in opposite directions. However, the mechanism of each type includes significant differences in their characteristics. Indeed, the selection of the suitable polarity for inducing corona wind mainly depends on the design and application of EHD devices. The main characteristics of both polarities can be summarized as follows:

2.4.1 Power consumption

In general, it was reported that ionic wind induced by positive polarity consumes less power at a given applied voltage and electrode gap, and has higher energy conversion efficiency than the negative corona wind [103-105].

2.4.2 Joule heating effects

Generally, negative corona generates less Joule heating than the positive polarity [103]. However, at higher applied voltages, Joule heating effects are significantly prone to occur in applications of negative corona compared to a positive one [38, 39]. Moreover, positive corona offers better cooling performance due to its low plasma temperature, and relatively low temperatures of ions and neutral molecules, compared to a negative one [106].

2.4.3 Corona inception voltage (CIV)

Compared to a positive corona, negative corona discharge requires lower voltage to be initiated due to the higher mobility of attracted positive ions that move towards the negative corona electrode, resulting in higher electric fields, greater emission current and lower onset voltages [107]. In addition, negative corona has a higher air gap breakdown voltage than a positive one at a given electrode gap [108].

2.4.4 Conversion efficiency and flow velocity

Under the same operating conditions, positive corona has better energy conversion efficiency [104, 105] and can generate a higher ionic wind velocity (or higher stream velocity) than the negative corona [109, 110]. This characteristic is attributed to the generated streamers of high energy ions as well as the nature of the positive discharge process, which includes large positive ions drifted by charge carriers with higher delivered energy [39], leading to a greater number of neutral molecules pushed towards the collector electrode.

2.4.5 Ozone production

Both coronas are efficient at producing ozone in air. However, experiments indicated that ozone production caused by negative coronas is higher than that by positive coronas under the same discharge conditions [32, 34, 111, 112]. This is due to the greater number of electrons in negative coronas, and also because of the low-energy of the reactions that produce ozone in positive coronas.

2.4.6 The external influences

In the case of negative corona, both the gas medium and the corona electrode material are important. In order to avoid a spark (like lightning), which may occurs instead of corona discharge, a medium that contains gases with high affinity for electrons such as oxygen, water vapour and carbon dioxide, is needed. Therefore, in pure gases of very low affinity for electrons such as nitrogen, hydrogen, and helium, no negative corona can occur [96]. In addition, electrode material also can affect creating negative corona discharge due to the nature of electron production from the surface of a negative corona electrode [102]. Moreover, the mobility of ions in a negative corona can be more affected by temperature, which causes a significant decrease in the ion current compared to a positive corona [113].

2.5 State of the Art

The ionic (corona) wind is not a new phenomenon and it was first noticed in the early 1700s by Francis Hauksbee [114] and Sir Isaac Newton [115], who (the latter) first named the phenomenon with electric wind. In the 1800s, other scientists such as Michael Faraday [116] and Maxwell [117] made and reported significant progress about the electric wind phenomenon and its effects.

In the mid twentieth century, the basic theory of EHD pumps was developed, and the mechanism of gas movement under the effect of corona discharge was investigated by Stuetzer (1959) [118], who studied ion conduction in both liquids and gases, and Robinson (1961) [119]. The latter showed experimentally that the average velocity of corona wind changes almost linearly with the applied voltage and is proportional to the square root of the ion current.

Two decades later, Yabe et al. [120] presented a significant advancement in their experimental and theoretical investigation and analysis of corona discharge flow induced in an enclosed dried nitrogen chamber by a 40μm-diameter corona wire anode placed under a collecting horizontal plate. Their experimental results clarified that the positive ions predominate over electrons in the space between electrodes except in the vicinity of the wire electrode. The electric potential distribution in the space and the distributions of current density and pressure on the grounded plate were numerically calculated and revealed good agreement with the measured experimental data. The authors were able to model the stream function and found that the fluid field has a circulating flow inside the chamber.

The first investigation on the use of ionic wind for convective heat transfer was presented in 1963 by Marco and Velkoff [121]. The use of electric field and ionic wind as a secondary flow to disrupt the thermal boundary layer and enhance heat transfer has been widely studied after the first investigation conducted by Velkoff in the early 1960’s [122]. However, it is only in the last decade or so that the EHD pumps have received an increasing attention as a potential alternative to mechanical cooling systems in microelectronics and thermal management applications.

Regarding the influence of environmental factors, a number of studies have investigated the effect of the ambient conditions on the characteristics of discharge processes such as air humidity and pressure [42, 123-125], whereas others focused on studying ozone generation as a normal by-product of corona discharge [31-33, 126].

A literature review reveals that the EHD technique has been widely examined in the heat transfer field either as a primary flow (purely) or in the presence of external flow for boundary layer modification, using different configurations such as point-to-plane or wire-to-plane electrodes. In this direction, a number of review studies were presented for the use of EHD flow based on heat transfer enhancement [127-130] and thermal management considerations [8] or for general applications [131]. The present review of the thesis focuses on the experimental and numerical studies reported for the investigation of EHD driven airflow in convective heat transfer, including those conducted to maximise and develop corona wind generation and conversion efficiency, or established for thermal management applications. A concise review over the modelling of corona discharge and EHD flow is presented later in this chapter.

2.5.1 EHD pumps based flow generation

One of the first studies to examine the possibility of employing electrostatic blowers for practical use were reported in the early 1960's by Stuetzer [132] and Robinson [119]. Both researchers used a needle-to-ring electrode configuration to generate electric wind in a tube and presented similar conclusions. Using air as a fluid medium and under negative potential, Robinson experimentally and theoretically investigated the main characteristics of electric wind, including the relationships between wind velocity and both voltage and current, the energy conversion efficiency, the effects of discharge polarity and fluid density, and the resulting ozone generation. The author concluded that despite the low conversion efficiency (less than 1%) achieved in his geometric design, he explicitly mentioned that electrostatic blowers have attractive advantages over conventional mechanical fans with silent operation, no vibrations, no gyroscopic or rotational effects, no lubrication requirements, and easy installation or replacement of parts. He also

recommended that more research on improving conversion efficiency of EHD pumps is required.

Although there were several attempts to develop corona wind generators, most investigations have been conducted only in the early 2000s. Rickard et al. [45] experimentally studied the outlet velocity profile of ionic wind induced in a tube by a needle-to-ring electrode configuration for a range of negative corona voltage (up to –11 kV), as shown in **Figure 2.5**. Both the grounded ring diameter and electrode gap were fixed at 9.27 and 9.5 mm, respectively. A converging nozzle was placed downstream of the EHD pump to control the exit-to-inlet area ratios and investigate its effect on wind velocity. Measured results of velocity profiles using Particle Image Velocimetry (PIV) revealed a velocity deficit at the centre of the generated flow for higher voltages due to the radial component of the charged ions, which enhances the axial flow at stronger electric field intensity. Results also demonstrated that the produced velocity was limited to around 2.4 m/s, regardless of the exit-to-inlet area ratio, and the nozzle had a slight influence on accelerating the induced flow and the ionic wind was unable to overcome pressure restrictions caused by converging channels.

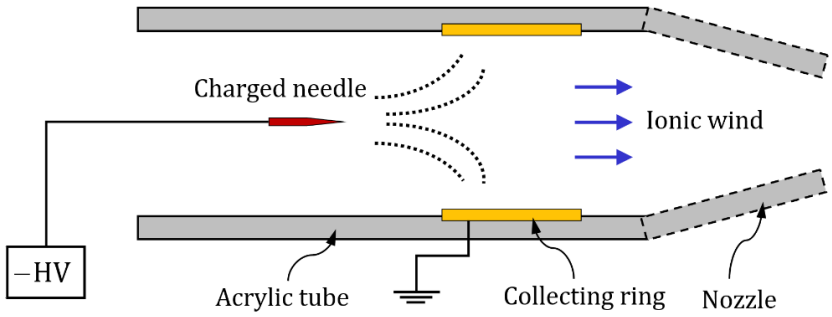

Figure 2.5 Cross-section sketch of a single-stage ionic wind generator of a needle-to-ring configuration inside a converging exit circular tube [45].

This study was extended and developed later by the same authors [41] using their previous EHD electrode configuration in a cascading design of up to seven stages placed in a tube of a converging exit nozzle, as illustrated in **Figure 2.6**. They showed that the exit nozzle provided considerable improvement in the generated wind velocity over that without a nozzle due to the improved driving pressure using

the staging design. Although both pressure and flow rate significantly increased with the number of operated stages with up to 38 Pa and 85 l/min, respectively, using the EHD pump with a nozzle, the conversion efficiency was extremely low (just 0.1%) due to the high power consumption.

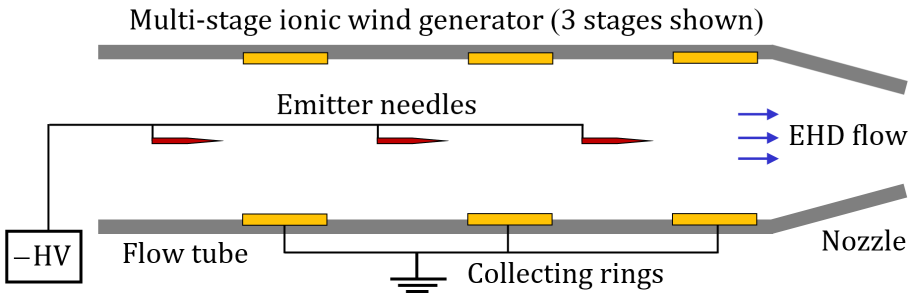

Figure 2.6 Cross-section sketch of a multi-stage EHD flow generator of a needle-to-ring configuration inside a converging exit circular tube [41].

Qiu et al. [133] presented an experimental and theoretical study of the velocity characteristics of corona wind generated in a tube by multi-stages cascading EHD pump. The effect of the collector geometry on corona wind induced by five stages of either needle array-to-ring or needle array-to-mesh electrodes (shown in **Figure 2.7**) was examined for ranges of electrode gaps and negative applied voltages. Results showed that the mesh collector geometry was more efficient and can induce higher wind velocity than a ring, resulting in a maximum average flow velocity up to 7.39 m/s and a volumetric flow rate of 140 l/min, with a conversion efficiency of 0.8%.

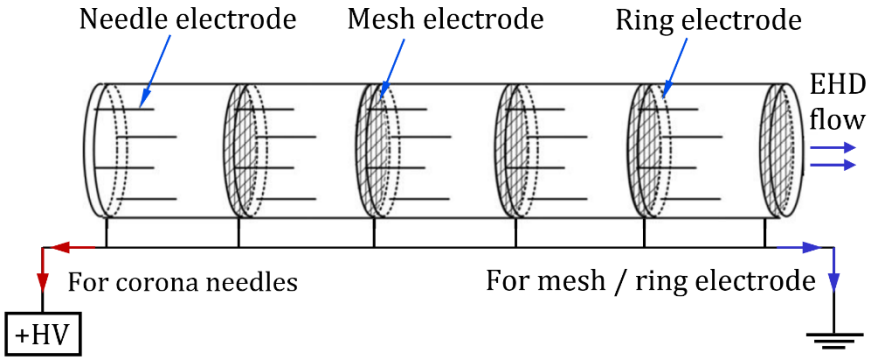

Figure 2.7 Schematic diagram of a multi-stage EHD flow pump of a needle-to-mesh/ring electrode configuration inside a circular pipe used in [133].

This study was developed later by Wei et al. [134] using the needle array-to-mesh electrodes configuration to explore the effect of the number of stages on EHD pump efficiency, considering different corona DC polarity and electrode gaps. The trends showed that the conversion efficiency of a single stage tends to decrease after certain increases in the applied voltage, depending on the electrode spacing. It was also found that the efficiency of the serial staged EHD pump increases with the number of stages, recording a maximum value of 2.2% using a 25-stage gas pump (out of 32 stages). This efficiency was associated with a maximum average wind velocity and volumetric flow of approximately 16 m/s and 303 l/min, respectively, using a negative corona discharge with −9 kV operating voltage.

Moon et al. [135] experimentally investigated the effect of using a ring as a further emitter electrode on the ionic wind velocity generated by a needle-to-mesh EHD pump in a tube, as shown in **Figure 2.8**. A positive corona discharge was induced by an emitter needle surrounded by a ring electrode and located at a fixed needle-to-grounded mesh gap spacing, whereas the effect of the ring location from the needle tip and the ring diameter were investigated for a range of applied voltages. Results revealed that using the ring as a further corona electrode enhanced the maximum ionic wind velocity and the corresponding efficiency of flow generation, which is defined by the corona wind velocity to the input EHD power, by 1.2 and 2.5 times, respectively, higher than that achieved by only a needle-to-mesh EHD configuration.

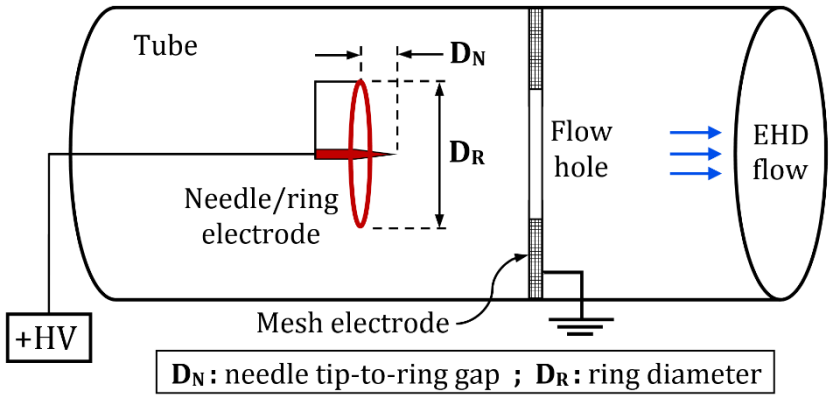

Figure 2.8 Schematic diagram of the electrode arrangement of the needle/ring-to-mesh EHD flow pump used in [135].

In another work, Moon et al. [105] examined the effect of using a wet porous point as a corona electrode on ionic wind velocity and the efficiency of flow generation induced by DC (positive and negative polarities) and AC corona discharges in a ducted needle-to-mesh EHD pump. Significant improvement in ionic wind generation was achieved using a wet porous corona electrode for all types of corona discharges compared to those of metal electrode. The maximum average wind velocity and the corresponding efficiency of flow generation were enhanced by 1.95 (1.23), 1.31 (1.24), and 1.30 (1.15) times for the positive, negative, and AC corona discharges, respectively, compared to those obtained using the same EHD pump design and polarity with non-porous electrode. Results revealed that positive corona discharge was the most efficient among other polarities in both cases, and the considerable enhancement with 95% in the wind velocity using wet porous electrode was due to its finest water particles induced with positive discharge compared to others.

Moreau and Touchard [104] presented a comprehensive experimental study to enhance the mechanical efficiency of corona wind induced by a needle emitter through a tube, as shown in **Figure 2.9**. The investigation considered the effect of voltage polarity, collecting electrode geometry (grid or ring configurations), grounded grid density as well as electrode gap ($G = 5 - 20$ mm) and tube diameter ($D = 10 - 30$ mm). It was found generally that a positive corona generates higher ionic wind velocity due to the presence of streamers in front of the needle compared to the negative one. Results of design optimization showed that the efficient electrode gap mainly depends on the tube diameter, and the best flow velocities were achieved within the ratio range of $0.5 \leq G/D \leq 0.75$. Results of the influence of collector geometry demonstrated that the grid was more efficient than the ring, and the grid density has an important influence on ionic wind generation. The optimal configuration was able to generate a maximum wind velocity and a flow rate up to 8 m/s and 0.4 l/s, respectively, with a conversion efficiency of 1.72%.

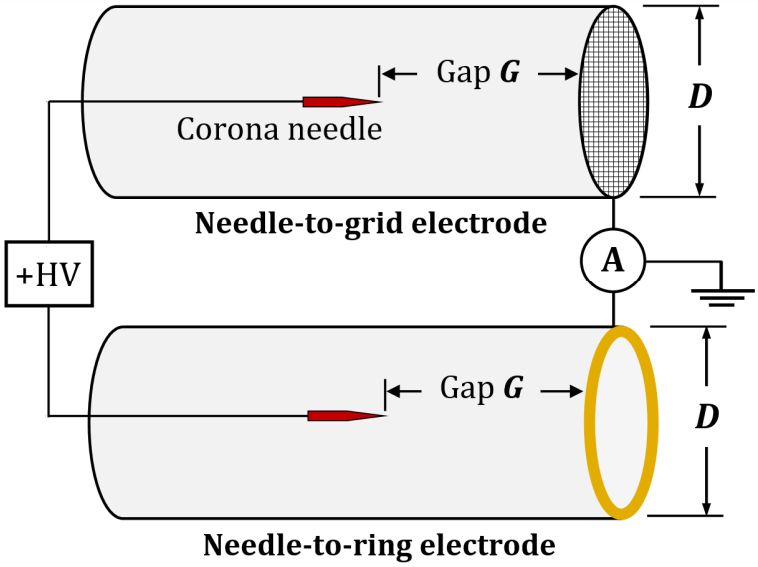

Figure 2.9 Schematic diagram of the needle-to-mesh/ring EHD air pump used in [104].

An experimental investigation was presented by June et al. [136] to determine the actual efficiency of EHD air movers and make fair comparisons against mechanical blowers. The ionic wind was generated between five emitter needles in coaxial arrangement and a cylindrical collector electrode, considering the effect of potential polarity (positive or negative), electrode gap and collector length. According to the literature, the authors noted that the efficiency of EHD devices, which is typically defined as the percentage between mechanical and electrical powers, has always revealed extremely low values (mostly less than 1 percent), compared to that of rotary blowers. They suggested that the efficiency of EHD devices has to be calculated based on static pressure instead of the dynamic pressure (related to the mechanical power term), following the same calculation method used for rotary blowers. Therefore, the method that has been used and presented in the literature to determine the efficiency of EHD devices is valid only for open space flow, where flow is unrestricted. Based on this method, results showed that the EHD static efficiency was highly sensitive to the considered parameters, and the peak values were recorded using positive polarity with 14 mm collector length and $\sqrt{2.5}\,r$ electrode gap, where r is cylindrical collector radius. It was found that, at a given electrode gap and collector length, static efficiency achieved using positive corona was significantly higher (with 14%) than that of the negative ones (only 2%).

Although the needle-to-mesh/ring electrode configuration has been widely used for years, EHD air pumps have also been explored using different electrode configurations. Komeili et al. [137] experimentally investigated the airflow characteristics using a wire-to-rod EHD pump operated in a circular duct with a corona wire diameter of 0.24 mm for ranges of negative applied potential (up to −24 kV), grounded rod diameter (1.5 – 3.1 mm), duct diameter (6.5 – 20 mm), and electrode gap. Details of electrode arrangement of the EHD air pump are shown in **Figure 2.10.** Experiments showed that the EHD pump was capable of producing a maximum airflow rate of 40 l/min at −16 kV, using a pipe diameter of 20 mm and consuming about 0.35 W input power.

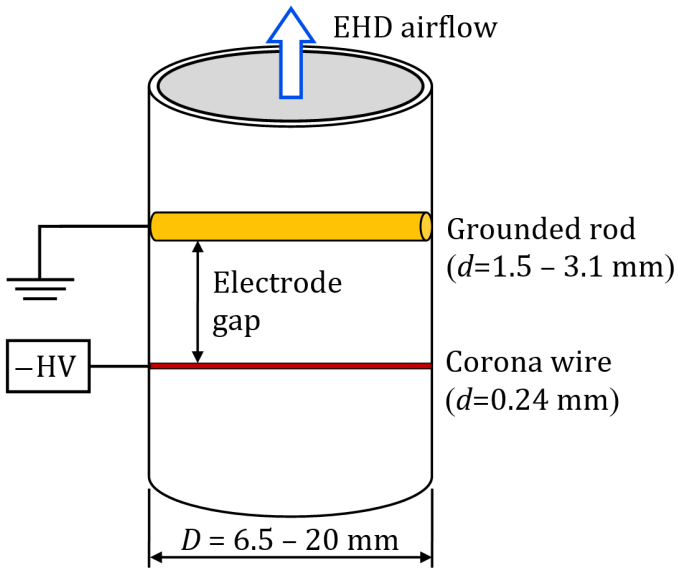

Figure 2.10 Electrode arrangement of the wire-to-rod EHD flow pump used in [137].

Colas et al. [138] experimentally and numerically investigated the effectiveness of using a wire-cylinder-plate EHD configuration on ionic wind generation. Two cylindrical grounded electrodes were placed between a corona wire and two collecting plates as further collectors to enhance the ion production and accelerate flow generation, as shown in **Figure 2.11**. Positive corona discharge was induced between the corona wire and two grounded cylinders, whereas a negative potential of up to –15 kV was applied to the collecting plates. Compared to previous results presented by the authors of optimized wire-to-plates and wire-to-wire

electrode configurations, the new proposed design was able to enhance the maximum flow velocity and the thrust force per unit length over the wire-plates EHD pump by 25% (from 8 to 10 m/s) and 46% (from 0.24 to 0.35 N/m), respectively, with an increase in the power consumption by 20%. Significant improvements were achieved using the wire-cylinder-plate configuration with up to three times in the ionic wind velocity and an order of magnitude in the thrust over those obtained by a simple wire-to-wire corona configuration.

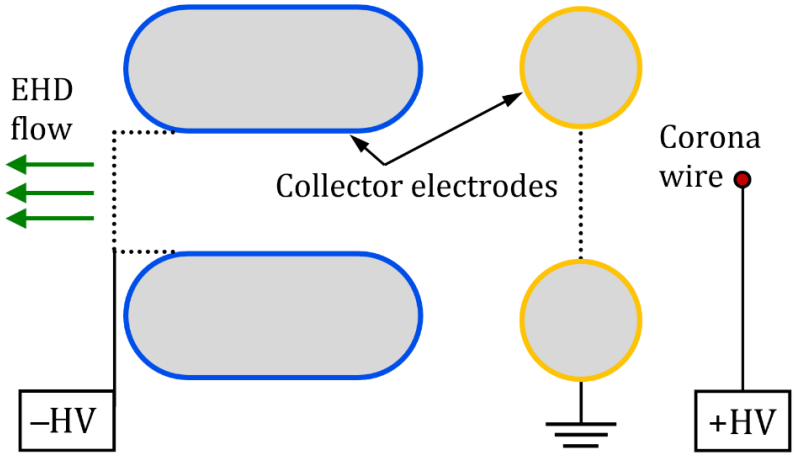

Figure 2.11 Cross-section of the wire-cylinder-plane EHD pump configuration used in [138].

A summary of the studies reviewed in this section for purely EHD flow generation is listed in **Table 2.1** below.

Table 2.1 Summary of the studies performed for purely EHD flow generation.

Author(s), Year	Electrode configure-ation	Device design	Flow field	Polarity	Remarks
Robinson [119], **1961**	Needle-to-ring	Single stage	Confined space	Positive and negative (up to 30 and – 55 kV, respectively)	Despite having low conversion efficiency (less than 1%) and undesired ozone production, EHD blowers offer attractive features over conventional fans due to the absence of moving parts and providing a silent operation.
Rickard et al. [45], **2005**	Needle-to-ring	Single stage	Confined space (flow inside a converging exit tube)	Negative (up to –11 kV)	The produced velocity was limited to around 2.4 m/s, regardless of the exit-to-inlet area ratio. The nozzle has a slight influence on accelerating the induced flow due to pressure restrictions caused by the nozzle.
Rickard et al. [41], **2006**	Needle-to-ring	Multi-stage	Confined space (flow inside a converging exit tube)	Negative (up to –12 kV)	The nozzle provided improved exit velocity. The pressure and flow rate increased with the number of stages with up to 38 Pa and 85 l/min, respectively. The conversion efficiency was extremely low (just 0.1%).
Qiu et al. [133], **2010**	Needle array-to-ring / mesh	Multi-stage	Confined space (flow inside a tube)	Negative (from –18 to –43 kV)	The max average outlet velocity and flow rate were up to 7.4 m/s and 140 l/min, respectively, with energy conversion efficiency of 0.8%.
Wei et al. [134], **2011**	Needle array-to-mesh	Multi-stage	Confined space (flow inside a tube)	Positive and negative (up to 12.5 and –17 kV, resp.)	Max average velocity and flow rate of 16 m/s and 303 l/min, respectively, were achieved using a 25-stage EHD pump, with an efficiency of 2.2%.
Moon et al. [135], **2009**	Needle/ring-to-mesh	Single stage	Confined space (flow inside a tube)	Positive (up to 17 kV)	Using the ring as a further corona electrode improved the velocity by 1.2 times over that obtained using only a needle-to-mesh configuration.
Moon et al. [105], **2009**	Wet porous/metal needle-to-mesh	Single stage	Confined space (flow inside a tube)	Positive, negative and AC (up to 18, –19 and 13 kV, respectively)	The wet porous corona needle led to max average velocities and efficiency up to 1.95 (1.23), 1.31 (1.24), and 1.30 (1.15) times for the positive, negative, and AC corona discharges, respectively, compared to those obtained using the non-porous electrode.
Moreau and Touchard [104], **2008**	Needle-to-grid/ ring	Single stage	Confined space (flow inside a tube)	Positive and negative (up to 17 and –15 kV, respectively)	The max velocity was higher in the case of positive corona than in the negative one. The grid was more efficient as a collector electrode than the ring. The max velocity and flow rate achieved were up to 8 m/s and 0.4 l/s, respectively, with a conversion efficiency of 1.72%.
June et al. [136], **2011**	Multi-needles-to-ring	Single stage	Open space	Positive and negative	Using the same calculation method adopted for rotary fans, the efficiency of EHD devices was evaluated based on the static pressure and found to be more reasonably compared to that of rotary fans.
Komeili et al. [137], **2008**	Wire-to-rod	Single stage	Confined space (flow inside a tube)	Negative (up to –24 kV)	The EHD pump was capable of producing a max airflow rate of 40 l/min at −16 kV, using a pipe diameter of 20 mm and consuming about 0.35 W input power.
Colas et al. [138], **2010**	Wire-to-cylinder-plate	Single stage	Confined space	At the corona wire: (up to +15 kV). At the plates: (up to –15 kV)	The proposed design was able to produce a max flow velocity and the thrust force per unit length over the classic wire-plates EHD pump by 25% (from 8 to 10 m/s) and 46% (from 0.24 to 0.35 N/m), respectively.

2.5.2 Research on EHD Flow based Heat Transfer

2.5.2.1 EHD flow for forced convection heat transfer

This section reviews the experimental studies that investigated corona wind for forced convection heat transfer without an external bulk flow, using different macro-scale electrode configurations in open or confined flow spaces.

In their seminal study conducted in 1963, Marco and Velkoff [121] were the pioneer to present the first investigation of using the corona wind in heat transfer enhancement. They used a wire electrode to generate impinging corona wind and cool a grounded and heated horizontal plate under the free convection. Results showed that the enhancement in the average heat transfer coefficient due to corona wind was six times higher than due to natural convection. Furthermore, they showed that heat transfer was proportional to the ¼ power of current.

Yabe et al. [139] included, in their extended study, a theoretical and experimental investigation on heat transfer augmentation by the corona wind mechanism using a wire corona anode and a downward-facing plate cathode heated under a constant temperature. The experiments were carried out using different arrangements of multi-wire electrodes to confirm theoretical predictions of heat transfer improvement. They verified their findings and found that the numerical and experimental results, based on local heat transfer coefficients, were consistent in the stagnation region of corona wind jet.

Franke et al. [40] presented an experimental study to investigate the effect of corona wind on heat transfer enhancement from a heated and grounded horizontal cylinder. The experiments were conducted to examine the efficiency of two types of positively charged emitters: single wire of diameter (either 0.1 or 0.32 mm) and multipoint (needles of 0.1 mm diameter) electrodes, on the heat transfer rates compared to free convection conditions. Each emitter type was separately placed under the grounded cylinder at electrode gaps between 6.4 and 31.8 mm, such that the air jet induced by corona wind was directed towards the lower surface of the cylinder, as shown in **Figure 2.12**. Results showed that the heat transfer rates were increased by a factor of six over free convection due to corona wind. At a given current or power level, results revealed that the increase in heat transfer rate using a multipoint emitter arrangement was higher than that achieved with a single corona

wire. It was noticed that the onset voltage required for the ion current to flow between electrodes decreases when the electrode gap and/or the wire diameter are reduced. Additionally, the results demonstrated that the heat transfer rate varied with the ion current, and the corona wind velocity increases with the square root of emitter current, showing agreement with previous reported results. At a given velocity, the heat transfer rates due to corona wind showed approximately similar results to those achieved due to a jet of air generated from a wedged-shaped plenum, indicating that the corona wind cooling is similar to that of an impinging air jet.

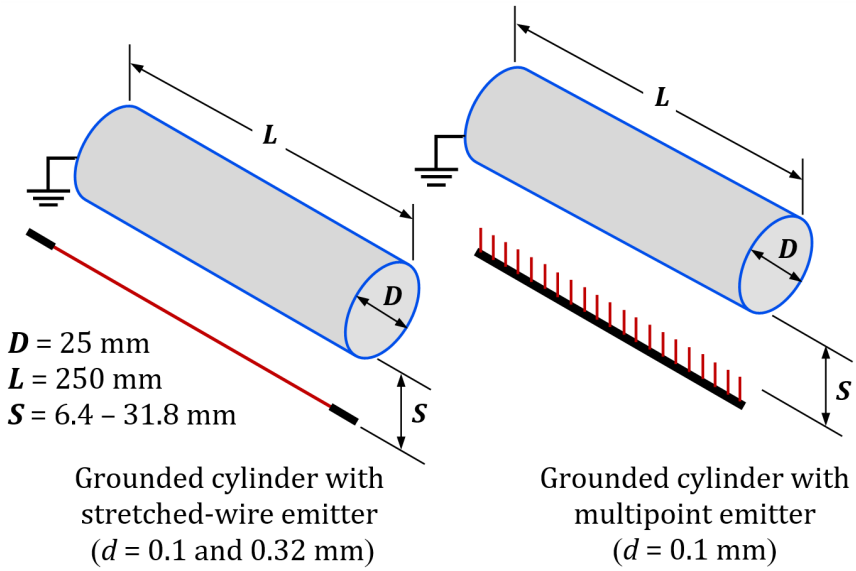

Figure 2.12 Electrode arrangements of the wire-to-cylinder EHD pump adopted in [40].

An experimental study was conducted by Owsenek et al. [103] to investigate heat transfer enhancement over free convection using corona wind generated by a needle-to-plate electrode configuration. The effect of electrode gap and corona polarity on the heat transfer coefficient was investigated for a range of applied potential. Results revealed that the local heat transfer coefficients were up to 65 W/m^2K, showing an enhancement of more than 25 times over natural convection. Results also showed that although negative corona consumes higher power but has less Joule heating generation compared to positive corona, the difference in heat transfer coefficient due to their ionic winds is small, revealing that positive corona wind was more efficient.

Two years later, Owsenek and Seyed-Yagoobi [140] experimentally and numerically examined the heat transfer enhancement from a grounded and heated horizontal surface using a jet impingement EHD airflow generated by single or multiple wire electrodes suspended above the heat exchange surface. An infrared camera system was used to obtain an accurate distribution of local heat transfer coefficients on the heated and impingement surface. Based on a given applied power per wire electrode, results revealed that each wire electrode in the multiple wires array led to smaller heat transfer enhancements over free convection compared to that achieved by a single wire configuration. This was due to the recirculation zones created between corona wires in the multiple wires arrangement, which led to increased temperatures and reduced heat transfer. Compared to results presented in previous work with a needle electrode, the authors stated that the relative lower heat transfer enhancements achieved using a wire electrode were due to the upward force created above the wire surface.

An experimental study was presented by Yue et al. [108] to investigate the effect of ionic wind induced by a needle electrode using different types of corona discharge (DC positive, DC negative, and AC) on heat transfer enhancement from a grounded and heated vertical plate over free convection conditions. Wide ranges of applied potential were used for AC (0 to 50 kV) and DC (0 to 80 kV) corona discharges, while the electrode gap was varied from 10 to 40 mm. At a given electrode gap, results showed that the highest heat transfer enhancements over free convection achieved by AC, positive, and negative discharges, before breakdown happens, were 6.74 (at 13 kV), 8.08 (at 18 kV), and 12.40 (at 35 kV), respectively. The highest enhancement obtained with negative corona discharge was due to its higher air gap breakdown voltage. It was found that the discharge intensity, which is mainly improved by electrode gap and discharge voltage, has a significant impact on heat transfer rates, and the heat transfer coefficients significantly increased with decreasing the diameter of the tip curvature electrode (examined only for a negatively charged needle). A small effect on heat transfer rates was observed using the different discharge types under the same operating conditions. The study concluded that the ionic wind induced by negative corona DC voltage is more effective in increasing the heat transfer rates at a given electrode gap when the high level of operating voltage is not a constraint.

2.5.2.2 EHD flow for boundary layer modification

The use of EHD pumps as secondary flow generators in the presence of a primary bulk flow represents the majority of studies reported for heat transfer enhancements, where the ionic wind plays a significant role in mixing airflows and disrupting the thermal boundary layer. One of the earliest investigations into heat transfer enhancement using EHD driven flow for boundary layer modification was conducted by Velkoff in 1962 [122]. Over three decades later, significant research into employing EHD flow for heat transfer enhancement was carried out, showing considerable enhancements in the heat transfer coefficients in a range of 250 – 320% [141-145]. Moreover, EHD discharge was shown to modify the velocity profile significantly within the viscous boundary layer of the external bulk flow on a flat plate for different velocities up to 25 m/s [146-148]. Among numerous experimental studies into thermal boundary layer modification, a brief review of the recent research is presented below.

An experimental and numerical study was performed by Shooshtari et al. [149] to investigate the effect of corona wind on heat transfer enhancement in a small laminar airflow duct. A square channel with a hydraulic diameter and length of 9.85 and 450 mm, respectively, was designed and heated under a uniform heat flux condition, as shown in **Figure 2.13**. A positively charged thin wire electrode of 0.065 mm-diameter was placed very close to the bottom side along the channel while the upper internal surface of the channel was grounded as a collector electrode. With an EHD power of 1.13 W, heat transfer enhancements of more than 200% were achieved, showing a considerable impact of corona discharge as a secondary flow generator on heat transfer enhancement. The study concluded that EHD flow is a promising technique to be adopted in compact heat exchangers or for improved cooling of high powered small-scale applications.

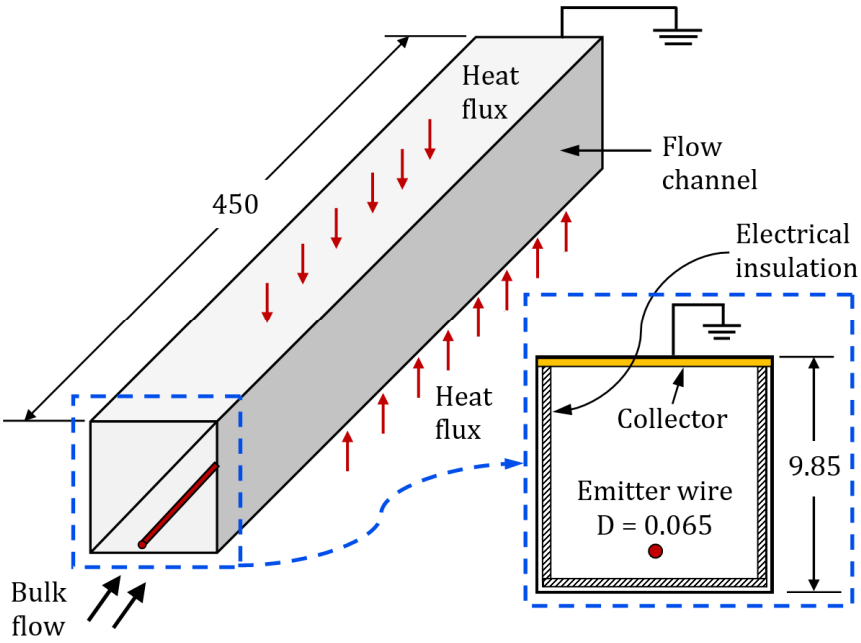

Figure 2.13 Position of emitter wire and collector surface inside a square channel EHD pump used in [149]. Dimensions in millimetres.

Ohadi et al. [150] experimentally investigated the effect of corona discharge induced by a wire electrode on forced convection heat transfer in a grounded and heated tube (inner diameter of 3.2 cm), as shown in **Figure 2.14**. The study considered three parameters; airflow regime (from laminar to fully turbulent conditions), applied potential, and the number of corona electrode; a single co-axial wire or two wires symmetrically positioned at 4 mm from the tube centre axis (each with a diameter of 0.25 mm). It was found that higher enhancements were generally achieved using the configuration of two wires at a constant operating power except for the case of fully laminar flow at high applied potentials, where the single electrode showed greater enhancements. For fully turbulent flows, the effect of corona wind on heat transfer enhancement increased with increasing applied potentials at given Reynolds numbers. However, it was observed that the levels of enhancements decrease with increasing Reynolds numbers at a given potential, leading to no effect of corona discharge with further increase in flow velocity, where the turbulent flow regime dominates. The maximum heat transfer enhancements recorded using the single and double-wire electrodes over those without ionic wind were at Reynolds numbers close to the transitional values (= 2000 and 3000) with 215% and 260%, respectively.

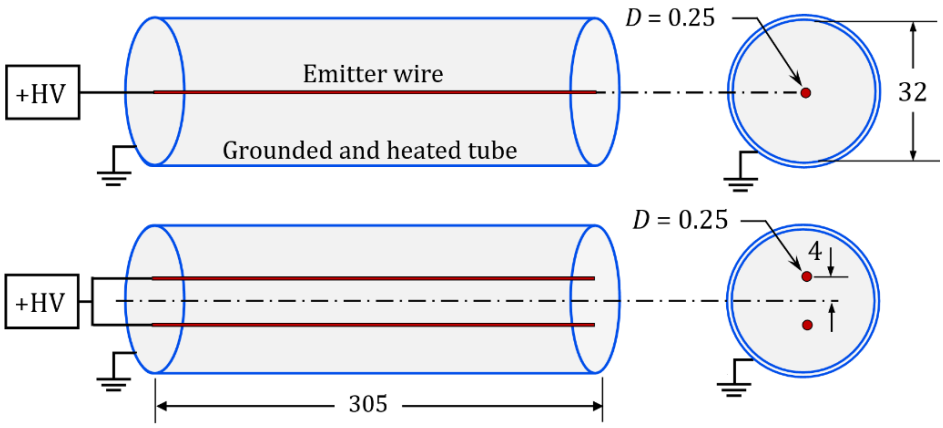

Figure 2.14 Schematic representation of the two electrode configurations and tube systems used in [150]. Dimensions in millimetres.

Ionic wind was experimentally and numerically employed as a method of local hot spot cooling in the presence of bulk airflow by Go et al. [26]. Positive corona discharge was generated between an emitter wire electrode of 50 µm-diameter and a collecting copper-tape placed on a heated plate imposed to a low-velocity laminar flow in open space, as shown in **Figure 2.15**. The corona wire was strung and elevated above the flat plate with a fixed height of 3.15 mm and placed 3.8 mm upstream of the collecting surface, so that the corona wind was perpendicular to the bulk flow direction. Multiphysics numerical simulations showed the ability of ionic wind to distort a bulk flow boundary layer over the heated surface, confirming the cooling trends of experimental results. Experimental results demonstrated that the local heat transfer coefficient was more than doubled due to ionic wind.

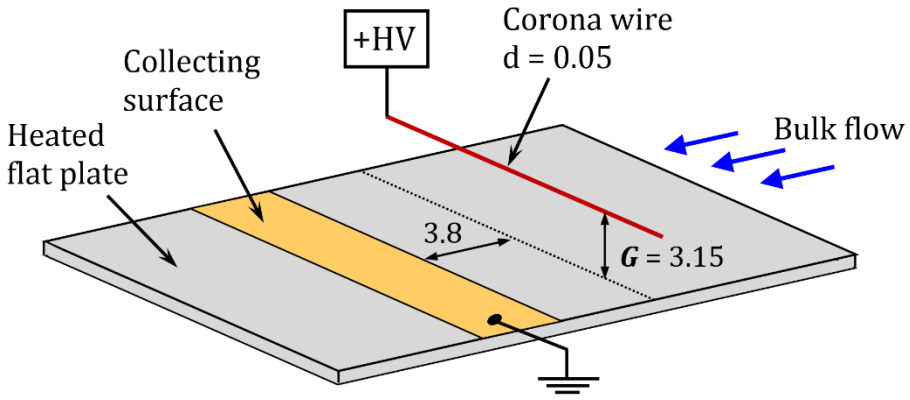

Figure 2.15 Configuration of a flat plate exposed to a bulk flow and corona wind perpendicular to the flow [26]. Dimensions in millimetres.

This work was extended later by Go et al. [27] by considering the impact of the horizontal electrode gap between corona wire and the edge of collecting surface on heat transfer enhancement. Results showed that the corona current was inversely proportional to the electrode gap at a given applied voltage. A linear relationship between the applied voltage and the square root of the corona current was obtained, confirming previous findings. Infrared images showed significant heat transfer enhancements due to corona wind both upstream and downstream of the electrode regions, reaching peak values under the position of corona wire. Compared to values obtained due to only the bulk flow, local heat transfer coefficient was enhanced due to the corona wind by more than 200%, for an operating power, gap spacing, bulk flow velocity, and heater power of 67.6 mW, 2 mm, 0.28 m/s and 4 W, respectively.

Table 2.2 summarises all reviewed studies of using EHD flow as a primary flow or in the presence of bulk flow for heat transfer applications.

Table 2.2 Summary of the reviewed research on EHD flow based heat transfer.

Author(s), year	Electrode configuration & polarity	Flow field	Flow pattern	EHD flow type	Remarks
Marco and Velkoff [121], **1963**	Wire-to-plane, (Positive)	Free space	Impinging airflow on a horizontal heated plate	Primary EHD flow	The enhancement in the average heat transfer coefficient was six times higher than due to natural convection. The heat transfer was proportional to the ¼ power of current.
Yabe et al. [139], **1978**	Multi-wire-to-plane, (Positive)	Open space in (inside a nitrogen chamber)	Impinging flow on a horizontal heated plate	Primary EHD flow	An accurate verification was obtained between the numerical and experimental results of local heat transfer coefficients in the stagnation region on the heated plate.
Franke et al. [40], **1991**	Wire/ multipoint-to-cylinder, (Positive)	Free space	Impinging airflow on a horizontal heated cylinder	Primary EHD flow	The heat transfer rates were increased by a factor of six over free convection due to corona wind and the multipoint emitter electrode was more effective than a single corona wire. The heat transfer rates due to EHD flow showed similar results to those achieved due to a jet of air.
Owsenek et al. [103], **1995**	Needle-to-plane, (Positive and negative)	Free space	Impinging airflow on a horizontal heated plate	Primary EHD flow	The local heat transfer coefficients achieved were up to 65 W/m2K, with an enhancement of more than 25 times over natural convection. Heat transfer due to a positive corona wind was more efficient than a negative one.
Owsenek and Seyed-Yagoobi [140], **1997**	single / multiple wire-to-plane, (Positive)	Free space	Impinging airflow on a horizontal heated plate	Primary EHD flow	Using a single wire electrode led to higher heat transfer than a multiple wires array due to the recirculation zones created between the wires. The upward force created above the wire surface led to a relative lower heat transfer enhancements compared to that previously achieved using a needle corona electrode.

Author(s), year	Electrode configuration & polarity	Flow field	Flow pattern	EHD flow type	Remarks
Yue et al. [108], **2006**	Needle-to-plane, (Positive, negative & AC)	Free space	Impinging airflow on a vertical heated plate	Primary EHD flow	The highest heat transfer enhancements over free convection achieved by AC, positive, and negative discharges were 6.74 (at 13 kV), 8.08 (at 18 kV), and 12.40 (at 35 kV), respectively, and negative corona discharge was the most efficient due to its higher air gap breakdown voltage.
Shooshtari et al. [149], **2003**	Wire-to-plane (corona wire placed along a duct), (Positive)	Confined space	Airflow inside a square channel	Mixed flows	More than 200% heat transfer enhancement was achieved due to the secondary EHD flow.
Ohadi et al. [150], **1991**	Co-axial electrode in pipe, and two wires in pipe, (Positive)	Confined space	Airflow inside a grounded heated pipe	Mixed flows (ionic wind with bulk flow)	The heat transfer enhancements decrease with increasing Reynolds numbers, where the turbulent flow regime due to the bulk flow dominates. Up to 215% and 260% heat transfer enhancements were achieved using the single and double-wire electrodes, respectively, due to the ionic wind as a secondary flow compared to case of using only a bulk flow.
Go et al. [26], **2007** & [27], **2008**	Wire-to-plane (tape), (Positive)	Free space	Airflow on a horizontal heated plate	Mixed flows	Compared to using only the bulk flow, local heat transfer coefficient was enhanced due to the secondary EHD flow by more than 200%.

2.5.3 EHD pumps for thermal management applications

Due to the rapid technological advances and the associated limitations in conventional cooling systems, research attention on the EHD technology has increased, aiming to explore the possibilities of applying EHD air movers as alternative cooling solution to mechanical fans in thermal management applications. Over the last two decades, EHD pumps have been investigated widely based on airflow production, cooling performance and physical size. One of the first studies to explore the possibility of developing microfabricated EHD pumps was presented in 1990 by Bart et al. [151], who investigated the issues of applying EHD pumps in micro-scale systems. Similar attempts in the same year were made by Richter and Sandmaier [152] using a micro EHD pump with two opposed grid electrodes, each with 30 μm thickness and 3×3 mm active area, and it was able to produce a maximum flow rate of 14 ml/min at 800 V operating voltage, representing almost three decades higher than that obtained with piezoelectric pumps available at that time.

With the aim of investigating the cooling performance in portable platforms, a free-standing EHD device was developed and experimentally examined with and

without a bulk flow by Go et al. [153]. Ionic wind was generated using positive potential between a 25μm-diameter corona wire and a collecting gold ribbon (125 μm wide) attached to a quartz substrate with an electrode spacing of approximately 700 μm. A corona wind engine was placed on a heated plate inside a wind tunnel of a bulk flow velocity up to 1.0 m/s, and operated by a range of corona currents from 1.0 to 8.0 μA, corresponding to an electrical power in a range of 3.8 – 16.3 mW. Experiments using infrared images revealed that the enhancement in heat transfer due to ionic wind occurred both upstream and downstream of the EHD engine location. This action reflects the ability of ionic wind to distort and modify the boundary layer under low-velocity bulk flows. Additionally, it was found that the impact of ionic wind on heat transfer enhancement decreases with increasing the bulk flow velocity. At a given EHD operating current, the temperature of the heated substrate was reduced due to ionic wind by 15 K and 3 K in the presence of a 0.12 m/s and 1.0 m/s bulk flows, respectively, below that obtained by the bulk flow alone. These temperature differences correspond to enhancements in local heat transfer coefficient of 52% and 10%, respectively. Moreover, under only radiation and free convection effects condition (no bulk airflow), the EHD flow generated at 2043 V with 16.3 mW power showed significant heat transfer enhancements with up to 68%.

A microfabricated EHD pump was experimentally developed by Hsu et al. [23] to improve local forced convection heat transfer for cooling of microelectronics. A corona wind was induced using a fabricated atomic force microscopy (AFM)-cantilever corona electrode with a tip height and tip-curvature radius of approximately 415 μm and 500 nm, respectively, placed over a heated and grounded horizontal plate, as shown in **Figure 2.16**. Two cantilevers with lengths of 5 and 8 mm were studied for a range of positive operating potentials (up to 7 kV) and electrode gaps (2 – 5 mm). Results revealed that the AFM-cantilever electrode with 8 mm length was more efficient than the shorter one, with a maximum convective heat transfer coefficient of 63.7 $W/m^2.K$ achieved at 7 kV, which corresponds to an enhancement ratio of 6.37 for the average heat transfer coefficient over free convection.

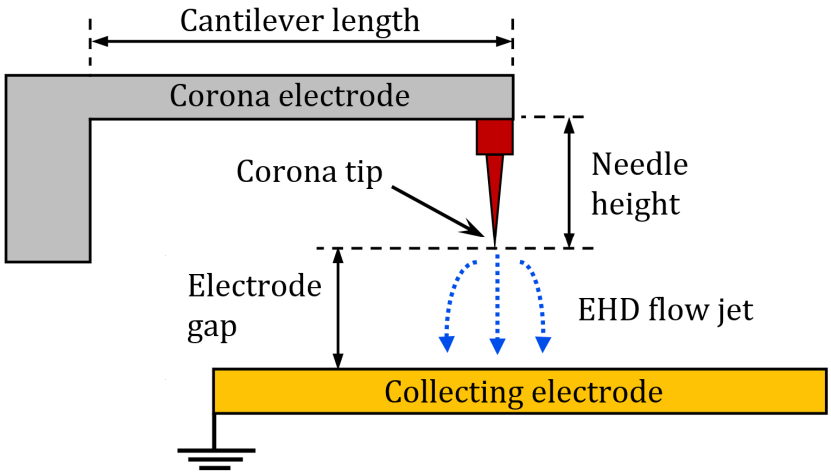

Figure 2.16 Diagram of the EHD air pump developed in [23], showing the AFM-cantilever corona electrode and a heated flat collecting electrode.

A recent study was conducted by Chen et al. [154] to employ the EHD driven flow as a cooling system for a chip of light-emitting diodes (LED). Ionic wind was generated using a needle electrode and different collector configurations: a point (needle), a line (wire), and a grid electrode, under a range of applied potentials up to –11 kV. Several parameters were considered, including the aligned angle of the emitter electrode, voltage polarity, vertical and horizontal electrode gap, as well as the collector geometry, to investigate their effect on the thermal resistance of an LED die attached on a substrate downstream of the grounded electrode. Results showed that the heat transfer performance obtained with negative polarity was higher and resulted in lower thermal resistance with up to 50% reduction compared to that of the positive one at the same operating voltage, due to the higher breakdown voltage and the longer operation range of the negative polarity. Among all tested collector configurations, the mesh electrode of coarse density offered the best heat transfer performance based on thermal resistance.

Kalman and Sher [109] were the first to investigate experimentally the optimization of an electrostatic blower and explore its potential use as a cooling system for electronic components. The EHD device consisted of a wire electrode of 0.5 mm-diameter stretched between two collecting inclined wings located over a heated horizontal plate, forming a longitudinal nozzle shape for the air stream, as illustrated in **Figure 2.17**. The design parameters of the EHD device, including the discharge polarity, the wing gap, the vertical electrode gap and the wing inclination

angle, were optimized in the first stage of the experiments based on the highest airflow production, while the second stage included the heat transfer experiments using the optimized configuration. Confirming previous observations [140], it was found that a positive corona discharge was more effective at converting electrical power into mechanical energy than a negative one. Results showed that the optimized EHD blower could enhance the heat transfer coefficient by more than a factor of two compared to free convection.

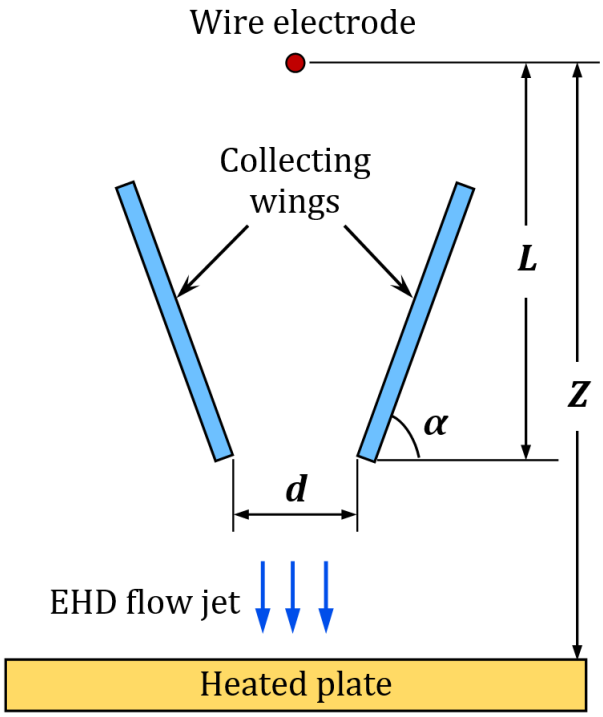

Figure 2.17 Schematic layout of the EHD air blower used in [109].

This study was extended later by Rashkovan et al. [155] by reducing the emitter wire diameter to 0.2 mm in order to enhance the electric field strength, aiming to develop the EHD air blower and improve its performance. Based on the highest heat transfer coefficient achieved, the optimum configuration was obtained by using a corona wire located between two parallel collecting wings, where the wire is collinear with the adjacent ends of the collecting plate wings, creating an angle of 55.5º with their far ends. The new optimized design was able to produce heat transfer coefficients up to 3 times higher than with free convection, resulting in a 50% increase in heat transfer over that obtained by the EHD blower presented in

the previous study. However, no information regarding the conversion efficiency values or the EHD operating power was included in both studies.

Chang et al. [156, 157] experimentally investigated the EHD driven flow through narrow channels using a wire-to-plate EHD pump proposed as a cooling system for advanced thermal management of microelectronics. The ionic wind was induced inside a converging tube with a 5 mm exit diameter using a corona wire placed between two non-parallel and grounded plates. The effect of using partially covered corona wire on the flow characteristics was examined for a range of positive applied voltages. Results showed that using a wire with an insulating cover was more efficient and had a significant influence on the flow characteristics with higher flow production and lower operating power compared to the case without insulation at a given operating voltage. For example, at 8 kV applied potential, the average outlet velocity was improved by 175% and the power was reduced by 65%, compared to the case without a covered wire. The maximum mean velocity of the corona wind achieved at the tube outlet was 1.7 m/s using an operating power and voltage of 0.8 W and 8.4 kV, respectively, representing approximately a threefold improvement in the maximum flow rate over the case without a covered wire. Indeed, using an insulating cover on the half of corona wire opposite to the upstream region forces the electric field lines and charged ions to concentrate on collecting surfaces downstream of the corona wire, enhancing the induced airflow towards the outlet direction. However, the maximum flow rate was only 2 l/min, indicating that the outlet average wind velocity of the EHD pump may considerably degrade over larger exit diameters.

Tsubone et al. [158] presented an experimental study to explore the benefits of design optimization of EHD air pumps for electronics cooling. Using a positive potential polarity, a design based on a partially covered wire to parallel plates channel was developed, as shown in **Figure 2.18**, to investigate the effect of channel width, the number of emitter wire electrodes and the distance between the emitter wires on both the ionic wind velocity and corona current. Results demonstrated ample scope for design optimization; with a maximum average air velocity and a corresponding flow rate of 3.2 m/s and 7.4 l/min, respectively. It was found that

increasing the number of corona wires led to higher wind velocities and better conversion efficiency.

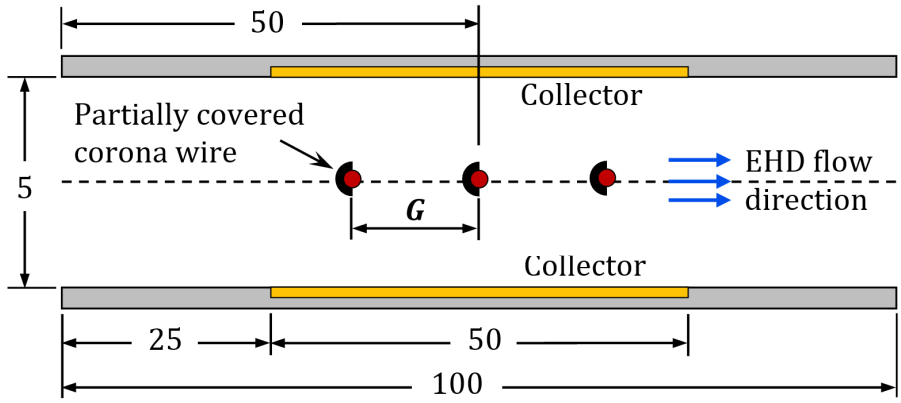

For single wire: channel width $\boldsymbol{w}$ = 10, 30 mm
For double wires: $\boldsymbol{G}$ = 5, 10, 15 mm, $\boldsymbol{w}$ = 10 mm
For triple wires: $\boldsymbol{G}$ = 10 mm, $\boldsymbol{w}$ = 10 mm

Figure 2.18 Ducted EHD blower of multi-wires-to-plane electrode configuration used in [158].

With the aim of developing a cooling system for fan-free high power generation applications, Huang et al. [107] presented an experimental study to enhance natural convection heat transfer using an EHD pump integrated within a heat sink. A framework of needle-arrayed electrodes was constructed over a heated and grounded plate-fin heat sink, such that the vertical electrode gap can be changed in a range of 10 – 55 mm. Four arrays of corona needles were utilized with 4, 6, 18, and 60 needle electrodes (0.7 mm in diameter), and operated using positive and negative DC voltages in a range of 0 – 18 kV. Results revealed that the heat transfer rate increased by 3 – 5 times compared to free convection, and the array of 6 needle electrodes offered the best cooling performance. Low levels of enhancement were also observed for small electrode gaps, which were attributed to the passive effect of Joule heating and inefficient entrainment of air, causing re-circulating of heated air through fin channels.

An operable integrated EHD pump with a thickness less than 2.0 mm shown in **Figure 2.19** was proposed by Schlitz and Singhal [159] for cooling heat sinks of low power chips. Using positive corona voltage, multi-stages of parallel emitter wires were stretched and placed over semi-cylindrical grooves made at the top of

grounded heat sink plate-fins, so that the wires and the fins were in a cross arrangement. They studied four electrode arrangements based on the number of corona wires and fin density with an electrode gap up to 1.5 mm. Results demonstrated that the optimal EHD cooling system was able to induce ionic wind with a maximum inlet velocity of 1.6 m/s and a pressure head up to 23 Pa using less than 3 kV operating voltage, showing promising airflow performance for cooling a 20 W chip. No more information was provided relating to the thermal performance except an estimated comparison based on experimental results against a rotary-fan system, which revealed that, at a pressure drop of 7.3 Pa and a constant temperature difference of 40 K between the heat sink and the ambient, the EHD system was compatible with a laptop cooling system based on size, power consumption and weight, with approximately 40% reduction in each characteristic.

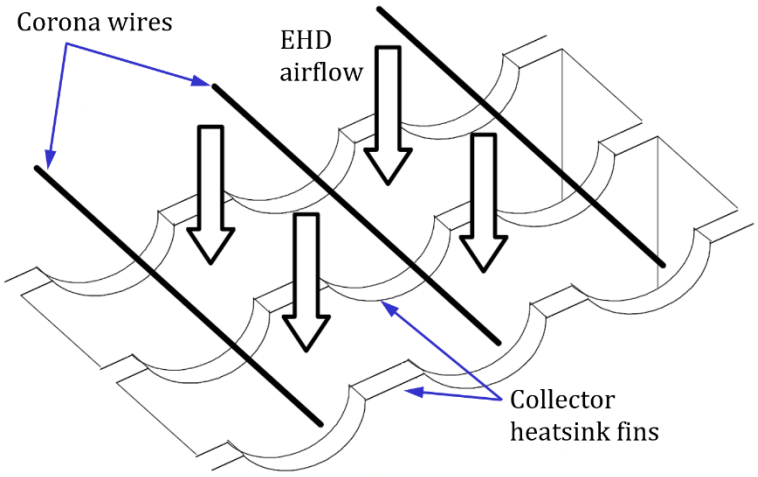

Figure 2.19 Prototype design of the integrated EHD air blower with micro-scale heat sink presented in [159].

Very recently, an integrated corona wind generator with heat sink shown in **Figure 2.20** was experimentally and numerically developed by Shin et al. [160] as a cooling system for LED applications. First, an experimental test was conducted to verify the numerical simulation method using a wire of 0.2mm-diameter stretched between two grounded parallel plates (each with 10 × 20 mm active area and separated by 20 mm air gap) and located over a heated horizontal surface. Based on accurate validation results, the location of the corona wire electrode was optimized

at a given applied voltage and found to be collinear with the adjacent ends of the plate electrodes. The experimental tests were developed for the prototype using a heat sink (with 30 × 30 mm base area and 30 mm height), of 10 plate fins; four of them were extended in height by 20 mm and acted as the collector electrodes. An array of three parallel corona wires was placed at the optimal locations between the grounded plate-fins, so that the emitter wires were parallel to the fin channels. The optimized prototype demonstrated that with a generated wind velocity up to 1.5 m/s, a cooling performance enhancement of 150% was achieved over the natural convection, using the same geometry.

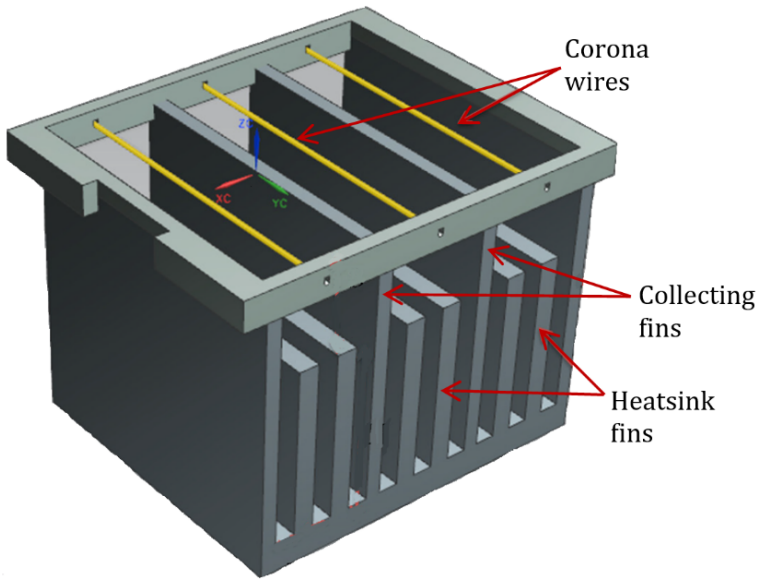

Figure 2.20 Prototype geometry of EHD air blower integrated with plate-fin heat sink used in [160] .

The first practical and successful integration of an EHD air pump into a real-world microelectronic application was performed by Jewell-Larsen et al. in 2009 [25], by replacing a conventional fan of a high performance laptop by a retrofitted EHD cooling system. Although the authors included a coupled physics EHD simulation model for the electrode configuration shown in **Figure 2.21**, no information regarding the geometric dimensions or detailed results was disclosed in their paper, which was followed by a number of related patents [161-163]. In the first generation of the work, two stock rotary centrifugal fans (65 mm diameter) of a consumer laptop of 60 W TDP (Thermal Design Power) were replaced with two

EHD blowers, each with a positively charged wire electrode and two parallel plates with a rounded leading edge acting as the collectors and electronic chip heat sink. Within a space of approximately 26 cm^2 by 1 cm tall cavity, a three-stage EHD device was installed to maximize airflow within the system and minimize the operating power. Comparisons against a stock mechanical fan in terms of CPU, GPU and skin temperatures were presented and showed promising cooling performance of the EHD system. To achieve the required cooling capacity from the EHD blowers of the retrofitted laptop, the second generation of the test system was installed by removing the existing fan footprint, spreader, heat sink, and heat pipe from the laptop. The results illustrated that, at the same airflow rate and temperature drop, the airflow generated by the modified EHD blower was able to remove up to 38% more heat than a conventional rotary fan. Results demonstrated that the coefficient of performance (COP) gained by the improved EHD cooling system was higher with a factor of 47 compared to a factor of 25 by the rotary fan, at the same cooling power of 33 W. Furthermore, the overall volume of the EHD cooling system was reduced by approximately 50% less than that of the stock fan with a thickness of less than 6 mm. The authors stated that the un-optimized design of the EHD blower exhibited a promising cooling performance with lower installation size and acoustic levels, compared to the traditional fan, and further modification and development are required.

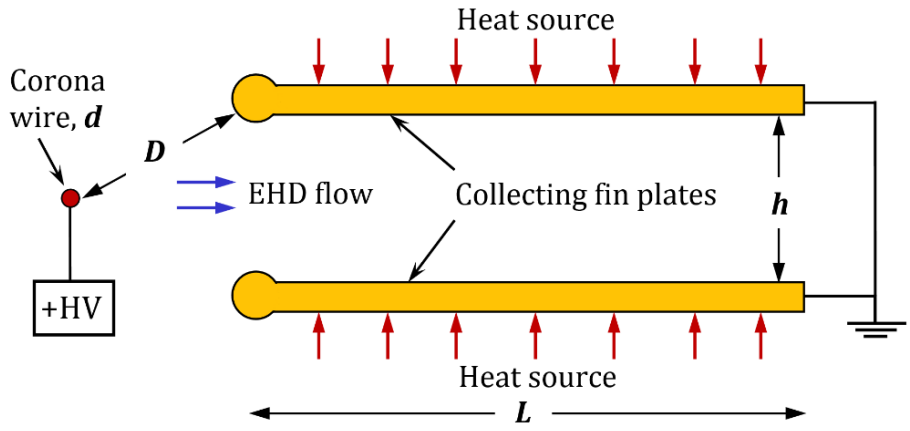

Figure 2.21 Electrode configuration of a wire-to-plane EHD cooling system developed to cool a laptop in [25]. Dimensions are not available.

As part of their work performed to develop and optimize EHD blowers for practical implementation, significant research over the airflow performance scaling laws for EHD air movers was first presented by Jewell-Larsen et al. [164]. Experimental and numerical investigations were conducted using a wire-to-plane electrode configuration operated with a positive voltage in thin ducts of thicknesses in a range from 2 to 6 mm. It was successfully proved that EHD air blower can be considered as an ideal pressure source with negligible flow resistance within the duct. The authors were the pioneers to present EHD scaling laws to predict both flow rate and static pressure generated by a wire-to-plane EHD blower based on channel width, thickness, and operating power.

Table 2.3 summarises the reviewed studies that employed EHD flow in micro- or meso-scale geometries for convective heat transfer in thermal management applications.

Table 2.3 Summary of the reviewed research on EHD flow for thermal management applications.

Author(s), year	**Electrode geometry**	**Polarity**	**Device design**	**Remarks**
Richter and Sandmaier [152], **1990**	Grid-to-grid	Positive (up to 800 V)	Microfabricated EHD pump of two opposed grids, each with 30 µm thickness and 3 × 3 mm active area.	The micro EHD pump was able to produce a maximum flow rate of 14 ml/ at 800 V operating voltage.
Go et al. [153], **2008**	Wire-to-plane	Positive, (up to 2.05 kV)	Microfabricated EHD pump of 25µm-diameter wire and a collecting tape (125 µm wide) attached to a quartz substrate with an electrode gap of 700 µm.	Using only ionic wind (no bulk airflow), the heat transfer enhancements were up to 68% at 16.3 mW power and 2043 V applied voltage.
Hsu et al. [23], **2009**	Point-to-plane	Positive, (up to 7 kV)	Microfabricated EHD pump of a cantilever corona electrode with a tip-curvature radius of 500 nm placed over a heated and grounded horizontal plate at an electrode gaps (2 – 5 mm).	The maximum heat transfer enhancement achieved was 6.37 over free convection.
Chen et al. [154], **2013**	Needle-to-needle/wire /grid	Positive and negative (up to 8.5 and –11 kV), resp.	The emitter needle was placed at a fixed vertical gap (5 mm) and varied horizontal gaps (3-5 mm) from each grounded structure (needle, wire and grid).	Heat transfer performance obtained with negative coronas was higher and resulted in lower thermal resistance with up to 50% reduction compared to that with positive ones. The coarse density of collecting mesh offered the best heat transfer rate among other collector configurations.
Kalman and Sher [109], **2001**	Wire-to-plane	Positive and negative (up to 30 and –40 kV), resp.	A wire electrode of 0.5 mm-diameter stretched between two collecting inclined wings located over a heated horizontal plate, forming a longitudinal nozzle shape.	Positive corona discharge was more effective with higher conversion efficiency than a negative one. Heat transfer coefficient was enhanced by more than two times compared to free convection.

Author(s), year	Electrode geometry	Polarity	Device design	Remarks
Rashkovan et al. [155], **2002**	Wire-to-plane	Positive, (up to 23 kV)	A corona wire of 0.2mm-diameter stretched and centred between two collecting plates (42 mm apart, and located over a heated horizontal plate.	An optimal geometry design was proposed as the wire is collinear with the adjacent ends of the collecting plate wings, creating an angle of 55.5º with their far ends. Heat transfer coefficient was increased by up to 3 times higher than free convection.
Chang et al. [156, 157], **2008** & [159], **2010**	Wire-to-plane	Positive, (up to 12 kV)	A partially covered corona wire placed between two inclined and grounded plates and located inside converging tube with a 5 mm exit diameter.	Average outlet velocity was improved by 175% and the power was reduced by 65%, compared to the case without a covered wire. The maximum outlet velocity was 1.7 m/s using a power and voltage of 0.8 W and 8.4 kV, respectively, which was a threefold improvement of flow rate over the case without a covered wire.
Tsubone et al. [158], **2012**	Muti-wires-to-plane	Positive, (up to 8 kV)	A set of partially covered wires (0.25 mm in dia.) was placed between parallel plates that form a flow channel.	The optimal design was able to produce a max average velocity and flow rate of 3.2 m/s and 7.4 l/min, respectively. Results showed that increasing the number of corona wires led to higher wind velocities and better conversion efficiency.
Huang et al. [107], **2009**	Muti-needles to-plane	Positive and negative (up to18 kV)	A framework of needle-arrayed electrodes was constructed over a heated and grounded plate-fin heat sink, such that the vertical electrode gap can be changed in a range of 10 – 55 mm.	The heat transfer rate increased by 3 – 5 times compared to free convection, and the array of 6 needle electrodes offered the best cooling performance.
Schlitz and Singhal [159], **2008**	Muti-wires-to-plane	Positive, (up to 3.5 kV)	Multi-stages of parallel wires were placed over semi-cylindrical grooves made at the top of grounded heat sink plate-fins, with an electrode gap up to 1.5 mm.	The optimal EHD cooling system was able to induce a max inlet velocity up to 1.6 m/s and a pressure head up to 23 Pa using less than 3 kV operating voltage. The EHD system was compatible with a laptop cooling system based on size, power consumption and weight, with approximately 40% reduction in each characteristic.
Shin et al. [160], **2016**	Muti-wires-to-plane	Positive (9 kV)	A set of wires of 0.2mm-diameter stretched in parallel over grounded plate-fin heat sink of 30 × 30 mm base area and 30 mm height.	The optimal prototype was capable of generating a wind velocity up to 1.5 m/s, and enhanced the cooling performance by 150% over the natural convection.
Jewell-Larsen et al. [25], **2009**	Wire-to-plane	Positive (up to 3 kV)	A retrofitted EHD cooling system was developed and integrated to replace a rotary fan in a laptop of 60 W TDP. A very fine corona wire was placed at an optimal distance in parallel to a flow duct entrance formed by two parallel collecting plates of rounded leading edges facing the emitter. The geometric dimensions or were not disclosed.	The EHD blower was able to remove up to 38% more heat than a rotary fan. The coefficient of performance gained by the improved EHD cooling system was higher with a factor of 47 compared to a factor of 25 by the rotary fan, at the same cooling power. the overall volume of the EHD cooling system was reduced by approximately 50% less than that of the stock fan with a thickness of less than 6 mm.
Jewell-Larsen et al. [164], **2011**	Wire-to-plane	Positive (up to 10 kV)	An EHD flow was purely induced inside a thin channel of height, length and width of (2-6 mm), 70 and 100 mm, respectively,	EHD scaling laws were presented to predict the flow rate and static pressure generated by a wire-to-plane channel based on blower width, thickness, and operating power.

2.5.4 Numerical modelling of EHD driven airflow

The modelling of EHD flow is essentially performed based on a coupling of electrostatic forces and a fluid, causing a drifting of the ionic charges and fluid particles across the electrodes under the effect of electric field, and resulting in fluid motion. This approach can be established by applying Coulomb forces as a body force term in the air momentum transport represented by the Navier-Stokes equations.

Typically, applying a high potential at a corona electrode such as a thin wire or sharp point creates a strong electric field around the corona electrode, which in turn ionizes the fluid particles in the ionization zone. In the drifting zone, where ions of single polarity are accelerated by the Coulomb force and move towards the collector electrode, a space charge is formed and a unipolar discharge current is created across the electrodes. In fact, the electric potential distribution, which is governed by Poisson's equation (3.3), is a linear equation with a given charge density distribution. However, for unipolar discharge currents, the charge density distribution mainly depends on the electric potential or field distributions and it is not easily deduced. Therefore, the mathematical relationship that describes the distribution of unipolar charge currents with coupled electric potential and charge density is inherently nonlinear [165]. Based on this fact, mathematical solutions using analytical means can be developed for simple problems, where a symmetry condition can be applied and a mathematical system is reduced to a nonlinear ordinary differential equation such as in a concentric wire-cylinder electrodes configuration [166].

One of the first mathematical solutions of the corona discharge phenomenon was presented by Townsend [167] in 1914 to analytically solve a concentric cylindrical electrodes problem. However, with the advancement in the computing techniques, numerical solutions of coupled electric field and charge density using complex nonlinear partial-differential equations have developed and become increasingly popular. McDonald et al. [168] presented the earliest attempt in 1977 at numerical solution using the finite difference method for a corona discharge problem in a simple rectangular domain generated with a uniform grid system.

While some later numerical approximations used the finite-difference method to solve the coupling of charge transport and electric field [169, 170], modelling

approaches using a finite element method have been widely applied for solving Poisson's equation and charge distribution in complex configurations and sharp corona electrodes, where a non-uniform mesh is adopted [171, 172]. However, although the finite-element method has been successfully used with considering the charge diffusion effects into account [165, 173], the method of characteristics (MOC) has been commonly used to determine space charge density with neglecting the diffusion term, and simplify the charge transport equation in the form a hyperbolic partial differential equation [174, 175].

As the processing power of computers increased further, especially since the middle of the last decade, numerical simulations of complex electric fields in space based on nonlinear partial differential equations have been developed extensively. However, the finite element method has remained the most popular numerical method to develop models of EHD driven flow and EHD based heat transfer via commercial computational fluid dynamics (CFD) software [176-180], while a few other studies used finite volume method-based software packages [26, 181], showing successful validations against experimental data.

In general, literature of the modelling of EHD flow based heat transfer reveals that the majority of numerical studies were performed in the presence of external airflow, using the EHD phenomenon for enhanced convection heat transfer [26, 182-186]. However, only a few models have been developed in recent years which apply EHD pumps as a primary airflow generator using complicated and micro-fabricated electrode configurations for cooling of microelectronics and thermal management applications (e.g., [23, 187-189]). Due to the wide range of geometrical parameters that strongly affect the discharge process and the performance of EHD airflow devices, numerical modelling offers great potential to explore the effect of various design and modelling parameters. Based on thermal management requirements and in order to save cost and time, most recent studies used a numerical approach to develop and optimize EHD devices and predict their characteristics in terms of flow generation, power consumption, cooling performance and pumping efficiency.

2.6 Chapter Summary

Air movement due to corona discharge has been widely investigated over three centuries since the first reported discovery of corona wind in the early 1700s. Since that time, corona discharge and its effects have been examined for a wide range of uses with little attention has been focused on EHD driven airflow, while the fundamentals and the underlying physics of corona discharge have been well understood, developed, and extensively documented.

Unlike the early efforts performed for developing EHD airflow, which have been modest and mostly academic curiosities, it is only over the last three decades that the research efforts have focused on employing EHD driven flow in the area of forced convection heat transfer. However, while the majority of the documented investigations have focused on the use of EHD flow in the presence of a primary bulk flow in the heat transfer applications, only few studies that used purely EHD flow and related to thermal management microelectronics cooling have occurred in the last decade with real intention to apply EHD technology commercially.

Over the last century, numerical solutions that solve the coupled equations of corona discharge and EHD flow based on nonlinear partial differential equations have been extensively developed in parallel with the advancement in the computing techniques. Numerical modelling of EHD driven flow have been shown successful validation against experiments with acceptable accuracy and been provided a significant tool for design optimization and performance development of EHD devices, offering great potential to explore various design parameters and save cost and time.

The literature review presented in this chapter revealed that the most recent efforts made for employing EHD flow technology for forced convection cooling of microelectronics still require further research based on thermal management considerations, while the available public data that related to the application of EHD cooling systems in small-scale microelectronics are relatively limited.

CHAPTER 3

Numerical Modelling of EHD Airflows

Numerical modelling methods for simulating EHD airflow, induced through wire-to-plane/grid channel configurations under the effect of positive corona discharge and electrostatic forces, are presented in this chapter. The numerical approach involves governing coupled equations that describe the interaction between the electric field and the movement of air particles across the electrode gap. For the charge transport process, a partial differential equation (PDE) with appropriate coefficients must be used to couple the electrostatics and fluid dynamics within the EHD flow simulation. A detailed explanation of the EHD governing equations, boundary conditions, assumptions used for the space charge generation, and validation of the numerical method are detailed in the following sections.

3.1 EHD Flow Governing Equations

3.1.1 Electrostatic and charge equations

Due to the high voltage applied to the corona electrode, a space charge is formed and an electric current is created and flows across the electrodes, where a high electric field gradient is generated. In order to simplify the numerical modelling and make an approximate analysis of the corona discharge, several assumptions were used in the literature as summarised in [190], which are adopted in the present study as follows:

- The space charge affects only the magnitude but not the direction of the electric field.
- The charge density is constant along the electric field lines.
- The ionic charges are unipolar (ions of a single polarity) from the corona surface towards the collector electrode through the drifting zone.
- The corona discharge can be achieved at stationary conditions.
- The ion mobility in air is constant and independent of the electric field strength.

- The thickness of the ionization zone is ignored.
- Corona discharge is created due to positive applied voltage and it is uniform across the electrodes.

The EHD flow induced by corona discharge is governed by the following set of equations:

The electric field intensity ($\vec{E}$) created between the electrodes can be described by Gauss's law,

$$\vec{\nabla}.\vec{E} = \frac{q}{\varepsilon_r\, \varepsilon_0} \tag{3.1}$$

where q is the space charge density (C/m^3), ε_r is the relative permittivity of air (= 1), and ε_0 is permittivity of free space (= 8.854×10^{-12} C/V.m). This can be defined in terms of the electric potential, V, by

$$\vec{E} = -\vec{\nabla}V \tag{3.2}$$

The electric potential in the air is governed by Poisson's equation, which can be obtained by substituting (3.2) into (3.1), yielding:

$$\vec{\nabla}.\vec{E} = -\nabla^2 V = \frac{q}{\varepsilon_0} \tag{3.3}$$

The charge transport equation that couples the electrostatic and Navier-Stokes equations for the airflow is derived by combining the following three equations:

i. The current density equation (Ohm's law): the ionic charges are accelerated and moved towards the grounded electrode under the effect of the Coulomb force, creating an electric current density, $\vec{J}$,

$$\vec{J} = \mu_p \vec{E} q + \vec{U} q - D\, \vec{\nabla} q \tag{3.4}$$

where D is the charge diffusion coefficient of ions (m^2/s), $\vec{U}$ is the velocity vector of airflow, and μ_p is the positive air ion mobility in the electric field ($m^2/V.s$).

The ion mobility is defined as the velocity of ions, v_i (m/s), moving through a gaseous medium divided by the electric field, E (V/m), as,

$$\mu_p = \frac{v_i}{E} \tag{3.5}$$

Indeed, the ion mobility coefficient depends on the polarity of the corona discharge and the physical properties of the drift gas such as relative density and humidity [191-193]. In this study, the value of air ion mobility is assumed constant [176, 194] for the positive corona discharge at standard ambient conditions.

The three terms on the right-hand side of equation (3.4) represent the charge conduction (the ion movement due to the electric field), charge convection (transport of charges by the airflow), and charge diffusion, respectively [27, 176].

ii. The continuity equation for electric current: for steady state conditions, the current density must satisfy the charge conservation equation,

$$\vec{\nabla} . \vec{J} = 0 \tag{3.6}$$

iii. The conservation of mass equation: the continuity equation for steady state incompressible airflow,

$$\vec{\nabla} . \vec{U} = 0 \tag{3.7}$$

Combining equations (3.4) and (3.6) and using the continuity equation (3.7) gives the charge transport equation that couples the electrostatic and Navier-Stokes equations for the airflow,

$$\vec{\nabla}.\left(\mu_{\mathrm{p}}\,\vec{E}q - D\,\vec{\nabla}q\right) + \vec{U}.\vec{\nabla}q = 0 \tag{3.8}$$

The drift velocity of ions ($\mu_{\mathrm{p}}\vec{E}$) in the charge conduction represents the dominant term in (3.8) over ion movement due to diffusion and charge convection (the second and third terms) in the system of EHD driven airflow, and they are often neglected in numerical simulations in the literature [27, 194].

Unlike corona discharges in liquids, where charge mobility of ions is very low, charge convection ($\vec{U}.\vec{\nabla}q$) due to fluid flow (air and other gases) has a drift velocity much less than that created due to charge mobility ($\mu_{\mathrm{p}}\vec{E}$) under the effect of an electric field. This assumption considerably simplifies equation (3.8) by allowing the electrostatic and charge transport equations to be decoupled from the hydrodynamic solution [140]. In the present numerical modelling of EHD flow, the charge diffusion coefficient is included with a constant value of 5.3×10^{-5} m^2/s [177], even though its effect on the numerical accuracy is relatively negligible [165, 194]. Thus, the charge transport equation can be rewritten as,

$$\vec{\nabla}.\left(\mu_{\mathrm{p}}\vec{E}q - D\,\vec{\nabla}q\right) = 0 \tag{3.9}$$

3.1.2 Fluid dynamic equations

When the ionization phenomenon occurs due to positive corona discharge, the produced positive ions are attracted to the negative electrode under the effect of Coulomb force. In their traveling path through the drifting region, they collide with neutral air molecules and transfer energy and momentum, causing an air movement. The hydrodynamic part of the EHD driven flow model is described by the Navier-Stokes equations that solve the steady state incompressible airflow in the drifting zone under the effect of the electrostatic force.

The EHD airflow model is simplified under the following assumptions:

- The fluid medium is air and assumed to be at room temperature and atmospheric pressure.
- The flow is laminar and incompressible with a constant density and viscosity.
- The flow is steady.
- No slip boundaries are applied for all solid surfaces.
- The ionic wind is induced through flow channels as a primary flow due to the effect of the electric field and electrostatic force.

The full form of the Navier-Stokes equations (or the conservation of momentum equation) is

$$\rho\left(\frac{\partial \vec{U}}{\partial t} + \vec{U}.\vec{\nabla}\vec{U}\right) = -\vec{\nabla}p + \mu\nabla^2\vec{U} + \vec{F} \tag{3.10}$$

where ρ is the air density (kg/m^3), p is the air pressure (Pa), μ is the air dynamic viscosity (Ns/m^2), $\vec{U}$ is the velocity vector of airflow, and $\vec{F}$ is the body or Coulomb force (N/m^3). The left-hand side of equation (3.10) is the rate of change of momentum per volume, and the right-hand side represents the resultant stress. The body force equation is defined as [195],

$$\vec{F} = q\vec{E} - \frac{1}{2}E^2\,\vec{\nabla}\varepsilon + \frac{1}{2}\,\vec{\nabla}\left[E^2\rho\left(\frac{\partial\varepsilon}{\partial\rho}\right)\right] \tag{3.11}$$

(**1**) (**2**) (**3**)

This equation includes a combination of three terms of forces:

(1) The first term, ($q\vec{E}$), represents the Coulomb force, which is the force per unit volume on a medium containing free electrical charge. This force is the strongest EHD force in the presence of the DC electric fields. Hence, it is the dominant term in the body forces for ion drag in air.

(2) The second term, $(\frac{1}{2}E^2\ \vec{\nabla}\varepsilon)$, represents the dielectric force due to the force exerted on a non-homogeneous dielectric liquid by an electric field. This force usually dominates in an AC electric field, and it is weak compared to the Coulomb force.

(3) The third term, $(\frac{1}{2}\ \vec{\nabla}[E^2\rho\left(\frac{\partial\varepsilon}{\partial\rho}\right))$, is called the electrostrictive term, the gradient of a scalar, and is required for compressible flows.

The second and the third terms are significant in phase change processes at liquid-vapour interface (two-phase interface), where a high variation in permittivity occurs [128]. For air, the permittivity variation is negligible. Hence, the Coulomb force term is the only body force affecting the system and dominates in (3.11). Therefore, the Navier-Stokes equations for steady flow can be rewritten as,

$$\rho\vec{U}\ .\ \vec{\nabla}\vec{U} = -\vec{\nabla}p\ +\ \mu\nabla^2\vec{U} + q\vec{E} \tag{3.12}$$

3.2 Space Charge Generation

The gap between the corona and collector electrodes can be divided into ionization and drifting regions. When the conductive region around the wire corona electrode increases due to an increase of the electric field, ionization of air molecules begins and a uniform sheath of positive or negative ions (depending on the polarity of applied voltage) is created over the ionization region. Indeed, this sheath of charged ions is formed when the radius of the corona electrode is much smaller than the gap between the electrodes.

Figure 3.1 shows the difference between the actual radius of a wire electrode and the effective radius of an ionization region. As described in the previous chapter, the conductive ions extend the effective area of the ionization region and the ionization layer increases the effective radius of the corona electrode. Due to this further extension of corona electrode that results a larger curvature of the corona radius, the electric field strength becomes insufficient to generate a corona and ionize air molecules [93].

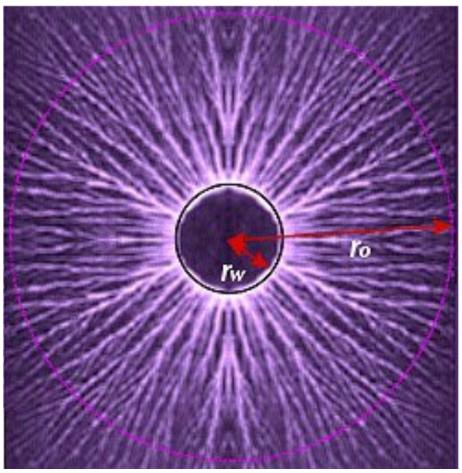

Figure 3.1 Representation of the physical (r_w) and effective (r_0) wire radius. Adapted from Blaze Lab Research [196].

The corona discharge starts when the electric field intensity reaches a sufficient level of electric field strength, which is, in turn, created when the applied potential exceeds the corona inception voltage (CIV). According to Peek's general formula [197], the electric field strength, E_e (V/m), at the surface of corona wire can be estimated by,

$$E_e = fA\delta + fB\sqrt{\delta/R_e} \tag{3.13}$$

where R_e is the actual radius of corona wire (m), f is a roughness factor of the wire surface, and δ is the relative air density, which is defined as [190],

$$\delta = \frac{2.94\,P}{273 + T} = \frac{\rho}{\rho_{STP}} \tag{3.14}$$

where T, P and ρ are the actual temperature (in ^oC), the pressure (in kPa), and the density of air, respectively. Thus, for a smooth wire at standard ambient conditions (STP), $\delta = f = 1$.

The values of A and B in Peek's equation are uncertain constants that depend on the corona electrode configuration and can be approximated based on the experimental measurements. However, for a positively charged corona wire in air, the values of 32.3×10^5 V/m and 0.846×10^5 V/m$^{1/2}$ for A and B, respectively, were suggested and used in Peek's formula for the modelling of corona discharge to estimate the electric field created at the surface of corona wire [165, 198, 199].

The value of constant A in (3.13) represents the electric field necessary for creating corona discharge, E_0, which is the breakdown electric strength of air (= 3.23×10^6 V/m). Thus, the equation of electric field strength, E_e (V/m), created on a smooth surface of a positively charged wire electrode at standard air conditions can be rewritten as,

$$E_\mathrm{e} = E_0 \left(1 + \frac{0.0262}{\sqrt{R_\mathrm{e}}}\right) \tag{3.15}$$

The CIV can be approximated using Peek's empirical formula suggested for a pair of concentric cylindrical electrodes [197] by setting the outer radius of the plasma region around the corona wire and the diameter of the hollow cylindrical shaped collector electrode to be the actual wire radius and the electrode gap for a wire-to-plane configuration in air, respectively, [165, 200] as follows,

$$\mathrm{CIV} = E_\mathrm{e}\, R_\mathrm{e}\, \ln\left(\frac{G}{R_\mathrm{e}}\right) \tag{3.16}$$

where E_e is the electric field strength at corona electrode surface (V/m), R_e is the actual radius of corona wire electrode (m), and G is the distance between the electrodes (m).

The electric potential and electric field intensity inside the ionization zone can be expressed by assuming that the tip radius of the corona electrode is much smaller than the distance between two electrodes [201], thus

$$V = V_e - E_e R_e \ln\frac{r}{R_e} \tag{3.17}$$

$$E = E_e \frac{R_e}{r} \tag{3.18}$$

where V is the voltage at a radius r within the ionization region (V), V_e is the voltage at the corona electrode surface (V), and r is the radius from the centre of the corona wire within the ionization region, (m). A graphical explanation of the notation is shown in **Figure 3.2**, which illustrates the position of the given variables.

The electric field strength at the layer between the ionization and drifting zones is equal to the breakdown electric field strength of air (E_0), and the external radius of the ionization layer, R_0 (m), can be approximated to increase proportionally to the inverse of the electric field strength,

$$\frac{E_e}{E_0} \sim \frac{R_0}{R_e} \tag{3.19}$$

Thus, using the equations (3.17), Peek's equation (3.15) can be rewritten to estimate the external radius of the ionization zone as,

$$R_0 = \frac{R_e E_e}{E_0} = R_e \left(1 + \frac{0.0262}{\sqrt{R_e}}\right) \tag{3.20}$$

By integrating the electric field strength from R_e to R_0 using equation (3.17), the voltage on the external boundary of the ionization zone, V_0 (V), is given by:

$$V_0 = V_e - (E_e R_e \ln\frac{E_e}{E_0}) \tag{3.21}$$

The space charge density in the ionization zone can be neglected as it contains a mix of electrons and positive ions of similar magnitudes, compared to the drift zone, which contains ions of a single polarity and neutral air molecules [165, 194, 201]. In the present numerical simulation, it is assumed that the ionization zone is

small enough to be ignored, following the tradition in corona discharge modelling in the literature [165, 177, 202].

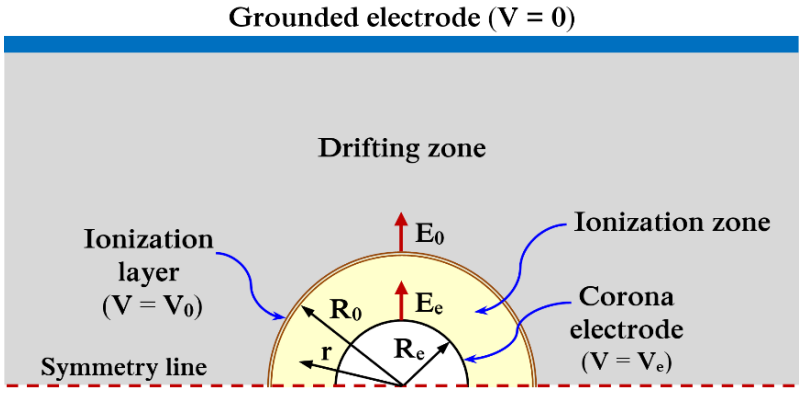

Figure 3.2 Graphical explanation of the ionization and drifting zones. Not in scale.

The boundary conditions for the space charge density can be obtained by applying the commonly accepted Kaptsov's assumption, which suggests that the electric field increases proportionally to the applied voltage below the corona onset level, but will preserve its value constant on the wire electrode surface after the corona is initiated even if the electric potential increases [97]. Under this assumption, the unipolar charge current can be considered in the drifting region between the corona wire surface and the collector electrodes. Thus, the space charge resulting from corona discharge can be estimated by assuming that the electric field strength created at the surface of the corona wire (E_c) due to the applied voltage (V_e) is equal to that obtained from Peek's equation (E_e) [177].

3.3 Numerical Solution Procedure

The governing equations of EHD driven airflow are modelled in two-dimensional (2D) and three-dimensional (3D) simulations using the commercial package, COMSOL Multiphysics (V5.1) software, a partial differential equations solver based on the finite element method [203]. COMSOL Multiphysics is a simulator, modelling tool, and post processing software platform that has the ability to solve complex multi-physics problems. This package has a large library of material properties and predefined physics equations, and can provide flexibility and

simplicity in the workflow. Since the charge transport equation is not available as a predefined module in COMSOL, a partial differential equation (PDE) in a coefficient form can be created to represent this mode into the simulation model. The simulation is developed using an iterative approach [165, 199, 204, 205] to specify the value of space charge density, starting with a guessed value. Then, the electric field strength at the wire surface (E_c) is examined and compared to that calculated from Peek's equation (3.15), E_e. Once $E_c = E_e$, the value of space charge density is fixed and adopted for the given applied voltage and electrode gap. Based on the solution of coupled electrostatic and charge transport equations solved with consistent charge density and electric field strength that satisfy Kaptsov's condition, the fluid dynamic equations can be run under the effect of Coulomb force. A summary of the solution procedure used for solving the modelling equations of EHD airflow is shown in **Figure 3.3**.

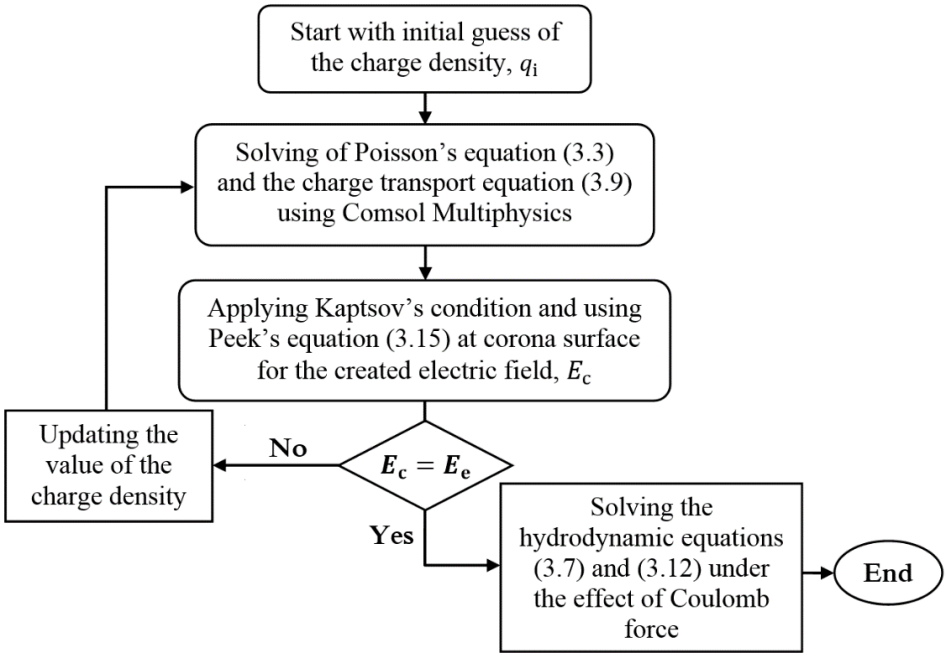

Figure 3.3 Numerical solution procedure used in the present modelling of EHD flow.

3.4 Validation of the Numerical Method

In order to verify the acuracy of the adopted numerical method, including the procudure and boundary conditions required for the EHD modelling approach using Comsol Multiphysics, benchmark comparisons against previous published data are

performed in this section. Among a wide range of experimental studies reported in the literature, the only available data that can be used to validate the modelling of miniature EHD air blower proposed in this thesis for thermal management microelectronics cooling have been found in the Refs. [164, 177, 206], where the EHD airflow is purely produced as a primary flow using a wire-to-plane configuration inside small-scale ducts of rectangular cross-section area. Indeed, the exclusion of using measured data of other studies to verify the present EHD flow simulation was due to the following reasons:

- **Emitter electrode type:** using a needle as an emitter electrode instead of a wire, where the modelling is completely different and does not use Peek's equation to estimate the electric field.
- **Flow pattern and flow field:** using the induced EHD airflow as an impinging air jet to cool heated surfaces in open flow field (for e.g., [40, 140, 155]), or maximise flow generation in a circular duct [137].
- **Mixed flows:** using ionic wind as a secondary flow in the presence of external bulk flow, where a turbulent flow regime is applied, in open flow fields [26], or in confined EHD flows using a wire electrode along a grounded heated duct [149, 150].
- **Nonstandard wire electrode:** although the measured data presented in [158] using a wire-to-plane EHD channel pump seem suitable for a validation model, the partially covered corona wire used in experiments causes difficulty and invalid comparison between the simulated electric field strength created on the wire surface and that calculated from Peek's equation.

The next subsections will present numerical validation models developed for inducing purely EHD airflows using wire-to-grid and wire-to-plane channel configurations, and verify the results in terms of applied voltage, corona current and the resulting ionic wind characteristics.

3.4.1 Wire-to-grid/plane EHD channel configuration

3.4.1.1 Solution domain and boundary conditions

A numerical validation model is established based on experimental data and the numerical results of a wire-to-grid EHD channel presented in [177]. The EHD channel geometry consists of a wire emitter electrode, a collecting grid of parallel wires, and collecting channel walls, as shown in **Figure 3.4**. A conductive wire of a diameter of 100 μm is used as a corona electrode and located mid-way between two conductive plates that represent both the collecting electrodes and channel walls. A symmetry boundary condition is applied at the horizontal plane centered between the channel walls to minimize the solution computation time. The coupled equations of the electric field (3.3), the charge transport (3.9), and the airflow (3.7 and 3.12), were solved in the half domain using the commercial package, COMSOL Multiphysics (V5.1), with the modelling parameters displayed in **Table 3.1**.

The boundary conditions were applied to the half of the numerical domain as follows. The electrostatic mode is modeled by applying a positive potential to the emitter wire surface, while the channel walls and surfaces of all collecting grid wires are grounded with zero volts. For charge transport, a zero diffusive flux condition (Neumann condition) is imposed on all boundaries excluding the surface of the corona wire, where a space charge surface density under Dirichlet condition is applied. This assumption is based on the fact that the diffusion term is very small compared to the conduction term in equation (3.9), so that its effect on charge density can be neglected [165, 202].

For the flow equations, a standard hydrodynamic boundary condition of no-slip is applied to all solid surfaces of corona electrode, collecting grid wires and channel walls. A zero pressure is applied at the channel outlet, while a normal flow with pressure prescribed from Bernoulli's equation ($= -\rho u^2/2$, where u is the velocity component of ionic wind in the flow direction), is used at the channel inlet [164, 177, 194]. This assumption is established on the fact that the neutral air particles are accelerated and driven to a certain velocity U_0 under the influence of electrostatic pressure, which is generated in the electric field due to the electrostatic force. Due to the kinetic energy of the gas flow, a stagnation (or dynamic) pressure ($= \rho U_0^2/2$) is created, which is equal to the electrostatic pressure that causes the gas

movement [207]. Based on this fact, it has been shown experimentally and numerically that the EHD air blower (duct) can be considered to be an ideal pressure source with negligible flow resistance through the duct. This is because the cross section of the emitter wire is very small compared to the duct height [164].

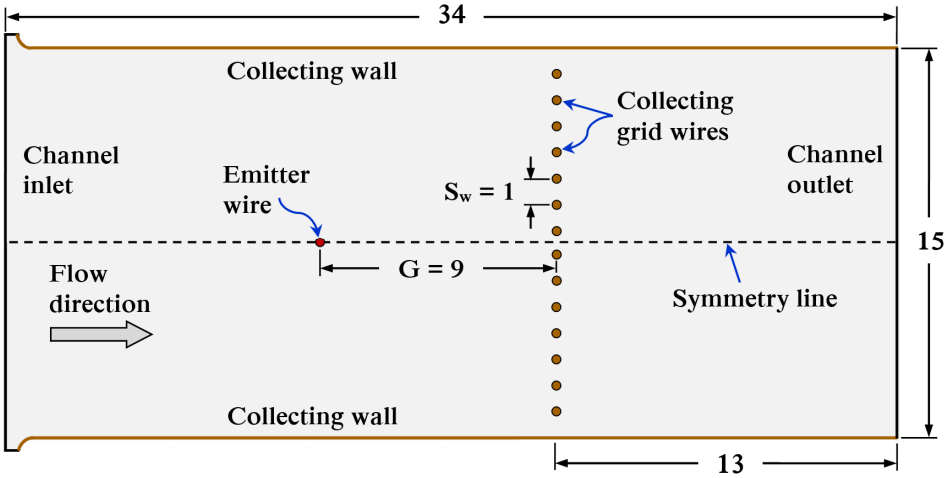

Figure 3.4 Numerical simulation domain of the EHD wire-to-grid channel geometry considered in [177]. Dimensions in millimetres.

Table 3.1 Numerical modelling and geometric parameters used in the model of [177] and in the present validation.

Parameter	**Value**
Applied potential, V_e	5 – 8 kV
Charge diffusion coefficient, D	5.3×10^{-5} m^2/s
Ion mobility coefficient, μ_p	1.8×10^{-4} m^2/V.s
Density of air, ρ	1.23 kg/m^3
Dynamic viscosity of air, μ	1.8×10^{-5} N.s/m^2
Corona wire to collecting grid distance, G	9 mm
Corona wire radius, R_e	0.05 mm
Collecting grid wire radius	0.05 mm
Number of collecting grid wires, N_w	14
Spacing between grid wires, S_w	1 mm
Channel height	15 mm
Channel length	34 mm
Channel width and corona wire length	277 mm

3.4.1.2 Mesh independence study

The modelling approach of EHD flow involves solving two sets of coupled equations. The first set includes the electrostatic and charge transport equations and is solved first to predict the current-voltage curve. When the predictions are verified against measured data, the second coupled physics of Coulomb force and fluid dynamic are then enabled to predict the EHD flow characteristics. Regarding the meshing procedure of EHD flow simulation, the most important and influential part of meshing process is the refinements at the corona wire and collector electrodes, which highly affect the accuracy of the predicted current-voltage results, whereas a sufficiently fine mesh density is mostly generated at this stage for the computational domain. Once good agreement is obtained for the current-voltage predictions, the mesh refinement level at the electrodes is fixed and the fluid dynamic mode is enabled to solve the flow equations and compute the air velocity.

At this stage, the mesh independence study is usually performed to test the effect of mesh density of the computational domain on the results, which is highly related to the gap between the emitter and collector electrodes, where the ions are moving through. Indeed, the mesh refinement at the wire electrode of a very fine diameter requires creating circular surfaces around it in order to ensure an accurate solution of the corona discharge and the created electric field gradient as well as enabling a suitable connection of mesh elements with those of the domain without any meshing error.

Unlike the traditional modelling of fluid flow or/and forced convection heat transfer inside channels, where the approach of mesh independence test is performed by increasing the mesh density for improved accuracy, the excessive refinement at the corona wire surface may lead to increased error in the current-voltage results. Moreover, meshing with a trial and error method (similar to that performed for the space charge density) is applied to obtain an appropriate mesh refinement at the corona wire. Based on these reasons and according to the author’s experience, the inclusion of mesh refinement at the corona wire as part of the mesh independence study is not applicable compared to that for the computational domain, where the mesh is always refined to increase the solution accuracy.

For the present numerical model, a mesh independence test was performed by solving the equations on three numerical meshes, with 15122, 22430 and 38350 triangular elements for the top half domain of the 2D geometry shown in **Figure 3.4**, each with high levels of mesh refinement in the regions of high electric field strength (large electric potential gradient) and space charge density, as shown in **Figure 3.5**. Results on the two finest grid levels were found to be effectively grid independent since the discrepancies in corona current and average air velocity were very slight with approximately 0.1% and 1%, respectively, showing that the solution accuracy was independent on the number of elements over the second mesh density of 22430 elements.

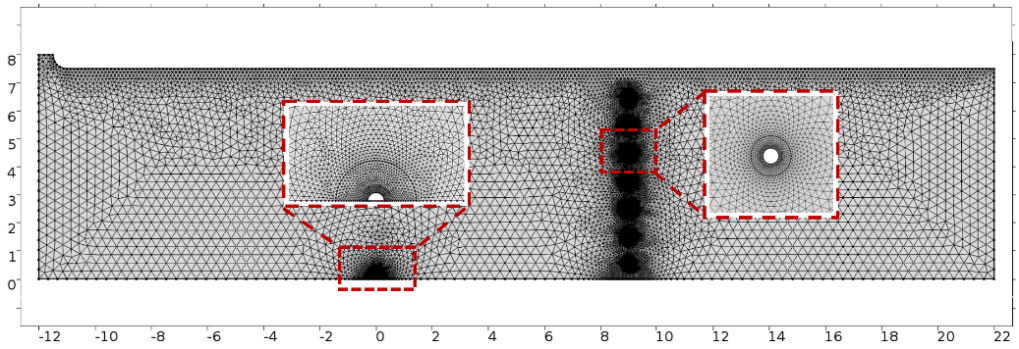

Figure 3.5 Distribution of mesh element density of a half computational domain of the wire-to-grid EHD channel geometry, showing the mesh refinement at the emitter wire and collecting surfaces. The semicircles around the corona wire were used to define mesh refinement. Dimensions in millimetres.

3.4.1.3 Numerical validation results

Figure 3.6 illustrates the results of the numerical solution as surface map distributions generated at 8 kV for the EHD airflow induced through a wire-to-grid channel considered in [177]. The plots agree very well with those presented in [177], and show the distributions of space charge density, the electric field lines, the volume force, and the air velocity through the channel.

Further validation results are shown in **Figure 3.7**, which compare the present predictions of corona current and air velocity with experimental data and numerical results presented in [177], for a range of applied voltage. The agreement is also very good in both cases, with maximum discrepancies against the experimental data of 3% and 7% for the corona current and air velocity, respectively, demonstrating the

accuracy of the present 2D numerical approach performed using COMSOL Multiphysics.

It is useful to mention that although following the modelling procedure of EHD flow and using the same modelling parameters and boundary conditions presented in [177] made the present numerical validation model easer to be implemented, the good predictions obtained against both measured and simulated data would reinforce the adopted numerical modelling method and provide further confirmation to the simulation accuracy of ducted EHD flow that will be used to develop models and investigate further design parameters using the same channel geometry and electrode arrangement, as will be presented in Chapter 4.

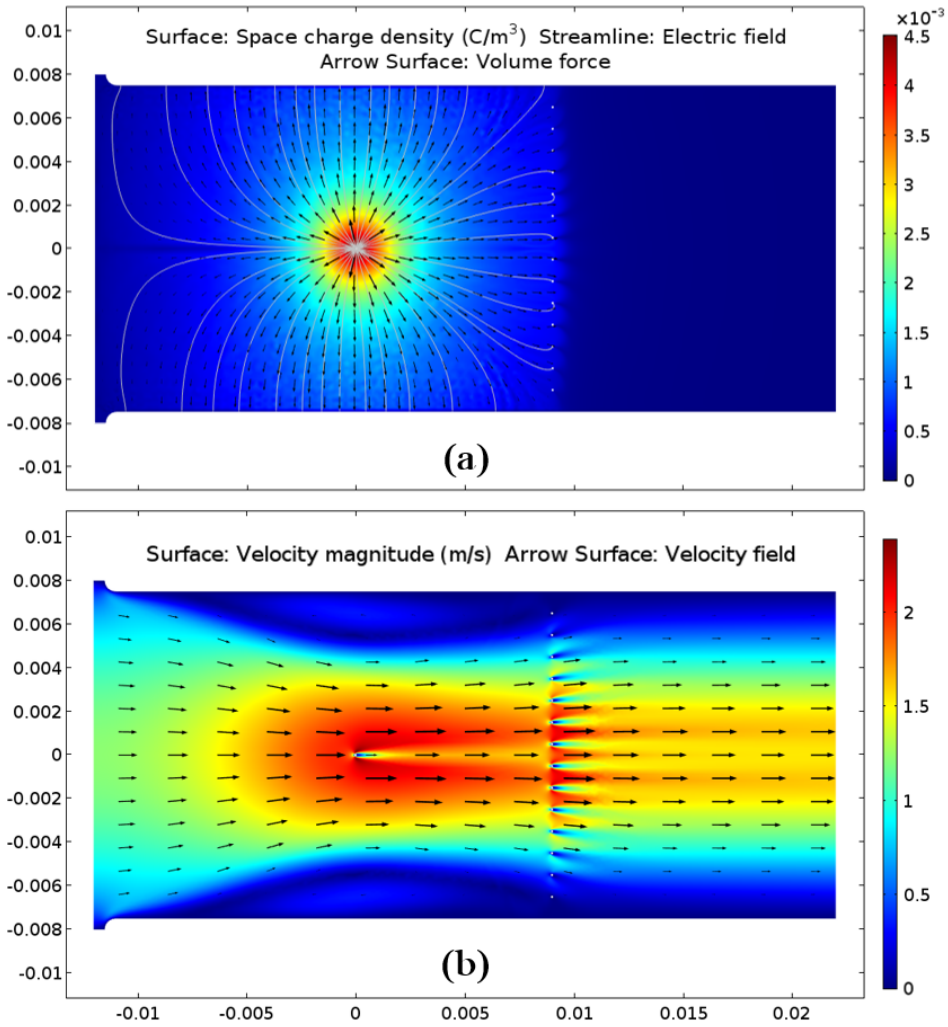

Figure 3.6 Numerical validation results in the form of surface map distributions generated at 8 kV, for (a) the space charge density with the electric field lines and the body force arrows, and (b) the air velocity. Dimensions in metres.

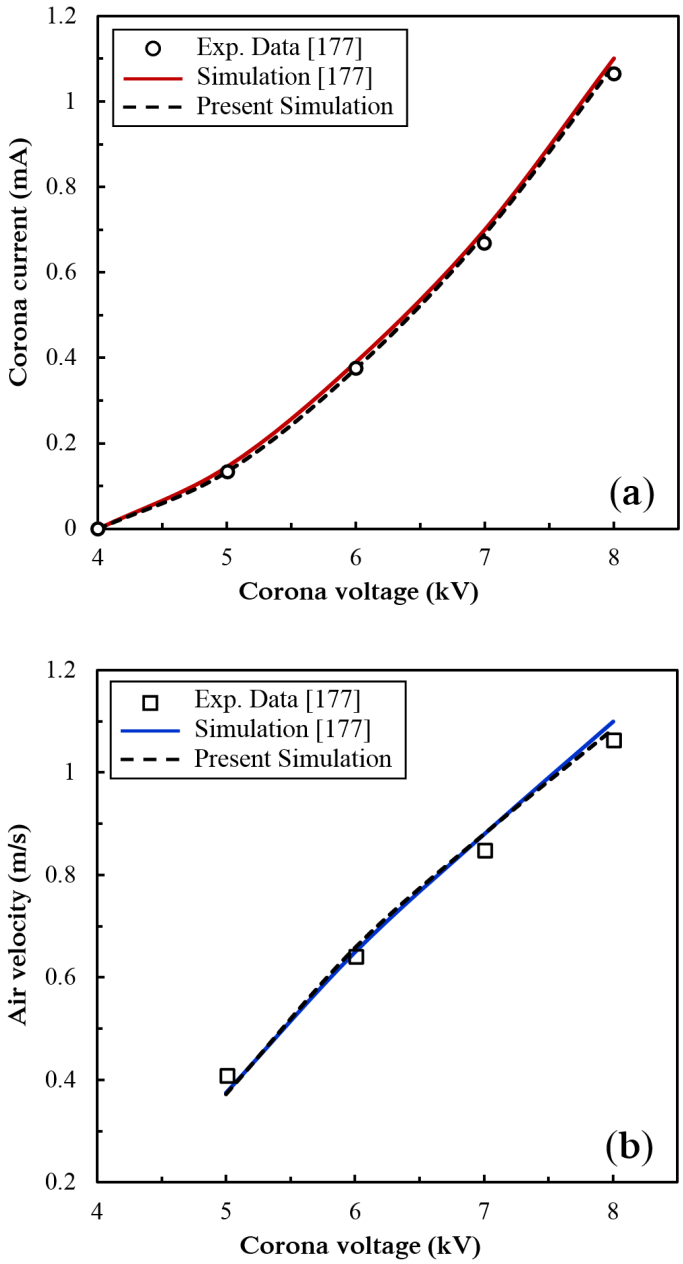

Figure 3.7 Comparisons of (a) corona current, and (b) average air velocity at the channel outlet, for a range of corona voltage.

3.4.2 Wire-to-plane EHD channel configuration

3.4.2.1 Solution domain and boundary conditions

The experimental data and numerical results presented in [164] were used to validate the accuracy of the simulation method performed in 2D and 3D numerical models developed for a wire-to-plane EHD blower. The EHD blower geometry consists of a fine wire electrode, 25 μm in diameter, stretched horizontally between and parallel to two dielectric plates, forming the channel walls. The channel width,

w, (or the distance between the dielectric channel sidewalls) is 100 mm. Two conductive and grounded stripes of 0.1 mm thickness and 5 mm length are positioned at the top and bottom of the channel walls and located downstream of the wire electrode at a distance equal to the channel height. A cross-section of the EHD channel geometry used in the validation model is shown in **Figure 3.8**. A symmetry boundary condition is applied at the horizontal plane centered between the channel walls of the 2D and 3D simulation domains. A further symmetry condition was applied at one of the channel sidewalls of the 3D simulation domain in order to reduce the solution computation time and memory requirements. The boundary conditions of the electrostatic, charge transport, space charge density and fluid dynamic modes, including the assumptions and numerical solution procedure, are similar to those used in the previous numerical validation model presented in section 3.4.1. The modelling parameters and the boundary conditions applied on the computational domain are listed and summarized in **Tables 3.2** and **3.3**, respectively.

A mesh independence study was performed for the half 2D domains of 2 and 6 mm channel thickness with increased mesh refinements at the corona and collector electrodes. The governing equations were solved on three levels of mesh density pre-defined in COMSOL Multiphysics and generated with (62230, 98464 and 151800 triangular elements) for h = 2 mm, and (34115, 53500 and 81075 elements) for h = 6 mm. In each channel, an appropriate mesh refinement at the corona wire and collecting surfaces was applied and fixed, whereas the mesh density was changed for the flow domain using the given three mesh densities to perform the grid independence test. The given numbers of mesh elements show that the thinner channel domain required larger number of mesh elements than the thicker domain. Indeed, this was due to the smaller effective angle of ion drifting area across the electrodes in the thinner domain of h = 2 mm, which increases as the channel height (or the vertical electrode gap) increases, as will be explained later in more detail in Chapter 5. Therefore, further mesh refinement for the thinner domain was required to improve the solution accuracy and achieve good agreement against measured current-voltage data. Results of grid independence test showed that the maximum discrepancy in the average air velocity was approximately 0.15% between the last two mesh densities of each domain height, and therefore the second density level of each domain was adopted.

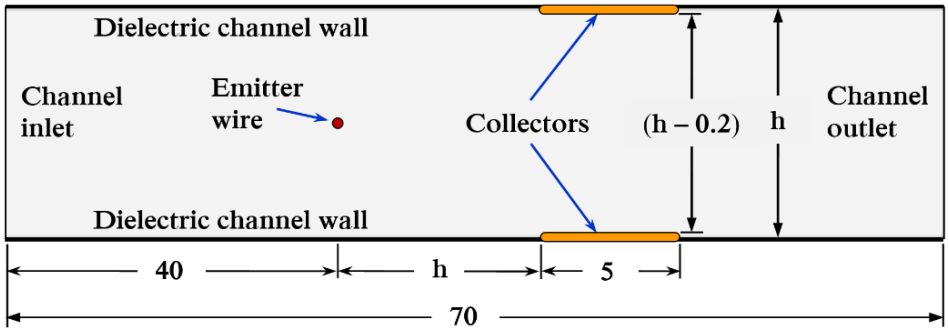

Figure 3.8 Cross-section of the EHD channel geometry used in the present numerical validation [164]. Dimensions in millimetres.

Table 3.2 Geometric and numerical modelling parameters used in the present validation model.

Parameter	**Value**
Applied potential, V_e	0 – 10 kV
The breakdown electric strength of air, E_0	3.23×10^{6} V/m
Ion mobility coefficient, μ_p	2.1×10^{-4} m^2/V.s
Charge diffusion coefficient, D	5.3×10^{-5} m^2/s
Density of air, ρ	1.23 kg/m^3
Dynamic viscosity of air, μ	1.8×10^{-5} N.s/m^2
Corona wire radius, R_e	0.0125 mm
Channel height, h	2 , 6 mm
Channel length, L	70 mm
Channel width, w (= corona wire length)	100 mm
Horizontal distance between the electrodes, (= h)	2 , 6 mm
Collecting surface length, b	5 mm

Table 3.3 Boundary conditions used in the validation and developed numerical models.

Boundary	**Electrostatics**	**Charge transport**	**Fluid dynamics**
Corona wire electrode	$V = V_e$	$q = q_i$	No-slip ($U = 0$)
Collecting surfaces	Grounded ($V = 0$)	$q = 0$	No-slip ($U = 0$)
Dielectric walls	Neumann condition ($\partial V/\partial n = 0$)	Zero diffusive flux ($\partial q/\partial n = 0$)	No-slip ($U = 0$)
Channel inlet	($\partial V/\partial n = 0$)	($\partial q/\partial n = 0$)	Normal flow with velocity prescribed from Bernoulli's equation [177]
Channel outlet	($\partial V/\partial n = 0$)	($\partial q/\partial n = 0$)	$P = 0$
Air boundaries	($\partial V/\partial n = 0$)	($\partial q/\partial n = 0$)	Symmetry

For the 3D solution domain, a similar mesh distribution to the 2D case was used with high element densities at the emitter and collecting surface, which was

generated only for the half domain of h = 6 mm with w = 50 mm. The second mesh density among 507550, 631000 and 757230 tetrahedral elements was selected to solve the 3D numerical domain, with a maximum difference in the value of outlet average velocity of approximately 0.6%, compared to the finest density level. This demonstrated that the second mesh density provides an acceptable balance between computational cost and solution accuracy. The 2D and 3D mesh distributions for the half solution domains of h = 6 mm are shown in **Figure 3.9**.

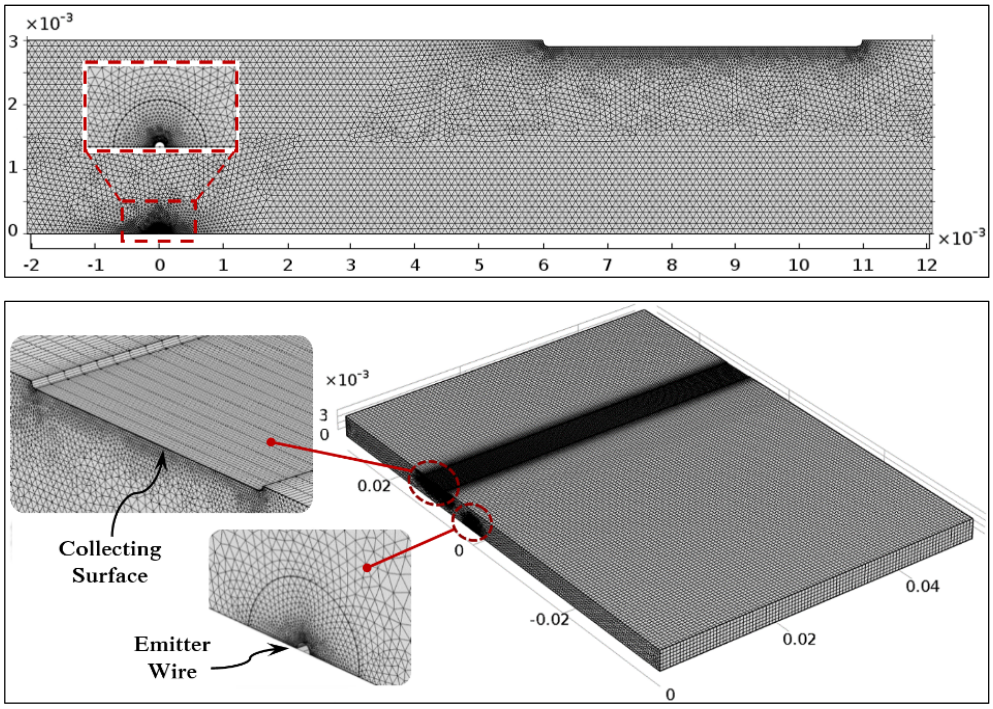

Figure 3.9 Distribution of mesh element density for the half domains (2D at top) and (3D at bottom) of the 6 mm thick, 70 mm long and 50 mm wide EHD duct, showing the mesh refinement at the corona and collector electrodes. The semicircles around the corona wire were used to define mesh refinement. Dimensions in metres.

3.4.2.2 Numerical validation results

The results of the 2D numerical solutions as surface map distributions for the EHD flow induced through ducts of 2 and 6 mm thickness at 15 W/m are illustrated in **Figure 3.10**. The plots show the distributions of the electric potential with the electric field lines (top panel), the charge density with the body force across the electrodes (center panel), and the generated air velocity (ionic wind) through the channel (bottom panel).

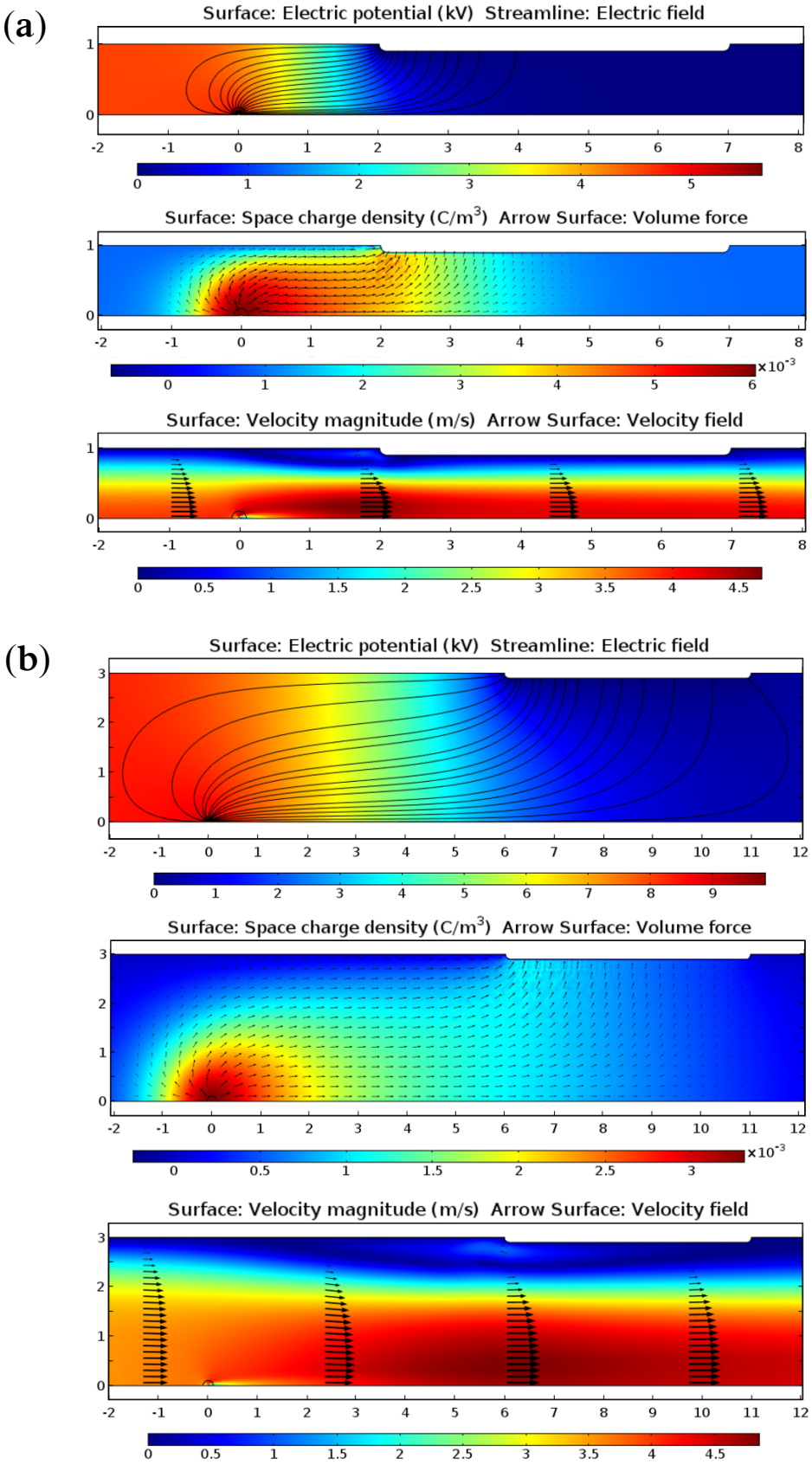

Figure 3.10 Two-dimensional numerical results as surface map distributions for the half of EHD duct geometry generated at 15 W/m for (a) h = 2 mm and (b) h = 6 mm, showing for each: (at top) electric potential with electric field lines, (at center) space charge density with Coulomb force distribution as arrows, and (at bottom) air velocity distribution. Dimensions in millimeters.

Further validation results are shown in **Figure 3.11**, which compares the airflow rates and static pressures of the present simulations with experimental data and numerical results presented in [164], for a range of input powers. The electrostatic pressure created due to the body force, which acts on the collecting surface and equals the channel static pressure, can be calculated by integrating the body force within the gap across the electrodes [164, 208]. The force balance equation for static gas equilibrium along the electrode gap, G, for an EHD wire-to-plane configuration is given as [208],

$$\frac{\mathrm{d}P}{\mathrm{d}z} = qE \tag{3.22}$$

where $\mathrm{d}P/\mathrm{d}z$ is the pressure gradient in the direction of ion motion (z), and q and E ($= |\vec{E}|$) are respectively the charge density and the electric field strength within the electrode gap. Thus, the electrostatic pressure at any point (z) along the electrode gap can be calculated as,

$$\Delta P = \int_{z}^{G} qE \, \mathrm{d}z \tag{3.23}$$

The trends in both figures **3.11**(a) and (b) show good agreement between the present numerical results and those performed in [164] though reasonably small differences can be seen in both models compared to the experimental data. As explained in [164], the noticeable deviation between the simulated and measured pressure values for the 2 mm channel thickness is due to emitter wire misalignment in the experiments.

The 3D simulation results are displayed in **Figure 3.12**, which were generated at 1.5 W for a channel height and width of h = 6 mm and w = 100 mm, respectively, showing the distributions of electric potential, space charge density and air velocity. **Figure 3.13** shows that the values of the average air velocity predicted by the present 3D simulations, where the duct sidewall effects are considered, are closer to the experimental data compared to the 2D simulation results. The average

discrepancies in the mean air velocities of the present 2D and 3D simulations are 9.2% and 5.4%, respectively, against the experimental data. The benchmark results also demonstrate here the accuracy of the present numerical approach of 2D and 3D simulations performed using COMSOL Multiphysics to predict the EHD flow characteristics.

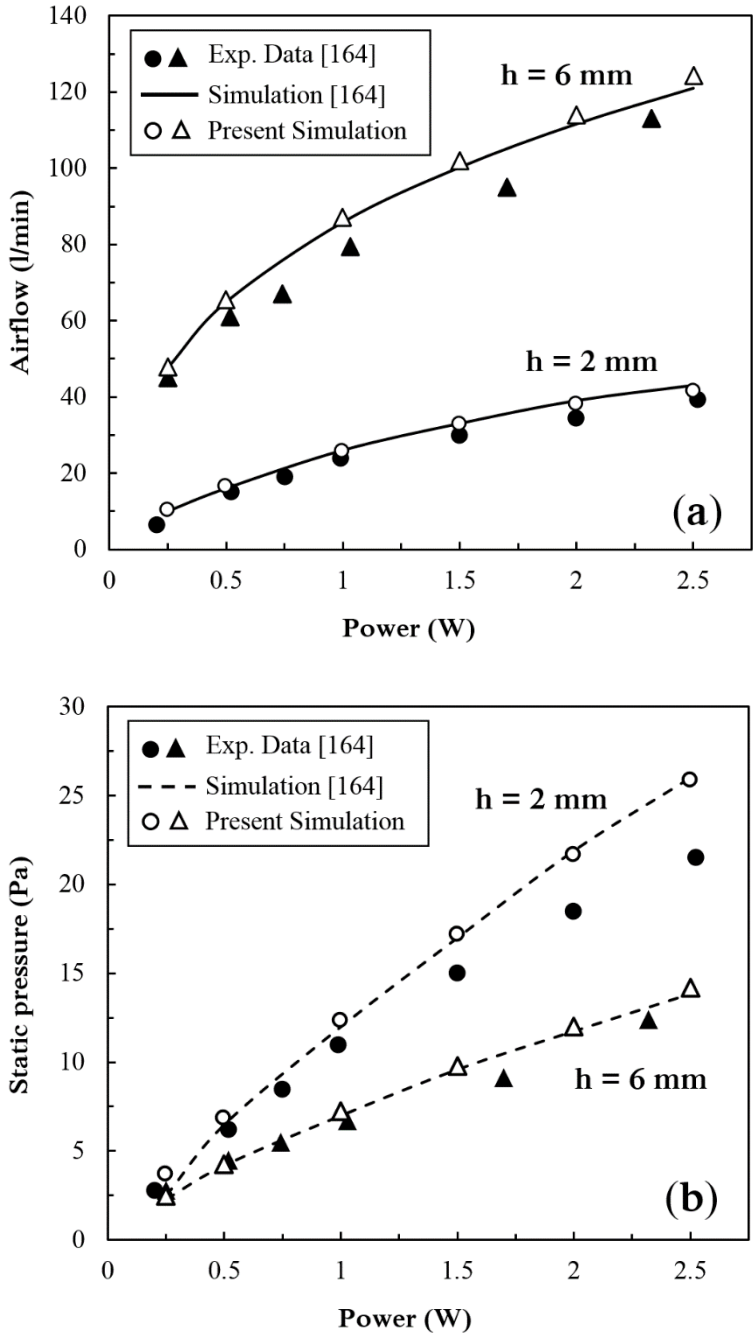

Figure 3.11 Comparison of experimental and numerical results of EHD air blowers of h = 2 and 6 mm with 100 mm wide, showing the operating power as a function of (a) airflow rate, and (b) static pressure.

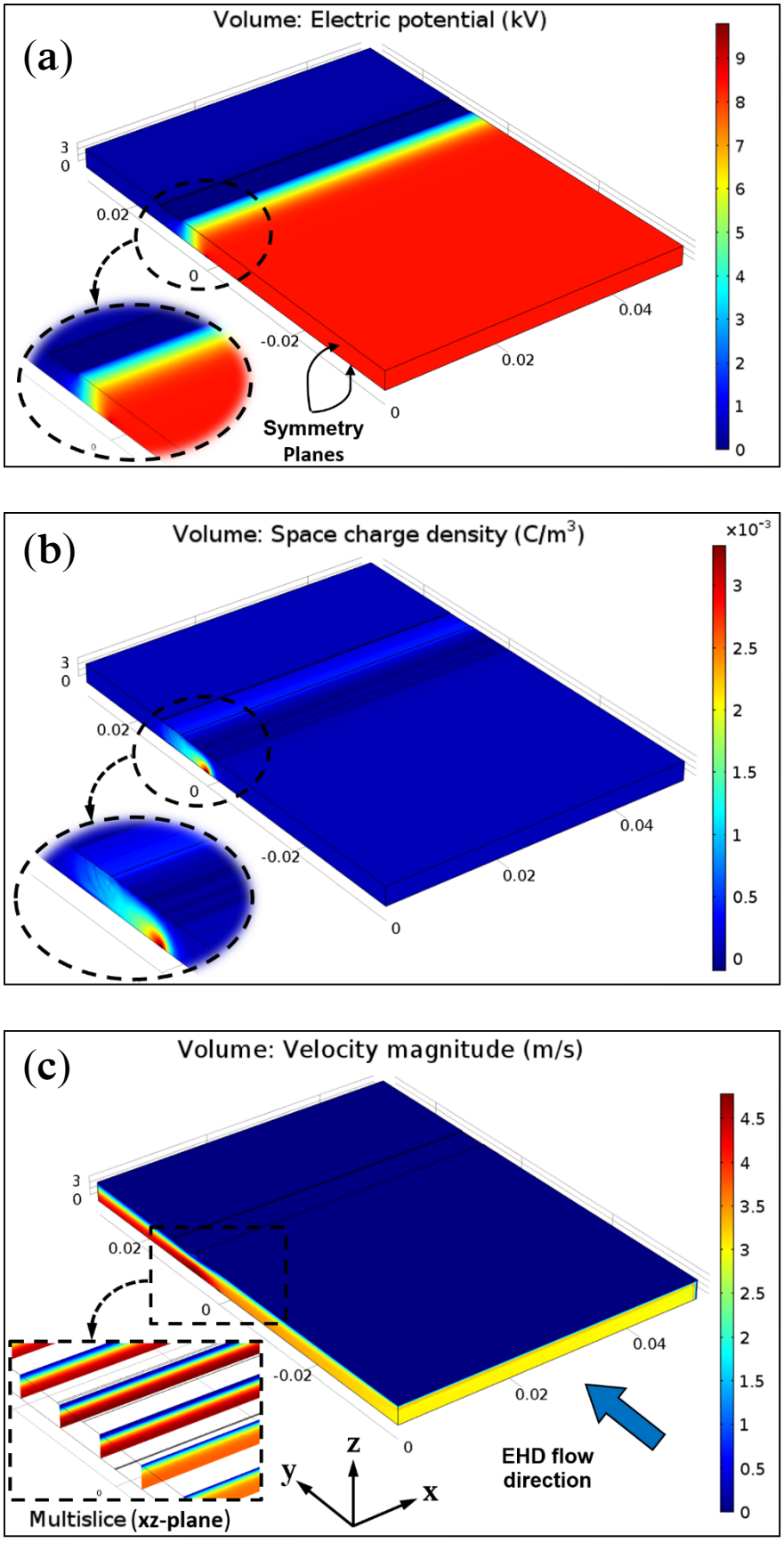

Figure 3.12 Three-dimensional numerical results as volume map distributions for a half of EHD channel generated at 1.5 W with 6 mm thickness, 100 mm width and 70 mm length, showing the distributions of: (a) electric potential, (b) space charge density, and (c) air velocity. Dimensions in meters.

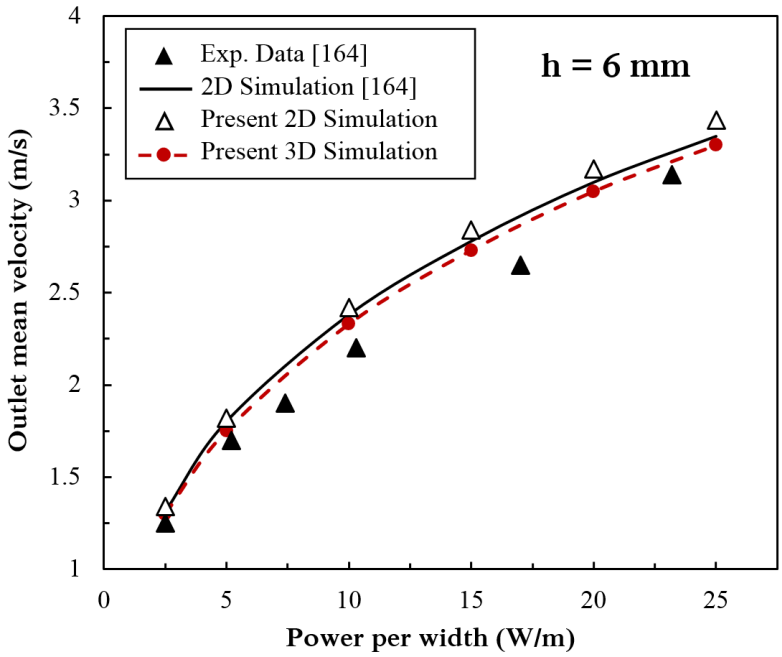

Figure 3.13 Validation results of the outlet mean velocity generated by an EHD blower of 6 mm thickness, 100 mm width and 70 mm length, for a range of operating power.

3.4.3 Wire-to-nonparallel plane EHD channel configuration

3.4.3.1 EHD channel geometry and solution domain

The experimental results of current-voltage and produced air velocity reported in [206] using a wire-to-nonparallel plane EHD channel configuration (Type B) were used to ensure the accuracy of the adopted numerical method. The EHD channel geometry consists of a wire electrode, 0.24 mm in diameter, stretched horizontally between two nonparallel dielectric plates, forming a converging channel of a 3º slope to the horizontal, with inlet and exit heights of 24 and 12 mm, respectively. The total width (or wire electrode length) and length of the channel were 33 and 117 mm, respectively. Two conductive and grounded plates of 0.15 mm thickness and 75 mm length were flush mounted on the top and bottom walls of the convergent channel and located upstream and downstream of the wire electrode at a distance of 36 mm from the channel inlet. A detailed cross-section of the EHD channel geometry with the electrode arrangements used in [206] is shown in **Figure 3.14**.

The same assumptions, boundary conditions and modelling procedure used in the validation models presented in the previous sections are adopted for the present

computational domain, whereas the modelling parameters are listed in **Table 3.4**. A non-uniform mesh density of 48500 triangular elements is generated for the half 2D simulation domain with increased mesh refinement at the corona and collecting electrodes, as shown in **Figure 3.15**.

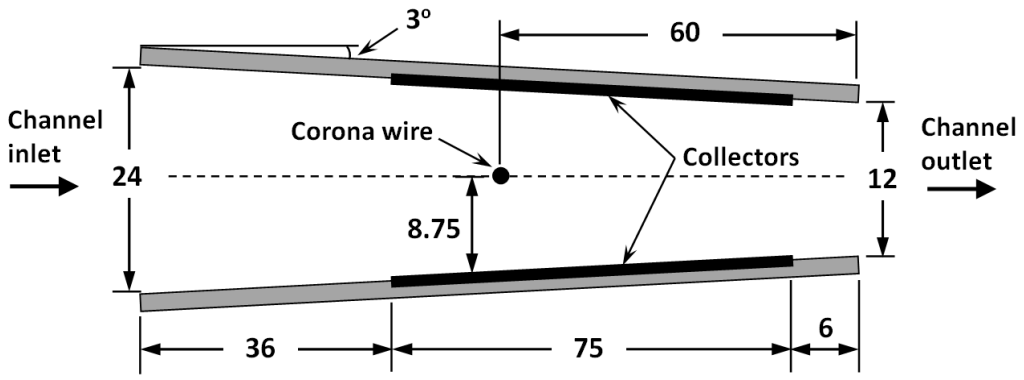

Figure 3.14 Cross-section of the EHD channel geometry used in [206]. Dimensions in millimetres.

Table 3.4 Numerical modelling parameters used in the present validation model.

Parameter	**Value**
Applied positive potential, V_e	6.5 – 12 kV
Breakdown electric strength of air, E_0	3.23×10^{6} V/m
Ion mobility coefficient, μ_p	2.1×10^{-4} m^2/V.s
Charge diffusion coefficient, D	5.3×10^{-5} m^2/s
Density of air, ρ	1.21 kg/m^3
Dynamic viscosity of air, μ	1.82×10^{-5} N.s/m^2

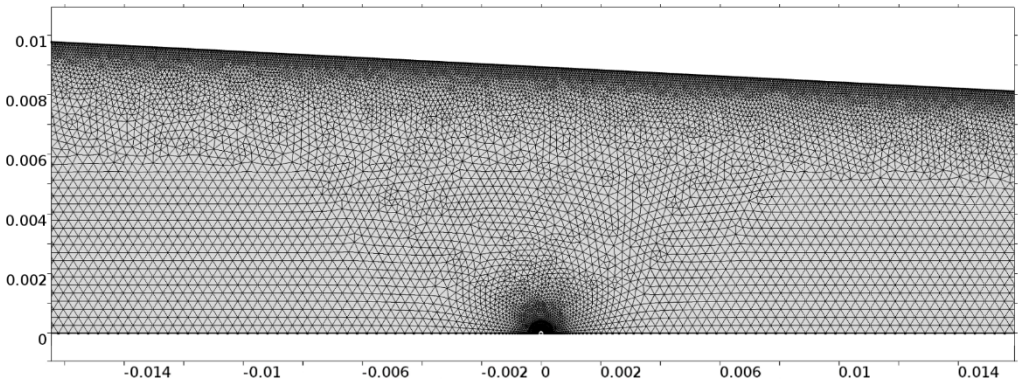

Figure 3.15 Distribution of mesh element density for the upper half of the computational domain of a wire-to-nonparallel plane EHD channel geometry (part of the domain), showing the mesh refinement at the emitter wire and collecting surface. Dimensions in metres.

3.4.3.2 Numerical validation results

Figure 3.16 illustrates the results of numerical solution as surface map distributions for the EHD flow induced through a converging duct at 7 kV positive potential. The plots show the distributions of the electric potential with the electric field lines (top panel), the charge density with body force across the electrodes (centre panel), and the generated air velocity through the channel (bottom panel). Unlike the case presented in the previous validation model of a wire-to-grid EHD channel, where the collecting grid located at the outlet direction, the presence of the collecting surface upstream the corona wire in the present geometry affects the distribution of electric field lines and electrostatic forces to be directed towards the channel outlet, leading to a flow recirculation and formation of eddies, and causing disturbance in the flow patterns downstream of the emitter electrode.

Indeed, the small slope in the collectors towards the channel outlet, which causes a gradient in the electrode gap, plays a main role in increasing the ion current creation downstream of emitter wire toward the desired flow direction, leading to low velocities of produced ionic wind. Moreover, the modest generated EHD airflow, even at high applied voltage, is also attributed to the significant effect of flow resistance due to the converging channel of a narrow flow exit. The phenomena of flow recirculation and formation of vortices observed in the present simulation are in well agreement with previous numerical results reported for ducted EHD flows using similar converging channel geometry [209, 210].

Figure 3.17 shows the results of ion current and average air velocity as functions of applied voltage, and compares the present predictions against the experimental data reported in [206]. The results of current-voltage curve reveal good agreement with the measured values for the given range of applied voltage with a maximum discrepancy of approximately 3.5%. However, the trend of predicted main outlet air velocities shows increased errors compared to the measured velocities with an average discrepancy of up to 20%. Indeed, this is attributed to the flow recirculation and vortices caused by the distributions of the electric field lines and Coulomb force towards the opposite direction of the outlet due to the inefficient location of the collector. This in turn affected the solution stability as the applied voltage increases, and resulted in no solution convergence beyond an applied voltage of 8.5 kV.

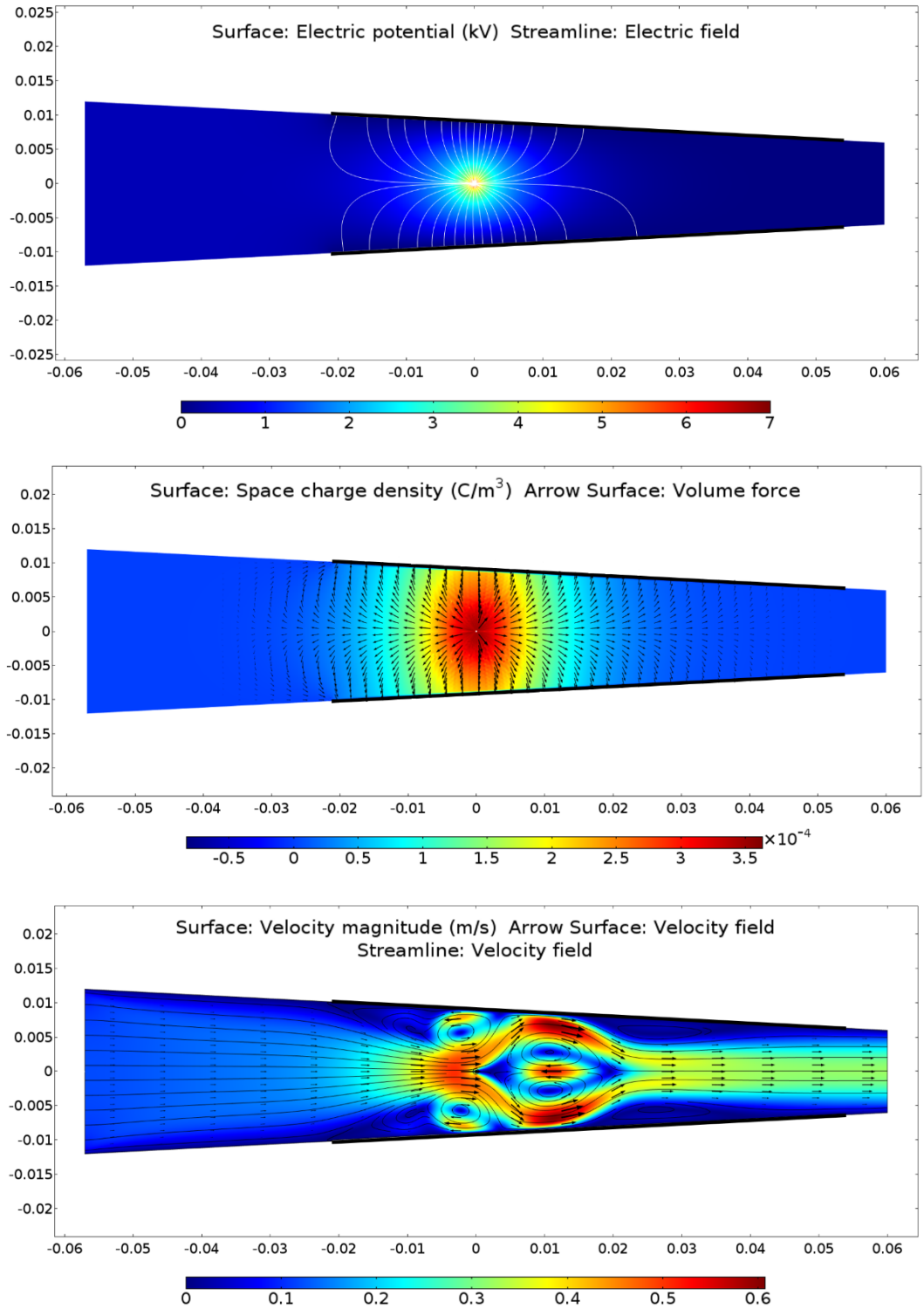

Figure 3.16 Numerical results as surface map distributions for the EHD flow generated at 7 kV, showing: (at top) electric potential with electric field streamlines, (at centre) space charge density with Coulomb force distribution as arrows, and (at bottom) air velocity as arrows and streamlines distribution. Dimensions in meters.

The present benchmark presents further sufficient accuracy of the numerical modelling approach used to predict the current-voltage characteristics and EHD flow induced using miniature scale of ducted wire-to-plane configurations using COMSOL Multiphysics.

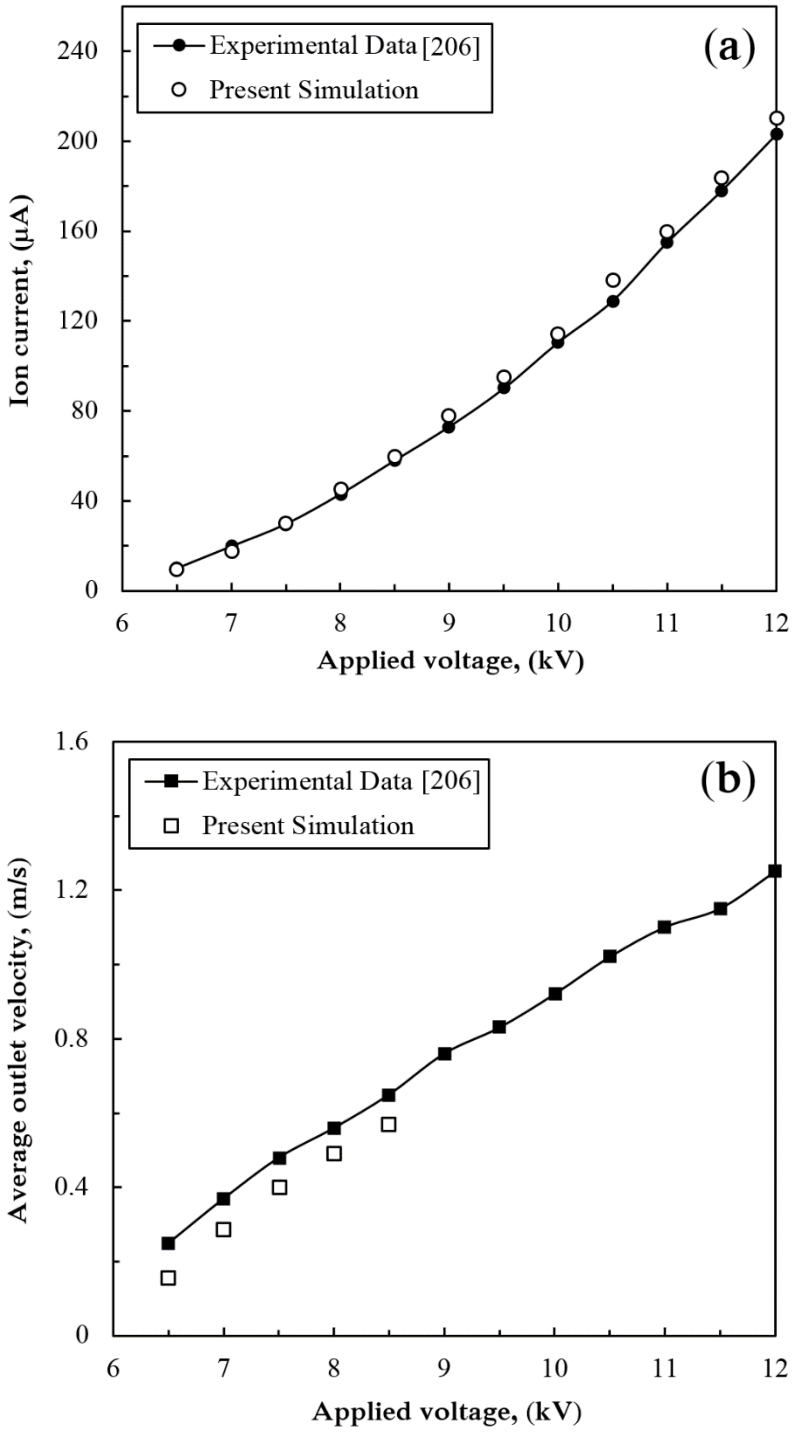

Figure 3.17 Comparisons of (a) corona current, and (b) average air velocity at the channel outlet, for a range of applied voltage. (Channel width = 33 mm).

3.5 Chapter Summary

Two- and three-dimensional numerical validation models for EHD airflows induced using ducted wire-to-grid/plane configurations were developed in this chapter. The coupled equations of the electric field, charge transport and fluid flow were solved using the commercial package, COMSOL Multiphysics (V5.1), a partial differential equations (PDEs) solver based on the finite-element method. Assumptions and boundary conditions applied to the numerical model for the space charge generation and fluid dynamics were discussed. Predicted results of current-voltage curves, produced air velocities, and generated static pressures showed good agreement against measured and numerical data available in the literature. The successful validation models demonstrated the accuracy of the numerical method used in the present thesis, showing that the EHD driven flows could be modeled reasonably within a duct to predict the electrical and fluid dynamic characteristics.

CHAPTER 4

Numerical Analysis of EHD Blowers

Numerical modelling of EHD flow has been performed by many studies and successfully validated against experimental findings (e.g., [177, 179, 211]). Due to the wide range of the geometrical parameters that strongly affect the discharge process and the performance of the EHD airflow devices, numerical studies offer great potential for exploring various design parameters at reduced cost and time.

From a design perspective, this chapter presents a comprehensive numerical analysis for EHD air blowers of wire-to-grid configuration. The analysis includes investigations on the influence of key design parameters on the electric field distribution, current-voltage characteristics, flow generation, and energy conversion efficiency for levels of operating power and voltage. In this direction, a new method of optimization based on fixing the operating power is presented, and optimal and efficient designs are determined.

4.1 Numerical Configuration

A cross-section of the EHD channel geometry used in the present numerical study is shown in **Figure 4.1**, which is similar to that used in the validation model in the previous chapter. The length of collecting surface located at the channel walls is set to be equal to the electrode gap between the emitter wire and the grounded grid. The emitter wire electrode is fixed at a distance of 10 mm from the channel inlet, whereas the location of the collecting grid is at different distances, G, from the corona wire.

The effect of design parameters on the efficiency and flow characteristics of EHD blowers are studied for different heights (h = 9 – 15 mm), and include the corona wire diameter, electrode gap between emitter and collecting grid, collecting surface location, and distribution of collecting grid wires.

The validity of the two-dimensional numerical models developed in this investigation for the wire-to-grid EHD channel are based on the benchmark results presented previously in Chapter 3.4.1, using the same modelling values used in the validation simulation. The geometric parameters of the present EHD blower configuration and the distribution of collecting grid wires for each blower height are detailed in **Tables 4.1** and **4.2**, respectively.

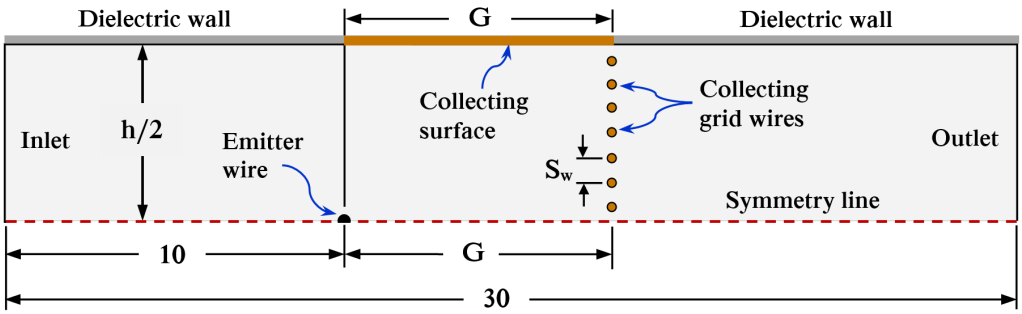

Figure 4.1 Half domain of the EHD blower geometry used in the present numerical study. Dimensions in millimetres.

Table 4.1 Modelling parameter values and ranges of the present numerical configuration.

Modelling parameter	**Value**
Corona wire diameter, d	50, 100, 150 µm
Blower length, L	30 mm
Blower height, h	9 – 15 mm
Collecting grid wire diameter	100 µm
Number of collecting grid wires, N_w	6 – 14 wires
Electrode gap between emitter and collecting grid, G	5 – 10 mm
Horizontal distance between emitter and collecting surface, X	0 – 4 mm

Table 4.2 Distribution of the collecting grid wires for different blower heights, each with S_w = 1 mm.

Blower height, h (mm)	**Number of grid wires, N_w**	**Spacing between grid wires, S_w (mm)**
9	8	1
11	10	1
13	12	1
15	14	1

4.2 Influence of Emitter Wire Diameter

The effect of the emitter wire diameter, d, on the EHD blower performance is first explored by considering three levels of wire diameter with 50, 100 and 150 µm, each modelled for an EHD blower with height of h = 15 mm at a fixed electrode gap of G = 8 mm. **Figure 4.2** shows how the corona current and the generated air velocity increase as the diameter of the emitter wire decreases at a given applied voltage, due to the stronger electric field created by the higher tip curvature. This trend can be explained based on the definition of the ion current, I_c

$$I_c = (\mu_p E q)\, A_w \tag{4.1}$$

where A_w is the surface area of the corona wire (calculated per wire length). Since both the ion mobility μ_p and A_w are assumed constant, the ion current changes proportionally to the body force, $\vec{F}$

$$I_c \propto \vec{F} \propto \vec{E} q \tag{4.2}$$

According to Peek's formula (3.15), the electric field intensity $\vec{E}$ is inversely proportional to the diameter squared of the corona wire. This in turn suggests that the ion current has the following relationship,

$$I_c \propto \vec{E} \propto \frac{1}{d^2} \tag{4.3}$$

Hence, at a given applied voltage and an electrode gap, when the emitter wire diameter decreases, both the corona current and the electric field intensity increase, enhancing the Coulomb force and the kinetic energy imparted to the airflow.

In all cases, the applied voltage must exceed the critical corona onset voltage before the corona wind is created. In addition, as reported in [40], the onset voltage decreases as d decreases, so that the power consumption required to generate a certain corona wind velocity can be reduced by decreasing d. For example, an

emitter wire with d = 50 µm requires 2.5 W/m (at a voltage of 5 kV) to generate an air velocity of 0.86 m/s, compared with 3 W/m (at 6 kV) consumed by a wire with d = 100 µm to produce nearly the same air velocity, as can be seen in **Figure 4.2**(b).

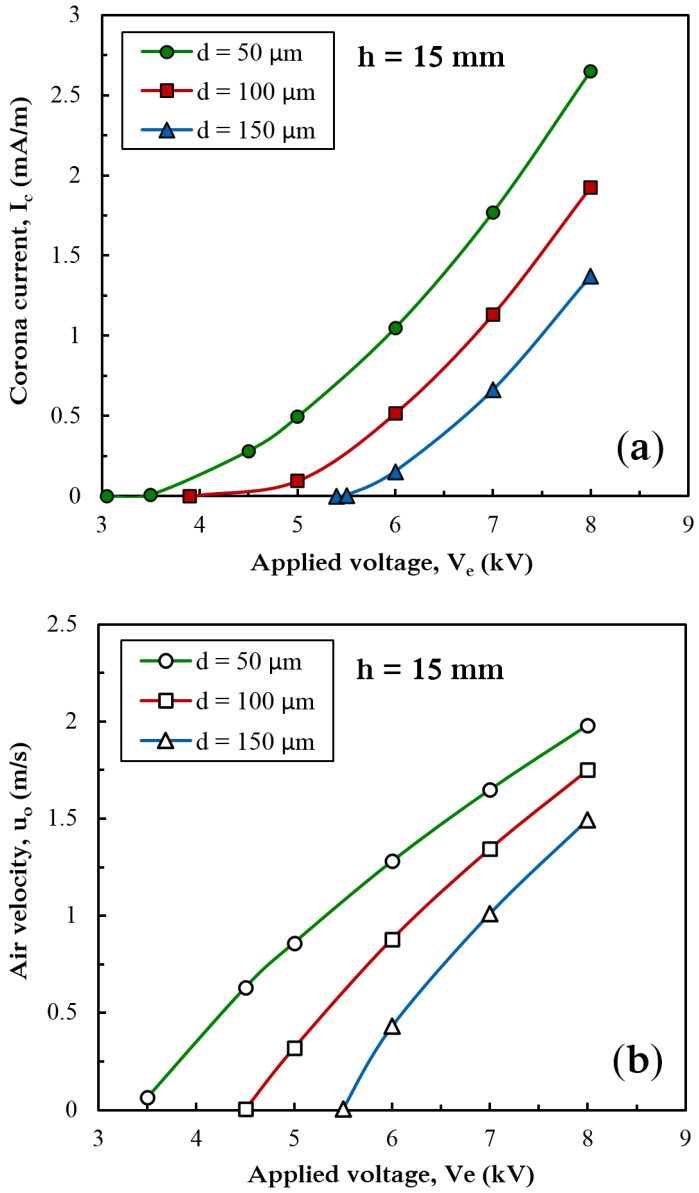

Figure 4.2 Effect of emitter wire diameter, d, at G = 8 mm, on (a) corona current, and (b) average air velocity, for a range of applied voltage.

In order to investigate the EHD blower performance for different emitter wire diameters and collecting grid locations, the electromechanical efficiency, which is the percentage of electrical power converted into mechanical (kinetic) power, is adopted and given by [104],

$$\eta = \frac{P_{\mathrm{m}}}{P_{\mathrm{elec}}} \tag{4.4}$$

The mechanical power P_{m} calculated per channel width can be expressed as,

$$P_{\mathrm{m}} = Q\Delta P = \frac{1}{2}\,\rho\, h\, u_{\mathrm{o}}^{3} \tag{4.5}$$

where Q is the flow rate per width ((m^3/s) per m), ΔP is the dynamic pressure rise (Pa), ρ is the air density (kg/m^3), u_{o} is the average air velocity at the channel outlet (m/s), and h is the channel outlet height (m).

The electrical power P_{elec} is given by,

$$P_{\mathrm{elec}} = V_{\mathrm{e}}\, I_{\mathrm{c}} \tag{4.6}$$

where V_{e} is the applied potential (V), and I_{c} is the corona current calculated per channel width (or corona wire length) (A/m).

Figure 4.3 studies the effect of both d and G on the blower performance at an applied voltage of 7 kV and a range of electrode gaps. The figure demonstrates that the blower efficiency, η, with the finer electrode is the highest for the range of electrode gaps, compared with using thicker wires, which reveal lower performance with a drop in efficiency as the gap increases. This indicates that the stronger electric field intensity created by the finest wire has greater impact on the ionic wind production, regardless of the increase in the created ion current.

It is important to mention that the energy conversion (electro-mechanical) efficiency of the EHD blowers developed in this thesis is just used as a useful indicator for performance comparison and design optimization purpose, regardless of its value. However, it is found that the very low values of conversion efficiency of the investigated EHD blowers lay within the expected range ($\ll 1$) that was previously reported in the literature [119, 148, 212]. Regarding this, it has been demonstrated that the losses in the electrical-to-kinetic power conversion of EHD

devices are related to the influence of flow resistance in ducted EHD flow and due to the nature of ionic wind generation that relies on the released discharge current and non-uniform electric field created between the electrodes [136, 213]. Indeed, not all travelling ions that are accelerated by the electric field towards the collector electrode always collide with air molecules and transfer their momentum and energy perfectly towards the desired flow outlet direction, leading to a reduced net flow at a constant created current [8].

In fact, the equation of mechanical power (4.5) was derived and provided by Moreau [148], and has been commonly used in the literature to determine the energy conversion efficiency of EHD pumps. However, as presented in Chapter 2, June et al. [136] experimentally demonstrated that the extremely low efficiency of EHD air movers compared to that of rotary fans is due to the difference in the methodology of determining the mechanical power of each, which is typically calculated for rotary fans by computer industries using (4.5) based on the static pressure rather than the dynamic one. Moreover, they stated that the conversion efficiency calculated from (4.4) is only valid for EHD flow in open space, where no flow impedance due to walls of ducted EHD devices is considered."

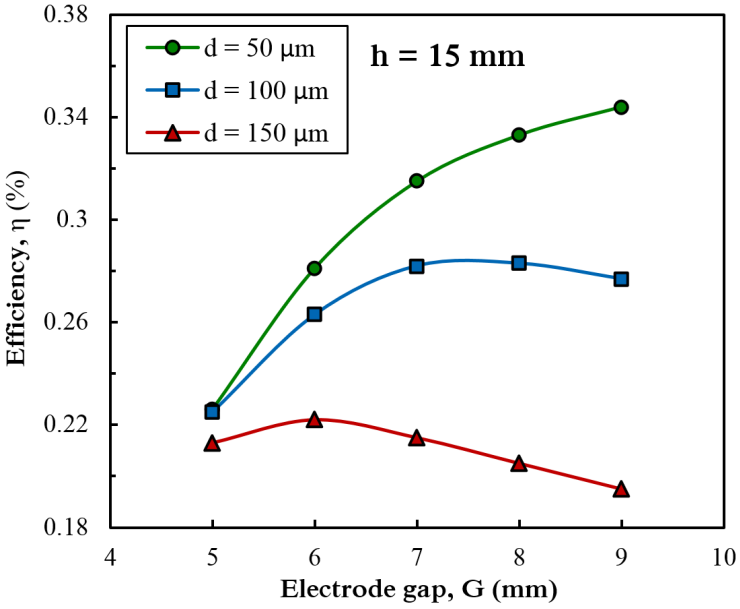

Figure 4.3 Effect of electrode gap on blower efficiency for different emitter wires modelled at 7 kV for blower of h = 15 mm.

Figure 4.4 compares the efficiency and the ion current created by two different wires with diameters of 50 and 100 µm at different applied voltages. It shows that the corona current created by both wires declines as the electrode gap increases, resulting in a significant growth in the blower efficiency. However, although the current created by the thicker wire with d = 100 µm at 8 kV is higher than that created by the finer wire with d = 50 µm at a lower potential (7 kV), the latter electrode is more efficient over the range of electrode gaps. This is mainly due to the stronger electric field intensity and the effective distribution of its lines along the collecting surface and the grid wires, which are responsible for imparting higher kinetic energy to the airflow in the outlet direction. In contrast, the lower electric field intensity created by the thicker wire is highly affected by the closer area at undesirable directions of the collecting surfaces, leading to a drop in the efficiency. It was noticed, for example, that using the finer wire at G = 8 mm reduces the power consumption and the required voltage by 3 W/m (20%) and 1 kV (13%), respectively, whereas the ionic wind velocity decreases by only 0.1 m/s (approximately 6% drop), compared to the case of using the thicker wire at the same electrode gap.

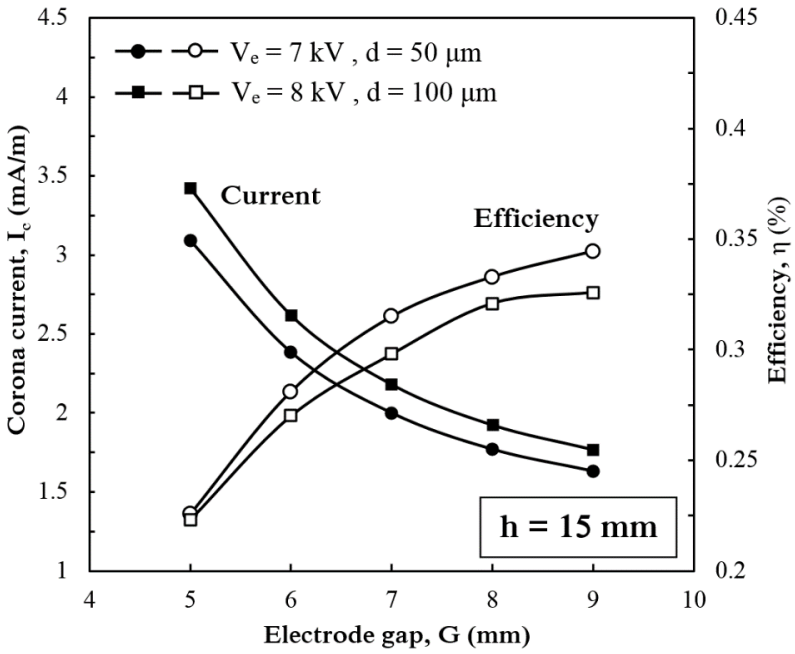

Figure 4.4 Comparisons of the ion current (left axis) and the efficiency (right axis) created by two different wires at different applied voltages, for h = 15 mm and a range of electrode gaps.

From a design perspective, using a finer wire electrode can decrease both the power consumption and the applied potential required to generate a certain air velocity, leading to improved EHD blower performance. Therefore, the finest emitter wire with 50 μm diameter will be adopted for the remainder of this investigation.

4.3 Influence of Electrode Gap

This section discusses the influence of the distance G between the emitter wire and the collecting grid electrodes on the EHD power and airflow velocity, which will be presented for the blower of 15 mm height as a case study. **Figure 4.5** shows plots of the square root of the corona current (calculated based on wire length) and the generated air velocity as functions of the applied voltage for different electrode gaps (G = 5 to 10 mm).

The general trends indicate that both the corona current and air velocity increase with increasing the applied voltage or decreasing the electrode gap. Indeed, the increase in the applied voltage at a given electrode gap, or the decrease in the latter at a given applied voltage, increases the electric field and the resulting Coulomb force, according to Poisson's equation (3.3). This in turn increases the kinetic energy imparted to the electrons (moving towards the positive wire electrode) and to the positive charged ions (moving towards the grounded electrode), leading to a greater corona current and higher ionic wind generation.

The current-voltage characteristics shown in **Figure 4.5**(a) demonstrate a linear relationship between the applied potential and the square root of the corona current in the present numerical configuration, confirming previous findings presented by Robinson [119] and others [103, 214].

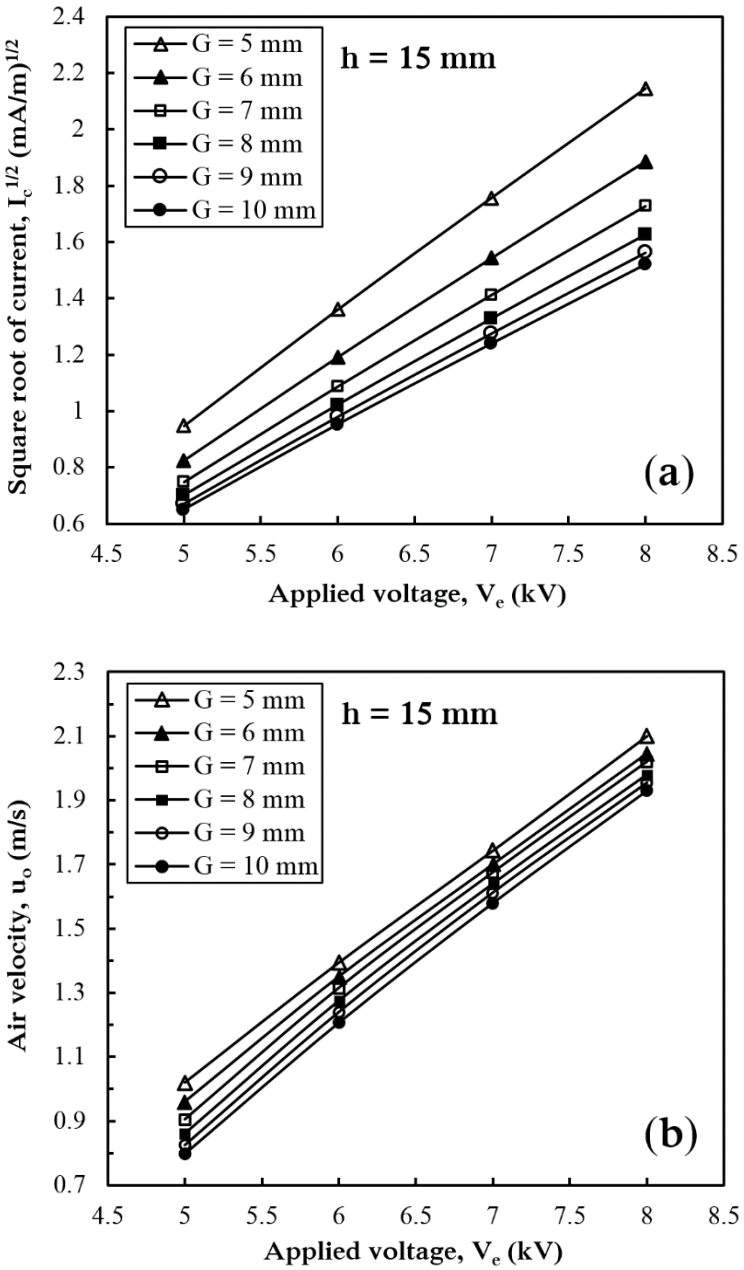

Figure 4.5 Effect of electrode gap, G, and applied voltage on (a) corona current, and (b) average air velocity at the channel outlet.

Figure 4.6 illustrates how the efficiency increases as the applied voltage and the electrode gap increase, reaching the peak level at their higher values. However, at smaller electrode gaps (G = 5 and 6 mm), the blower efficiency tends to remain constant or decline slightly with increasing applied voltage. This can be attributed to the impact of the electric field distribution along the grounded grid wires, and is also due to the effect of the collecting surface length at the channel walls, which increases with the electrode gap.

Indeed, when the applied voltage increases at small electrode gaps, the electric field intensity becomes stronger and highly affected by the grid wires close to the corona electrode, and the short grounded surfaces located above and below it, which are not the desired flow direction. Therefore, the concentration of the electric field lines and the body force vectors towards the collecting surfaces will relatively decrease the impact of the horizontal components of the Coulomb force, which is responsible for moving the ionic wind towards the channel outlet, and leading to lower efficiency due to the related high power consumption. Moreover, the same behaviour occurs for the higher electrode gaps (G = 9 and 10 mm) at low applied voltage, where the electric field lines are highly affected by the collecting surfaces, which is closer to the corona wire than the grounded grid.

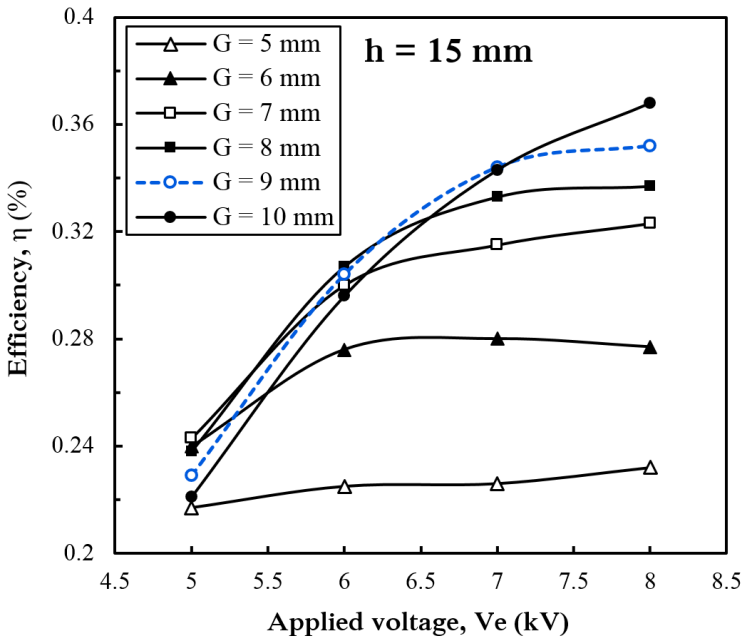

Figure 4.6 Effect of electrode gap G and applied voltage on blower efficiency.

In contrast, at higher potential and electric field intensity, the increase in the electrode gap and the collecting surface length improves the distribution of the electric field lines along the grounded surfaces and increases the drifting angle between the emitter and the grid electrodes, enhancing the charged ions drifted in the horizontal path. Further insight can be obtained from **Figure 4.7**, which shows two distributions of the space charge density with the body force arrows generated at 8 kV for electrode gaps of G = 5 and 8 mm. It is found that although the power

consumed by the blower of G = 5 mm is approximately 36.8 W/m, compared to 21.2 W/m at G = 8 mm (with 42.4% drop), the difference in the average velocity is no more than 0.11 m/s (about 5% decrease), showing a significant effect of the locations of the grounded surfaces and grid on the EHD blower efficiency.

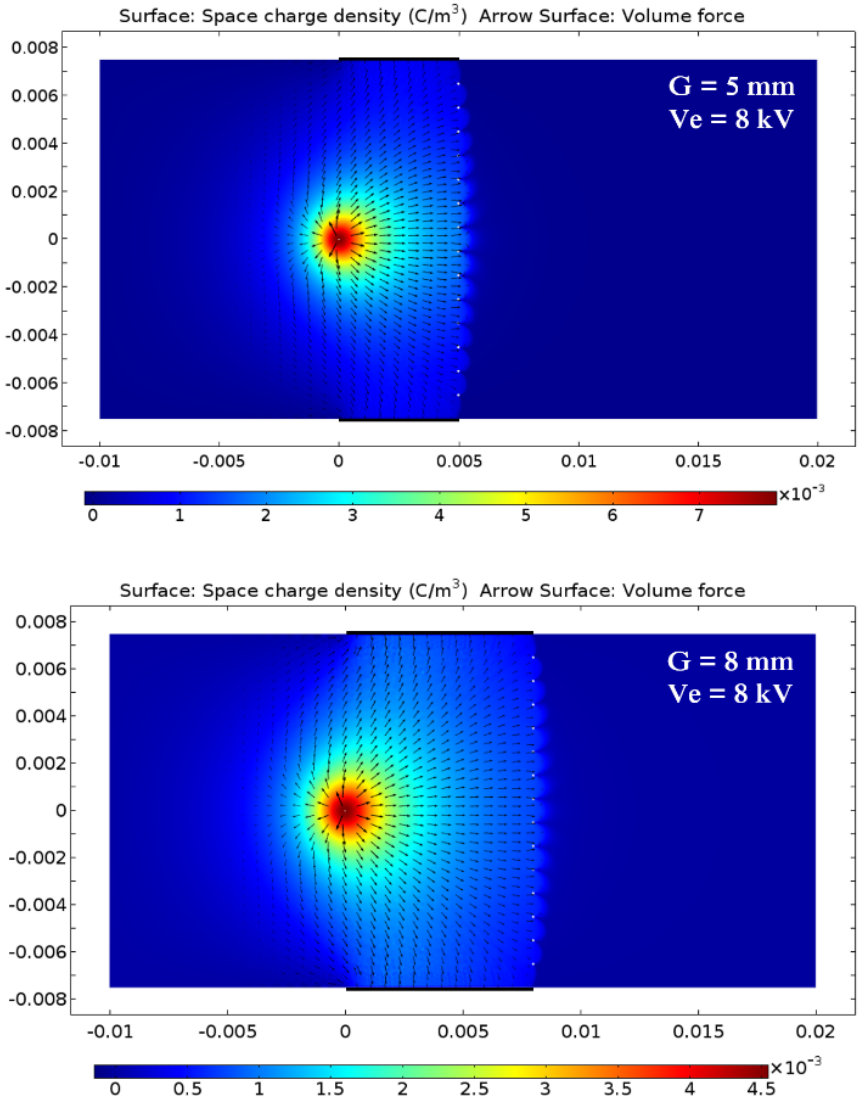

Figure 4.7 Distributions of the space charge density with the body force arrows generated at 8 kV for h = 15 mm and electrode gaps of G = 5 mm (at top) and G = 8 mm (at bottom).

4.4 Optimization of Blower Configuration

4.4.1 Collecting grid location

The optimization of the collecting grid location from the emitter electrode, defined by electrode gap G for each blower height is now explored by fixing the operating power at constant levels. The input power was varied from 2.5 to 15 W/m, which corresponds to an overall range of applied voltage from 4 to 7.6 kV required for all ranges of electrode gaps and blower heights. **Figure 4.8** shows the influence of the electrode gap on the efficiency of different blowers for a range of input power. It can be observed that the efficiency increases as the input power increases at each electrode gap for all blowers, which is due to the stronger electric field created by the higher potential. Furthermore, the difference in the blower efficiency values due to changing the electrode gap fluctuates from one blower to another, depending on the height and the level of operating power.

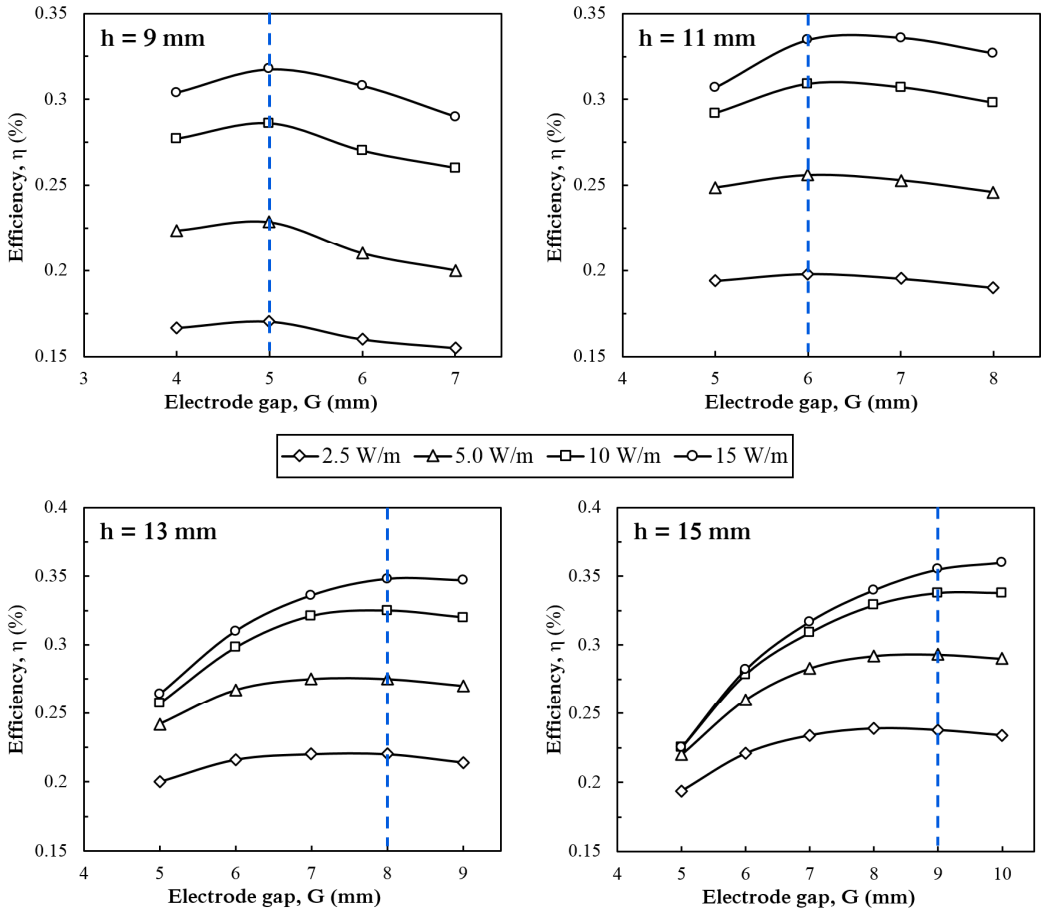

Figure 4.8 Effect of electrode gap on efficiency of different blowers at fixed input powers. (Dashed lines indicate the optimal electrode gaps).

However, the trends show that the efficiency of each blower reaches its maximum value at certain location for all input powers, revealing the unfavorable impact of increasing the electrode gap beyond this point. Indeed, with further increases in the electrode gap, the electric field lines become highly affected by the collecting surfaces, which will be closer to the corona wire than the grounded grid, leading to a drop in the efficiency. Therefore, these locations (identified in **Figure 4.8** by dashed lines), where the highest blower efficiency is achieved, can be considered the optimal electrode gaps for the present configuration, and are listed in **Table 4.3**.

Table 4.3 Optimal locations (defined by the electrode gap G) of the collecting grid from the emitter wire for different EHD blowers.

Blower height, h (mm)	**Electrode gap, G (mm)**	**Collector length (= G), (mm)**	**Number of grid wires, N_w**
9	5	5	8
11	6	6	10
13	8	8	12
15	9	9	14

4.4.2 Collecting surface location

The influence of the collecting surface location at the blower walls on the EHD blower performance is now discussed. The collecting grid was fixed at the optimal electrode gap of each blower, while the horizontal distance X between the emitter wire and the edge of the collecting surface was changed in 1 mm steps from X = 0 (the original position), decreasing the collector length to a distance of $(G - X)$, as shown in **Figure 4.9**.

In order to predict the optimal location of the collecting surface of each blower and examine its impact on the EHD blower performance, the investigation is performed based on the blower efficiency by fixing the applied potential (calculated only for the blower of 15 mm height as a case study) and the input power, and the results are compared to those of blowers without collecting surfaces (NCS).

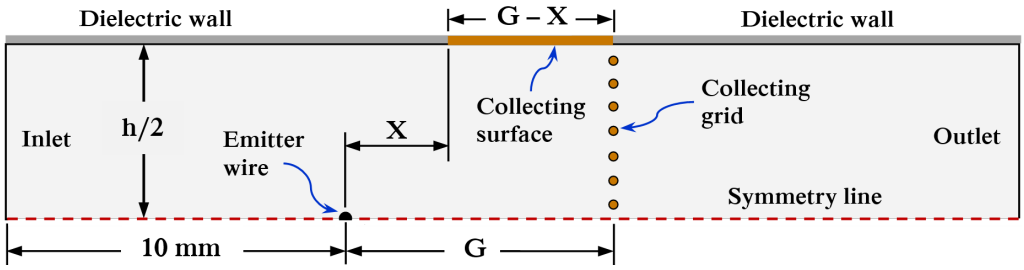

Figure 4.9 Collecting surface location based on the horizontal distance X from the wire electrode.

Figure 4.10 shows the effect of collector location on the EHD blower efficiency and the resulting air velocity for a range of applied voltages. It can be seen that the ionic wind velocity grows significantly in the presence of the collecting surface at X = 0, compared to the case of no collectors, before it tends to decrease as the distance X increases, whereas their efficiency are very similar. This is attributed to the higher corona current created between the electrodes due to the larger collector area, compared to that created just by the grounded grid, resulting in higher ionic wind production. In addition, the trends of the efficiency bars show an obvious increase as the collecting surface moves apart from the emitter wire, reaching peak values at nearly X = 3 mm.

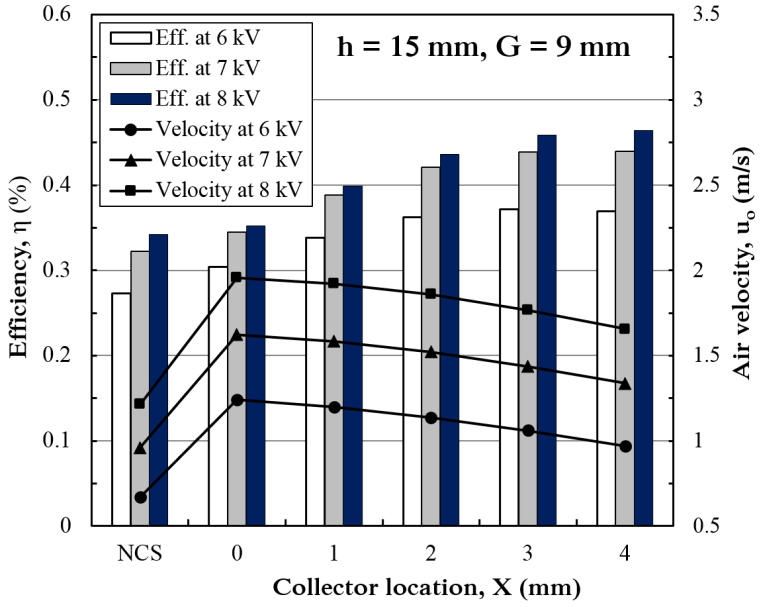

Figure 4.10 Effect of collector location (defined by X) on blower efficiency (left axis) and outlet average air velocity (right axis), for a range of applied voltage.

Despite the highest air production being obtained at X = 0, which agrees well with previous experimental findings presented in [155], moving the collector to the location X = 3 mm shows that the maximum decrease in the velocity at 8 kV (for instance) is approximately 10%, while a significant reduction in the power consumption of 43.5% is achieved. Indeed, moving the collecting surfaces with the flow direction towards the channel outlet can enhance the electric field distribution on the collecting surfaces and strengthen the horizontal component of the Coulomb force, decreasing the corona current created due to the narrow gaps, and resulting in better EHD efficiency.

For the case of fixing the input power, **Figure 4.11** illustrates the impact of the collector location of different blowers on the outlet air velocity and the applied voltage that corresponds to each level of input power. It also indicates that the presence of the collecting surface at X = 0 can reduce the required voltage by approximately 3 kV at 15 W/m for h = 15 mm, as an example, while producing nearly the same air velocity as that generated by a blower with just a collecting grid.

The general trends show that both the ionic wind velocity and the corona voltage required to preserve the input power at a constant level increase with the distance X. These observations are similar to the experimental observations of a flow in an open space reported in [27]. However, the values of air velocity produced by each blower tend to decrease or increase very slightly after certain locations, for the two levels of operating power.

In order to reduce the level of the applied voltage and determine the most effective location of the collecting surface for each blower height, the percentage increase of both the average velocity and the applied potential were calculated for different collector locations (defined by X) at two levels of input power, as illustrated in **Figure 4.12**. It is clear that the percentage increase in the air velocity at the first step (X = 1 mm), over that generated at the location of X = 0, is higher than that of the required applied potential for all blower heights. However, the rate of increase in the velocity tends to decrease with increasing X, compared to that of the potential, and (the latter) reaches its peak level at certain locations before it tends to decrease.

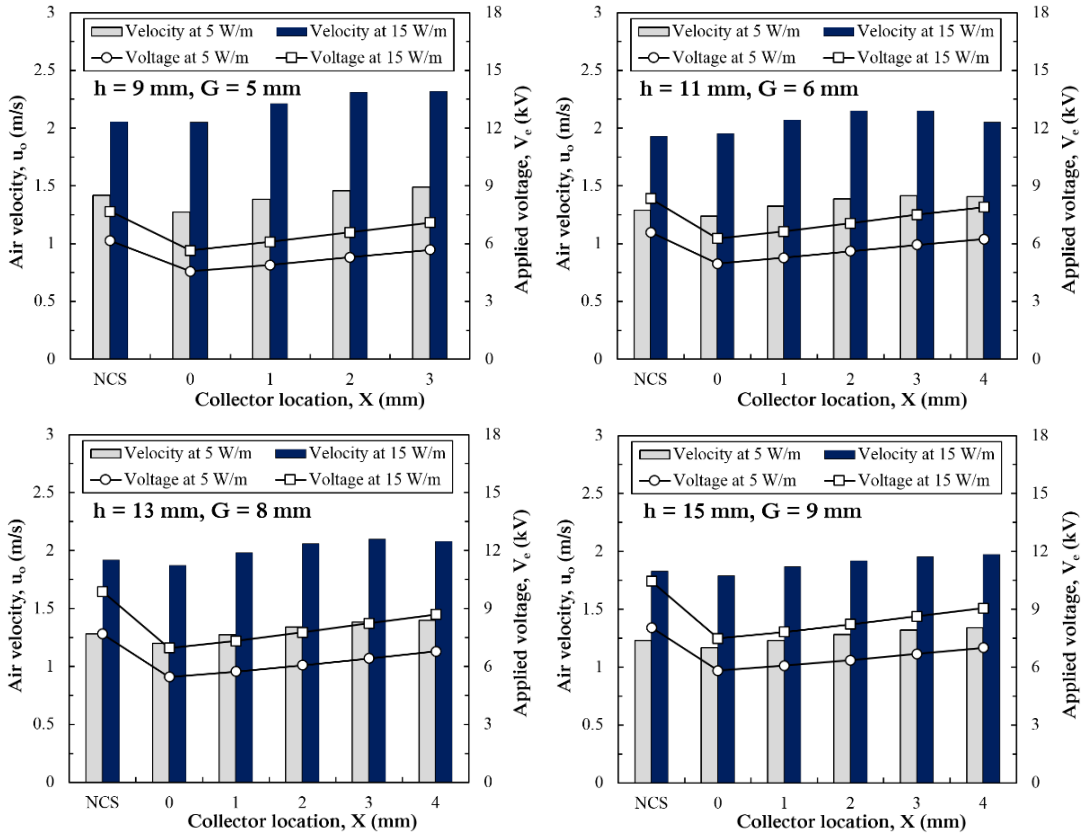

Figure 4.11 Effect of collector location of different EHD blowers on the air velocity (left axis) and applied voltage (right axis), at two levels of fixed input power.

It is found that when the increase in the potential reaches its peak, the increase in the air production is approximately 50% or higher than that in the applied voltage, and all increases in the voltage beyond these gaps lead to a drop (shown with red bars) or relatively very slight improvements in the air velocity. These locations, which are indicated by arrows in the figure, can be considered as the optimal and the most effective gaps at a constant input power, as detailed in **Table 4.4**.

Based on these optimal locations, the maximum enhancements achieved in the average outlet velocity are between 9% and 15%, depending on blower thickness, compared to those obtained at $X = 0$, using the same operating power.

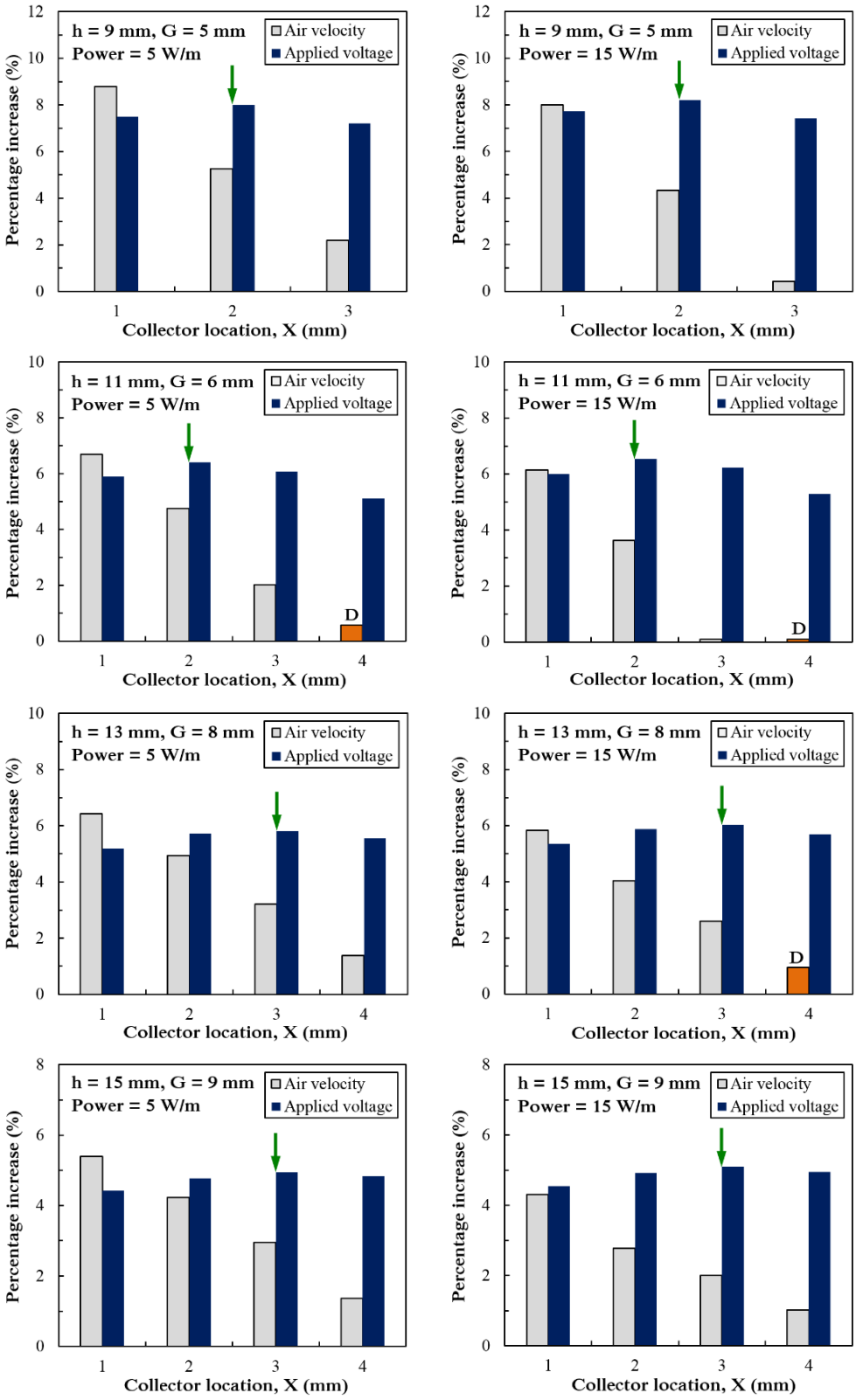

Figure 4.12 Collector location as a function of the percentage increase (each calculated over that of the former location, *X*) in both air velocity and applied potential for different blowers at fixed input powers (5 W/m for left column and 15 W/m for right column). Arrows indicate the optimal collector locations, and red bars refer to a decrease (D).

Table 4.4 Optimal collector locations from the emitter wire for different EHD blowers, determined based on effective increase in the applied voltages at fixed operating powers.

Blower height, h (mm)	**Optimal collector location, X (mm)**	**Electrode gap, G (mm)**	**Collector length, CL (= $G - X$) (mm)**	**Number of grid wires, N_w**
9	2	5	3	8
11	2	6	4	10
13	3	8	5	12
15	3	9	6	14

4.5 Influence of the Collecting Grid

4.5.1 Benefits of using a collecting grid

In order to explore the advantage of using the grid wires as further collecting surfaces for the blower performance, a comparison based on the required operating voltage and the blower length (or size) was established. Two blower heights with h = 9 and 15 mm were selected and modelled with no collecting grid (named as the NG case) at a fixed power of 15 W/m, and their results were compared to those obtained by equivalent blowers with a collecting grid (named as the WG case). The first comparison was performed based on the required operating voltage by fixing the collector length at (CL = $G - X$), in order to ensure using the same blower length in both compared cases.

Figure 4.13 shows that the NG case requires a higher applied voltage to fix the operating power at a constant level at all given collector locations of both presented blowers, with a required increase of approximately 12% at the optimal locations of both blowers, compared to the WG case. In contrast, the velocity trends reveal obvious reductions at all collector locations of both blowers, which appear higher for the thinner blower due to its shorter collector length. This clearly reflects the important role of using the collecting grid in increasing the collecting surface area and thereby reducing the level of operating voltage, and at the same time improving the electric field distribution in the desirable direction with higher kinetic energy imparted to the flow towards the blower outlet.

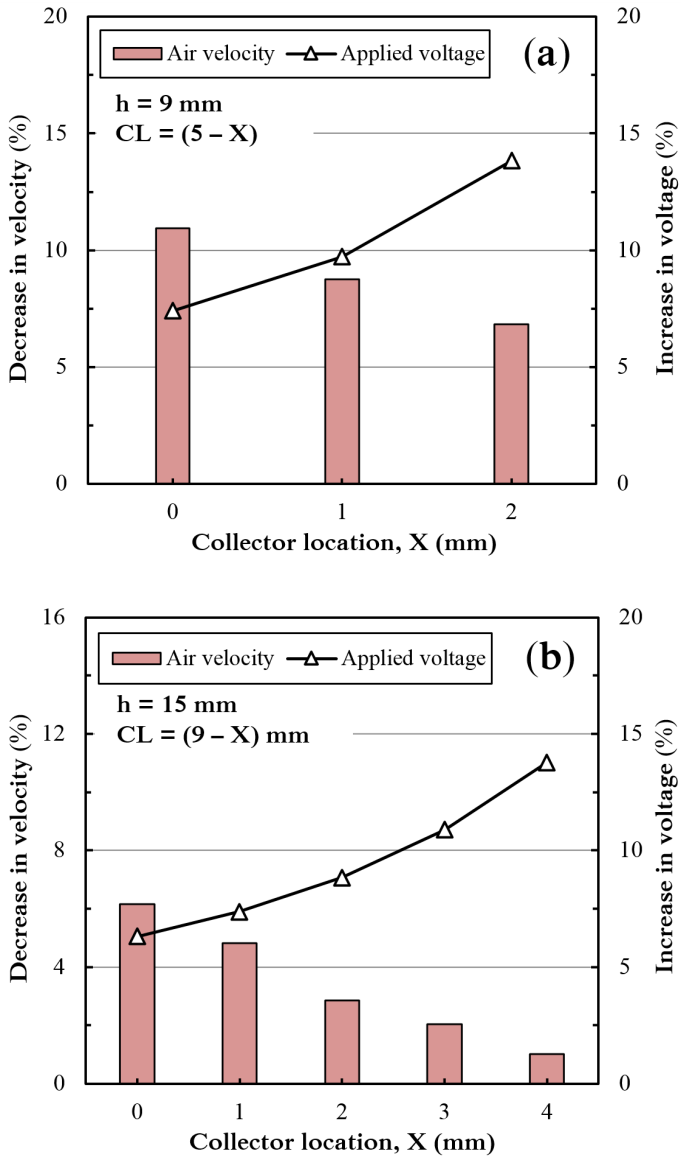

Figure 4.13 Percentage decrease in air velocity and increase in applied voltage for blowers without a collecting grid (NG), compared to those with a grid (WG), modelled at a fixed collector length of $(G - X)$ and different collector locations, for blower heights of (a) h = 9 mm, and (b) h = 15 mm.

The second comparison is based on the blower length, which can be defined as the actual distance between the corona wire and the far end of the collector electrode. Although the numerical domain length used in the presented comparison is 30 mm, the percentage increase in the blower length is calculated by assuming that the blower lengths of WG case are 6 mm (for h = 9 mm) and 10 mm (for h = 15 mm), which are the actual minimum lengths that can be used in the practical implementation.

For the NG case, the collector lengths were fixed at 5 and 9 mm for blowers of h = 9 and 15 mm, respectively, regardless of the collector locations from the emitter wire, whereas their results were compared to those obtained by optimized blowers for the WG case but with collector lengths equal to $(G - X)$, as shown in **Figure 4.14**. This in turn leads to an increase in the blower length for the NG case as the collector moves away from the emitter wire, compared to that of the WG case, which is restricted by the wire-to-grid electrode gap, G.

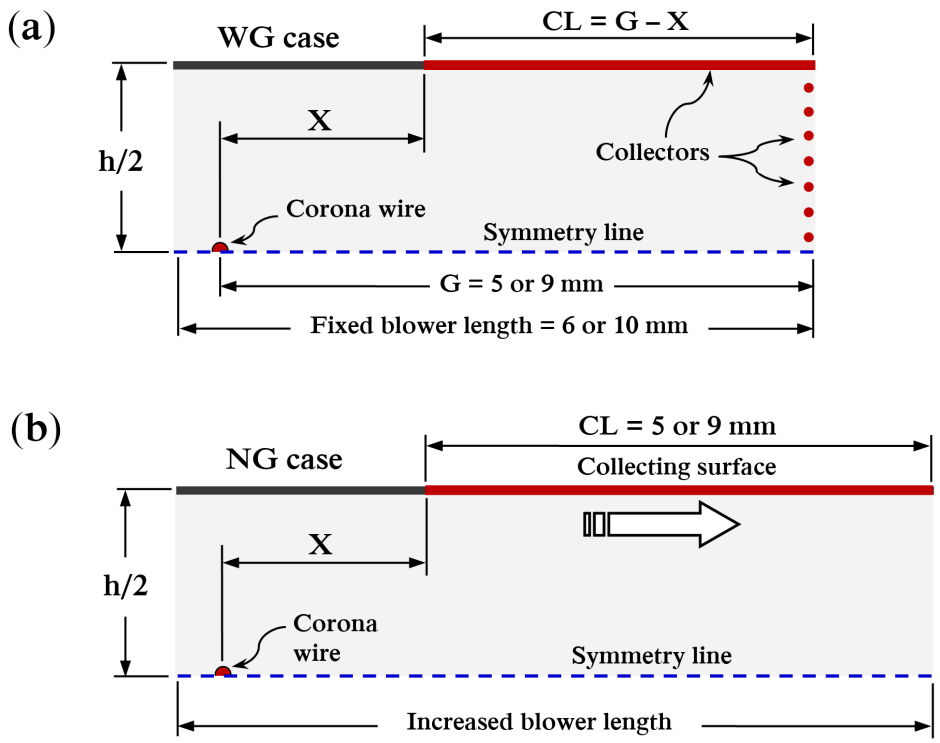

Figure 4.14 Effect of the presence of collecting grid on the blower length, showing the cases of (a) with a grid (WG), and (b) without a grid (NG), for the two considered heights of h = 9 and 15 mm. Not in scale.

Figure 4.15 shows that although the collecting surface lengths of the blowers for the NG case remain constant at all locations, the use of collecting grid still offers lower operating voltage required for both blowers at all collector locations. This increase is accompanied by a drop in the air velocity (shown by red bars) and an increase in the blower length before modest enhancements in the velocity (green bars) are achieved as the collectors move towards the blower outlet but with higher operating voltage and larger blower size. These observations also indicate that using

the grid as an additional collector electrode has significantly beneficial impacts on the blower performance with higher flow production and lower size and operating voltage, meeting the design and thermal management requirements.

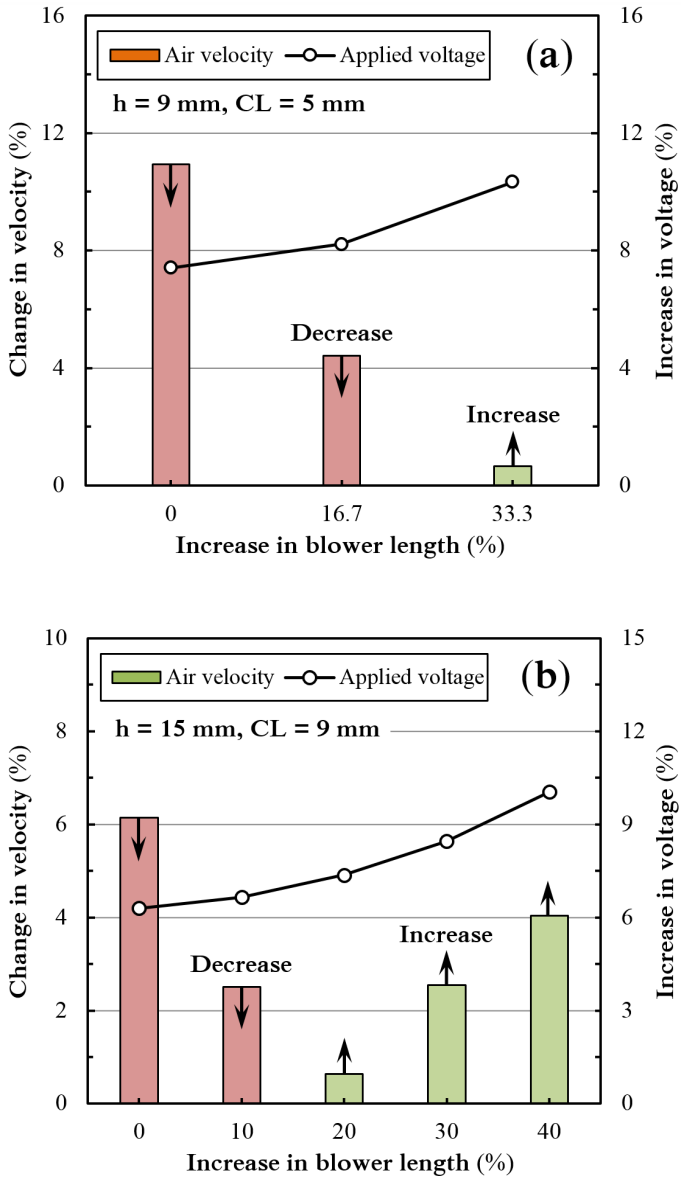

Figure 4.15 Percentage change in blower length, air velocity, and applied voltage of blowers without a collecting grid (NG), compared to those with a grid, for heights of (a) h = 9 mm, and (b) h = 15 mm.

4.5.2 Effect of collecting grid density

The final section illustrates the effect of the collecting grid density on the efficiency of each optimized blower by considering different levels of grid density,

defined by the number of wires (N_w) and the spacing of the gaps separating two successive wires (S_w), as described in **Table 4.5**. The locations of both the grid and the collecting surface of each blower are fixed at their optimal predicted gaps from the emitter wire. The investigation is performed at two levels of constant applied voltage, which correspond to those required to fix the power at 5 and 15 W/m, respectively, and used in each case of an optimized blower. The case that is without a collecting grid (N_w = 0) is included to reflect its impact on the blower performance.

Table 4.5 Description of the collecting grid densities used in different blowers based on the number of grid wires (N_w) and distances between two successive wires (S_w).

Blower height, h (mm)	**Grid density**	**GN0**	**GN6**	**GN8**	**GN10**	**GN12**	**GN14**
15	Number of wires, N_w	0	6	8	10	12	**14**
	Spacing, S_w (mm)	–	2.5	2	1.5	1.25	**1**
13	N_w	0	6	8	10	**12**	–
	S_w	–	2	1.5	1.25	**1**	–
11	N_w	0	6	8	**10**	–	–
	S_w	–	1.8	1.25	**1**	–	–
9	N_w	0	6	**8**	–	–	–
	S_w	–	1.5	**1**	–	–	–

Figure 4.16 shows air velocity and power consumption as functions of the number of collecting grid wires for different blower heights modelled at a constant voltage required to fix the power at 15 W/m for each blower. It reflects that decreasing the grid density reduces the power consumed by each blower, whereas the velocity trends show different behaviour depending on the number of grid wires of each blower. In addition, both the velocity and power consumption values obtained by using any grid density of each blower are higher than those of the no-grid case, GN0 (N_w = 0).

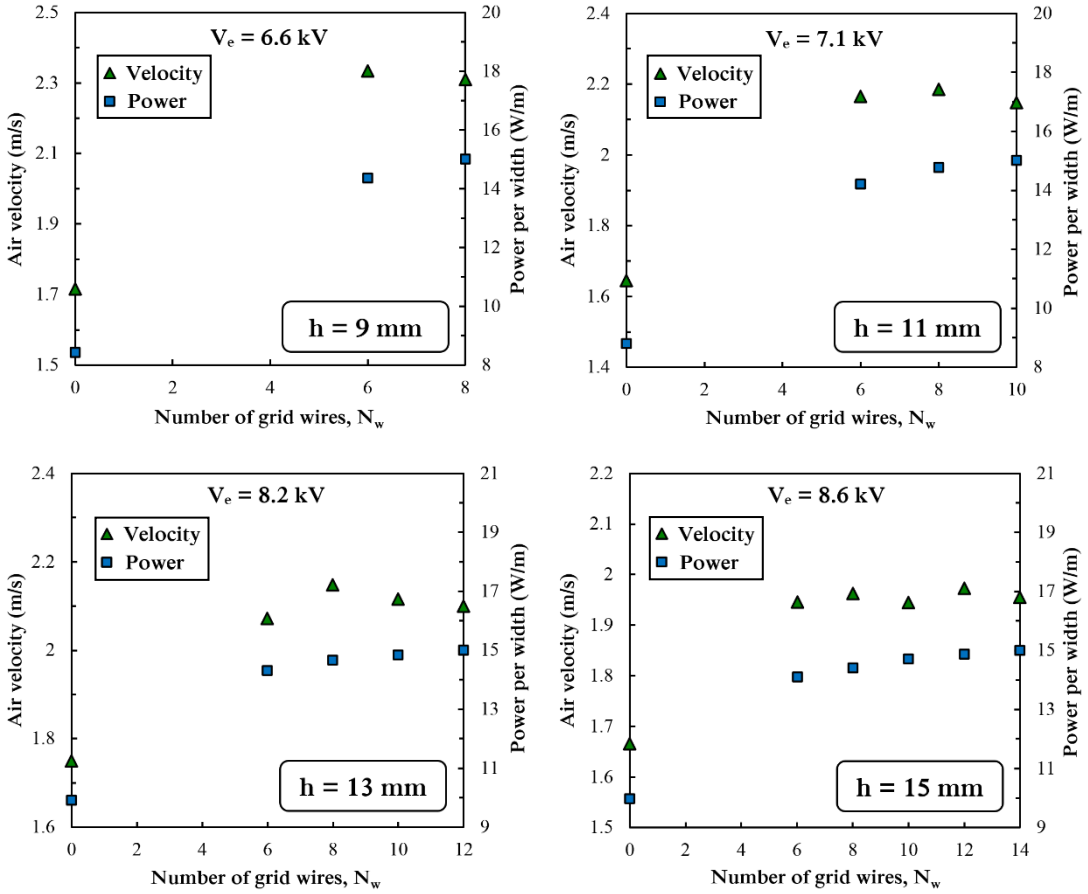

Figure 4.16 Effect of collecting grid density on average air velocity (left axis) and power consumption (right axis) for different blowers, each operated at a constant applied voltage required to fix the power at 15 W/m.

In order to reflect the impact of the grid density on the blower performance, the electromechanical efficiency of each blower was calculated at two levels of applied voltage, as shown in **Figure 4.17**. It shows that the efficiency of each blower at the two applied voltages reaches its highest values with a certain grid density before it tends to fall as the grid becomes denser. In all cases, using the grid as a further collecting electrode reveals higher blower efficiency over the case of a blower without a grid. The figures of the highest efficiency show that using coarse collecting grids with 6 and 8 wires for the thin and thick blowers, respectively, is effective and offers better blower performance, which agrees with previous recommendations presented in [104, 215].

This behaviour can be attributed to the balance occurring between the decrease in the grounded area and the increase in the spacing of flow paths through the grid. Indeed, the slight reduction in both the ion current and the impact of the body force due to decreasing the number of collecting wires can be compensated by a decrease in the pressure losses caused by the narrow flow paths through the grid wires. Based on these predicted results and from a design perspective, using coarse collecting grids offers better flow velocity and reduces the power consumption, the pressure losses and additionally the manufacturing complexity.

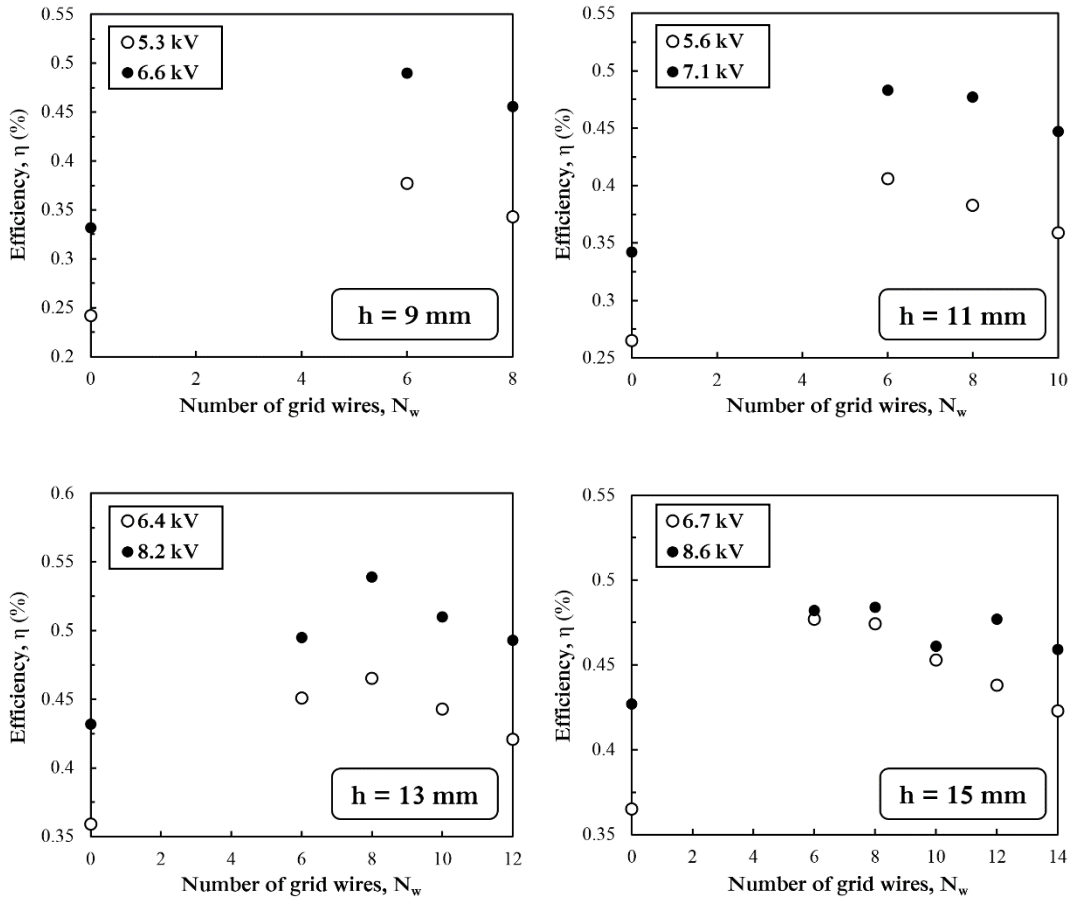

Figure 4.17 Effect of grid density on blower efficiency for different heights at two levels of applied potential required to fix the powers at 5 and 15 W/m in each blower.

4.6 Chapter Summary

This chapter presented 2D numerical models developed to investigate the influence of design and geometric parameters on the EHD flow induced using a wire-to-grid channel configuration. Based on the efficient locations of electrodes, design optimization was performed by fixing the applied voltage and operating power for a range of blower heights up to 15 mm. The effect, location and arrangement of the collector grid were investigated and showed significant effect on the blower efficiency and performance of EHD flow generation.

Based on the results achieved in this chapter and in order to develop EHD blowers for thinner applications and optimize the electrode configuration based on geometry scale, it is useful to remove the collector grid and exclude its effect on the blower performance and other design parameters. In the next chapter, the efficient length of collecting surfaces and their location from corona wire electrode using a classic wire-to-plane EHD blower will be investigated and optimized based on flow generation for lower profile heights using the optimization methods adopted in this chapter. Using the optimized blowers, further investigation on the blower width and EHD scaling laws, as well as the pumping performance will be included.

CHAPTER 5

Optimization and Development of Miniature EHD Blowers

5.1 Introduction

Design optimization is a critical factor in developing EHD devices and improving their performance and efficiency for practical implementation, where the thermal management requirements are essentially considered. It is well known that the optimization of any EHD device mainly depends on its geometry and the operating conditions, and is usually established based on airflow generation. However, when the electronic application cooled by an EHD blower is specified, further key design factors must be taken into consideration, including the blower size and thickness, the required flow rate, the limits of consumed power and the levels of applied potential.

Indeed, the term of design optimization based on thermal management considerations used throughout the thesis refers to the investigation of the optimal (or most efficient) electrode arrangements that ensure using the minimum possible levels of power or voltage while maintaining the pumping performance and flow production within the required levels, i.e., improving the energy conversion efficiency of the developed EHD blower. To the best of the author's knowledge, the present study is the first to optimize the geometry of miniature wire-to-plane EHD air blowers of thicknesses less than 10 mm for microelectronic applications based on the pumping efficiency and the level of operating conditions (power and voltage). Previous attempts used macro-scale geometries of similar configuration but did not include the levels of operating conditions in consideration. For example, Rashkovan et al. [155] studied the optimization of a macro-scale EHD blower using a wire of 0.2mm-diameter stretched and centred between two collecting plates (42 mm apart) and operated by a range of voltages from 9 to 23 kV. They suggested the optimal configuration shown in **Figure 5.1** based on the highest flow generation without

including any information regarding the conversion efficiency or the EHD operating power. However, although the optimal location of the corona wire found in their experiments can generate the highest velocity due to the small electrode gap, which is also the finding that has been borne out in this study as will be explained later in this chapter, the efficiency of this location is very low due to the significant associated power composition.

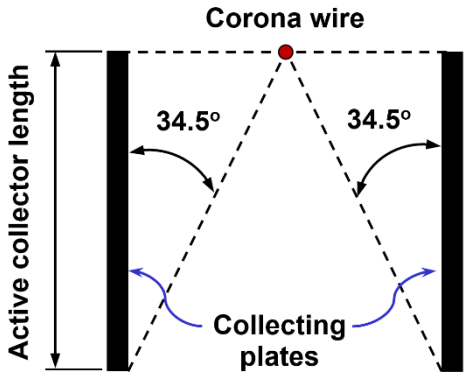

Figure 5.1 Optimal EHD blower configuration suggested in [155].

In this chapter, 2D numerical models are developed for a wire-to-plane EHD channel configuration to optimize the location and length of the collector electrode based on the efficient levels of operating voltage and power. Based on the optimization results, further 3D models are developed to evaluate the performance and flow characteristics of miniature EHD blowers, and investigate the effects of blower sidewalls on the magnitude and profile of the induced air velocity. A combined EHD blower is developed and a comparison against miniature rotary blowers based on device size, power consumption and flow rate is presented at the end of this chapter.

5.2 EHD Blower Geometry

The EHD channel geometry of the wire-to-plane configuration used in the present numerical investigation is shown in **Figure 5.2**. A corona wire of 0.025mm-diameter is centred between two parallel dielectric plates that form the flow channel with a length of 50 mm. The selection of a very fine wire diameter is recommended for use in compact EHD blowers, which enables creation of a strong electric field

using low levels of operating voltage. Two collecting surfaces of 10 mm length are assumed to be within the upper and lower channel walls, and located at a distance G downstream of the emitter wire. The modelling parameters used in the developed two- and three-dimensional simulations of the present investigation are the same of that used in the validation models presented in Chapter 3 for a similar channel configuration. The numerical analysis is established to explore the impact of the main design parameters on the efficiency of EHD air blowers and to optimize its geometry for ranges of fixed operating powers and applied positive voltages. These parameters include the location and length of the collecting surface from the emitter electrode for a range of blower heights (2 – 10 mm), as listed in **Table 5.1**. In the present 2D simulation, it is assumed that the EHD blowers are wide enough with negligible sidewall effects on the flow characteristics.

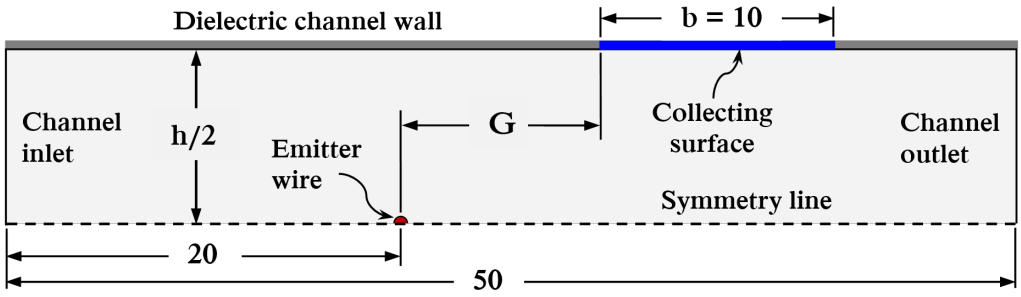

Figure 5.2 Half domain of the EHD blower geometry used in the present numerical investigation. Dimensions in millimetres.

Table 5.1 Geometric and modelling parameters of the present investigation.

Parameter	Value
Overall range of applied potential, V_e	2 – 17 kV (Positive)
Corona wire diameter, d	0.025 mm
Channel length, L	50 mm
Channel height, h	2 – 10 mm (in 2 mm steps)
Horizontal gap between electrodes, G	0 – 7 mm
Collecting surface length, b	3 – 17 mm

5.3 Optimization of EHD Blower

5.3.1 Optimization of the collector location

In this section, the prediction of the optimal collector location relative to the emitter electrode, which is defined by the horizontal electrode gap G, and its

influence on the EHD air blower performance are discussed. The electrode gap was changed from G = 0 to 7 mm (in 1-mm steps), whereas the blower height h was varied by five levels from 2 to 10 mm. It is important to bear in mind that the wire-to-plane EHD channel of a rectangular cross-sectional area is the most popular geometry proposed for integration in EHD cooling systems in thin electronic applications such as laptops, where the flexibility to control the blower thickness and width is required. In addition, the range of blower heights considered in this study lies within the thickness of current miniaturized and highly demanded consumer devices, where the performance of rotary fan degrades as the device dimensions reduce. Therefore, when the miniature EHD blowers are applied practically within cooling systems, both the operating power and the level of applied voltage represent critical factors in the thermal management considerations due to their impact on the produced airflow rate and the feasibility of practical implementation. In small form factor electronic applications, a compact high-voltage multiplier (usually on the order of kilovolts) must be integrated as part of the EHD system in order to initiate and sustain the corona discharge process, and generate EHD flow. The design of miniaturized, efficient, and low cost high-voltage multipliers represents one of the most integration and practical challenges [25]. From a design perspective, reducing the operating voltage to an efficient level for compact applications is important, and a delicate balance between reducing the applied voltage and improving the flow generation must be made carefully. Therefore, the design optimization of the EHD blower geometry will be performed based on pumping performance by fixing the operating power and the applied voltage at the corona wire for a range of blower thicknesses in order to predict the optimal and the most effective locations of the collecting surface.

5.3.1.1 The case of constant input power

For a range of fixed input power from 5 to 25 W/m (calculated per wire length), **Figure 5.3** illustrates how the collector location of different blower heights affects the outlet mean velocity and the applied voltage that corresponds to each level of input power. It can be seen that, for each height, both the ionic wind velocity and the applied voltage required to preserve the input power at a fixed level increase as the consumed power and the gap G increase. The figure also shows how

the blower height (or the vertical electrode gap) affects the magnitude of the outlet velocity, as will be discussed later. In fact, the increase in the horizontal gap and the associated potential improves the distribution and the directions of the enhanced electric field lines along the grounded surface, adding relatively higher kinetic energy to the horizontal components of the Coulomb force, which have the main impact of moving the ionic wind toward the channel outlet. However, the trends show that the increase in the air velocity becomes small after certain locations, regardless of the value of applied voltage, and can be neglected after G = 5 mm for all given levels of heights and input powers. Indeed, further increases in the electrode gap at a fixed operating power cause a decrease in the effective angle of the drifting region between the emitter and the collecting surface, leading to an increase in the applied voltage required and resulting in a modest enhancement in the ionic wind velocity.

In order to reduce the level of the applied voltage and determine the most effective location of the collecting surface for each height, the percentage increase of both the average air velocity and the applied potential was calculated for shorter steps of G and two levels of input power (the lowest and highest levels considered in this investigation), as shown in **Figure 5.4**. It can be observed that the percentage increase in the air velocity at the first step (G = 0.5 mm) over that generated at the location of G = 0, is higher than that of the required applied potential for all blower heights. However, the increase in the velocity tends to decrease with increasing G, compared to that of the potential, which (the latter) reaches its peak level at certain locations before it tends to drop. Following the same method used in the previous developed model of a wire-to-grid blower, it was found that when the increase in the potential reaches its peak, the percentage increase in the air production accounts for approximately 50% of that in the applied voltage, and all increases in the voltage beyond these gaps are relatively inefficient in improving the air velocity.

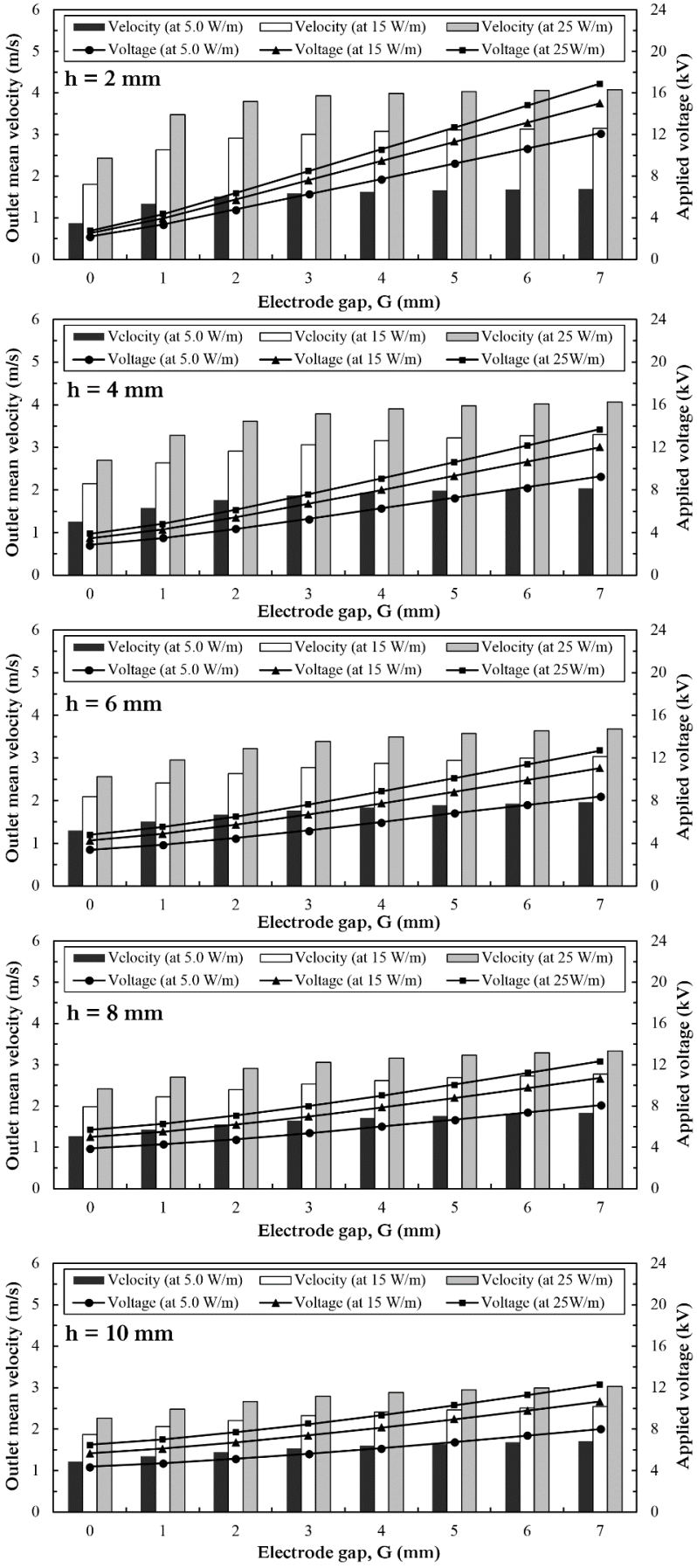

Figure 5.3 Variation of average air velocity and applied potential with the horizontal electrode gap, G, for different blowers and a range of fixed input power.

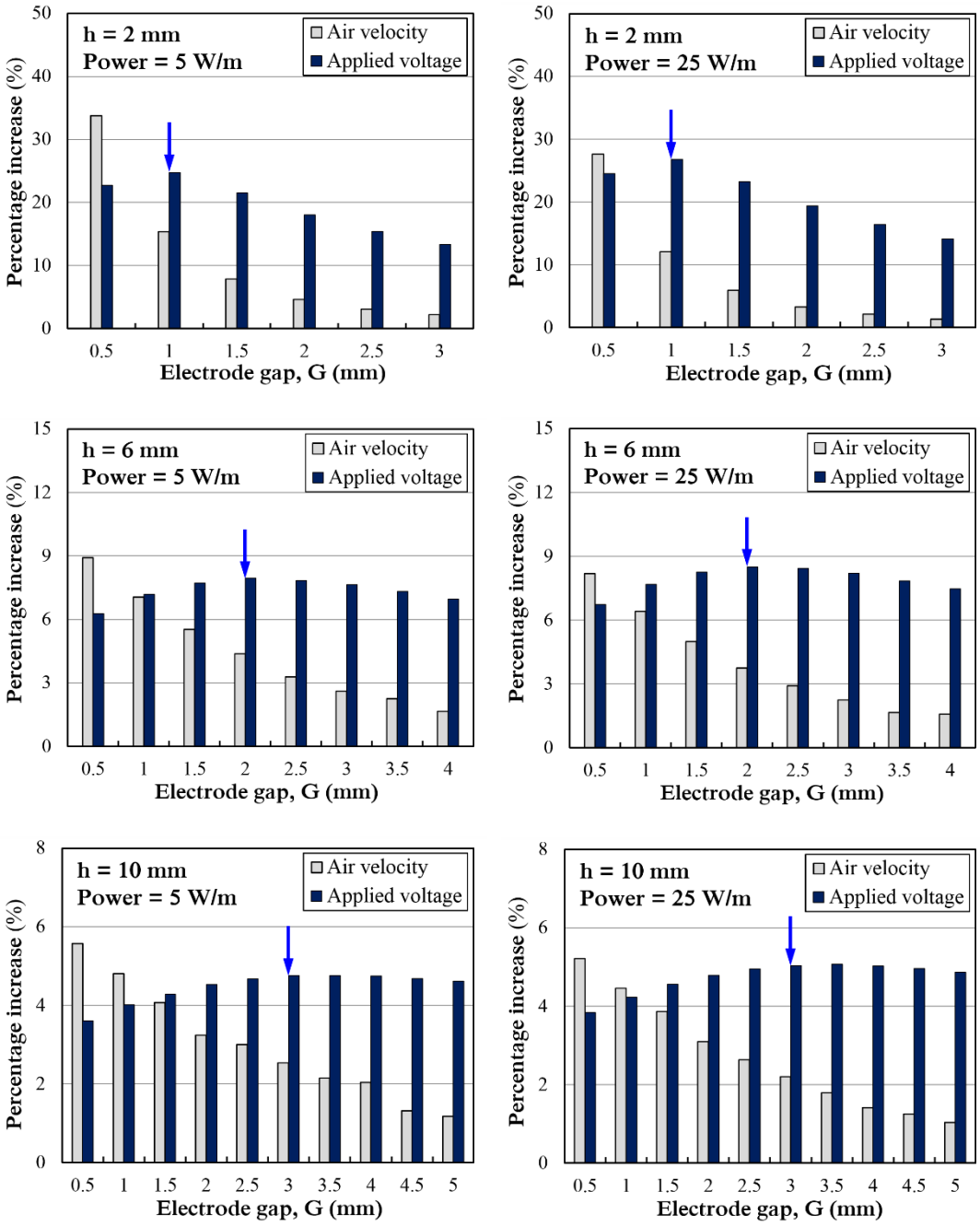

Figure 5.4 Effect of electrode gap on the percentage increase (each calculated over that of the former step of G) in both average air velocity and applied potential for different blowers at fixed input powers (5 W/m for left column and 25 W/m for right column). Figures for h = 4 and 8 mm are not shown.

Table 5.2 summarizes the total percentage increase in both the produced air velocity and the required applied voltage calculated at the predicted optimal locations over that at the initial location (G = 0), for two fixed levels of operating power. The increase in the required voltage is associated with approximately an equivalent improvement in the air velocity. However, further increases in the

electrode gap beyond the optimal locations do not lead to efficient balance in both voltage and velocity.

For example, although moving the collecting surface by 0.5 mm beyond the proposed optimal location in the blower of h = 2 mm improves the air velocity by approximately 6% – 8%, a significant relative increase in the applied voltage by more than 20% is required. Moreover, for the thicker blowers, increasing G by 0.5 mm leads to modest increases in the velocity by only 3% or less, regardless of the increases in the associated applied voltages, which are still higher (typically three times higher) compared to the corresponding velocity increases.

Therefore, the locations, which are indicated by arrows in **Figure 5.4**, can be considered as the optimal and the most effective gaps for the case of constant input power, and given by the following formula,

$$G_{\mathrm{P}} = (h/4) + 0.5 \tag{5.1}$$

where G_{P} is the optimal electrode gap (mm) for the case of constant input power, and h is the blower height (from 2 to 10 mm).

Table 5.2 Total percentage increase in the average velocity and applied voltage calculated at the optimal locations of different blowers for two levels of fixed operating power.

Blower height, h (mm)	**Optimal electrode gap, G_{P} (mm)**	**Operating Power (W/m)**	Total percentage increase over that at the initial location (G = 0)		Percentage increase calculated at one step (0.5 mm) beyond the optimal locations	
			Velocity (%)	**Voltage** (%)	**Velocity** (%)	**Voltage** (%)
2	**1.0**	5	49	47.5	7.8	21.5
		25	40	51	5.9	23
4	**1.5**	5	30.6	33.3	4.8	11.6
		25	26.2	36	4	12.5
6	**2.0**	5	26	29	3.1	7.9
		25	23.3	31	2.9	8.4
8	**2.5**	5	24.2	27.2	2.5	6
		25	22	28.8	2.3	6.3
10	**3.0**	5	23.2	25.7	2.1	4.8
		25	21.5	27.4	1.8	5.1

5.3.1.2 The case of constant applied voltage

In order to optimize the EHD blower geometry at a constant applied potential, an appropriate range of three operating voltages (increased by 1 kV) were applied for each blower height. Each range of applied voltage was chosen to be close to that required to fix the operating power (from 5 to 25 W/m) used in the previous optimization method. In this case, the optimal locations of the collector for each height can be estimated based on the EHD blower performance for a given range of operating voltage. Therefore, the electro-mechanical (or transduction) efficiency, which is the percentage of electrical power converted into mechanical (kinetic) power, is adopted using the set of equations (4.4) – (4.6), previously defined.

Figure 5.5 shows that the efficiency of each blower grows with increasing the horizontal gap G, reaching its maximum value before it tends to drop or maintain its value at the low applied voltage, or show a slight increase at a higher potential as the blower becomes thicker. As mentioned in the previous section, moving the collector electrode toward the outlet direction can enhance the distribution of the electric field lines and improve the kinetic energy imparted to the flow by the horizontal components of the Coulomb force. However, further increases in the gap at a given applied potential reduce the impact of the electric field, especially for the thin channels, due to the reduction in the effective collector area. In addition, the trends reveal that the blower efficiency increases as the blower height increases for all applied voltages, reaching its highest values at the highest applied voltages.

Indeed, as the duct becomes thicker and the applied voltage increases, the electric field lines across the electrodes can be strong enough with a wider effective drifting angle to reach a larger area of the collecting surface, compared to the thinner ducts, leading to a better ionic wind generation associated with relatively low power consumption.

Therefore, the locations that show the highest EHD blower's efficiency for the range of applied voltage, which are identified in **Figure 5.5** by dashed lines, can be considered as the optimal gaps, although modest increases in the efficiency can be observed beyond them at the highest applied voltage. These locations can be simply given by the following formula,

$$G_V = (h/2) - 0.5 \tag{5.2}$$

where G_V is the optimal electrode gap (mm) at a constant applied voltage, and h is the blower thickness (from 2 to 10 mm).

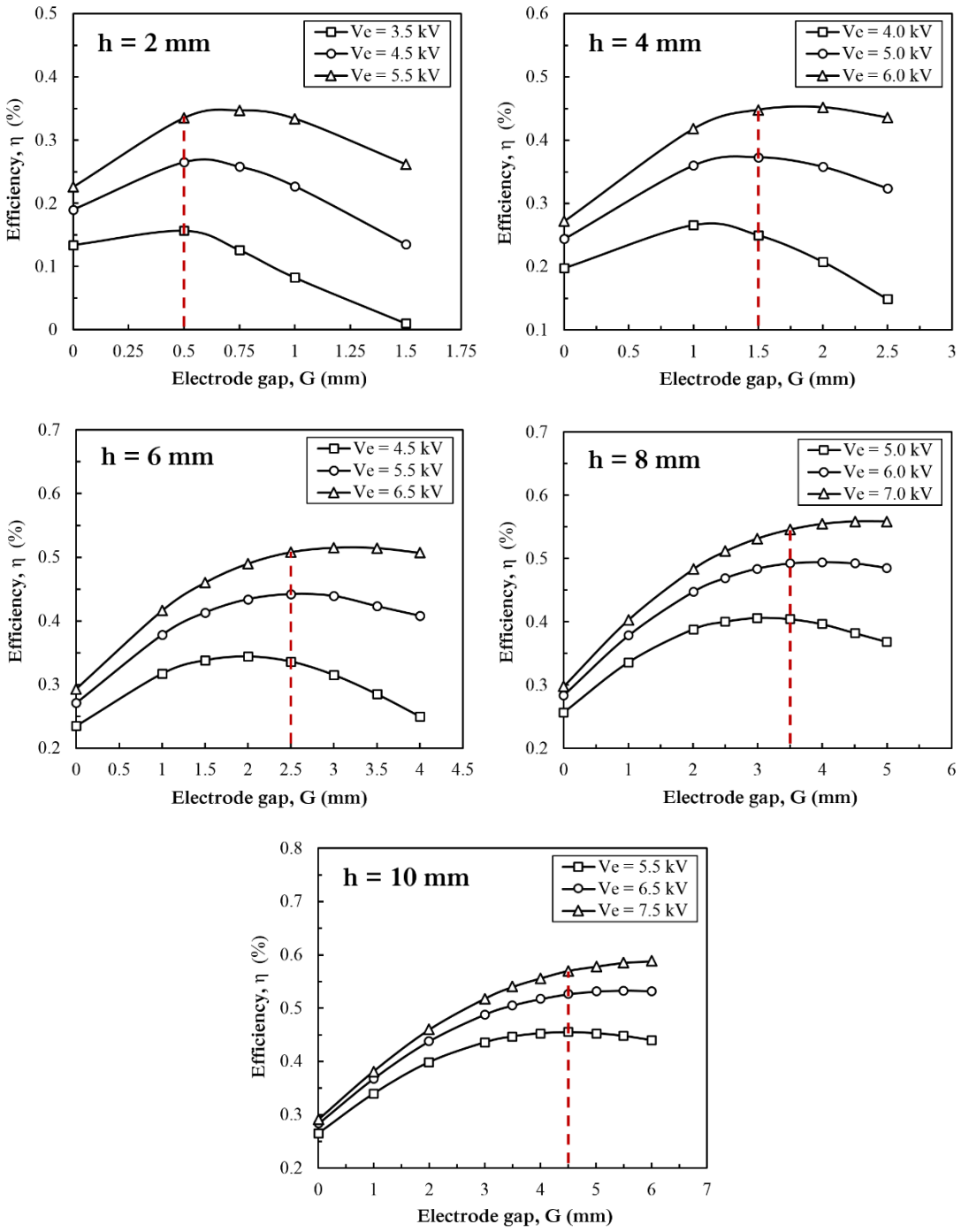

Figure 5.5 Effect of electrode gap on the electro-mechanical efficiency for different blowers at fixed applied voltages.

It is useful to state that the difference in the optimal collector locations in both cases is mainly attributed to the optimization method used in each case. In the first method, the level of input power is fixed, whereas the ion current decreases and the applied voltage increases with the electrode gap. In contrast, the second method has fixed applied voltages, whereas the ion current and thereby the consumed power decrease with increasing electrode gap. Therefore, when the practical application is mainly controlled by a limited range of operating power, regardless of the level of applied voltage, the selection of the first optimization method is recommended, whereas the second method offers the best predicted efficiency of the EHD device when its operating voltage is limited.

5.3.2 Optimization of the collector length

In the previous section, the optimal locations of the collecting surface were estimated with a fixed length of b = 10 mm. However, the effective collector length is not equal for all presented cases but depends on its location (the horizontal electrode gap), the blower height (the vertical electrode gap), and the level of applied potential (the electric field strength). Therefore, the effective collector length can be determined at its optimal location for each blower thickness, based on both operating methods. The highest values of the power and applied potential used in each optimization case were adopted in order to create the strongest electric field across the electrodes, and also to ensure the validity for lower operating levels.

Figure 5.6 shows the influence of the collector length on the ion current created at a fixed input power of 25 W/m (generated by a range of corresponding voltages from 4.3 to 8.5 kV), and a fixed applied voltage (in a range from 5.5 to 7.5 kV), for different blower heights. It can be observed that the effective collector length increases as the blower becomes thicker for both operating methods. For example, the collector length required for the blower of h = 2 mm at a fixed power is 3 mm, and there is no effect on the corona current beyond this length, whereas the blower of h = 10 mm requires a collector with a length of at least 15 mm before being independent of the created current.

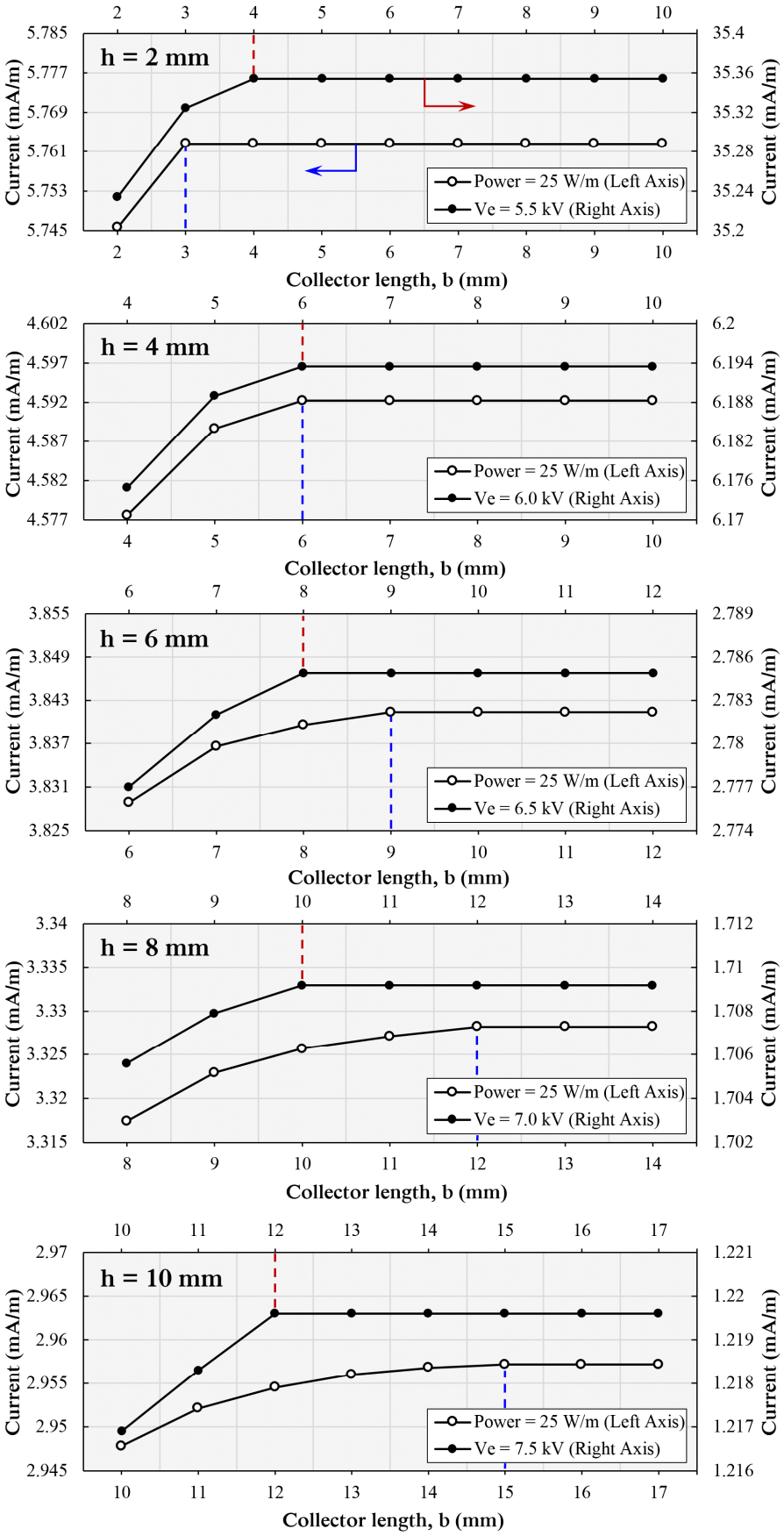

Figure 5.6 Effect of collector length on the discharge current created by different optimized EHD blowers using the two operating methods.

This behaviour is due to the change in the effective drifting angle of charged ions across the electrodes, which increases as the blower height (or the vertical electrode gap) increases, as shown in **Figure 5.7**. The trends also reveal that the maximum effective length of the collector electrode for each blower differs depending on the method of applying voltage. Indeed, this change is due to the difference in the level of applied voltage and the optimal collector location defined by equations (5.1) and (5.2).

The predicted results indicate that extending the collector electrode over certain lengths does not have any impact on the ion current and the generated ionic wind, within the overall range of operating voltage used in the present investigation. The dashed lines in **Figure 5.6** indicate the maximum effective lengths required for each optimized blower based on each optimization method, and can be defined by the following expressions,

$$b_{\mathrm{P}} = 1.5\,h \tag{5.3}$$

$$b_{\mathrm{V}} = h + 2 \tag{5.4}$$

where b_{P} and b_{V} are the maximum effective lengths (each in mm) for the cases of constant power and applied voltage, respectively, and h is the blower thickness (2 – 10 mm).

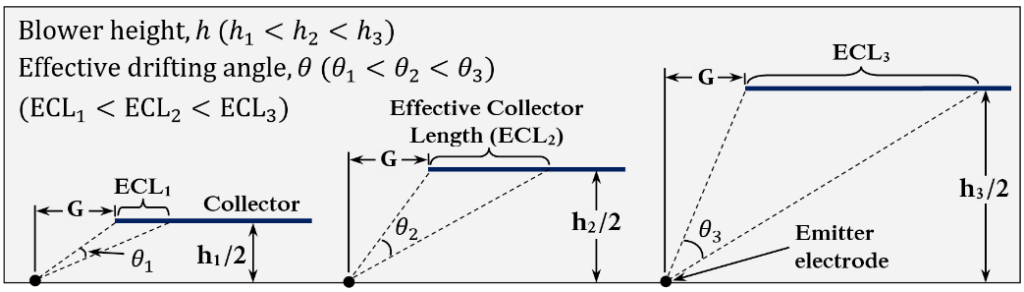

Figure 5.7 Effect of blower height, h, on the effective drifting angle, θ, created between the emitter electrode and the effective collector length.

From a design perspective, reducing the collector to its effective length in the thin EHD blowers offers further miniaturization in size, which is beneficial in space constrained applications. In addition, using the whole effective length of the collecting surface in the thicker EHD pumps can enhance the heat removal from the channel walls when the heated surface is used as a collector electrode in heat transfer applications.

Figure 5.8 illustrates and summarizes the optimal electrode gaps, G, and the maximum effective lengths, b, of the collector electrode predicted using the two operating methods for the range of blower heights considered in this study.

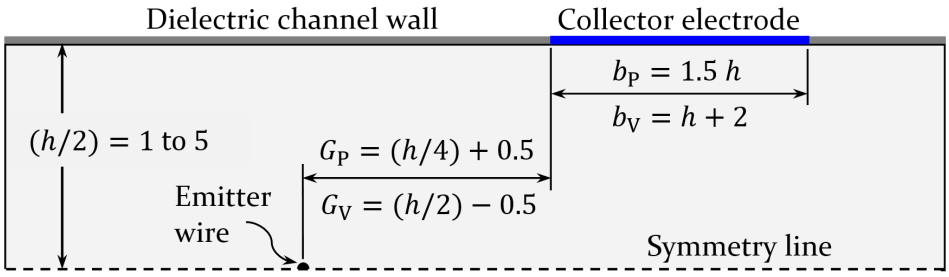

Figure 5.8 Optimal electrode gaps, G, and the maximum effective lengths, b, of the collecting surfaces for the two cases of operating method. Dimensions in millimetres.

It is useful to state that the design optimization implemented in this chapter to achieve the most efficient electrode arrangement does not represent a global optimisation due to the restricted ranges of geometric parameters and operating conditions. Therefore, the predicted optimal design parameters from equations (5.1) – (5.4) are only valid for the wire-to- plane EHD channel configuration using the corona wire diameter adopted in this investigation within the ranges of blower heights and levels of operating conditions. However, using thicker corona wires of diameters larger than 25 μm will decrease the electric field strength created across the electrodes and the resultant airflow. In this case, these equations can be used as a reference to determine the maximum electrode gaps and collector lengths for the given range of blower heights.

Moreover, using thicker emitter wires leads to lower efficiency and a significant increase in the voltage required to generate a given flow rate in miniature EHD blowers, which is practically undesirable. On the other hand, although using finer corona wire is possible but more complex in practical integration, the presented

equations here can also be used as a useful baseline to predict the optimal design parameters (the electrode gap and collector length) using the same EHD geometry, which are expected to be higher in values due to the stronger electric field created.

Regarding the application of the investigated blowers based on the considered range of heights, the thicker optimized EHD blowers (h = 6 – 10 mm) can be used in small-scale and thin consumer devices such as laptops to cool heat sinks of equivalent thickness. Unlike conventional fans, the height of EHD blowers is independent of the length and width dimensions, offering an attractive geometric flexibility so that one can shorten the length and extend the width as required. For the thinner optimized blowers (h = 2 – 4 mm), a set of multiple wires can be integrated as emitter electrodes with a grounded plate-fin heat sink and positioned at the predicted optimal locations to generate effective cooling airflow through the fin channels, even at low velocities. In this case, the wire diameter, the level of operating voltage, and the power consumption are critically important factors to be accounted for practical cooling solutions.

5.4 Influence of the Blower Height

Figure 5.9 shows the effect of both the operating input power and blower thickness on the average air velocity generated by different optimized EHD blowers. The trends reveal that the air velocity produced by each blower increases with increasing the power and decreasing the blower height. When the power increases at a given electrode gap, the impact of the electric field and the electrostatic forces becomes stronger and can impart higher kinetic energy into the flow, leading to an enhanced ionic wind generation, as shown in **Figure 5.9**(a).

However, at a given fixed power, the ionic wind production decreases as the blower becomes thicker, although both the required potential and the optimal location steps of the collector toward the outlet direction increase with the height, as shown in **Figure 5.9**(b). Indeed, the increase in the blower height or the vertical distance between the electrodes leads to an increase in the vertical components of the Coulomb force, causing a reduction in the flow production toward the desirable direction. The blower of h = 2 mm shows different behaviour at low input powers among other heights due to the short effective length of its collector.

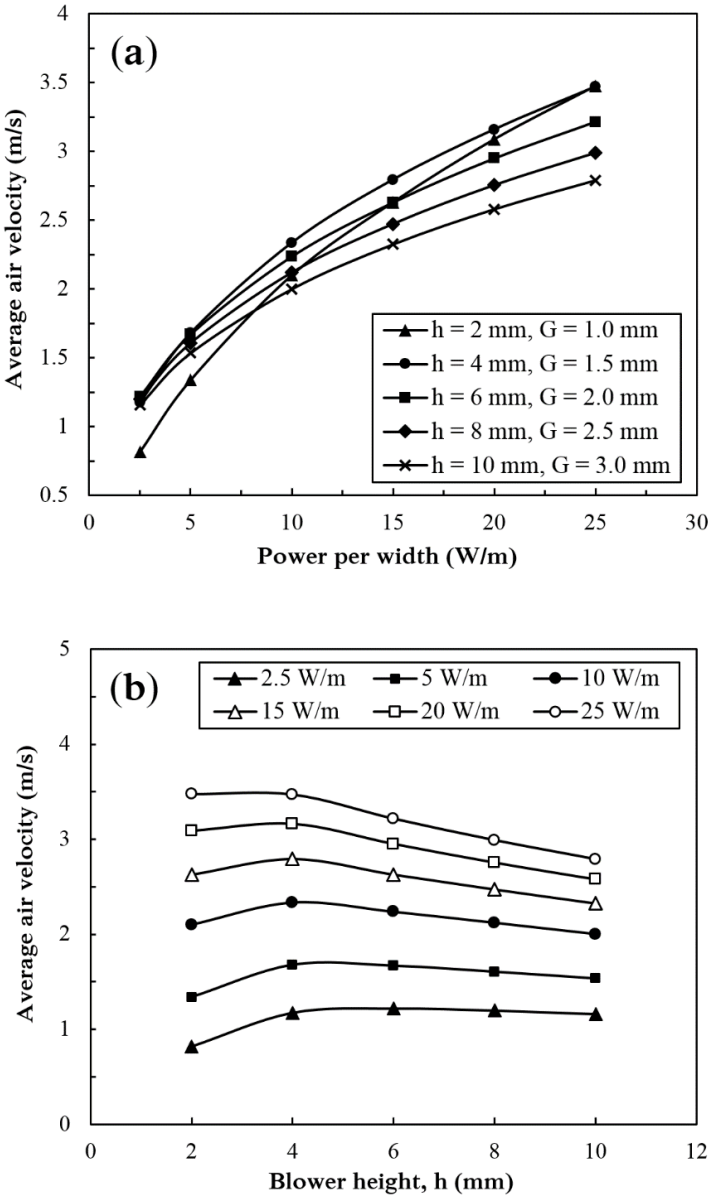

Figure 5.9 Effect of (a) input power and (b) blower height, on outlet average air velocity.

5.5 Scaling Laws for Optimized EHD Blowers

Airflow performance scaling laws for EHD blowers have been first investigated by Jewell-Larsen et al. [164]. Based on experiments and numerical modelling, they demonstrated that EHD air movers can be considered to be an ideal pressure source by neglecting the internal flow resistance of the EHD duct. Moreover, they presented scaling law relations as a function of the width, thickness, and operating power of the device to predict airflow rates and static pressures of

EHD air blowers. Their results showed that the scaling laws of the EHD-driven flow devices can be expressed as follows,

For the airflow rate, $$Q \propto (Power)^{1/3}\ h^{2/3} \tag{5.5}$$

For the static pressure, $$\Delta P \propto \left(\frac{Power}{h}\right)^{2/3} \tag{5.6}$$

Following these scaling laws of the ideal EHD flow device, **Figure 5.10** shows both the flow rate and static pressure as functions of the power density for a range of blower heights. The power density of each term can be calculated from equations (5.5) and (5.6), respectively, assuming that a constant transduction efficiency relates the mechanical (4.5) and electric (4.6) powers [164], with including the blower width, w. The predicted results of flow rate and static pressure of various optimized blowers show good agreement with those expected from the scaling laws as the data of all heights falls onto a straight line. This indicates that the proposed optimal collector location of each blower height of the present configuration is valid to provide an airflow performance that lies within the scaling laws of ideal EHD flow devices.

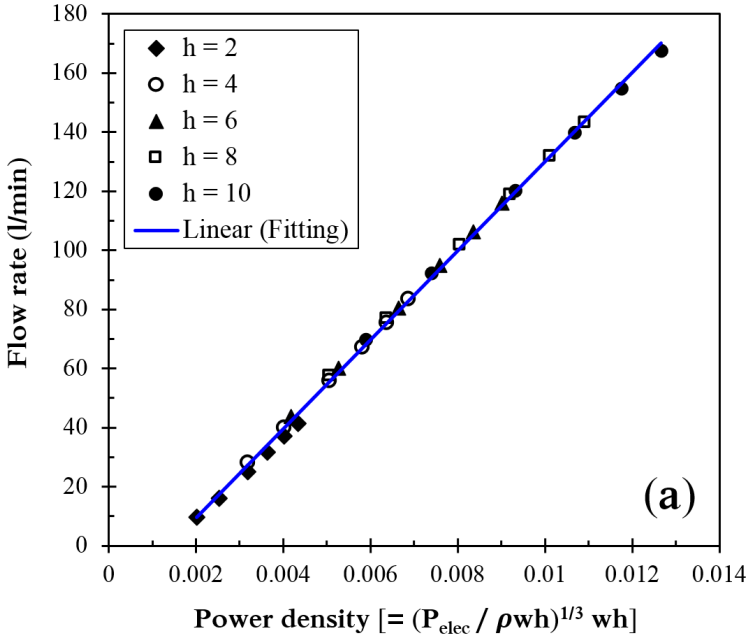

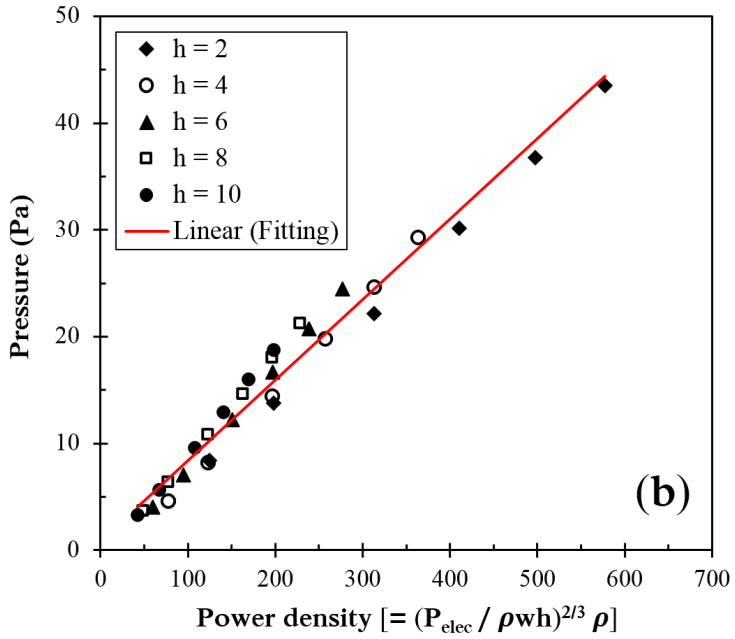

Figure 5.10 Power density related to the scaling laws of ideal EHD devices vs. (a) flow rate and (b) static pressure, for different optimized EHD blowers.

5.6 Dimensionless Analysis

In order to provide better understanding and allow a logical analysis of the results for efficient designs, it is useful to represent the power conversion efficiency of optimized EHD blowers based on non-dimensional groupings of EHD flow. Basically, the dimensionless parameters of EHD flow were derived based on the fundamental governing conservation equations, and they typically contain critical influential parameters such as the working fluid properties and operating conditions that highly related to the performance and pumping efficiency of EHD devices [216, 217]. In this section, three non-dimensional parameters, namely, the electric Reynolds number (Re_{E}), the electric slip number (Esl), and the electric source number (Es), are introduced to reflect their influence on the power efficiency of different EHD blowers optimized based on a fixed operating power, and can be defined as [217],

Electric Reynolds number, $$Re_{\mathrm{E}} = \frac{\varepsilon\, u_{\mathrm{o}}}{\sigma\, d_{\mathrm{P}}} \tag{5.7}$$

Electric slip number, $$Esl = \frac{\mu_{\mathrm{p}}\, V_{\mathrm{e}}}{d_{\mathrm{P}}\, u_{\mathrm{o}}} \tag{5.8}$$

Electric source number, $$Es = \frac{q\, {d_{\mathrm{P}}}^2}{\varepsilon\, V_{\mathrm{e}}} \tag{5.9}$$

where ε is the is permittivity of air (≈ 8.854×10^{-12} F/m), u_{o} is the average outlet air velocity (m/s), σ is the electrical conductivity of air (≈ 3×10^{-15} S/m at 20 °C [218]), V_{e} is the applied voltage at corona wire (V), μ_{p} is the positive ion mobility of air (= 2.1 m^2/V.s), q is the space charge density at corona wire (C/m^3), and d_{P} is the electrode gap (m). For the investigated EHD air blowers of a wire-to-plane configuration, the electrode gap (d_{P}) is defined as the actual distance between the emitter wire and the edge of collecting surface at the channel wall (m), and is calculated for each blower based on its height (h = 2 – 10 mm) and optimal horizontal electrode gap (G_{P} = 1 – 3 mm) as following,

$$d_{\mathrm{P}} = \sqrt{(G_{\mathrm{P}})^2 + (h/2)^2} \tag{5.10}$$

Indeed, the electric Reynolds number reflects the characteristics of the EHD flow such as the efficiency of energy conversion, and is defined as the ratio of the charge convection by flow to that for charge relaxation by ohmic conduction. The electric slip number indicates the relative motion of the injected charges with respect to the induced fluid velocity, while the electric source number is established based on the analogy between electrostatics (Poisson's equation) and heat conduction (Fourier equation) [217, 219].

The simulated EHD airflow is induced using a channel of different heights (2 – 10 mm) and fixed length and width of 30 and 100 mm, respectively, under a condition of fixed operating power ranged from 0.25 to 2.5 W. The power efficiency (power output to power input), previously defined by (4.4), is adopted as an indicator to reflect the effect of the non-dimensional parameters (Re_{E}, Esl and Es) on the efficiency of each optimized EHD blower.

Figure 5.11 shows the power conversion efficiency as a function of the electric Reynolds number, Re_{E}, for different EHD blowers. The trends reveal that the efficiency of each blower increases with increasing Re_{E}, which is due to the increased power (or corresponding applied voltage) that improves the electrostatic forces and air velocity induced at constant values of electrode gap, permittivity and electrical conductivity. In addition, the results show that the efficiency increases as the blower becomes thicker at given Re_{E} and operating power, although the electrode gap increases and the induced air velocity relatively decreases. Indeed, this is attributed to the increase in the flow rate due to the blower height, which is related to the mechanical (input) power of the efficiency equation (4.4). Moreover, as the electrode gap increases with the blower height, where the increase in the applied voltage becomes less effective to improve air velocity over the range of operating power, the thinner blowers show wider range of Re_{E} compared to thicker ones. The trends of the investigated blowers illustrate that the thicker blowers (h = 6 – 10 mm) have approximately equivalent efficiency at the highest levels of power regardless of the values of Re_{E}.

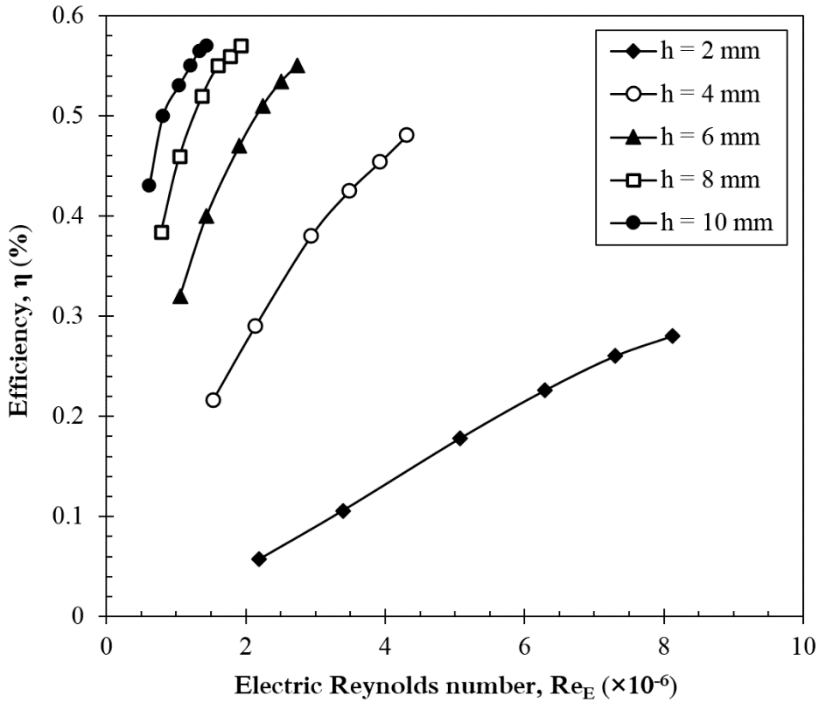

Figure 5.11 Power conversion efficiency as a function of electric Reynolds number calculated for different optimized EHD blowers for a range of operation power (0.25 – 2.5 W).

Figure 5.12 shows how the electric slip number, Esl, affects the power conversion efficiency at a constant value of ion mobility. For a given blower height and fixed electrode gap, the trends reveal that the efficiency decreases as Esl increases, indicating that the increase in the applied voltage required for fixing the operating power is higher than the increase in the produced air velocity, leading to lower efficiency. This observation is consistent with the trends of voltage and velocity shown in **Figures 5.3 and 5.4** previously presented in this chapter for the case of constant power, and is in agreement with a previous statement reported based on Esl number in [217]. Results based on blower heights indicate that the thicker blowers are more efficient and have lower values of Esl due to their higher flow rates and larger electrode gaps, respectively, although they require higher levels of corresponding voltage compared to thinner blowers.

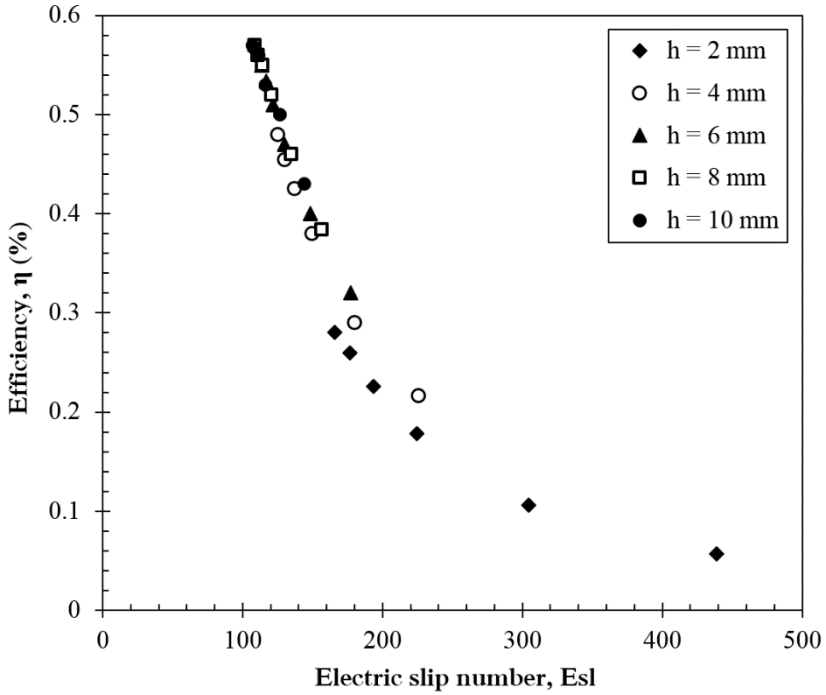

Figure 5.12 Power conversion efficiency as a function of electric slip number calculated for different optimized EHD blowers for a range of operation power (0.25 – 2.5 W).

The effect of electric source number, Es, on the blower efficiency is shown in **Figure 5.13**. The trends of each blower show obvious increase in the efficiency as Es increases, which is due to the effective increase in the space charge density over

the applied voltage at constant values of electrode gap and permittivity. As the blower height and the associated electrode gap increase, the overall curve of efficiency versus Es reveals a continuously growth, showing again that the thicker blowers are more efficient due to their higher flow rates than the thinner ones at a constant operating power.

However, the associated applied voltages required to fix the level of operating power are significantly higher in the thicker blowers due to their larger electrode spacing. For example, the voltage required to fix the power at 2.5 W in the blower of h = 10 mm is approximately 100% higher than that required by the blower of h = 2 mm to fix the power at the same level. Based on these results and in order to improve the efficiency of the thinner EHD blowers adopted in this investigation, a design of combined EHD blower of thin channels that require low levels of voltage and allow increased flow rates will be developed and investigated later in this chapter.

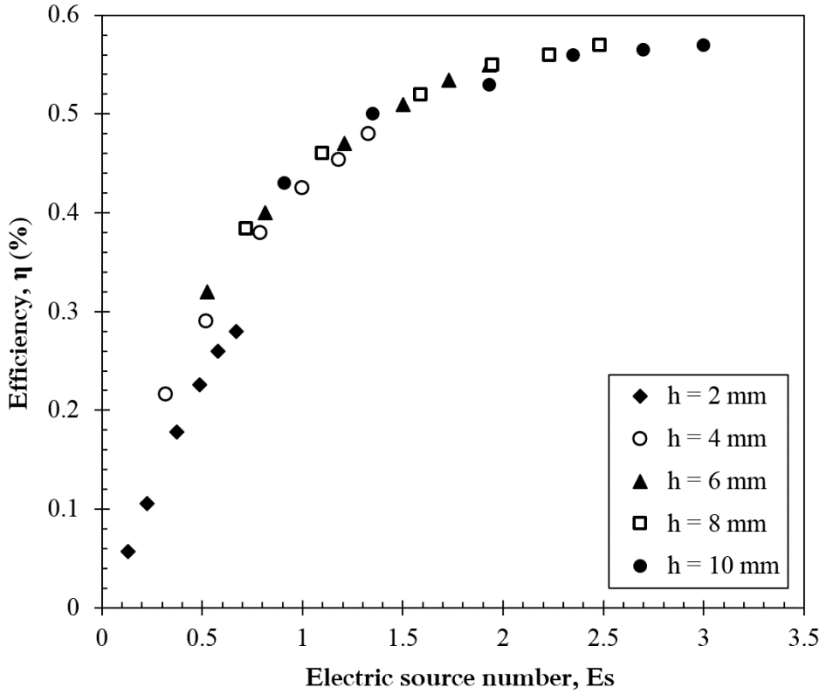

Figure 5.13 Power conversion efficiency as a function of electric source number calculated for different optimized EHD blowers for a range of operation power (0.25 – 2.5 W).

5.7 Influence of Blower Width

This section discusses the impact of the blower sidewalls on the air velocity profile and magnitude for a range of channel widths. It also studies the accuracy of the 2D numerical models to predict flow rates compared to the 3D modelling, where the friction losses due to channel sidewalls are included. To the author's knowledge, this is the first 3D numerical investigation of the impact of the channel sidewalls on the flow characteristics for narrow EHD ducts, although the 2D simulation of EHD flow performed in previous studies has shown acceptable agreement against experimental data for wide flow channels. Due to limitations caused by the large solution memory required for the 3D modelling of thick domains (thicker than 6 mm), only blowers of h = 2 and 6 mm are considered in the present investigation. The optimal location and length of the collecting surface were assigned according to equations (5.1) and (5.3), whereas the length of each blower was reduced to 20 mm and the blower width was varied between 10 and 60 mm.

Figure 5.14 illustrates the effect of the channel sidewalls on the outlet average velocity generated by each EHD blower at a fixed operating voltage that corresponds to 15 W/m input power used in the 2D simulation, showing the percentage decrease in the velocity magnitude for each blower width compared to that predicted by the 2D simulation. It is important to mention that fixing the operating voltage ensures that the generated air velocity through each blower remains constant regardless of the blower width, and any change in its magnitude is only caused by the effects of blower sidewalls.

Although there are slight differences between the values of percentage decrease at a given width of both blowers, the actual impact of the flow losses are different and can be determined based on the blower aspect ratio, which is defined by the ratio of the blower height to its width (h/w). For instance, the blower of h = 2 mm with an aspect ratio of 0.2 (at w = 10 mm), leads to a reduction in the velocity by 5.5% lower than that predicted by the 2D simulation, compared to an approximately 3% reduction for a blower of equivalent aspect ratio with h = 6 mm and w = 30 mm.

However, the figures demonstrate that the influence of the flow resistance through shortened and thin EHD blowers decreases and can be neglected as the blower becomes wider (or the aspect ratio decreases). This indicates that using 2D

modelling for short and wide EHD blowers is valid to predict flow rates effectively compared to that obtained by the means of the 3D simulation. The results of the 3D numerical solution for the velocity distribution through narrow and wide EHD blowers with h = 2 and 6 mm are displayed in **Figure 5.15**, showing that the induced flow at the exit of both blowers has uniform velocity gradient and the impact of flow resistance is insignificant.

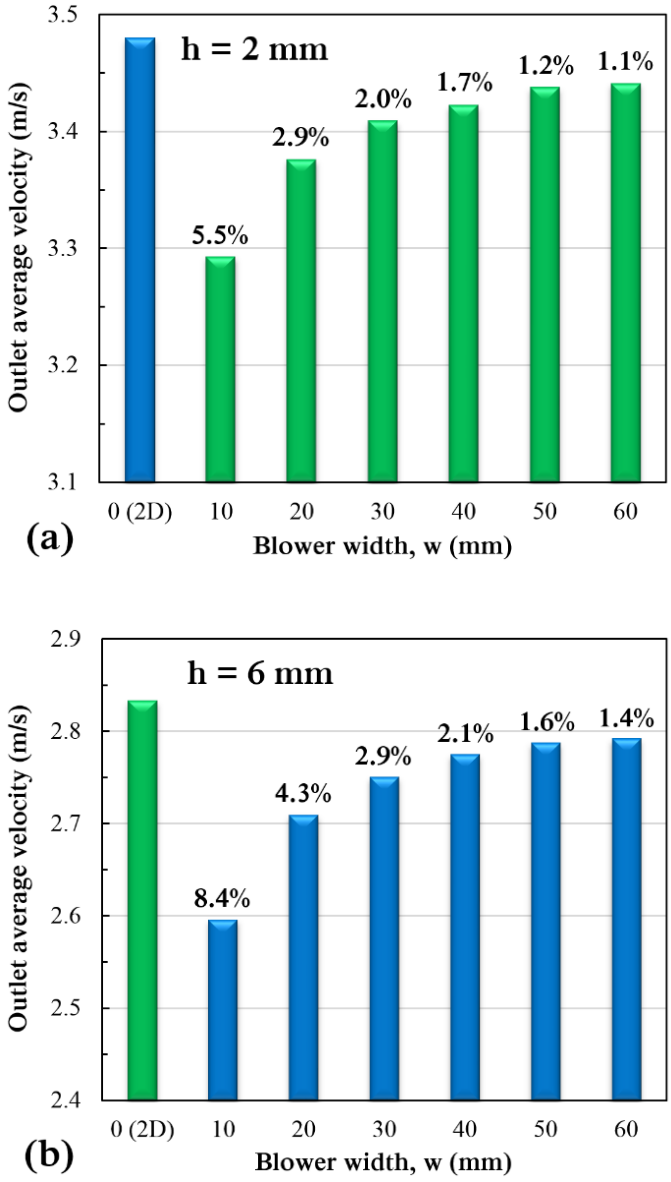

Figure 5.14 Influence of blower width on the average outlet velocity generated in 3D modelling at a fixed operating voltage, showing the percentage decrease in the velocity magnitudes compared to the 2D results for optimized blowers of (a) h = 2 mm at ≈ 3.9 kV, and (b) h = 6 mm at ≈ 5.7 kV, each with 20 mm long.

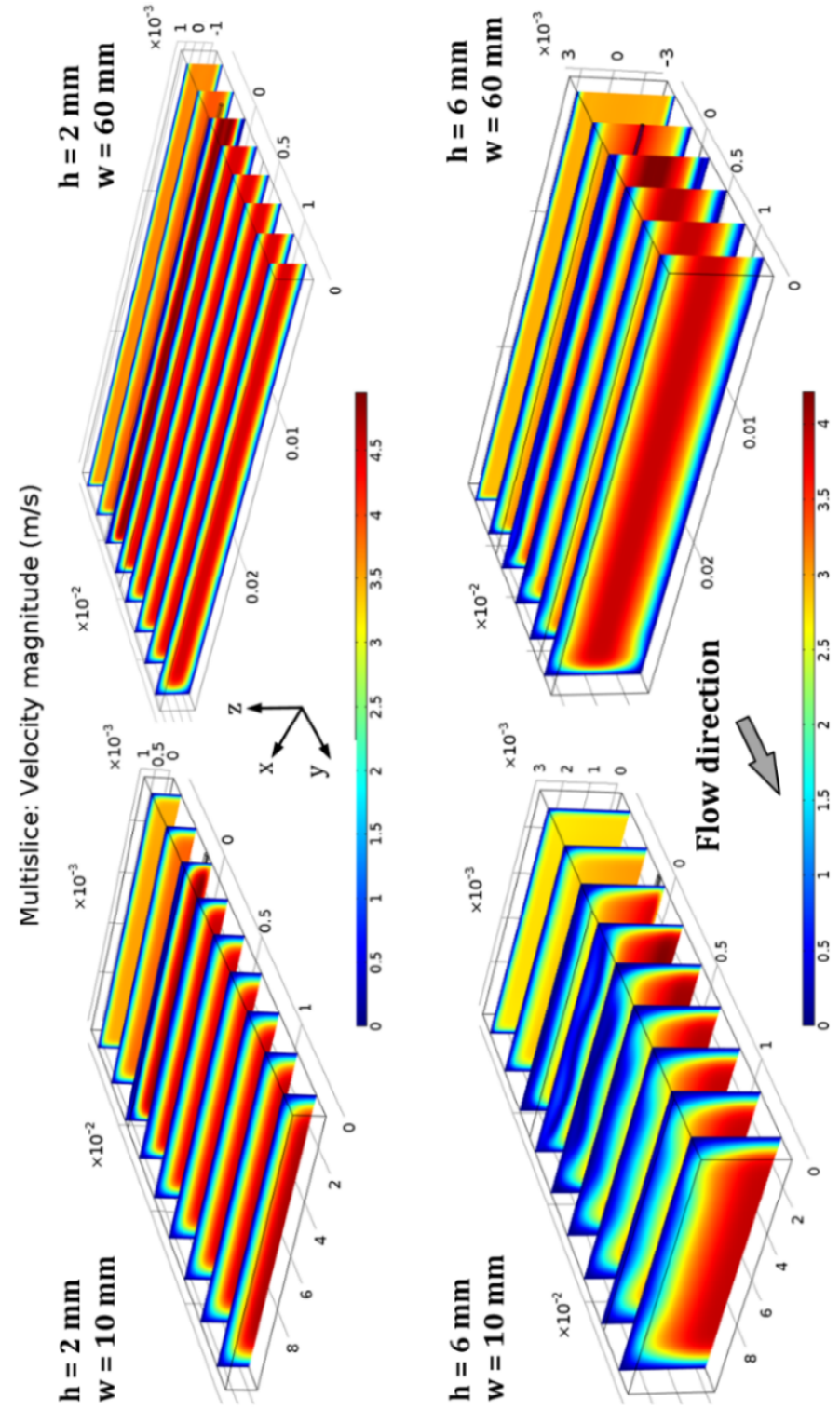

Figure 5.15 Velocity distribution induced at a fixed operating voltage that corresponds to 15 W/m, through narrow and wide optimized EHD blowers for h = 2 mm (top) and h = 6 mm (bottom). Dimensions in metres.

Figure 5.16 shows that the outlet velocity profile is uniform and has a parabolic distribution along the vertical *y*-*z* plane (at x = 30 mm) for the both wide blowers considered in **Figure 5.15**, based on the coordinate system shown in **Figure 5.17**.

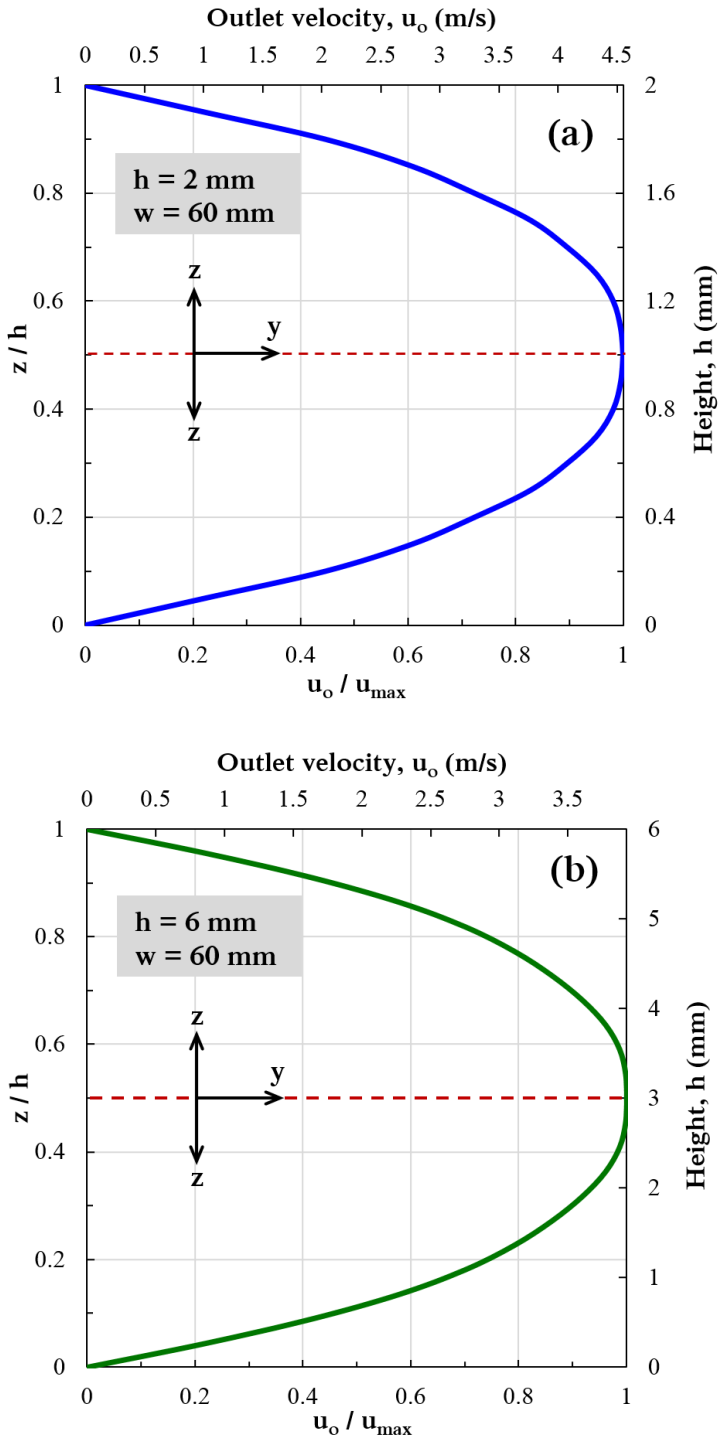

Figure 5.16 Normalized velocity profiles in the central vertical *y*-*z* plane (at $x = w/2$), along the blower outlet of (a) h = 2 mm and (b) h = 6 mm.

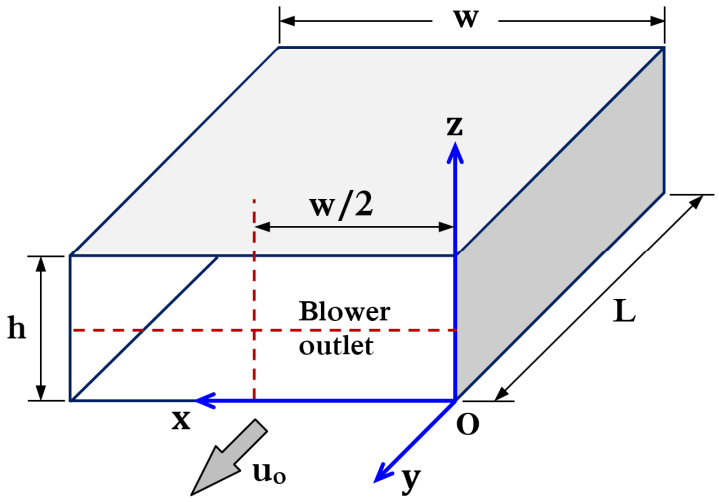

Figure 5.17 Schematic diagram of the rectangular EHD blower's coordinate system.

Figure 5.18 shows the velocity distribution on different *x*-*y* planes along the blower width for the two blowers considered here. For the thinner blower of h = 2 mm, it can be seen that the outlet velocity profile is similar (flat) for all selected planes (at z = 0.25, 0.5 and 1 mm), whereas the velocity magnitude is affected by the friction losses at the sidewalls (along the *x*-axis) and the bottom and upper walls (along the *z*-axis) of the blower, as shown in figures 5.15(a) and (b). The same behaviour is observed for the thicker blower of h = 6 mm, but with a slight disruption in the top-hat profile at the regions close to the upper and bottom walls (z = 0.5 and 1 mm), as shown in figures 5.15(c) and (d). This can be attributed to the impact of the electric field distribution caused by the increase in the vertical components of the Coulomb force as the blower becomes thicker.

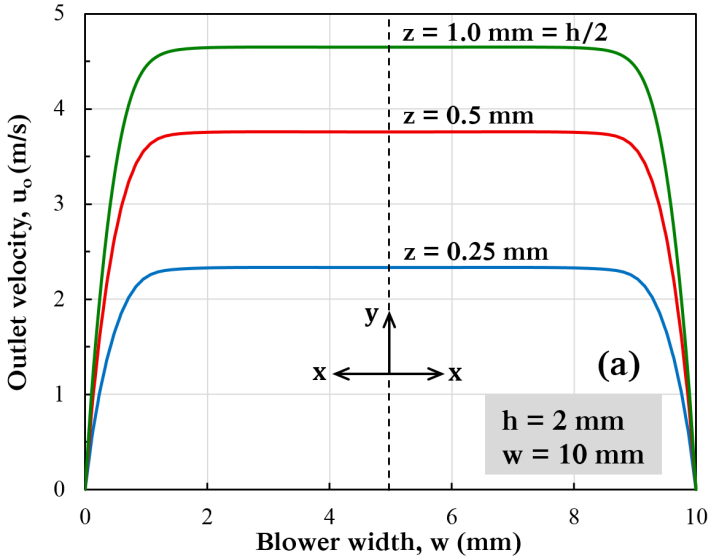
z = 1.0 mm = h/2
z = 0.5 mm
z = 0.25 mm
y
x
x
(a)
h = 2 mm
w = 10 mm
Outlet velocity, u_o (m/s)
Blower width, w (mm)

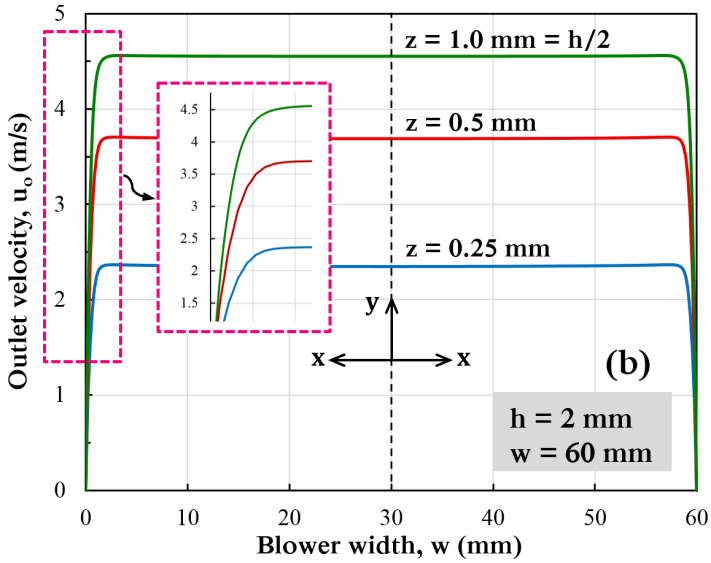
z = 1.0 mm = h/2
z = 0.5 mm
z = 0.25 mm
y
x
x
(b)
h = 2 mm
w = 60 mm
Outlet velocity, u_o (m/s)
Blower width, w (mm)

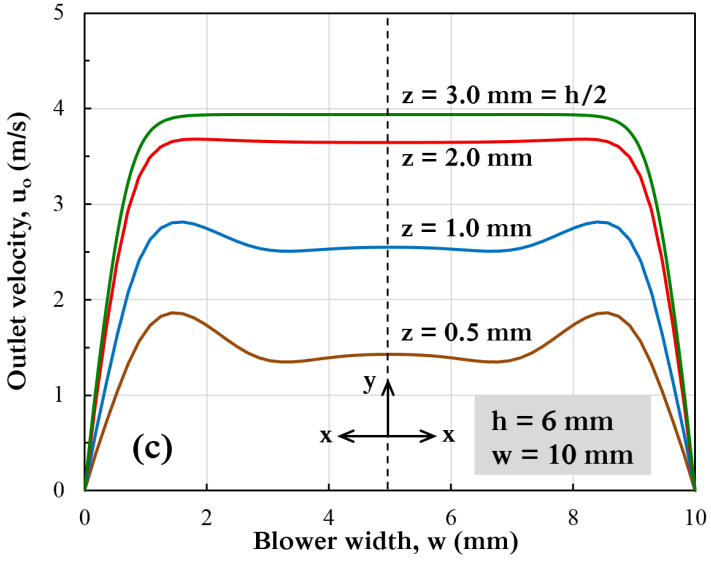
z = 3.0 mm = h/2
z = 2.0 mm
z = 1.0 mm
z = 0.5 mm
y
x
x
(c)
h = 6 mm
w = 10 mm
Outlet velocity, u_o (m/s)
Blower width, w (mm)

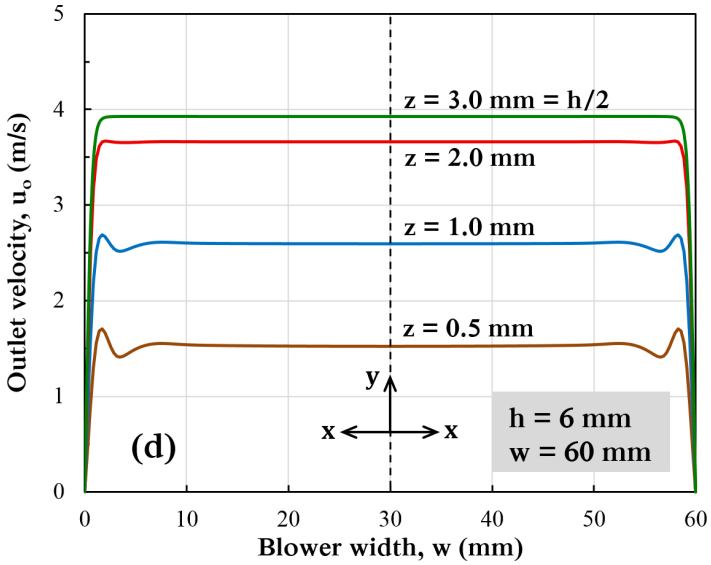

Figure 5.18 Velocity profile at the blower outlet in the *x*-*y* plane, for different widths of the blowers of h = 2 mm (a and b), and h = 6 mm (c and d).

In order to highlight that EHD blowers produce a uniform velocity profile, their flow pattern is compared with that produced by rotary fans, as presented in [220]. **Figure 5.19** shows experimental measurements of air velocity distribution at the exit flow region of a centrifugal fan of a diameter and height of 60 mm and 11 mm, respectively. It can be clearly observed that the velocity profile of the airflow induced by rotary air movers is highly non-uniform, which is due to the non-uniform distribution of the static pressure on the fan impellers.

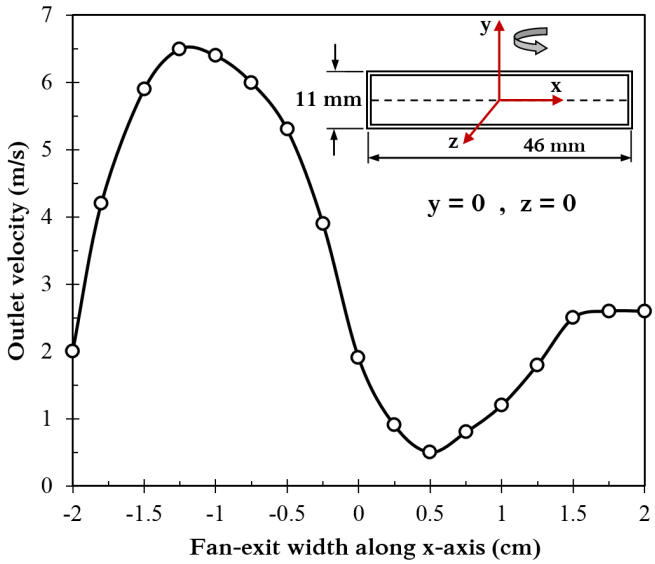

Figure 5.19 Distribution of outlet velocity on the *x*-*z* plane at the exit region of a centrifugal rotary fan at 3100 rpm [220].

In a wire-to-plane EHD channels, the blower width is usually equal to the emitter wire length, and therefore, it can be employed to control the flow rate, static pressure, produced velocity and operating voltage. An EHD blower with 4 mm thickness and 15 mm length was modelled in 2D simulations at a fixed power of 0.5 W to demonstrate these relations. **Figure 5.20**(a) shows how the blower static pressure, calculated using equation (3.23), decreases and the flow rate increases as the blower becomes wider or the wire extends at a fixed input power. This behaviour is attributed to the reductions in the operating voltage and the electric field (or the body force) created across the electrodes, leading to reduced air velocities, as shown in **Figure 5.20**(b). In this case, the increase in the ion current required for keeping the input power at a fixed level is due to the increase in the wire length. This can be explained based on the definition of the ion current,

$$I_{\mathrm{c}} = (\mu_{\mathrm{p}} E q)\, A_{\mathrm{w}} \tag{5.7}$$

where A_{w} is the surface area of the corona wire (m^2). Since the ion mobility is assumed constant and both the applied voltage and electric field strength decrease in this case, thus the ion current increases as A_{w} increases. Practically, this trend is attractive for cooling extended heated surfaces such as heat sinks, where higher flow rates using lower operating voltages are required.

The performance of rotary fans and blowers are typically characterized using a P-Q curve (pressure head vs. flow rate), which shows the relationship between the pressure (P) that builds-up as the flow (Q) is throttled, causing the maximum loss at zero flow rates. Using the same manner of rotary fans, it has been shown experimentally that it is possible to adjust equivalent P-Q curve for the EHD blowers by reducing the throttled exit area based on blower width (or corona wire length) and assuming that the maximum airflow is generated in open flow at zero static pressure [25, 136, 164]. Based on this, the wire length can provide an additional useful degree of freedom by representing the EHD blowers in P-Q curves to reflect their specifications based on static pressure and generated flow rate, as shown in **Figure 5.20**(c).

For EHD devices of a wire-to-plane channel configuration, Jewell–Larsen et al. [25] stated that both the static pressure P and outlet velocity u_o are functions of power per wire length. They demonstrated that the static pressure changes proportionally to $(Power)^{2/3}$, while the average velocity is proportional to $(Power)^{1/3}$. **Figure 5.20** shows that the present predicted trends of static pressure and outlet average velocity change proportionally against the blower width w at a fixed operating power, and agree very well with those obtained from scaling relations presented in [25], which are identified by dashed lines in **Figures 5.20**(a) and (b).

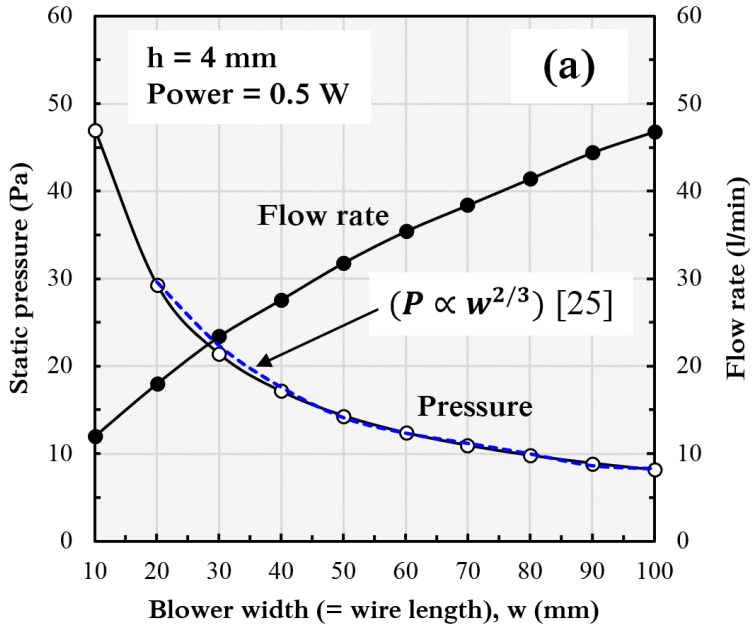

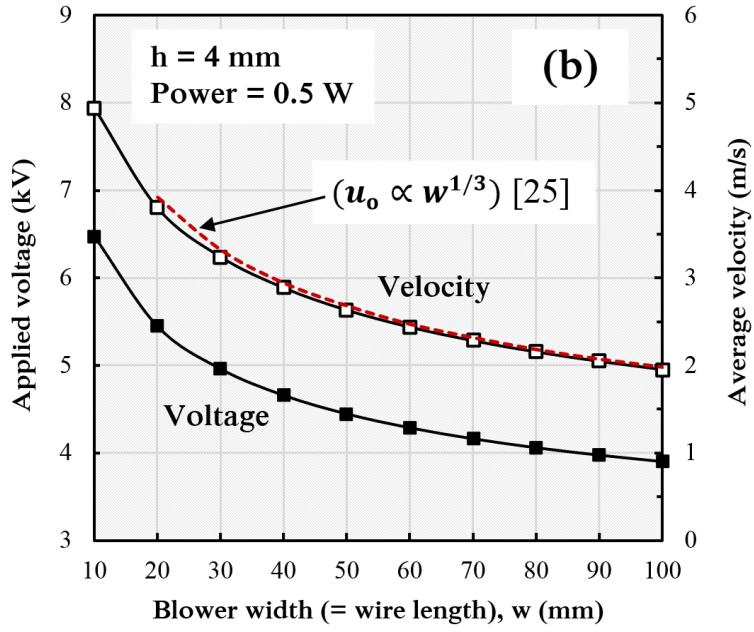

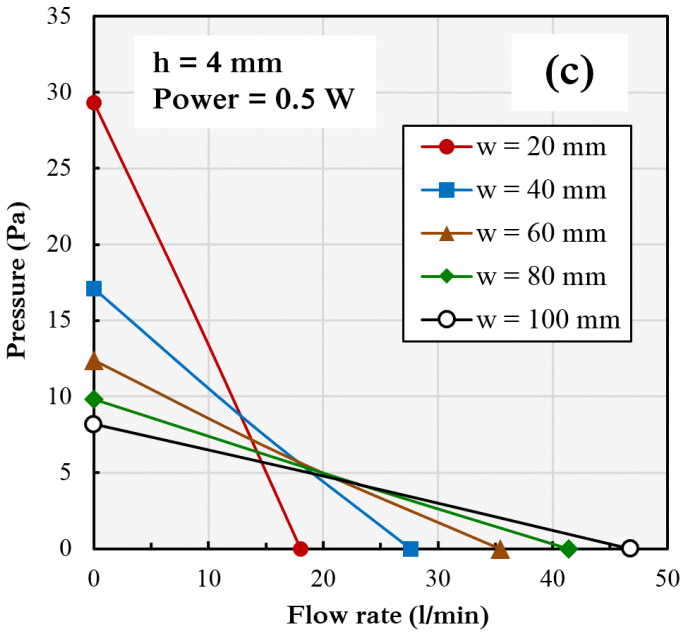

Figure 5.20 Effect of the blower width (or the emitter wire length) on the (a) static pressure and flow rate, (b) average velocity and applied voltage, and (c) fan P-Q curves, for a blower of h = 4 mm operated at 0.5 W.

5.8 Combined EHD Blower

In the practical applications, EHD blowers are usually designed to fit the limited thickness of the electronic device, regardless if the used blower height is not the most efficient one compared to other levels of blower heights at a given operating power. **Figure 5.21**(a) shows the average outlet velocity as a function of input power for different optimized blowers of length 20 mm. It can be seen that the average velocities generated by thinner blowers are higher than those obtained by thicker ones at a given input power. However, although the expected airflow rates produced by the thicker blowers are higher, the applied potential required to fix the power at a certain level increases as the blower becomes thicker, as shown in **Figure 5.21**(b). Typically, reducing the blower height at a given wire length and fixed input power leads to a higher air velocity, lower operating voltage, and reduced installation size, meeting the thermal management requirements for cooling thin microelectronics. Based on this fact and in order to balance these related factors, an EHD blower of two combined thin channels are developed and compared with a blower of an equivalent height at a fixed operating power. Two EHD blowers, each with 4 mm thickness and optimal design parameters (G_P = 1.5 mm and b_P = 6 mm), are combined, forming an integrated blower of 8 mm thickness.

In order to reduce the friction losses of the EHD-driven flow, the middle wall separating the two thin channels (located downstream of the collector) is removed, while the wall located upstream of the collector is kept to avoid electric field interference. The combined blower is operated at an overall power of 25 W/m, which is divided equally between the thin channels each with 12.5 W/m, and the generated airflow velocity is compared with that generated by an optimized blower of h = 8 mm (G_P= 2.5 mm and b_P = 12 mm), using the same total operating power.

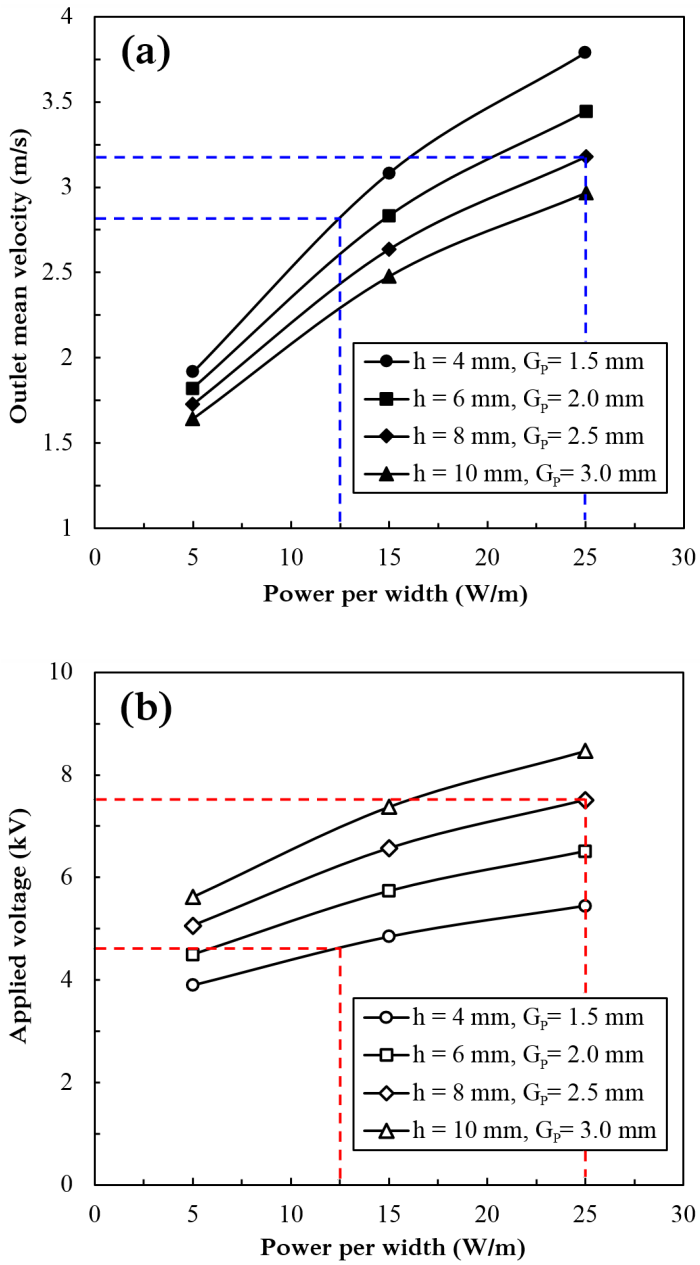

Figure 5.21 Average outlet velocity (a), and the required applied voltage (b), as functions of the operating input power for different miniature EHD blowers.

The predicted distributions of the air velocity generated by both blowers are shown in **Figure 5.22**. The results demonstrate that the combined blower of two 4mm-channels is able to produce an outlet average air velocity up to approximately 3 m/s, which is a little higher than that identified by a blue dashed line in **Figure 5.22**(a) for a blower of h = 4 mm at 12.5 W/m due to the reduced friction losses, and is very close to that obtained by the blower of h = 8 mm (3.2 m/s). This indicates that the combined blower has almost the same pumping efficiency of that of h = 8 mm, consuming the same total electrical power but with a reduced operating voltage by approximately 3 kV (39%), as shown with red dashed lines in **Figure 5.22**(b).

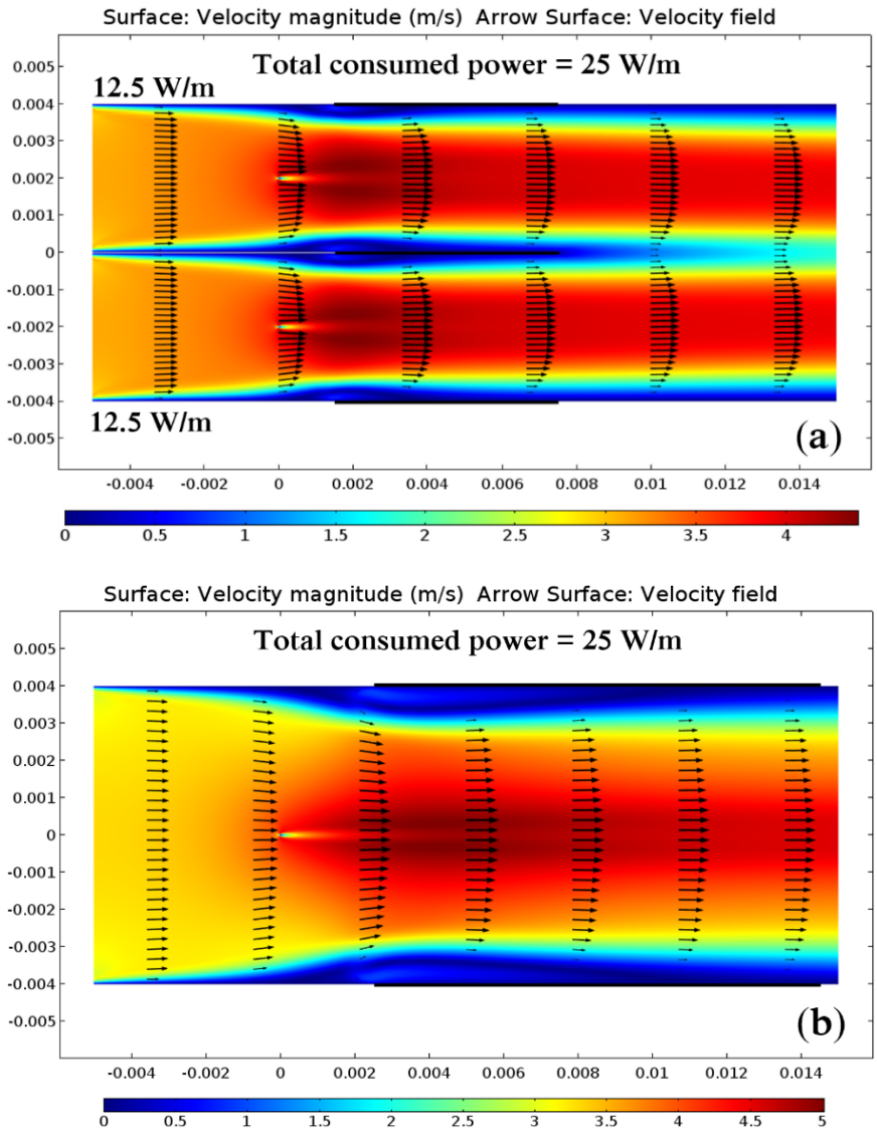

Figure 5.22 Distribution of air velocity generated at 25 W/m through: (a) combined EHD blower of two 4 mm-thick channels, and (b) EHD blower with h = 8 mm. Dimensions in metres.

Table 5.3 compares different EHD blowers generated at 2.5 W, each of 100 mm width, showing that the combined blower has the best performance among others due to its relatively high flow rate produced using a low operating voltage. In addition, due to the shorter length of the collectors used in the combined blower (6 mm each), the length (or the overall size) of the new blower can be reduced further compared to those of the blower of h = 8 mm (12 mm). Moreover, the new blower offers an improved outlet velocity profile with two high stream paths, which is highly beneficial for cooling specific electronic components.

Table 5.3 Comparison of airflow rate generated at 2.5 W by different EHD blowers, each of 100 mm width and 20 mm length.

Trend	Blower height, h (mm)	Collector length, b_P (mm)	Electrode gap, G_P (mm)	Operating voltage (kV)	Airflow rate	
					l/min	CFM
(**a**)	4	6	1.5	**5.4**	91	3.21
(**b**)	6	9	2.0	6.5	124	4.37
(**c**)	8	**12**	2.5	**7.5**	**152**	**5.39**
(**d**)	10	15	3.0	8.4	178	6.28
(**e**)	8 (Combined)	**6**	1.5	**4.6**	**143**	**5.03**

Figure 5.23 illustrates the curves of static pressure against airflow rate generated at 2.5 W by the EHD blowers listed in **Table 5.3**. The trends from (**a**) to (**d**) in the figure reveal that the flow rate decreases as the blower height is reduced at a fixed blower width while the static pressure increases. Indeed, as the blower becomes thinner at a given operating power, both the horizontal (G_P) and vertical (height parameter) electrode gaps decrease, increasing the electric field strength created across the electrodes. Unlike the case explained using equation (5.7) in the previous section, both the electric field and the ion current increase here due to the reduction in the electrode gap at a fixed wire length, which improves the body force and leads to a higher pressure head.

For the combined blower (**e**), the thin EHD channels that have small electrode gaps and a shared outlet area can create high electric fields and contribute together to generate the total flow rate and pressure head of the combined blower, which (the total pressure) is found to be higher compared to that of the blower (**a**) although they have the same electrode gap and consume equal total power. This can be attributed

to the level of applied voltage required to fix the input power at a certain level in both blowers (**a** and **e**), as listed in **Table 5.3**, which highly affects the electric field strength and its distribution along the collecting surfaces. It is found that the change in the static pressure generated by a single channel of the combined blower (at 12.5 W/m) and that of the blower (**a**) (at 25 W/m) confirms the relationship between the static pressure and input power reported in References [25, 164] for ideal EHD devices, which suggests that $\Delta P \propto \text{Power}^{2/3}$. The total static pressure of the combined blower is calculated following the relation given in [25], which states that a multi-stage EHD device operated by a number of wires (N) at a reduced electric field interference has N times the static pressure of a single wire device.

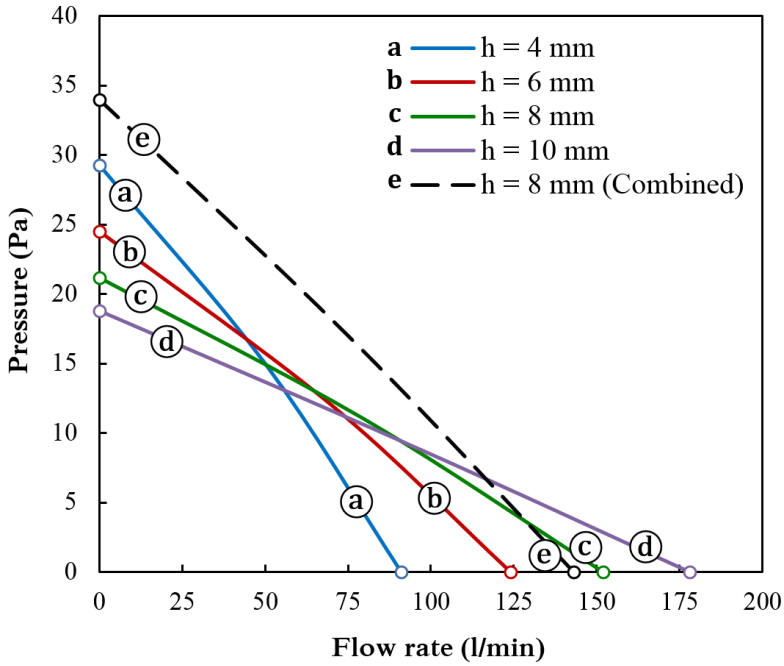

Figure 5.23 Fan P-Q curves of different EHD blowers generated at 2.5 W, each of w = 100 mm.

The combined blower can provide another important advantage when it is used as a flow-controlled cooling system in thermal management applications. In this case, the flow velocity generated by the combined blower can be controlled by changing the operating power supplied to each of its channels, depending on the local cooling rate required for the application.

Figure 5.24 shows the simulation results of a flow-controlled EHD blower at 25 W/m total power, which is consumed differently with 10 and 15 W/m by the upper and bottom channels, respectively. Both the average outlet velocity and the flow rate are kept constant but a different velocity profile along the blower outlet is achieved. It is useful to bear in mind that the presented combined EHD blower of two 4-mm channels was developed as an example, and further developments for other thicknesses with more than two thin channels can also be investigated.

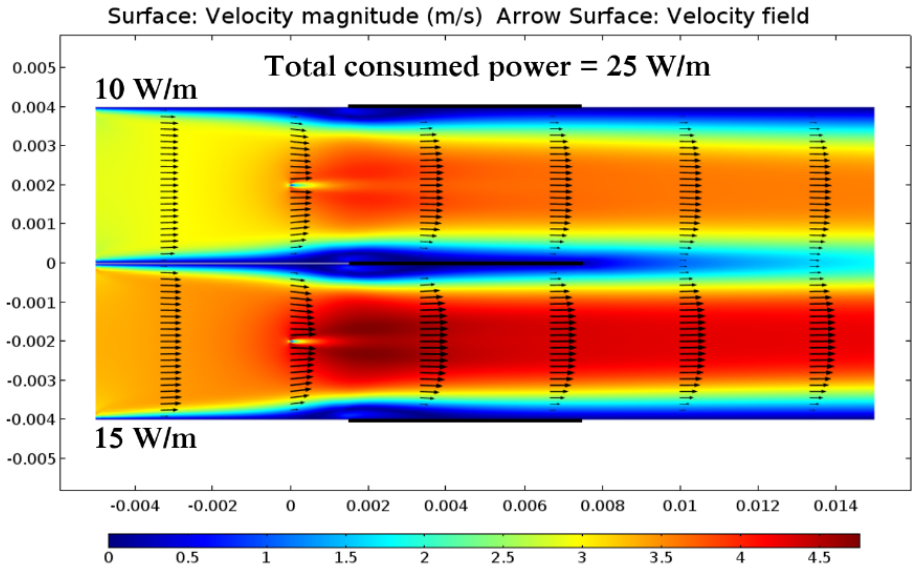

Figure 5.24 Distribution of air velocity through a flow-controlled combined EHD blower generated at 25 W/m. Dimensions in metres.

5.9 Comparisons against Rotary Blowers

This section presents a comparison of the performance of miniature EHD blowers and mechanical centrifugal fans. The results of 3D simulations developed for thin EHD blowers of 3 mm thickness and 12 mm length were compared with those of equivalent commercial rotary blowers provided by SUNON Inc. [221], based on blower size, power consumption and flow rate production, as illustrated in **Table 5.4**. It can be observed that the EHD air movers are more competitive as cooling solutions than the conventional blowers for miniaturized applications and extended heated surfaces. Unlike traditional rotary blowers, the reduction or extension of the height and width of the EHD blowers are independent of the device length, offering flexible fabrication for the blower structure to fit limited spaces or

extended heated components, whereas the rotary blowers are restricted by the circular rotation of the blades.

For example, at a fixed blower width, the EHD blower (**g**) can produce approximately the same flow rate of that provided by the rotary blower (**a**) with a slight increase in the power consumption but with a 60% reduction in the size. Moreover, increasing the operating power of the blower (**f**) by 0.14 W, over that consumed by blower (**a**), leads to improvement in the flow rate with reduction of the size by approximately 37% and 33%, respectively, showing nearly similar efficiency with a gain in the width of 20 mm. Furthermore, the narrow EHD blower (**j**) shows higher efficiency than the rotary one (**d**) by more than 1050%, generating up to 75% higher airflow and a 180% reduction in electrical power, but with an increase in the device size by 48%. However, decreasing the length of the blower (**j**) to 8 mm can reduce its size to 240 mm^3, which is equivalent to that of (**d**).

Table 5.4 Comparison of characteristics of EHD blowers with 3 mm thickness modelled in 3D simulations at a range of operating voltage from 4 to 4.3 kV, against those of mechanical blowers of the same height presented by SUNON [221].

Blower type		**Width, *w* (mm)**	**Length, *L* (mm)**	**Size (mm^3)**	**Consumed power (W)**	**Flow rate, *Q***		**Transduction efficiency (CFM/W)**
						(l/min)	**(CFM)**	
Rotary Blowers	(**a**)	30	30	**2700**	**0.36**	**18**	**0.64**	**1.78**
	(**b**)	17	17	867	0.1	6.5	0.23	2.3
	(**c**)	12	12	432	0.1	2.67	0.094	0.94
	(**d**)	9	9	**243**	**0.28**	**1.17**	**0.0413**	**0.147**
EHD Blowers	(**e**)	50	12	1800	0.75	29.4	1.04	1.4
	(**f**)	50	12	**1800**	**0.5**	**24.6**	**0.87**	**1.74**
	(**g**)	30	12	**1080**	**0.45**	**17.4**	**0.614**	1.36
	(**h**)	30	12	1080	0.3	14.4	0.51	1.7
	(**i**)	20	12	720	0.2	9.6	0.34	1.7
	(**j**)	10	12	**360**	**0.1**	**4.8**	**0.17**	**1.7**

In addition to other merits that the EHD-driven flow devices have over the rotary blowers such as silent operation, and no vibration or moving parts, they have the further advantage of producing more uniform outlet velocity profiles across their width [25, 164], as shown in **Figure 5.25**. This advantage offers active heat dissipation from narrow flow paths such as heat sink fin-channels, compared to the non-uniform outlet velocity profile obtained by mechanical blowers, especially when they are miniaturized.

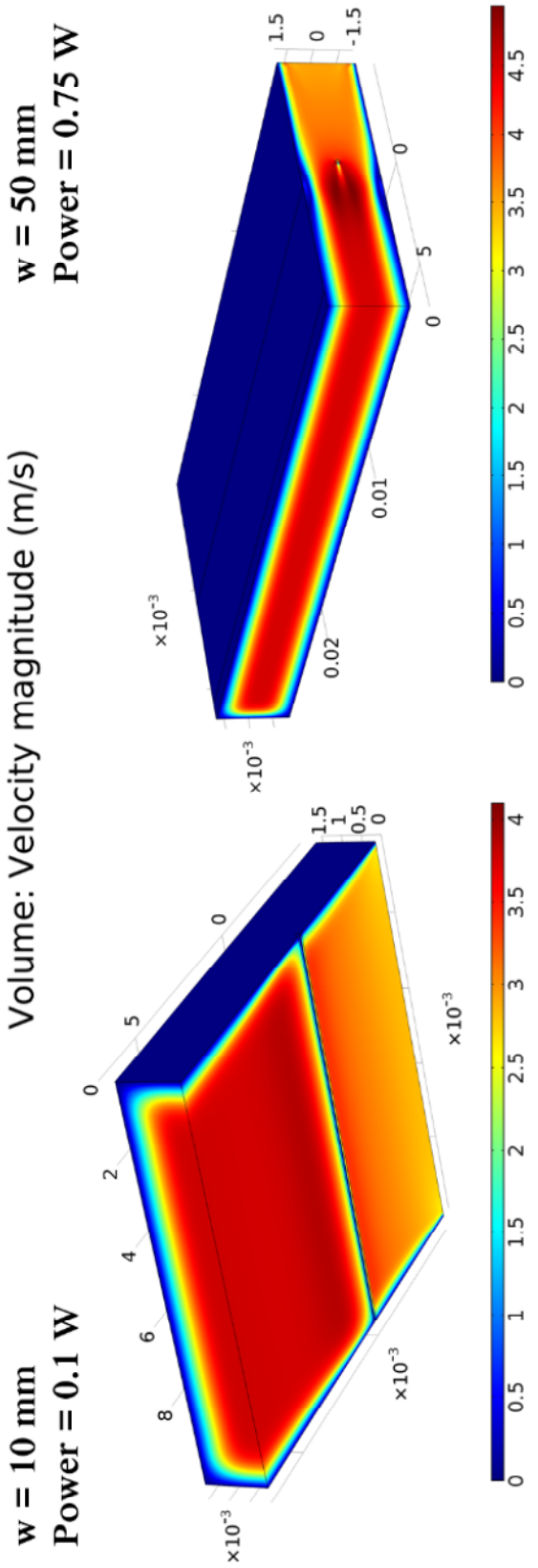

Figure 5.25 Three-dimensional simulation results of EHD blower of 3 mm thickness with different widths and operating power, showing a uniform outlet velocity profile. Dimensions in metres.

It is important to note also that the rotary blowers presented in this comparison are the thinnest blowers commercially available, according to the authors' knowledge, while further reduction in the miniature EHD blower size (with heights less than 2 mm and lengths less than 12 mm) is possible. However, the high voltage required to operate the EHD discharge still presents a practical challenge for using it to cool portable microelectronic devices such as laptops. In fact, the applied potential can be minimized for thin EHD blowers by using specific collector geometry, very fine emitter wire and optimized electrode gap

From a design and thermal management perspective, the balance between the key design factors, including the space available for the cooling system, the limitations of operating power, and the required cooling flow rate, is the key criteria for optimizing EHD devices for small-scale electronic applications. Once the balance between the aforementioned factors is determined, depending on the limitations and requirements of the application itself, design optimization and modification of the miniature EHD blowers can make them feasible alternatives to mechanical cooling solutions in real-world applications.

5.10 Chapter Summary

As part of development of EHD blowers for the application in thin thermal management microelectronics, electrode arrangement of compact wire-to-plane EHD blowers was optimized based on the effective level of operating conditions. Predictions of flow rate and static pressure obtained by the optimized configurations of EHD blowers showed very good agreement with those estimated by the EHD scaling laws. The effect of friction losses caused by blower sidewalls on the outlet velocity magnitude and profile was investigated based on blower width parameter.

Based on dimensionless analysis, results achieved using developed arrangements of combined EHD blowers demonstrated that the operating voltage can be extremely reduced while maintaining the pumping performance and the produced flow rates at the required levels. Comparisons against rotary blowers revealed that the EHD blowers are more efficient and have promising performance in thin and small-scale microelectronic applications.

In the present chapter, the performance of developed EHD blowers was investigated and shown based on the pumping efficiency and flow rate production, and then compared with that of rotary fans. However, further investigation is needed to examine the cooling performance based on heat dissipation rates due to EHD driven flow. In this direction, the next chapter will employ optimized combined EHD blowers of thin channels as a cooling system integrated with compact plate-fin heat sinks. The heat sink dimensions, EHD operating powers and levels of thermal load will also be investigated to study their effect on the overall thermal performance.

CHAPTER 6

Integrated EHD-Blower Cooled Heat Sink

6.1 Preface

The continued growing demand for smaller, thinner and more powerful consumer electronics and the associated high levels of heat generation are challenging the capabilities of conventional air cooling solutions to meet the required cooling performance. In thin electronic applications such as laptops, the integration of centrifugal fans with heat sinks is usually used as part of cooling system to dissipate the heat generated by the electronic components, maintain the processors within safe operating temperatures, and ensure the reliable operation of the electronic device. However, when the thickness of the electronic device is reduced at given operating conditions, the performance of the cooling system degrades due to the physical limitations in heat transfer capabilities created in both miniaturized centrifugal fan and compact heat sinks. Indeed, reducing the heat sink height at a given applied thermal load results in a considerable drop in the thermal performance due to the reduction in the heat exchange area.

Further degradation in the cooling performance is also created when the size of combined centrifugal fan becomes smaller, leading to a reduced flow rate, less reliability and, ultimately, lower heat transfer capability and energy efficiency, as presented previously in Chapter 1. Previous findings and analysis showed that the flow produced by a centrifugal blower, prior to entering heat sink fins, is non-uniform and does not enter the heat sink parallel to the fins, resulting in non-uniform flow rates within the fin channels and causing a rise in entrance pressure losses and, ultimately, a reduction in thermal performance [222]. These challenges have increased the need for novel and improved cooling devices that meet the thermal management requirements for small form factor advanced microelectronics.

In addition to the attractive advantages of EHD air movers with no moving parts, silent operation, flexible form factor, good reliability, uniform velocity profile, and feasible flow rates, EHD technology can provide further unique means of generating airflows inside narrow channels, where the heat exchange surface acts as a collector electrode, changing the traditional way of cooling heat sinks by rotary fans and leading to more effective heat dissipation and a reduction in the installation space [25].

In fact, the flow stream generated by rotary blowers to cool parallel plate-fins is associated with significant entrance pressure losses and is inefficient at penetrating inside the narrow spaces of the closely positioned fins. In contrast, EHD devices can be fitted and installed between narrow fin channels and generate effective cooling airflow of a uniform velocity profile, even at low velocities, offering great potential for integrating EHD blowers with heat sinks for improved cooling performance.

In this chapter, the benefits of integrating miniature EHD blowers with low-profile plate-fin heat sinks as a cooling system for thin consumer electronics and low-profile laptop applications are discussed. This chapter also presents the first, to the author's knowledge, developed 3D numerical model that solves the coupled equations of EHD flow and conjugate heat transfer. Moreover, a novel design of EHD cooling system is proposed and a parametric study is performed to evaluate the impact of design parameters on the thermal performance of the developed EHD system.

6.2 Numerical Modelling of EHD Cooling System

6.2.1 EHD Governing Equations

The set of equations of electrostatics, charge transport and fluid flow that describe the modelling of EHD airflow induced by corona discharge through a wire-to-plane channel configuration is described in detail in Chapter 3 of this thesis, whereas further equations are included here to couple the heat transfer model and predict the resulting heat dissipation from a heat exchanger due to EHD flow.

The equations of heat transfer due to the EHD airflow are governed by a coupled conjugate heat transfer model that describes the process of temperature variations and the rate of heat conduction through the heat sink surfaces in a balance with the heat transferred into the moving air by convection.

In the energy equation of convective heat transfer, the Joule heating effect is included as a source term of heat generation, which is caused by the released energy due to the ion current passing through the air gap [140], and defined as $q_{\mathrm{J}} = \mu_{\mathrm{p}} q E^2$. By neglecting viscous heating, the energy equation can be expressed for the air and the heat sink, respectively, as

$$\vec{\nabla}.\left(\rho \vec{U}\, c_{\mathrm{p}} T_{\mathrm{a}}\right) = \vec{\nabla}.\left(k_{\mathrm{a}}\, \vec{\nabla} T_{\mathrm{a}}\right) + \mu_{\mathrm{p}} q E^2 \tag{6.1}$$

$$\vec{\nabla}.\left(k_{\mathrm{s}}\, \vec{\nabla} T_{\mathrm{s}}\right) = 0 \tag{6.2}$$

where T_{a} and T_{s} are the air and solid (heat sink) temperatures (K), respectively, c_{p} is the specific heat of the air (J/kg.K), and k_{a} and k_{s} denote the thermal conductivity of the air and solid, respectively, (W/m.K).

The coupled equations of the electric field (3.3), the charge transport (3.9), airflow (3.7 and 3.12), previously presented in Chapter 3, and the conjugate heat transfer (6.1 and 6.2) are solved using the commercial package, COMSOL Multiphysics (V5.1), a partial differential equations (PDEs) solver based on the finite-element method. The 3D modelling of EHD cooling system was solved using a high performance computing server (POLARIS) at the University of Leeds.

6.2.2 Validation of EHD flow modelling

The accuracy of the numerical method developed here for the 3D modelling of EHD flow induced through a 2 mm channel thickness is validated against a range of experimental and numerical data of a wire-to-plane EHD channel presented in [164]. The channel geometry of a wire-to-plane configuration and modelling procedure presented and described in Chapter 3 for a channel thickness of 6 mm are adopted, using the same modelling parameters and boundary conditions. A non-uniform mesh

density of 693720 tetrahedral elements was generated for the upper half of the 3D simulation domain of 50 mm width with increased mesh refinement near the corona and collector electrodes.

Figure 6.1 compares the produced flow rate of the present simulation against experimental data and 2D numerical results presented in [164] for a range of input powers. The trends reveal very good agreement between the present predicted values and measured data, demonstrating the accuracy of the present numerical approach performed using COMSOL Multiphysics.

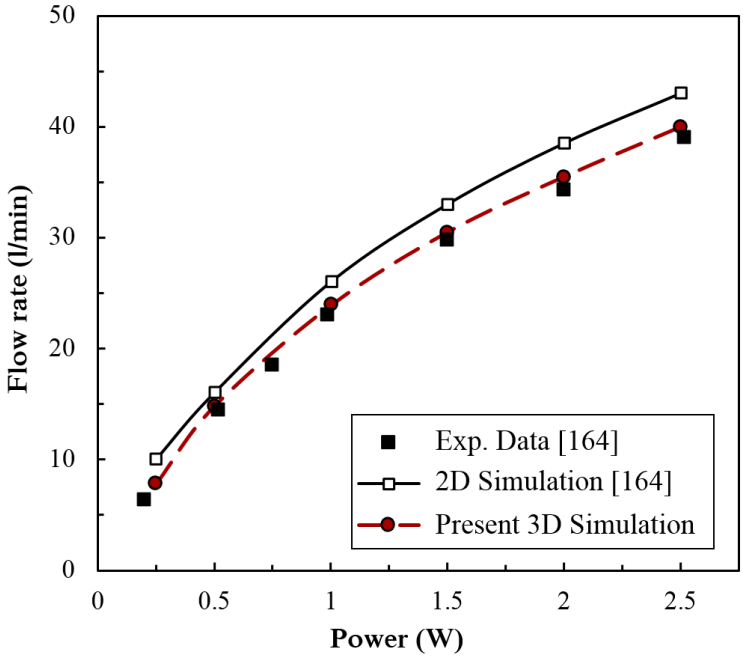

Figure 6.1 Validation results of the flow rate produced by an EHD channel of height, length and width of 2 mm, 70 and 100 mm, respectively, for a range of operating power.

6.2.3 Numerical configuration

The proposed EHD cooling system mainly consists of EHD air blowers of a wire-to-plane configuration integrated with a heat sink of parallel plate fins, as shown in **Figure 6.2**. Typically, plate fin heat sinks are commonly used as thermal solutions in many electronic applications such as laptops, due to their simple design, easy manufacturing and low pressure drop, and they have lower thermal resistance compared to other types such as pin-fin heat sinks at low pumping power [223]. A simple structure of plate-fin heat sink is employed as the heat exchange surface and

to act as the collector electrode of the integrated EHD blower. The fin spacing of the heat sink is fixed at 2 mm to be within the range of channel thicknesses used in the design optimization study of miniature EHD air blowers presented in Chapter 5.

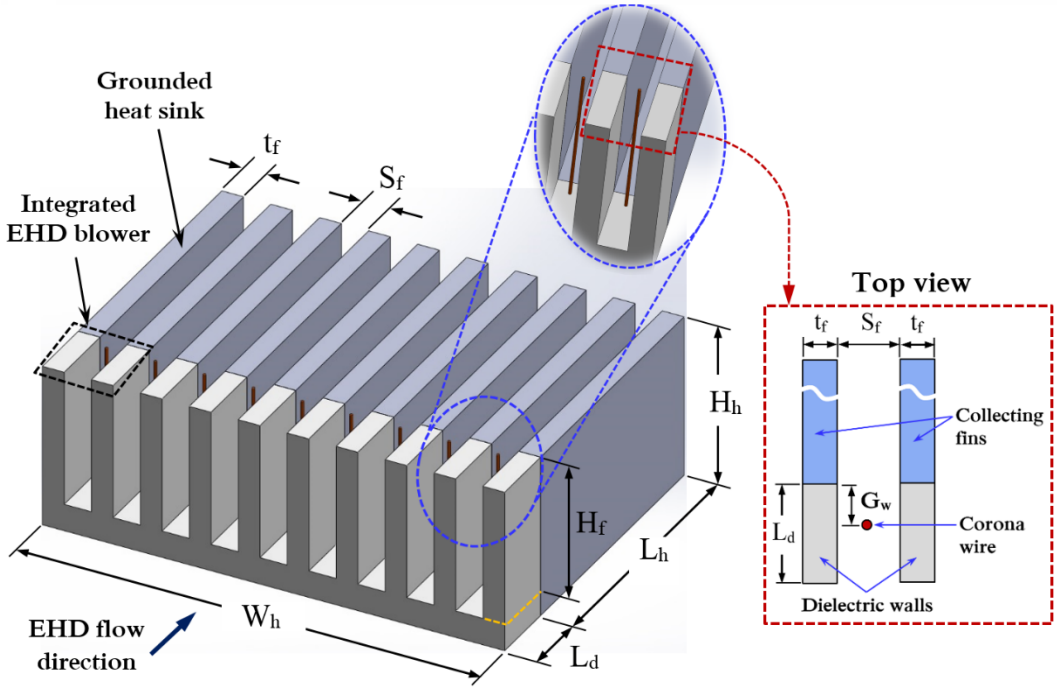

Figure 6.2 Geometry of EHD cooling system, showing the integrated corona wires with a plate-fin heat sink.

A set of fine wires of 0.025-mm-diameter are positioned vertically within the flow direction upstream of the grounded heat sink. Each wire is centered halfway between two successive collecting fins and located at a fixed distance of 1 mm from the edges of the fins and heat sink base, which is the optimal electrode gap predicted for a channel of 2 mm thickness at a constant operating power. The material of the heat sink is assumed to be Aluminium with a thermal conductivity of 200 W/m.K.

In order to avoid any interference between electric fields created by corona discharge of emitter electrodes, dielectric and insulating walls of thicknesses equal to that of the fins are used to separate the corona wires. In practical applications, these walls with a frame act as a holder of the emitter wires and also form an entrance region of the flow channels, which can be directed to the required slot in the electronic device where the cooling ambient air is pulled from. The EHD flow is induced using positive corona discharge for a range of constant operating power

from 0.6 to 1.6 W, with a corresponding range of applied voltages between 3.2 and 3.7 kV. A reference model of the integrated EHD flow cooled heat sink of 10 mm height is developed to describe the modelling procedure of the coupled EHD flow and conjugate heat transfer using the geometric parameters listed in **Table 6.1**.

Table 6.1 Geometric parameters and dimensions of the EHD cooling system used in the reference model.

Portion	Parameter	Value
Heat sink	Width, W_h	70 mm
	Length, L_h	30 mm
	Height, H_h	10 mm
	Fin height, H_f	8 mm
	Fin thickness, t_f	1.6 mm
	Base thickness, t_b	2 mm (= H_h– H_f)
	Fins spacing, S_f	2 mm
	Number of fins, N_f	20
	Heat sink material	Aluminium (k_s = 200 W/m.K)
EHD air blower	Electrode gap, G_w	1 mm
	Number of wires, n_w	= (N_f – 1) = 19
	Corona wire length	= Fin height = 8 mm
	Corona wire diameter, d	0.025 mm
Dielectric walls	Wall width	= Fin thickness = 1.6 mm
	Wall length, L_d	5 mm
	Wall height	= Fin height = 8 mm
	Number of walls	= Number of fins = 20

6.2.4 Computational domain and boundary conditions

A three-dimensional computational domain of the reference model is developed for an EHD flow induced through a single fin channel to dissipate heat via convection from the surfaces of the channel base and internal walls of the two parallel fins, under a constant heat flux condition, as shown in **Figure 6.3**.

A fine corona wire electrode is assigned vertically and centred between two parallel vertical collecting fins at an electrode gap of 1.0 mm upstream of the fin channel inlet. The length of the numerical domain is extended further at the outflow region for improved solution convergence. In order to reduce the computation time and memory, symmetry boundary conditions were applied at the vertical plane centered between the flow channel walls and at the other side of the extended region

of the simulation domain. For the coupled conjugate heat transfer module, a constant heat source of 10 W is applied at the bottom surface of the heat sink base. A further heat source is applied at the corona wire due to Joule heating, while buoyancy and radiation heat transfer effects are neglected. The air temperature at the flow channel inlet is assumed to be 20 ^{o}C. The modelling parameters used in the present simulation of EHD flow are listed in **Table 6.2**, whereas the applied boundary conditions are summarized in **Table 6.3**.

A non-uniform mesh was generated for the half 3D simulation domain with increased mesh densities at the corona electrode and both heat exchange surfaces at the fin and channel base, which also act as collector electrodes, as shown in **Figure 6.4**. Three mesh densities with approximately 1264390, 1449240 and 1612710 tetrahedral elements were used to solve the 3D modelling equations of EHD flow and conjugate heat transfer. Results of mesh independency test showed that the discrepancies in the inlet average air velocity and base temperature between the second and finest densities were approximately 3% and 0.4%, respectively, as shown in **Table 6.4**, and therefore, the second mesh density was selected to reduce the computational memory required.

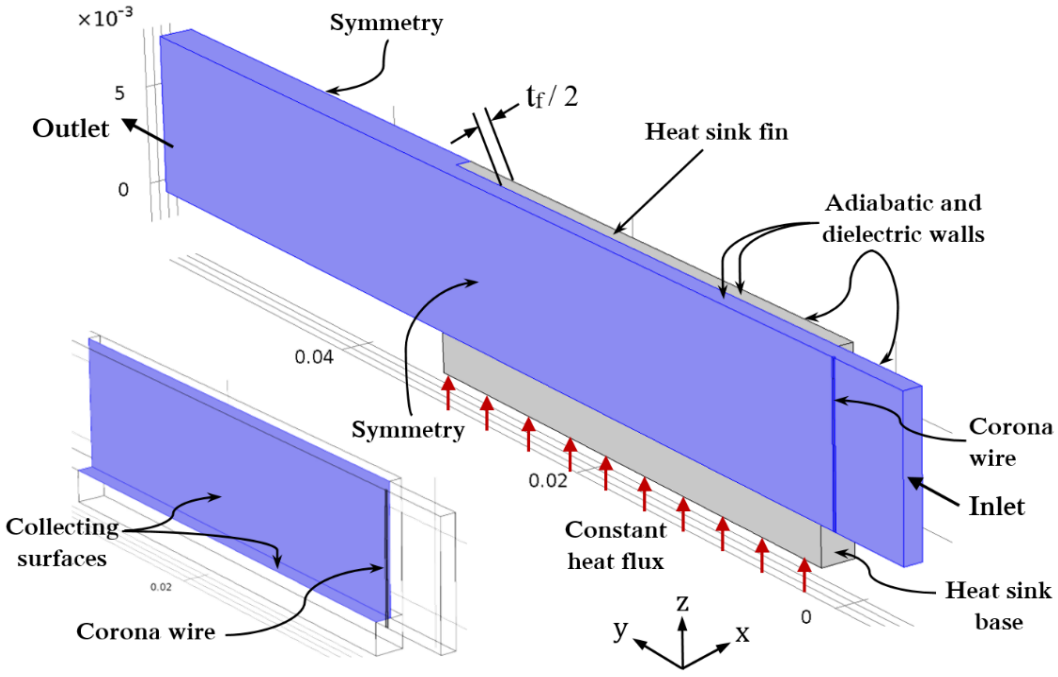

Figure 6.3 Computational domain of the EHD flow and conjugate heat transfer model.

Table 6.2 Modelling parameters used in the EHD flow simulation of the reference model.

Parameter	Value
Applied potential, V_e	3.2 – 3.7 kV
Breakdown electric strength of air, E_0	3.23×10^{6} V/m
Ion mobility coefficient, μ_p	2.0×10^{-4} m^2/V.s
Charge diffusion coefficient, D	5.3×10^{-5} m^2/s
Density of air, ρ	1.21 kg/m^3
Dynamic viscosity of air, μ	1.82×10^{-5} N.s/m^2
Kinematic viscosity of air, ν	1.51×10^{-5} m^2/s
Thermal conductivity of air, k_a	0.0256 W/m.K
Specific heat of air, c_p	1.0061×10^{3} J/kg.K

Table 6.3 Boundary conditions applied to the computational domain for the EHD flow and conjugate heat transfer.

Boundary	Electrostatics	Charge transport	Fluid dynamics	Heat transfer
Corona wire electrode	$V = V_e$	$q = q_i$	No-slip ($U = 0$)	$q_j = \mu_p q E^2$
Fin surface and channel base	Grounded ($V = 0$)	$q = 0$	No-slip ($U = 0$)	$k_a.\frac{\partial T_a}{\partial n} = k_s.\frac{\partial T_s}{\partial n}$
Dielectric walls	Neumann condition ($\partial V/\partial n = 0$)	Zero diffusive flux ($\partial q/\partial n = 0$)	No-slip ($U = 0$)	Adiabatic $-\vec{n}.(-k\vec{\nabla}T)) = 0$
Channel inlet	($\partial V/\partial n = 0$)	($\partial q/\partial n = 0$)	Prescribed velocity [177]	$T_a = 20$ °C
Channel outlet	($\partial V/\partial n = 0$)	($\partial q/\partial n = 0$)	$P = 0$	Outflow ($\partial T/\partial x = 0$)
Air boundaries	($\partial V/\partial n = 0$)	($\partial q/\partial n = 0$)	Symmetry ($\partial U/\partial x = 0$)	($\partial T/\partial x = 0$)

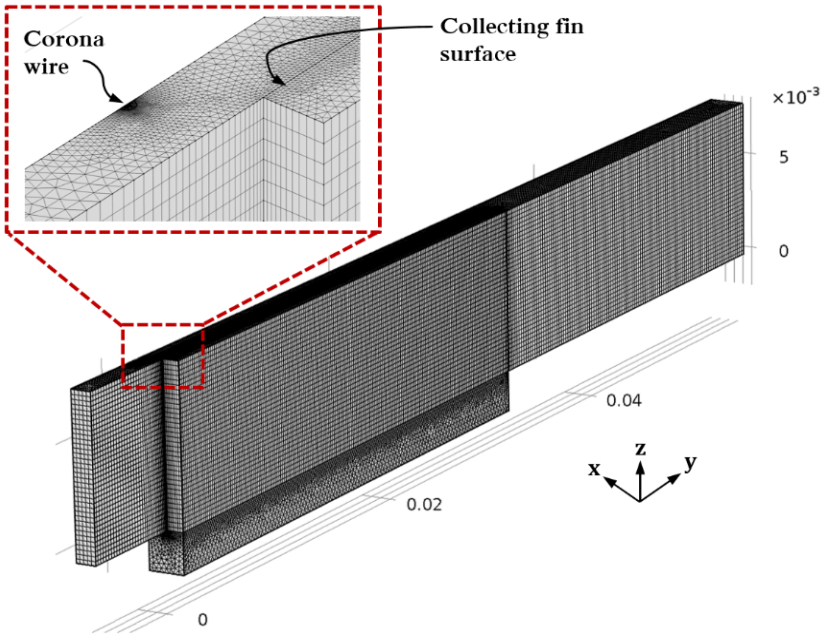

Figure 6.4 Distribution of mesh element density generated for a half computational domain of fin channel with a total heat sink height of 10 mm. Dimensions in metres.

Table 6.4 Results of mesh independence test.

Number of mesh elements	Average velocity at channel inlet (m/s)	Discrepancy (%)	Base temperature (°C)	Discrepancy (%)
1264390	1.76	–	46.8	–
1449240	1.88	6.8	46.3	1.1
1612710	1.93	2.7	46.1	0.43

6.3 Numerical Results of the Reference Model

The numerical results for the integrated EHD cooling system as volume map and multislice distributions through a fins channel for electric potential, space charge density, air velocity and temperature are shown in **Figure 6.5**, which are modelled at a total constant EHD power of 1.0 W and a corresponding applied voltage of approximately 3.4 kV.

The thermal performance of the developed EHD system can be characterized through the thermal resistance of the heat sink, which can be defined as,

$$R_{\mathrm{th}} = \frac{T_{\mathrm{b}} - T_{\mathrm{a}}}{q_{\mathrm{o}}} \tag{6.7}$$

where T_{b} is the highest temperature on the bottom surface of heat sink base (°C), T_{a} is the inlet air temperature (°C), and q_{o} is heat dissipation power applied on the heat sink base (W).

Due to the absence of experimental data and numerical predictions of convection heat transfer through a channel under a constant heat flux condition using purely EHD driven flows in the literature, the present heat transfer results are verified based on a comparison with results of traditional airflow cooled heat sink under the same operating conditions and geometric dimensions. Teertstra et al. [224] presented an accurate and validated analytical model to predict the average heat transfer rate for forced convection of air cooled plate fin heat sinks. The equations of their analysis are summarized below.

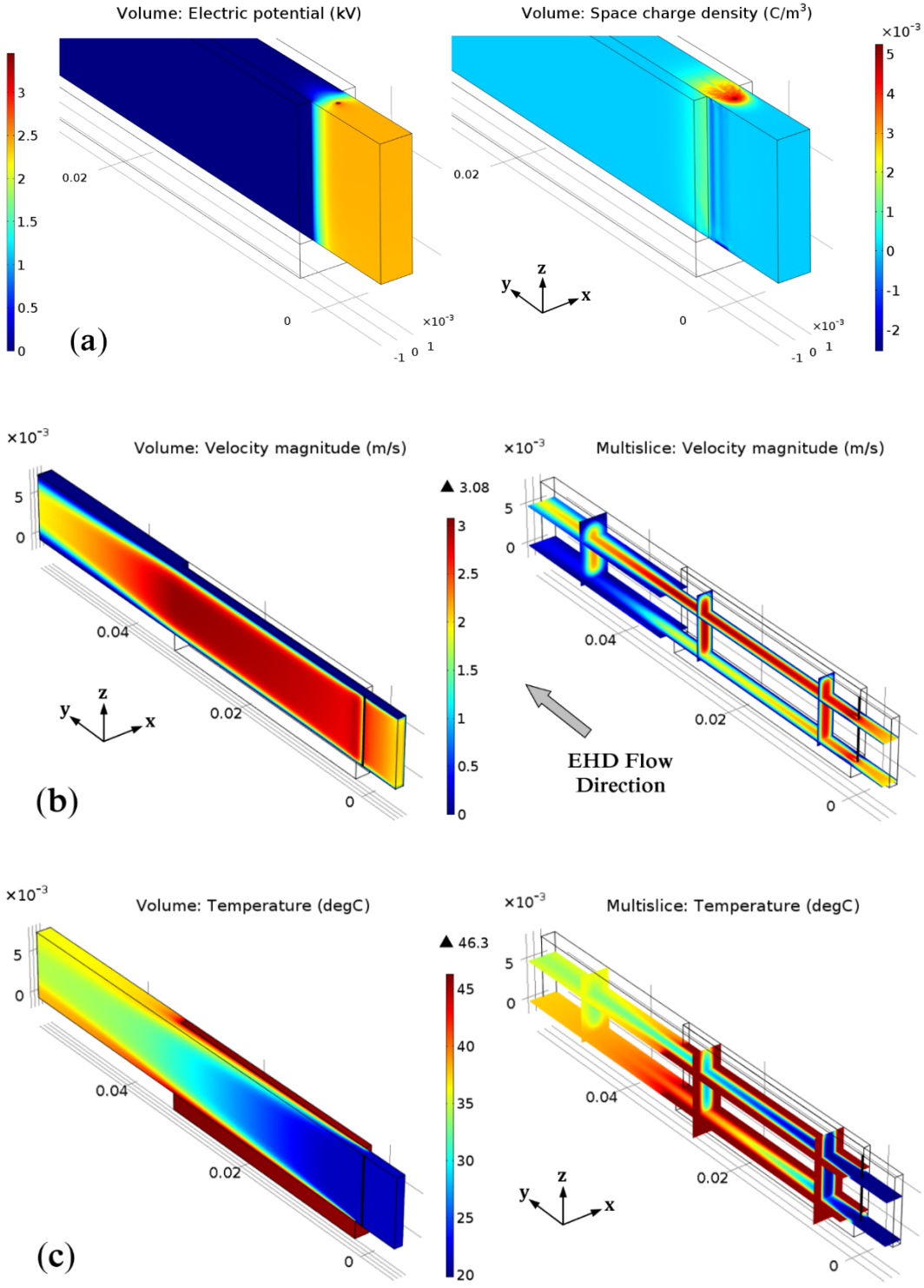

Figure 6.5 Numerical solution results of the integrated EHD cooling system modelled at a constant operating power of 1.0 W for a heat sink height of 10 mm, showing the distributions of (a) electric potential and space charge density, (b) air velocity, and (c) temperature. Dimensions in metres.

The Nusselt number can be calculated from the following developed equation,

$$Nu = \left[\left(\frac{Re^* \times Pr}{2} \right)^{-3} + \left(0.664 \sqrt{Re^*}\, Pr^{(1/3)} \sqrt{1 + \frac{3.65}{\sqrt{Re^*}}} \right)^{-3} \right]^{(-1/3)} \tag{6.8}$$

where Pr is the Prandtl number ($= \mu c_\mathrm{p}/k_\mathrm{a}$), and Re^* is a modified channel Reynolds number, defined as,

$$Re^* = \frac{u_\mathrm{c}\, S_\mathrm{f}}{\nu} \frac{S_\mathrm{f}}{L_\mathrm{f}} \tag{6.9}$$

where μ is the dynamic viscosity of air (N.s/m^2), c_p the specific heat of air at constant pressure (J/kg.K), k_a is the thermal conductivity of air (W/m.K), ν is the kinematic viscosity of air (m^2/s), u_c is the fin channel inlet velocity (m/s), S_f is fin spacing (m), and L_f is the fin length in the flow direction (m).

The average heat transfer coefficient, h_a (W/m^2.K) is given by

$$h_\mathrm{a} = Nu\, \frac{k_\mathrm{a}}{S_\mathrm{f}} \tag{6.10}$$

The efficiency of the fins may be calculated by

$$\eta_\mathrm{f} = \frac{\tanh(m\,.H_\mathrm{f})}{m\,.H_\mathrm{f}} \tag{6.11}$$

where H_f is the fin height (m), and m is given by $m = \sqrt{2h_\mathrm{a}/k_\mathrm{s}\, t_\mathrm{f}}$, where k_s is the thermal conductivity of fin material (W/m.K), and t_f is the fin thickness (m).

Thus, the thermal resistance of the heat sink is given by,

$$R_{\mathrm{hs}} = \frac{1}{h_{\mathrm{a}}\,(A_{\mathrm{b}} + \eta_{\mathrm{f}}\,N_{\mathrm{f}}\,A_{\mathrm{f}})} \tag{6.12}$$

where A_{b} is the exposed base surface area ($= (N_{\mathrm{f}} - 1)\,S_{\mathrm{f}}\,L_{\mathrm{f}}$), ($\mathrm{m}^2$), A_{f} is the heat transfer area per fin ($= 2\,H_{\mathrm{f}}\,L_{\mathrm{f}}$), ($\mathrm{m}^2$). However, in order to obtain the total thermal resistance, R_{th}, it is necessary to add the thermal conduction resistance across the base of the heat sink, R_{b}, which is defined as,

$$R_{\mathrm{b}} = \frac{t_{\mathrm{b}}}{k_{\mathrm{s}}\,W_{\mathrm{h}}\,L_{\mathrm{h}}} \tag{6.13}$$

where t_{b} is the base thickness (m), and W_{h} and L_{h} are the width and length of the heat sink (each in m). Therefore, the total thermal resistance of the heat sink can be given as,

$$R_{\mathrm{th}} = R_{\mathrm{hs}} + R_{\mathrm{b}} \tag{6.14}$$

Figure 5.6 shows how the channel average inlet velocity affects the heat sink thermal resistance obtained from the present 3D model of EHD system and that calculated from equation (6.14), using the heat sink geometric dimensions presented in **Table 6.1**. In the EHD model, the channel velocity is averaged at the fin channel inlet plane, downstream of the corona wire. Results show that the integrated EHD system is able to provide thermal performance close to that obtained by traditional air movers at a given inlet channel velocity. However, although the present comparison is generally not valid due to the difference in the mechanism of generating airflow, it can reflect the capability of miniature and low profile EHD blowers to dissipate heat through narrow channels within the expected heat transfer rates with slight deviations. Indeed, the differences in the predicted results are expected as the assumptions used in the analysis reported in [224] are valid for fins with high aspect ratio ($S_{\mathrm{f}} \ll H_{\mathrm{f}}$), where the effects of the channel base is neglected.

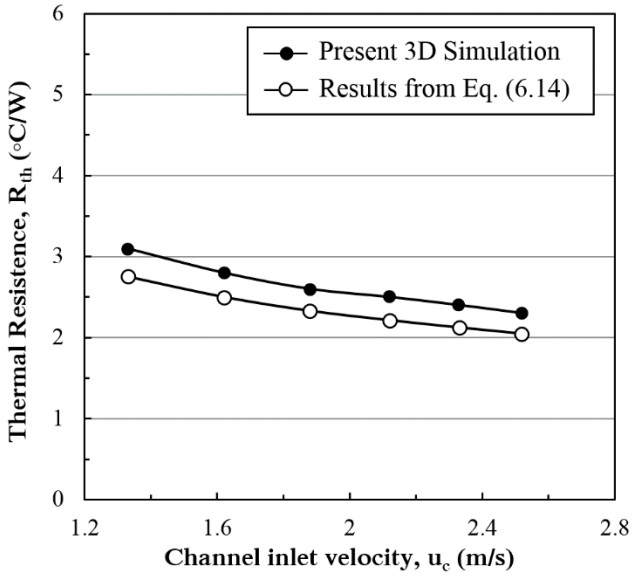

Figure 6.6 Effect of the channel inlet velocity on heat sink thermal resistance for the present EHD model and that calculated analytically for traditional air cooling [224].

6.4 Parametric Study of the EHD Cooling System

A parametric study was performed using the developed 3D conjugate heat transfer models to evaluate the thermal performance of a plate-fin heat sink cooled by integrated EHD air blowers. The study was established to investigate the effect of the main design dimensions of heat sink structure (height, length, and width) on the heat transfer characteristics for a range of operating conditions, whereas the other geometric parameters are fixed in all investigations, as listed in **Table 6.5**. It is useful to mention that, at a fixed fin thickness and fin spacing, the number of fins with a constant fin density can be used to control both the heat dissipation area (or the increased heat sink width), and the total consumed power (or the number of integrated corona wires), at a given operating power per wire.

Table 6.5 Fixed geometric parameters of the heat sink structure used in the parametric study.

Fixed Parameter	**Value**
Fin thickness, t_f	1.6 mm
Fin spacing, S_f	2 mm
Heat sink base thickness, t_b	2 mm (= $H_h - H_f$)
Electrode gap, G_w	1 mm
Corona wire diameter, d	0.025 mm
Corona wire length	= fin height, H_f
Number of wires, n_w	= Number of fins (N_f) – 1

6.4.1 Influence of heat sink height, H_h

This section studies the influence of heat sink height, H_h, on the cooling performance for a heat sink length, width, and number of fins of 20 mm, 70 mm, and 20, respectively. The total heat sink height (including the base thickness) was varied from 6 to 12 mm (in 2 mm steps), which lay within the range of the thinnest ultra-thin laptops currently available (10.16 – 16.5 mm) [225].

Figure 6.7 shows the effect of heat sink height on both the thermal resistance and total operating power consumed by the integrated corona wires. The value of applied voltage is fixed at 3.4 kV to ensure generating a constant flow velocity through fin channels for all heights. The trend of total power, which is calculated by multiplying the number of wires by the power consumed by each wire, shows an increase as the heat sink becomes thicker due to the increase in the lengths of corona wires at a fixed applied potential. In contrast, increasing the height extends the heat exchange area of the fins, leading to a higher heat transfer rate and lower thermal resistance, at constant inlet air velocity and thermal load.

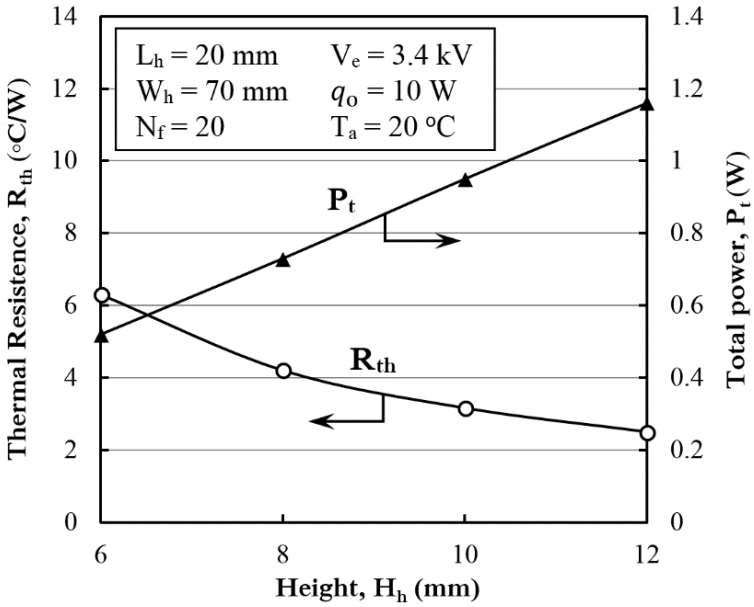

Figure 6.7 Effect of heat sink height on thermal resistance and total operating power.

6.4.2 Influence of number of fins, N_f

The effect of increasing the number of fins, which is associated with increasing the heat sink width, on the thermal resistance, base temperature, and power consumption is discussed here for a range of heat sink heights. The EHD blowers are operated at a fixed applied voltage of 3.4 kV for all heights and widths, generating a constant channel inlet velocity of approximately 2 m/s.

Figure 6.8(a) shows that the heat sink thermal resistance for each height decreases as the number of fins (or heat sink width) increases due to the increase in the heat dissipation area at a given thermal load, resulting in a significant drop in the base temperatures, as shown in **Figure 6.8**(b). However, the advantage of increasing the heat transfer due to extending the heat sink width is associated with an increase in the EHD power consumption due to increasing the number of corona wires, as shown in **Figure 6.8**(c).

In fact, the number and length of corona wires, and the level of applied voltage are the main factors that determine the level of power consumption of the integrated EHD blowers at a given electrode gap. The trends also can reflect a relationship between the heat sink width and the power consumption based on the height parameter. For instance, in order to maintain the operating temperature at 70 ^{o}C under a thermal load of 10 W, the EHD cooling system of H_h = 12 mm requires only 10 fins with 34 mm width, and 0.55 W of power. However, with decreasing the height of the same cooling system to 6 mm, the number of fins, heat sink width and total power are required to increase to 25, 88 mm and 0.66 W, respectively, in order to maintain the maximum operating temperature at the given level.

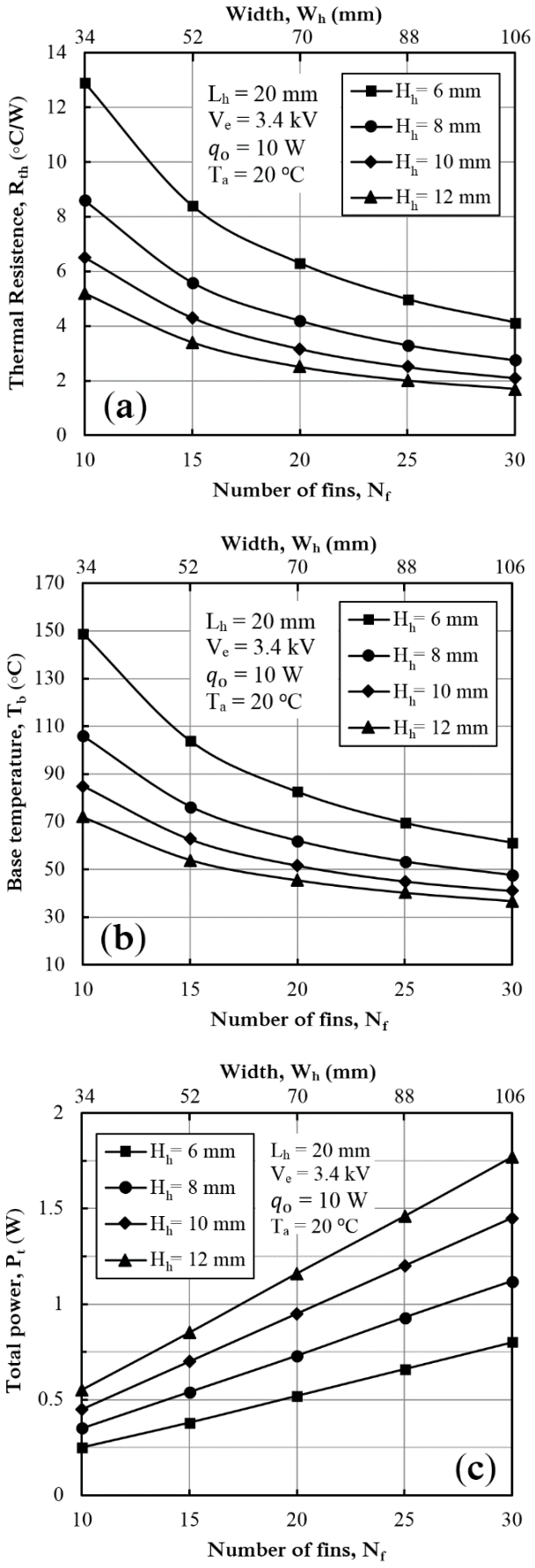

Figure 6.8 Effect of the number of fins (or heat sink width) on (a) thermal resistance, (b) base temperature, and (c) total operating power, for a range of heat sink heights.

6.4.3 Influence of heat sink length, L_h

In this section, two heat sink heights of 6 and 10 mm with a fixed width of 70 mm are selected to study the effect of the length parameter on the thermal resistance and base temperature. The total EHD power is fixed at 0.57 (0.03 W per wire) and 0.95 W (0.05 W per wire) for the heights of 6 and 10 mm, respectively.

Figure 6.9 shows that both thermal resistance and base temperature decrease for both heights as the length of the fin channels is extended due to the associated increase in the heat dissipation area. In this case, increasing the heat sink length is independent of the operating power or the number of integrated wires. It can be seen that increasing the length from 10 mm to 50 mm, at a given operating power and fixed width, leads to a drop in the base temperature from 105 to 68 ^{o}C and from 65 to 44 ^{o}C, for the heights of 6 and 10 mm, respectively. However, the trends of base temperature show that increasing the length beyond 40 mm leads to a slight drop in the temperature with only 1 ^{o}C for both heights. This, indeed, is attributed to the increase in the flow resistance and friction losses through the fin channels at a given induced air velocity.

Referring to the given example in the previous section, it can be seen here that the thin heat sink of H_h= 6 mm is able now to maintain the operating temperature at 70 ^{o}C with less width (70 mm) and lower total power (0.57 W), by doubling the heat sink length from 20 to 40 mm, under the same operating conditions. It is very important that these factors are carefully taken in consideration for the efficient design of EHD cooling systems.

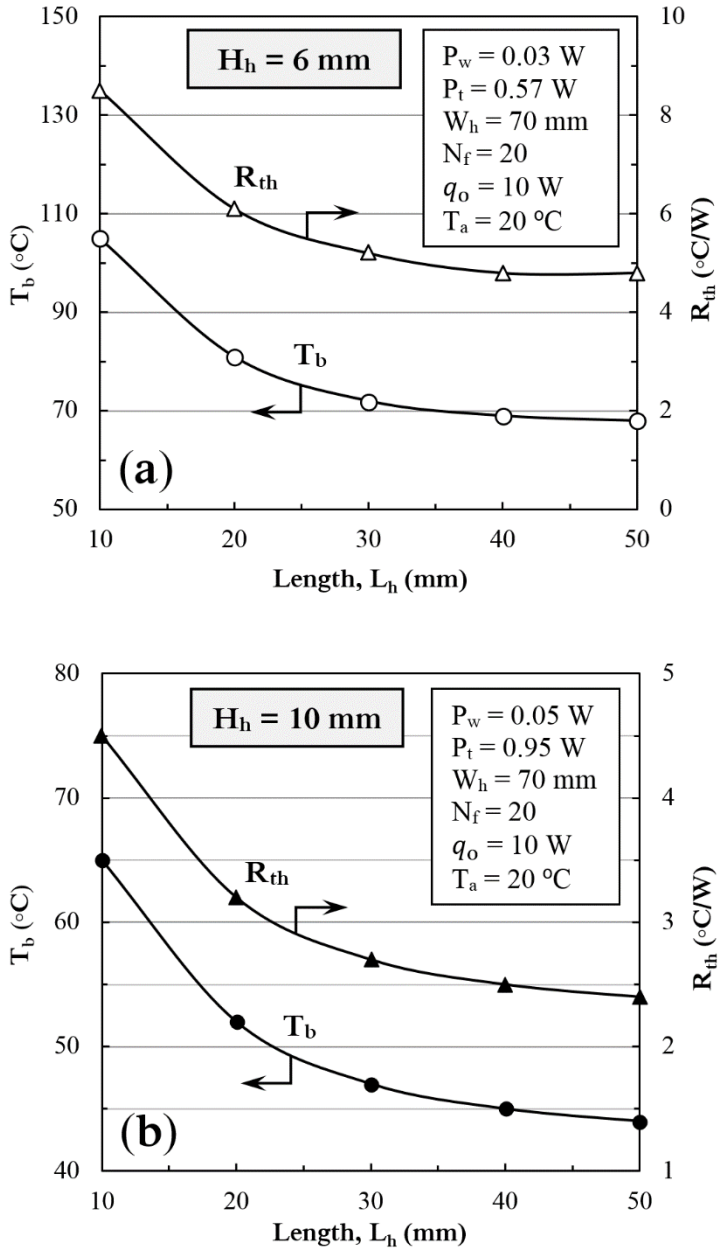

Figure 6.9 Effect of heat sink length on both base temperature and thermal resistance for heights of (a) 6 mm and (b) 10 mm.

6.4.4 Influence of operating power, P_t

This section discusses the influence of operating power on the thermal and flow characteristics for two levels of heat sink heights (6 and 10 mm), while fixing the parameters of width and length at 70 and 30 mm, respectively. In this case, the total power and the induced air velocity increase due to increasing the level of applied potential, at a given number of corona wires. It can be seen from **Figure 6.10** that increasing the operating power from 0.3 to 0.8 W for the thinner EHD

cooling system under a constant heat generation source can double the air velocity magnitude (from 1.2 to 2.3 m/s) and decrease the base temperature by 19 ºC (from 86 to 67 ºC) but with an increase in the required applied voltage by 0.45 kV (from 3.2 to 3.65 kV).

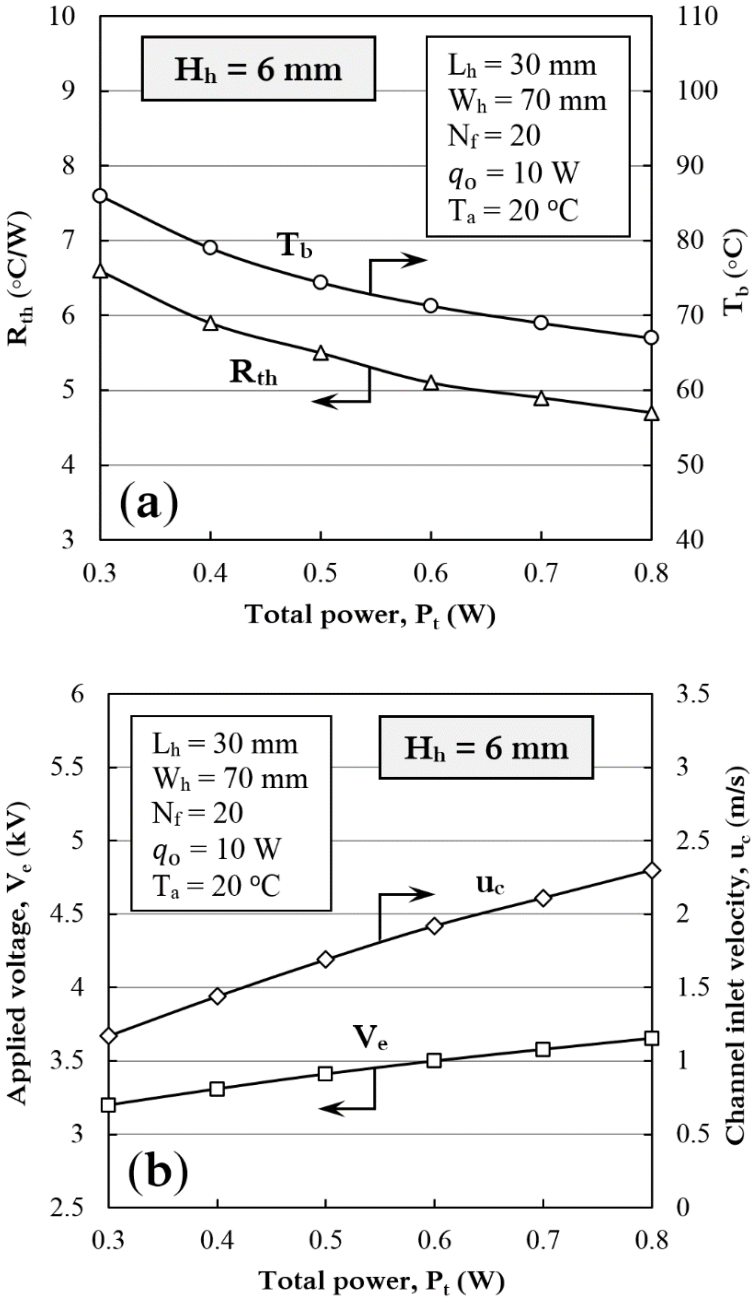

Figure 6.10 Effect of operating power on (a) thermal resistance and base temperature, and (b) applied voltage and channel inlet velocity, for an EHD cooling system of H_h = 6 mm.

Similar trends with different values can be noticed for the thicker EHD cooling system of H_h= 10 mm, as shown in **Figure 6.11**. The predictions reveal that increasing the total power up to 1.6 W can generate an inlet air velocity of 2.5 m/s and decrease both the base temperature and thermal resistance to 43 ^oC and 2.3 $^oC/W$, respectively, using 3.7 kV operating voltage.

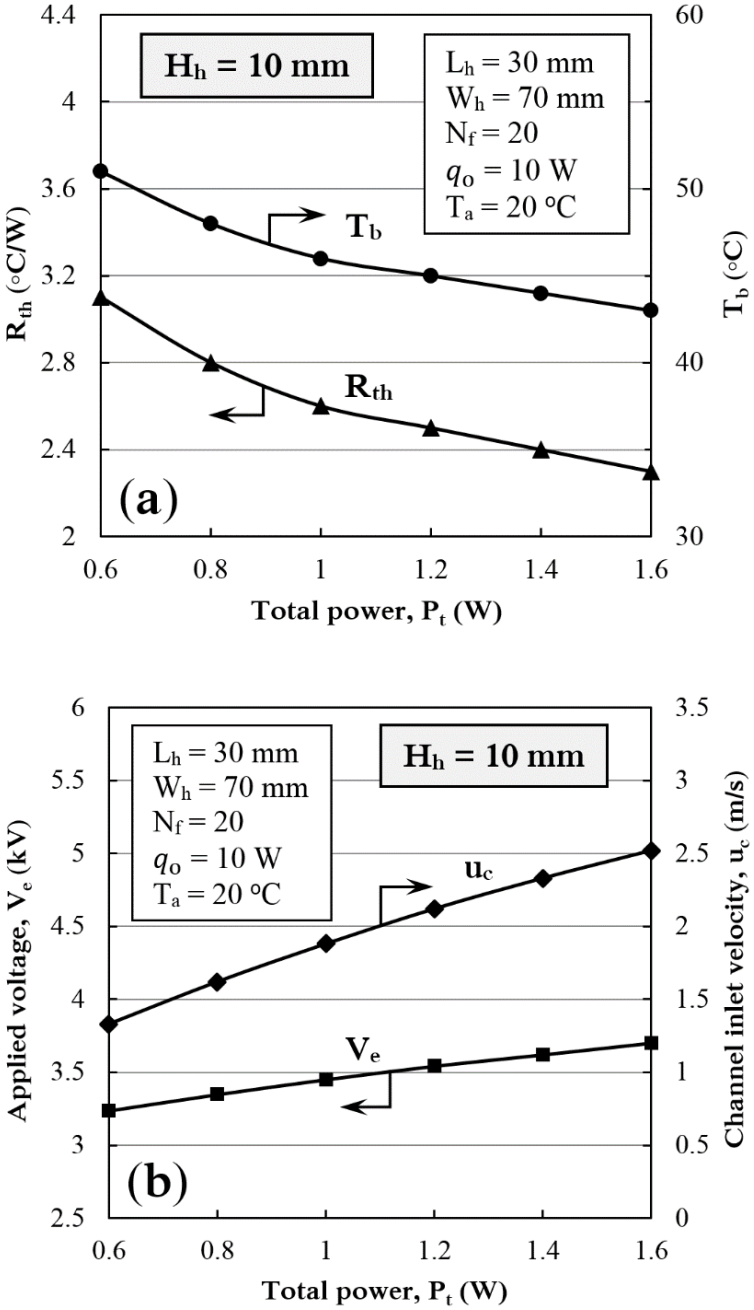

Figure 6.11 Effect of operating power on (a) thermal resistance and base temperature, and (b) applied voltage and channel inlet velocity, for an EHD cooling system of H_h= 10 mm.

The trends of temperatures show that increasing the total power over 0.6 and 1.2 W for the heights of 6 and 10 mm, respectively, does not lead to a significant drop in the maximum temperature, despite the associated increase in the induced air velocity. Therefore, in the case of applying higher thermal load or if it is required to decrease the maximum temperature further, it is recommended for both heights to increase the heat dissipation area (by increasing the number of fins) and the number of integrated wires (the total power) rather than increasing the consumed power per wire that also requires higher applied voltage.

For example, the total operating power of the thinner cooling system (H_h= 6 mm) can be increased from 0.6 to approximately 0.8 W at a fixed applied voltage of 3.5 kV by adding 7 fins and 6 wires. In this case, the drop in the temperature is expected to be higher compared to that shown in **Figure 6.10** (4 ^{o}C), using lower operating voltage. Indeed, achieving an appropriate balance between the levels of operating power and applied voltage, design of compact high-voltage multiplier, installation space of the cooling system and applied thermal power is essential in the practical implementation of EHD cooling systems in low height electronic devices.

6.5 Performance of EHD Cooling System

The thermal performance of the developed EHD systems of different heights (6 – 12 mm) can be examined based on the applied thermal load or thermal design power (TDP), as it is usually called. The TDP is a good indicator that helps to determine the power efficiency and performance of a component, and is defined as the maximum amount of heat generated by a chip in the electronic device that the cooling system is designed to dissipate in typical operation [226].

All integrated EHD blowers are operated at a constant total power of 1.25 W, using (for fixing the power) different geometric and operating conditions, as listed in **Table 6.6**. The inlet air temperature is set at 30 ^{o}C, which is the expected value in the real operation. The applied thermal load is varied from 10 to 30 W, and the heat dissipation capacity of each EHD cooling system is considered based on the highest temperature at the bottom surface of the heat sink base, T_b.

In this investigation, it is useful to use the maximum operating temperature allowed in laptops as a reference to evaluate the cooling performance of EHD systems proposed to be used in same application field. NVIDIA states that the typical temperature of GPU, which is one of the hottest running components in a computer, averages between 40 and 90 ^{o}C, with a maximum permissible operating GPU temperature of 105 ^{o}C before overheating [227]. In the present evaluation, the maximum temperature is assumed to be lower, namely 100 ^{o}C.

Figure 6.12 shows the maximum temperature as a function of the thermal load for different heights of EHD systems, which are related to the geometric dimensions and operating conditions presented in **Table 6.6**. At a given total power of 1.25 W, the trends **A** and **B** reveal that thinner EHD cooling systems with heights of 6 and 8 mm are able to maintain the highest temperatures within the typical safe operating range under thermal loads up to 20 and 25 W, respectively, before they hit the region close to the maximum permissible temperature. When the EHD cooling systems become thicker (H_{h} = 10 and 12 mm), the trends **C** and **D** show improved cooling performance with keeping the highest temperatures within the safe range under a thermal load of 30 W.

Table 6.6 also shows that the error in the thermal resistance of the present modelling decreases compared to that calculated from equation (6.14) as the heat sink height increases, confirming that the accuracy of the analytical approach presented in [224] improves as the aspect ratio of ($S_{\mathrm{f}}/H_{\mathrm{f}}$) decreases.

Table 6.6 Geometric dimensions and operating conditions used to examine the performance of developed EHD cooling systems.

Trend	H_{h} (mm)	L_{h} (mm)	W_{h} (mm)	N_{f}	A_{base} (mm^2)	P_{w} (W)	V_{e} (kV)	R_{th} (^{o}C /W)	R_{th} [Eq. (**6.14**)] (^{o}C /W)
A	**6**	30	124	35	3720	0.037	3.57	2.8	2.34
B	**8**	30	106	30	3180	0.043	3.47	2.3	2.00
C	**10**	30	88	25	2640	0.052	3.44	2.1	1.90
D	**12**	30	88	25	2640	0.052	3.35	1.8	1.65

It is useful to mention that further improvements can be achieved with lower operating temperatures by increasing the heat exchange area, which can be obtained by extending the width and length of the heat sink, or increasing the operating power per wire, which results in greater induced air velocities, depending on the requirements and limitations of the application itself.

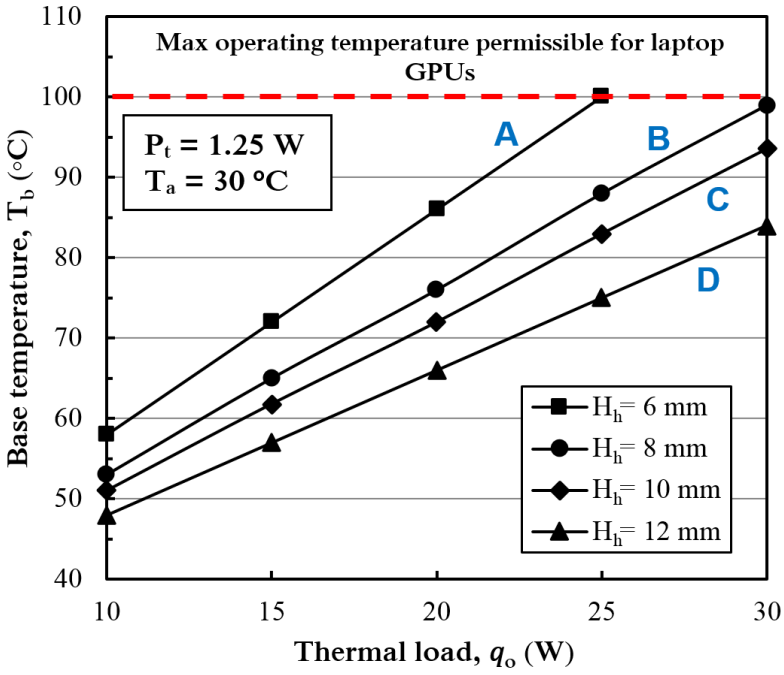

Figure 6.12 Comparison of cooling performance of different EHD cooling systems, showing the thermal load as a function of base temperature. Trends symbols are related to the information presented in **Table 6.6**.

In order to assess the capability of the present EHD cooling systems in real applications, a list of examples of the current standard laptops powered by Intel technology are selected and presented in **Table 6.7** as a guide for comparison, showing the max TDP and total thickness of different laptops. The figures reveal that the developed EHD cooling systems have great potential to compete with mechanical rotary fans in low-profile laptops with higher TDP and lower device height, even if the laptop screen thickness is added.

Indeed, the ability to extend the width of the heat exchanger cooled by traditional centrifugal fans used in laptops is limited by the width of the fan exit region, which is always smaller than the total fan diameter. Furthermore, compared to conventional centrifugal fans, the present EHD system requires smaller

installation volume even if the size of the compact high-voltage multiplier is included [25]. These significant advantages establish the integrated EHD cooling systems as a promising alternative thermal solution in low-profile laptop applications.

Table 6.7 Examples of the current standard laptops powered by Intel technology available commercially [228].

Product	Max TDP	Total height
ASUS VivoBook S200E-CT320H notebook	17 W	20.9 mm
Acer Aspire 430	17 W	25.3 mm
Dell Latitude 7380 2.8GHz i7-7600U-13.3"	15 W	17.3 mm
ASUS VivoBook S510UA-BQ079T 2.4GHz i3-7100U-15.6"	15 W	17.9 mm
Lenovo IdeaPad 310-15 2GHz i3-6006U-15.6"	15 W	22.9 mm
Dell Latitude 3480 2.5GHz i5-7200U-14"	15 W	23.3 mm
ASUS Chromebook C300MA	7.5 W	20.3 mm
ASUS X553MA, 4Gb RAM, 750Gb Hard Drive, Wi-Fi, 15.6"	7.5 W	25.3 mm
Acer Aspire A114-31-C6S1 1.1GHz N3350 14"	6 W	18 mm
Lenovo N22 Chrome book - Celeron N3060 - 32GB Flash-11.6"	6 W	21.8 mm
ASUS VivoBook E201NA-GJ008T-OSS 1.1GHz N3350-11.6"	6 W	22.5 mm
ASUS VivoBook Max X541NA-GO230T 1.10GHz N4200 15.6"	6 W	27.6 mm
ASUS Zenbook UX305FA-FC004P 0.8GHz M-5Y10-13.3"	4.5 W	12.3 mm
HP EliteBook Folio 1020 G1 1.1GHz M-5Y51-12.5"	4.5 W	15.7 mm

6.6 Chapter Summary

The main points presented in this chapter can be outlined as follows:

1. A novel design of an EHD system integrated with compact heat sinks in a range of heights from 6 to 12 mm was proposed as a thermal management cooling solution for small-scale and thin advanced consumer applications.

2. A 3D numerical model was successfully developed to solve the coupled equations of EHD flow and conjugate heat transfer, showing an acceptable thermal performance compared to that obtained by traditional fans at a given inlet fin channel velocity.

3. Results of a parametric study demonstrated that the efficient design of integrated EHD systems can be obtained based on an appropriate balance between the heat sink dimensions, and the developed EHD systems offered a flexible design to be installed in low-profile laptops.

4. At a given operating electrical power of 1.25 W, predictions of thermal performance revealed that a compact EHD cooling system of 6 mm thick under a thermal load (TDP) of 20 W was able to maintain the operating temperature within the typical range recommended for GPUs (40 – 90 ^{o}C), whereas a thicker EHD system of 12 mm height showed higher thermal performance with a maximum operating temperature below 85 ^{o}C under a TDP up to 30 W.

5. Compared to traditional cooling systems used in the current standard low power laptops, integrated EHD systems were found to be competitive to rotary fans based on cooling performance, installation volume and device thickness.

CHAPTER 7

Conclusions and Future Work

7.1 Conclusions

EHD air movers are receiving increasing attention from the academic research community as a novel cooling solution for advanced microelectronics and consumer devices. As part of this attention, this thesis has been devoted to investigating the unique features of using EHD flow in thermal management cooling systems, and support previous efforts performed to employ this technology in the real-world applications.

The main conclusions of the present work can be drawn as follows:

- A numerical approach is performed using the commercial package, COMSOL Multiphysics software, to solve the coupled equations of electric field, charge transport and fluid dynamics for EHD driven airflows. Numerical validation results are shown to agree well with previous experimental data and demonstrate the accuracy of the numerical method used to predict the current-voltage, flow rate, static pressure, outlet velocity profile, and heat transfer characteristics. Compared to measured data, the developed models are shown to accurately predict current-voltage curves and outlet average air velocities with errors of less than 4% and 10%, respectively.

- As the corona discharge process and the induced EHD flow are highly affected by the configuration parameters and operating conditions, EHD numerical modelling is shown to provide a rigorous tool to investigate a wide range of aspects of EHD process, predict the performance and efficiency of EHD blowers in small-scale structures, design and optimize configurations, and, ultimately, save time and cost. Moreover, the successful 3D modelling developed in this thesis enables the inclusion of conjugate heat transfer models

and offers the ability to simulate of a wide range of non-symmetric and complex emitter/collector geometries.

- Numerical simulations are developed to carry out a comprehensive parametric study into the effect of the corona wire diameter, collecting electrode gap and collecting grid distribution on the efficiency of the EHD wire-to-grid blowers for a range of blower heights (from 9 to 15 mm). Results reveal that using a fine emitter wire is more efficient than a thicker one, and leads to lower onset voltage, considerable reductions in both power consumption and applied potential required to generate a certain air velocity, confirming previous findings. It is noticed, for example, that reducing the emitter wire diameter from 100 μm to 50 μm can reduce the power consumption and the required voltage by approximately 20% and 13%, respectively, with just 6% drop in the produced average air velocity, using the same electrode gap.

- The predictions also show that using a grid of parallel wires as a further collector has significantly beneficial impacts on the blower performance, with higher flow production, lower operating voltage and reduced blower size, meeting the design and thermal management requirements. Furthermore, it is found that the grounded electrode locations highly affect the electric field distribution and the blower efficiency, and the latter can be enhanced by increasing the electrode gap of both collectors from the emitter wire, since this increases both the drifting angle of the charged ions and the kinetic energy imparted to the flow towards the blower outlet.

- The optimal electrode gap of both the grid and the collecting surface for each investigated blower can be determined based on the effective increase in the applied voltage by fixing the operating power. The optimal locations of both collectors show that the average outlet velocity is enhanced with maximum increases in the range from 9% to 15%, depending on blower thickness, compared to that obtained with inefficient collector locations using the same operating power. An investigation into the effect of grid density reveals that using coarse collecting grids is generally beneficial, leading to higher efficiency

with lower pressure losses. For example, using a collecting grid density of 6 wires in a blower of 11 mm height can improve the blower efficiency by approximately 55% over the case of no grid, and by 14% compared to the case of using a denser grid with 10 wires, at a given applied voltage of 5.6 kV.

- Aiming to optimize a miniature configuration of wire-to-plane EHD blower, which is the most preferred geometry for integrating into cooling systems for thin microelectronic applications, the horizontal electrode gap and the most effective collector length for a range of blower heights (from 2 to 10 mm) are determined by fixing both the input power and the applied voltage and defined by simple expressions. Results demonstrate that using the optimal electrode gaps predicted at a constant applied voltage can improve the energy conversion efficiency by 55% to 93% for the range of blower heights compared to that obtained using inefficient locations (at $G = 0$).

- The new method of fixing the operating power presented first in this thesis is found to be a useful tool for efficient design optimization when the practical application is controlled by a limited range of operating power. Using this method, the optimal electrode gaps are determined based on effective increases in the applied voltages, which are found to be nearly equivalent to the improvements in the induced air velocities. Furthermore, using the effective collector length in the thin EHD blowers offers further miniaturization in the installation size, whereas using the whole effective collector length in the thicker EHD blowers provide effective heat removal when the collector acts as a heat exchange surface.

- Although the predicted optimized wire-to-plane EHD channel configurations are valid only for the corona wire diameter adopted in this study, these optimal parameters can be used as a useful reference when thicker or finer corona wires are used for the given ranges of blower heights and operating conditions. Results of produced flow rates and static pressures obtained by the optimized blowers are found to agree well with those predicted by the previously reported EHD scaling laws of ideal EHD flow devices.

- Unlike flow profiles produced by rotary fans, results of 3D numerical investigations performed to highlight the performance and flow characteristics of miniature EHD blowers show that the profile of the outlet mean velocity is uniform with a parabolic distribution along the vertical plane and has a top-hat distribution (flat) along the horizontal plane. Furthermore, it is found that the flow resistance and sidewalls friction through shortened and thin EHD blowers decreases and can be neglected as the blower becomes wider, indicating that using 2D modelling for short and wide EHD blowers can predict flow rates effectively compared to that obtained by the means of the 3D simulations. For example, results show that the outlet mean velocity magnitudes predicted using 3D models for blowers of 2 mm and 6 mm heights with 60 mm widths are just approximately 1% and 1.5% lower than that predicted by 2D simulations, under the same operating voltage. This observation can aid to ensure acceptable predictions of flow rates using 2D simulations with slight differences compared to those that include flow losses, and also save time and the large computational memory required for 3D modelling of ducted EHD driven airflow.

- In order to minimize the operating voltage required to generate a certain flow rate, a configuration of two combined thin EHD blowers is developed and compared against other levels of blower height. Results reveal that the combined blower is able to produce flow rates close to that obtained by a blower of the same thickness, consuming the same electrical power while reducing the applied potential by approximately 40%. Furthermore, combined EHD blowers provide further advantages when the operating power is controlled to produce different flow patterns for local cooling in thermal management applications.

- Performance comparisons against commercial rotary blowers demonstrate that the optimized miniature EHD blowers are more competitive for cooling miniaturized and extended heated surfaces based on blower size, flow rates with uniform velocity profiles, and power consumption. For example, at a fixed blower width at 30 mm, an EHD blower of 3 mm height can produce approximately the same flow rate of that provided by an equivalent rotary

blower (18 l/min) with an increase in the power consumption by 25% (0.1 W) but with a 60% reduction in the size. On the other hand, reducing the EHD blower width to 10 mm shows higher efficiency than an equivalent rotary fan by more than 1050%, higher airflow rate by up to 75% and a reduction in electrical power by 180%, using the same installation size. Results of performance comparison indicate that the balance between the key design factors, including the space available for the cooling system, the limitations of operating power, and the required cooling flow rate, is the key criteria for optimizing EHD devices for small-scale microelectronic applications.

- The benefits of integrating optimized EHD air blowers with a heat exchanger of parallel plate-fins are investigated, and a novel design of EHD cooling system is proposed as a thermal management cooling solution in microelectronics and low-profile laptop applications. A validated three-dimensional numerical model is developed to solve the coupled physics of EHD flow and conjugate heat transfer. For a range of heat sink heights from 6 to 12 mm, a parametric study is performed to investigate the effect of main design parameters and operation conditions on the heat transfer characteristics and cooling performance of integrated EHD systems. Results show that the main dimensions of the heat sink have significant effects on the dissipated and operating powers, and a delicate balance between these factors must be made carefully for efficient design of EHD cooling systems.

- At a given operating power of 1.25 W, predictions reveal that a compact EHD cooling system of 6 mm thick, 124 mm wide and 30 mm long, is able to maintain the operating temperature within the typical range, between 40 and 90 ^{o}C, under a thermal load (TDP) up to 20 W. By increasing the thickness to 12 and decreasing the width to 88 mm, the EHD system can maintain the operating temperature below 85 ^{o}C for a TDP of 30 W.

- Unlike conventional rotary blowers, integrated EHD blowers have flexible structure design with the ability of reducing the height and increasing the width as required, offering a unique feature to be installed in low-profile laptops.

Compared to traditional cooling systems used in the current standard laptops, the proposed EHD systems show promising cooling performance for laptops operated at higher TDP with reduced thermal solution volume and low height profile.

While most previous studies have focused on improving EHD flow generation for general applications using macro-scale geometries regardless of the level of applied voltage or consumed electrical power, only few attempts have been made to develop efficient and high performance EHD cooling systems for real-world applications. However, this step requires significant efforts to meet the thermal management requirements and overtake the associated failure modes of EHD technology such as electrode degradation and dust accumulation, as well as reducing the ozone production. In fact, the real implementation of EHD cooling systems in electronic devices can reflect the real challenges and integration difficulties and guide the efforts to develop efficient designs of EHD devices with long term reliability and acceptable ozone generation.

One of the inherent requirements of EHD technology is the high voltage source required to initiate and sustain the corona discharge, which may represent a challenge depending on the application scale. For example, when the EHD devices are employed as a cooling solution in macro-scale electronic applications such as desktop computers or game consoles, the high voltage source, the level of operating voltage, and even installation space for a voltage converter are not likely to represent technical challenges. However, in small-scale and thin microelectronics such as portable laptops, where both the profile height and integration volume are restricted, the design of a compact voltage converter capable of converting a 12 V DC voltage of a laptop battery to the level required to operate the EHD cooling system (approximately 3 kV) represents one of the integration challenges [25].

As the EHD blowers investigated in this thesis were developed and proposed to be employed in the field of thermal management microelectronic applications, this thesis strived to minimize both the blower size and level of operating conditions by using optimization methods established based on the effective level of applied voltage, and suggested integrated EHD cooling systems operated at low voltage of approximately 3.5 kV for cooling compact heat sinks in thin laptops. Indeed, the

applied voltage of 3 kV mentioned in [25] is the not a threshold but it mainly depended on the required EHD flow rate and the design of EHD cooling system developed in the reference, which mainly related to the corona wire diameter and electrode gap, while reducing the maximum level of voltage to less than 3 kV can be obtained by using smaller electrode arrangement, as that presented in [159]. Moreover, reducing the levels of operating conditions may contribute in decreasing the chances of electrode failure due to corona discharge process and leads to improved device reliability.

In summary, although there is not a commercial microelectronic application cooled based on EHD technology on the market to date, the continuous development efforts could yield EHD thermal management products in the near future. In this direction, significant efforts have been made and supported by Tessera Technologies after the successful integration of an EHD system into a real-world laptop application presented in 2009 [25]. Since that time, the foundation stone was laid by Jewell-Larsen, who is the author of a number of patents in the EHD development area (e.g., [229, 230]), and a research group from the University of Washington in collaboration with Kronos Air technologies toward commercially producing EHD cooling devices for microelectronics modules such as notebooks. Furthermore, a patent application published by the US Patent and Trademark Office [231] revealed the intention of the Apple Company to insert the ionic wind generator technique in its products industry. According to an Apple report, this progress will extend the range of options to use specialty sensors and mechanisms, and also lead to possibility of steering the air cooling system to reach different areas inside a computer or microelectronic device [232].

Eventually, the criterion of the success or failure of the EHD devices as a thermal management cooling solution mainly depends on the need of the growing microelectronics technology for the key advantages and novel merits of EHD air movers such as their flexible form factor, silent operation, small and thin installation volume, promising cooling performance and competitive heat transfer capabilities.

7.2 Future work

EHD technology still requires more research and development before being commercially adopted for consumer microelectronic applications. This thesis has highlighted the novel merits of EHD air movers and revealed their ability to compete with mechanical centrifugal fans in terms of cooling performance in miniaturized structures, uniform outlet velocity profile, and efficient flow generation for effective heat removal in reduced installation volume and thin applications. However, future scientific research and industrial development are needed to focus on the following areas.

7.2.1 Modelling tools

Although the modelling of EHD flow presented in this thesis and that performed in previous studies has demonstrated good accuracy at predicting the performance and pumping efficiency of EHD systems, further modelling efforts would be useful to be improved.

- Further numerical investigations on the geometric and operating conditions of EHD devices, with the inclusion of the impact of chemical reactions in plasmas, material of electrodes and environmental factors, can improve the modelling reliability to better understand the electric field distributions, charge and current densities, and ozone production for feasible EHD devices and long term operation.

- Peek's empirical equation based numerical modelling methods have shown accuracy compared to experiments to calculate the electric field created by wire or sphere emitter geometries. However, more developments are needed to extend the ability of Peek's equation to predict electric the field created by complex emitter geometries.

- Including ozone predictions in EHD modelling can aid in design optimization, not only based on performance and efficiency, but also to minimize ozone generation. Although it is complex, using correlations for ozone destruction and including integrated material in the modelling would be useful for improved design optimization.

7.2.2 System design and integration

In this thesis, a set of EHD blowers have been integrated with a classic structure of heat exchanger of parallel plate fins as a cooling system. However, the attractive features of EHD devices with a wide range of flexibility need specific designs of thermal systems to achieve the optimum cooling performance. This in turn requires from designers and industries to increase their attention on the unique integration merits and capabilities of EHD air movers that meet the growing demand for ultra-thin consumer microelectronics. This can be considered with the ability of EHD devices to control flow velocities and directions within the thermal system with a rapid switching or changing pressure head. Moreover, further developments on the optimization of multi-stage designs for EHD systems in integration with heat exchange surfaces are required for improved flow rates, reduced operating voltage and installation space, and effective cooling performance.

7.2.3 Integration with other technologies

Although this thesis has focused on the development of EHD blowers for primary airflows, EHD flow can be used in the presence of bulk flow to disturb flows and enhance heat dissipation in thermal management systems, as presented earlier in this thesis. In this light, EHD air movers can be integrated with rotary fans or other mechanical air cooling technologies such as synthetic jets and piezo fans, and optimized together for improved cooling performance that cannot be achieved by anyone of these technologies individually. As part of hybrid technology development, electrostatic forces in liquids can also be employed to improve liquid transport in ultra-thin heat pipes used in cooling systems.

7.2.4 Other challenges

Due to the corona discharge possess, EHD flow is associated with several disadvantages such as, ozone production, reliability, and the need for compact high voltage multipliers. The absence of any commercial application cooled by EHD driven flow in the market to date reveals that these issues may remain challenges and need more research.

7.2.4.1 Ozone production

As presented early in Chapter 1, ozone is an undesirable by-product of the ion generation process in air. In addition to the use of positive polarity and very fine emitter electrode, further research for reduced ozone generation can be devoted in the following directions:

- Optimization of EHD devices for reduced ion current in a balance with maintaining the pumping performance.
- Integrating improved catalyst materials in the EHD systems at optimized locations downstream of corona wire to destruct ozone before leaving with the produced air.
- Research for catalyst materials of high capability to destruct ozone and investigation for the optimal material shape within the flow channel to reduce flow restrictions.

7.2.4.2 Reliability

Although EHD devices have no moving parts in their operating mechanism, emitter electrode degradation and dust accumulation represent major challenges against reliability. Degradation on corona electrode surface is mainly caused due to associated chemical and ionization processes such as oxidation and erosion through ion bombardment, leading to a reduced device life. Ingress of dust into the EHD cooling system and its accumulation on the corona electrode and heat exchange surfaces lead to reductions in the pumping and thermal performance and longevity of EHD devices. The following development areas can lead to improved reliability:

- Investigation and research for reliable materials for emitter and collector electrodes that offer long-time operation under the effects of corona discharge process.

- Development of flow control systems using smart algorithms that manage the operating power and voltage as required can offer improved EHD device lifetime.

- Using pre-filters for the pulled air into the EHD blower to reduce the dust particles entering the system during operation.

- Development of designs that enable easy removal and cleaning of dust and debris from the EHD device

7.2.4.3 The need for high voltage

The use of EHD driven flow in thin microelectronics requires a compact and low-cost high voltage power supply (usually on the order of kilovolts) that is able to initiate and sustain corona discharge. However, although this may seem a challenge against EHD technology to be practically adopted, compact high voltage power supplies used in laptops' monitor backlights for the cold cathode florescent lamp (CCFL) can be feasible for EHD devices but they will require further development and miniaturization [25].

References

1. Shao, S., D. Liu, Y. Niu, K. O'Donnell, D. Sengupta, and S. Park, *A Study on the Thermomechanical Reliability Risks of Through-Silicon-Vias in Sensor Applications.* Sensors, 2017. **17**(2): p. 322.
2. Moore, G., *Cramming more components onto integrated circuits,[Electronics, vol. 38.* Apr, 1965. **19**: p. 114-117.
3. International Technology Roadmap for Semiconductors (ITRS) 2015; Available from: https://www.semiconductors.org/.
4. Stanford, E. *Power delivery challenges in computer platforms*. in *Applied Power Electronics Conference–Plenary Session*. 2006.
5. Samsung Electronics 2017; Available from: https://news.samsung.com/global/.
6. Bu, H. IBM Research 2017; Available from: https://www.ibm.com/blogs/think/2017/06/5-nanometer-transistors/.
7. Waldrop, M.M., *The chips are down for Moore's law.* Nature, 2016. **530**(7589): p. 144-147.
8. Wang, H.-C., N.E. Jewell-Larsen, and A.V. Mamishev, *Thermal management of microelectronics with electrostatic fluid accelerators.* Applied Thermal Engineering, 2013. **51**(1): p. 190-211.
9. Böhm, J., *Electrostatic precipitators*. Vol. 14. 1982: Elsevier Science & Technology.
10. Kihm, K., M. Mitchner, and S. Self, *Comparison of wire—plate and plate—plate electrostatic precipitators in turbulent flow.* Journal of electrostatics, 1987. **19**(1): p. 21-32.
11. Enliang, L., W. Yingmin, and J.A. Raper, *Study of gas velocity distribution in electrostatic precipitators.* Aerosol Science and Technology, 1990. **12**(4): p. 947-952.
12. Park, S.J. and S.S. Kim, *Electrohydrodynamic flow and particle transport mechanism in electrostatic precipitators with cavity walls.* Aerosol Science & Technology, 2000. **33**(3): p. 205-221.
13. Adamiak, K. and P. Atten, *Numerical simulation of the 2-D gas flow modified by the action of charged fine particles in a single-wire ESP*. IEEE Transactions on Dielectrics and Electrical Insulation, 2009. **16**(3): p. 608-614.
14. Niewulis, A., J. Podlinski, V. Shapoval, and J. Mizeraczyk, *Collection efficiency in narrow electrostatic precipitators with a longitudinal or transverse wire electrode.* IEEE Transactions on Dielectrics and Electrical Insulation, 2011. **18**(5): p. 1423-1428.
15. Bastien, F., *Acoustics and gas discharges: applications to loudspeakers.* Journal of Physics D: Applied Physics, 1987. **20**(12): p. 1547.
16. Béquin, P., V. Montembault, and P. Herzog, *Modelling of negative point-to-plane corona loudspeaker.* The European Physical Journal Applied Physics, 2001. **15**(1): p. 57-67.

17. Krichtafovitch, I.A., S.V. Karpov, N.E. Jewell-Larsen, J. Oharah, and V. Korolev. *EFA Loudspeakers*. in *Proc. ESA Annual Meeting on Electrostatics*. 2008.

18. Jyumonji, M. and H. Uchiyama, *Field experiment on the abatement of stock-raising odors by an electrostatic fog-liquefier.* Journal of electrostatics, 1997. **40**: p. 645-650.

19. Uchiyama, H. and M. Jyumonji, *Field experiments of an electrostatic fog-liquefier.* Journal of electrostatics, 1995. **35**(1): p. 133-143.

20. Uchiyama, H. and M. Jyumonji, *Development of an electrostatic fogliquefier and its field experiments.* Japanese Journal of Applied Physics, 1989. **28**(11R): p. 2319.

21. Kelly-Wintenberg, K., A. Hodge, T. Montie, L. Deleanu, D. Sherman, J.R. Roth, et al., *Use of a one atmosphere uniform glow discharge plasma to kill a broad spectrum of microorganisms.* Journal of Vacuum Science & Technology A, 1999. **17**(4): p. 1539-1544.

22. Yamamoto, M., M. Nishioka, and M. Sadakata, *Sterilization by H 2 O 2 droplets under corona discharge.* Journal of Electrostatics, 2002. **55**(2): p. 173-187.

23. Hsu, C.-P., N.E. Jewell-Larsen, I.A. Krichtafovitch, and A.V. Mamishev, *Heat-transfer-enhancement measurement for microfabricated electrostatic fluid accelerators.* Journal of Microelectromechanical Systems, 2009. **18**(1): p. 111-118.

24. Hand, J. *Silent Air Cooling: A New Approach to Thermal Management.* Electronics Cooling 2013; Available from: https://www.comsol.com/story/download/179895/Tessera_CN2013.pdf.

25. Jewell-Larsen, N., H. Ran, Y. Zhang, M. Schwiebert, K.H. Tessera, and A. Mamishev. *Electrohydrodynamic (EHD) cooled laptop*. in *Semiconductor Thermal Measurement and Management Symposium, 2009. SEMI-THERM 2009. 25th Annual IEEE*. 2009. IEEE.

26. Go, D.B., S.V. Garimella, T.S. Fisher, and R.K. Mongia, *Ionic winds for locally enhanced cooling.* Journal of Applied Physics, 2007. **102**(5): p. 053302.

27. Go, D.B., R.A. Maturana, T.S. Fisher, and S.V. Garimella, *Enhancement of external forced convection by ionic wind.* International Journal of Heat and Mass Transfer, 2008. **51**(25): p. 6047-6053.

28. Yang, F., *Corona-driven air propulsion for cooling of microelectronics.* Master Thesis, University of Washington, Seattle, WA, 2002.

29. United States Environmental Protection Agency (EPA) 2017; Available from: https://www.epa.gov/ozone-pollution/2015-national-ambient-air-quality-standards-naaqs-ozone.

30. Lagarias, J., *Discharge electrodes and electrostatic precipitators.* Journal of the Air Pollution Control Association, 1960. **10**(4): p. 271-274.

31. Moon, J.D., S.T. Geum, G.T. Lee, and D.K. Park, *Corona discharge and ozone generation characteristics of a point-plate type nonthermal plasma*

reactor with ferroelectric pellet barrier. Journal of the Korean Physical Society, 2001. **38**(6): p. 680-685.

32. Kawamoto, H. and S. Umezu, *Electrostatic micro-ozone fan that utilizes ionic wind induced in pin-to-plate corona discharge system.* Journal of Electrostatics, 2008. **66**(7): p. 445-454.
33. Castle, G.P., I.I. Inculet, and K.I. Burgess, *Ozone generation in positive corona electrostatic precipitators.* IEEE Transactions on Industry and General Applications, 1969(4): p. 489-496.
34. Chen, J. and J.H. Davidson, *Ozone production in the positive DC corona discharge: Model and comparison to experiments.* Plasma chemistry and plasma processing, 2002. **22**(4): p. 495-522.
35. Jewell-Larsen, N., K.A. Honer, and M.K. Schwiebert, *Electronic system with ventilation path through inlet-positioned ehd air mover, over ozone reducing surfaces, and out through outlet-positioned heat exchanger*, 2011, Google Patents.
36. Noll, C.G. and P.A. Lawless, *Comparison of germanium and silicon needles as emitter electrodes for air ionizers.* Journal of electrostatics, 1998. **44**(3): p. 221-238.
37. Ongkodjojo Ong, A., *Electrohydrodynamic Microfabricated Ionic Wind Pumps for Electronics Cooling Applications*, 2013, Case Western Reserve University.
38. Nasser, E., *Fundamentals of gaseous ionization and plasma electronics*. 1971: Wiley-Interscience.
39. Goldman, M., A. Goldman, and R. Sigmond, *The corona discharge, its properties and specific uses.* Pure and Applied Chemistry, 1985. **57**(9): p. 1353-1362.
40. Franke, M. and L. Hogue, *Electrostatic cooling of a horizontal cylinder.* Journal of heat transfer, 1991. **113**(3): p. 544-548.
41. Rickard, M., D. Dunn-Rankin, F. Weinberg, and F. Carleton, *Maximizing ion-driven gas flows.* Journal of Electrostatics, 2006. **64**(6): p. 368-376.
42. Fouad, L. and S. Elhazek, *Effect of humidity on positive corona discharge in a three electrode system.* Journal of Electrostatics, 1995. **35**(1): p. 21-30.
43. Wang, X. and C. You, *Effect of humidity on negative corona discharge of electrostatic precipitators.* IEEE Transactions on Dielectrics and Electrical Insulation, 2013. **20**(5): p. 1720-1726.
44. Jewell-Larsen, N., S. Karpov, H. Ran, P. Savalia, and K. Honer. *Investigation of dust in electrohydrodynamic (EHD) systems*. in *Semiconductor Thermal Measurement and Management Symposium, 2010. SEMI-THERM 2010. 26th Annual IEEE*. 2010. IEEE.
45. Rickard, M., D. Dunn-Rankin, F. Weinberg, and F. Carleton, *Characterization of ionic wind velocity.* Journal of Electrostatics, 2005. **63**(6): p. 711-716.
46. Semiconductor Industry Association (SIA) 2017; Available from: http://www.semiconductors.org/.

47. Oprins, H., G. Van der Veken, C.C. Nicole, C.J. Lasance, and M. Baelmans, *On-chip liquid cooling with integrated pump technology.* IEEE Transactions on Components and Packaging Technologies, 2007. **30**(2): p. 209-217.

48. Zimmermann, S., I. Meijer, M.K. Tiwari, S. Paredes, B. Michel, and D. Poulikakos, *Aquasar: A hot water cooled data center with direct energy reuse.* Energy, 2012. **43**(1): p. 237-245.

49. Hopton, P. and J. Summers. *Enclosed liquid natural convection as a means of transferring heat from microelectronics to cold plates*. in *Semiconductor Thermal Measurement and Management Symposium (SEMI-THERM), 2013 29th Annual IEEE*. 2013. IEEE.

50. Chi, Y.Q., J. Summers, P. Hopton, K. Deakin, A. Real, N. Kapur, et al. *Case study of a data centre using enclosed, immersed, direct liquid-cooled servers*. in *2014 Semiconductor Thermal Measurement and Management Symposium (SEMI-THERM)*. 2014. IEEE.

51. Capozzoli, A. and G. Primiceri, *Cooling Systems in Data Centers: State of Art and Emerging Technologies.* Energy Procedia, 2015. **83**: p. 484-493.

52. Mochizuki, M., T. Nguyen, Y. Saito, T. Nguyen, V. Wuttijumnong, and M.S. Ahamed. *Development of High Performance Thin Heat Pipe for Cooling Small Form Factor Devices*. in *2010 14th International Heat Transfer Conference*. 2010. American Society of Mechanical Engineers.

53. Yadavalli, Y., J.A. Weibel, and S.V. Garimella, *Performance-Governing Transport Mechanisms for Heat Pipes at Ultrathin Form Factors.* IEEE Transactions on Components, Packaging and Manufacturing Technology, 2015. **5**(11): p. 1618-1627.

54. Jiang, L., J. Mikkelsen, J.-M. Koo, D. Huber, S. Yao, L. Zhang, et al., *Closed-loop electroosmotic microchannel cooling system for VLSI circuits.* IEEE Transactions on Components and Packaging Technologies, 2002. **25**(3): p. 347-355.

55. Kandlikar, S.G. and H.R. Upadhye. *Extending the heat flux limit with enhanced microchannels in direct single-phase cooling of computer chips*. in *Semiconductor Thermal Measurement and Management IEEE Twenty First Annual IEEE Symposium, 2005*. 2005. IEEE.

56. Colgan, E.G., B. Furman, M. Gaynes, W.S. Graham, N.C. LaBianca, J.H. Magerlein, et al., *A practical implementation of silicon microchannel coolers for high power chips.* IEEE Transactions on Components and Packaging Technologies, 2007. **30**(2): p. 218-225.

57. Baird, E. and K. Mohseni, *Digitized heat transfer: a new paradigm for thermal management of compact micro systems.* IEEE Transactions on Components and packaging Technologies, 2008. **31**(1): p. 143-151.

58. Bleier, F.P., *Fan Handbook: selection, application, and design*. 1998: McGraw-Hill New York.

59. Walsh, P., V. Egan, R. Grimes, and E. Walsh. *Scaling of Flow Characteristics and Power Consumption With Profile Height for Miniature Centrifugal Fans*. in *ASME 2007 5th International Conference on Nanochannels,*

Microchannels, and Minichannels. 2007. American Society of Mechanical Engineers.

60. Quin, D., *Micro scale axial flow fans.* Stokes Research Institute, Dept. of Mechanical and Aeronautical Engineering, PhD, University of Limerick, Limerick, Ireland, 2006.

61. Quin, D. and R. Grimes, *The effect of reynolds number on microaxial flow fan performance.* Journal of Fluids Engineering, 2008. **130**(10): p. 101101.

62. Day, S.W., P.P. Lemire, R.D. Flack, and J.C. McDaniel. *Effect of Reynolds Number on Performance of a Small Centrifugal Pump*. in *ASME/JSME 2003 4th Joint Fluids Summer Engineering Conference*. 2003. American Society of Mechanical Engineers.

63. Hanly, K., R. Grimes, E. Walsh, B. Rodgers, and J. Punch. *The effect of Reynolds number on the aerodynamic performance of micro radial flow fans*. in *ASME 2005 Summer Heat Transfer Conference collocated with the ASME 2005 Pacific Rim Technical Conference and Exhibition on Integration and Packaging of MEMS, NEMS, and Electronic Systems*. 2005. American Society of Mechanical Engineers.

64. Grimes, R., P. Walsh, E. Walsh, and V. Egan. *The Effects of Diameter and Rotational Speed on the Aerodynamic Performance of Low Profile Miniature Radial Flow Fans*. in *ASME 2007 5th International Conference on Nanochannels, Microchannels, and Minichannels*. 2007. American Society of Mechanical Engineers.

65. Walsh, E., P. Walsh, J. Punch, and R. Grimes, *Acoustic emissions from active cooling solutions for portable devices.* IEEE Transactions on Components and Packaging Technologies, 2009. **32**(4): p. 776-783.

66. Rodgers, P., V. Eveloy, and M.G. Pecht. *Limits of air-cooling: Status and challenges*. in *Semiconductor Thermal Measurement and Management Symposium, 2005 IEEE Twenty First Annual IEEE*. 2005. IEEE.

67. Abali, B., D. Guthridge, R. Harper, P. Manson, and H. Marr, *Mutual active cancellation of fan noise and vibration*, 2004, Google Patents.

68. Mahalingam, R., S. Heffington, L. Jones, and M. Schwickert. *Newisys server processor cooling augmentation using synthetic jet ejectors*. in *Thermal and Thermomechanical Proceedings 10th Intersociety Conference on Phenomena in Electronics Systems, 2006. ITHERM 2006.* 2006. IEEE.

69. Mahalingam, R., N. Rumigny, and A. Glezer, *Thermal management using synthetic jet ejectors.* IEEE Transactions on components and packaging technologies, 2004. **27**(3): p. 439-444.

70. Kercher, D.S., J.-B. Lee, O. Brand, M.G. Allen, and A. Glezer, *Microjet cooling devices for thermal management of electronics.* IEEE Transactions on Components and Packaging Technologies, 2003. **26**(2): p. 359-366.

71. Campbell, S., W. Black, A. Glezer, and J. Hartley. *Thermal management of a laptop computer with synthetic air microjets*. in *Thermal and Thermomechanical Phenomena in Electronic Systems, 1998. ITHERM'98. The Sixth Intersociety Conference on*. 1998. IEEE.

72. Go, D.B. and R.K. Mongia. *Experimental studies on synthetic jet cooling enhancement for portable platforms*. in *Thermal and Thermomechanical Phenomena in Electronic Systems, 2008. ITHERM 2008. 11th Intersociety Conference on*. 2008. IEEE.

73. Wang, Y., G. Yuan, Y.-K. Yoon, M.G. Allen, and S.A. Bidstrup, *Optimization of synthetic jet fluidic structures in printed wiring boards.* Journal of electronic packaging, 2006. **128**(4): p. 353-359.

74. Mahalingam, R. and A. Glezer, *Design and thermal characteristics of a synthetic jet ejector heat sink.* Journal of Electronic Packaging, 2005. **127**(2): p. 172-177.

75. Chaudhari, M.B., B. Puranik, and A. Agrawal, *Heat transfer characteristics of a heat sink in presence of a synthetic jet.* IEEE Transactions on Components, Packaging and Manufacturing Technology, 2012. **2**(3): p. 457-463.

76. Jones, L. *Synthetic jet cooling for small form factor computing*. 2014; Available from: http://smallformfactors.mil-embedded.com/articles/synthetic-form-factor-computing/.

77. Tesař, V., C.-H. Hung, and W.B. Zimmerman, *No-moving-part hybrid-synthetic jet actuator*. Sensors and Actuators A: Physical, 2006. **125**(2): p. 159-169.

78. Schwickert, M., *Synjet thermal management technology increases led lighting system reliability*. IEEE Reliability Society Annual Technical Report 2009, 2009.

79. Ahearn, R. *Active cooling can boost lumen output in LED lighting*. LEDs Magazine 2011; Available from: http://www.ledsmagazine.com/articles/print/volume-8/issue-6/features/active-cooling-can-boost-lumen-output-in-led-lighting-magazine.html.

80. Açikalin, T., S.V. Garimella, J. Petroski, and A. Raman. *Optimal design of miniature piezoelectric fans for cooling light emitting diodes*. in *Thermal and Thermomechanical Phenomena in Electronic Systems, 2004. ITHERM'04. The Ninth Intersociety Conference on*. 2004. IEEE.

81. Kimber, M., S.V. Garimella, and A. Raman. *An experimental study of fluidic coupling between multiple piezoelectric fans*. in *Thermal and Thermomechanical Proceedings 10th Intersociety Conference on Phenomena in Electronics Systems, 2006. ITHERM 2006.* 2006. IEEE.

82. Wait, S.M., S. Basak, S.V. Garimella, and A. Raman, *Piezoelectric fans using higher flexural modes for electronics cooling applications.* IEEE transactions on components and packaging technologies, 2007. **30**(1): p. 119-128.

83. Petroski, J., M. Arik, and M. Gursoy, *Optimization of piezoelectric oscillating fan-cooled heat sinks for electronics cooling.* IEEE Transactions on Components and Packaging Technologies, 2010. **33**(1): p. 25-31.

84. Ma, H., H. Su, C. Liu, and W. Ho, *Investigation of a piezoelectric fan embedded in a heat sink.* International Communications in Heat and Mass Transfer, 2012. **39**(5): p. 603-609.

85. Kimber, M., S.V. Garimella, and A. Raman, *Local heat transfer coefficients induced by piezoelectrically actuated vibrating cantilevers.* Journal of Heat Transfer, 2007. **129**(9): p. 1168-1176.

86. Sufian, S., M. Abdullah, and J. Mohamed, *Effect of synchronized piezoelectric fans on microelectronic cooling performance.* International Communications in Heat and Mass Transfer, 2013. **43**: p. 81-89.

87. Sufian, S., Z. Fairuz, M. Zubair, M. Abdullah, and J.J. Mohamed, *Thermal analysis of dual piezoelectric fans for cooling multi-LED packages.* Microelectronics Reliability, 2014. **54**(8): p. 1534-1543.

88. Ma, H., S. Liao, Y. Li, Y. Li, and C. Liu. *The application of micro multiple piezoelectric-magnetic fans (m-MPMF) on LEDs thermal management*. in *2014 Semiconductor Thermal Measurement and Management Symposium (SEMI-THERM)*. 2014. IEEE.

89. Fukue, T., K. Hirose, and H. Terao. *Cooling performance of impinging jet from piezoelectric micro blower mounted in narrow flow passage*. in *Electronics Packaging and iMAPS All Asia Conference (ICEP-IACC), 2015 International Conference on*. 2015. IEEE.

90. Maaspuro, M., *Piezoelectric oscillating cantilever fan for thermal management of electronics and LEDs—A review.* Microelectronics Reliability, 2016. **63**: p. 342-353.

91. Hippler, R., S. Pfau, M. Schmidt, and K.H. Schoenbach, *Low temperature plasma physics: fundamental aspects and applications.* Low Temperature Plasma Physics: Fundamental Aspects and Applications, by Rainer Hippler (Editor), Sigismund Pfau (Editor), Martin Schmidt (Editor), Karl H. Schoenbach (Editor), pp. 530. ISBN 3-527-28887-2. Wiley-VCH, June 2001., 2001. **1**.

92. Loeb, L.B., *Fundamental processes of electrical discharge in gases*. 1939: John Wiley & Sons.

93. Loeb, L.B., *Electrical coronas: their basic physical mechanisms*. 1965: University of California press.

94. Morrow, R., *Theory of positive corona in SF 6 due to a voltage impulse.* IEEE Transactions on Plasma Science, 1991. **19**(2): p. 86-94.

95. Morrow, R., *The theory of positive glow corona.* Journal of Physics D: Applied Physics, 1997. **30**(22): p. 3099.

96. Chen, J., *Direct current corona-enhanced chemical reactions*, 2002, UNIVERSITY OF MINNESOTA.

97. Kaptsov, N., *Elektricheskie yavleniya v gazakh i vakuume.* Moscow, OGIZ, 1947.

98. Platzman, R.L., *Basic Processes of Gaseous Electronics.* Journal of the American Chemical Society, 1956. **78**(10): p. 2343-2344.

99. Cobine, J.D., *Gaseous conductors: theory and engineering applications*. 1958: Dover Publications.

100. Morrow, R., *Theory of negative corona in oxygen.* Physical Review A, 1985. **32**(3): p. 1799.

101. Aleksandrov, G., *Physical conditions for the formation of an alternating-current corona discharge.* Soviet Phys. Tech. Phys, 1956: p. 1714-1726.

102. Boelter, K., *Ozone Generation of Indoor Electronic Air Cleaners*. 1996.

103. Owsenek, B., J. Seyed-Yagoobi, and R. Page, *Experimental investigation of corona wind heat transfer enhancement with a heated horizontal flat plate.* Journal of Heat Transfer, 1995. **117**(2): p. 309-315.

104. Moreau, E. and G. Touchard, *Enhancing the mechanical efficiency of electric wind in corona discharges.* Journal of Electrostatics, 2008. **66**(1): p. 39-44.

105. Moon, J.-D., J.-S. Jung, J.-G. Kim, and S.-T. Geum, *An EHD gas pump utilizing a wet porous point electrode.* IEEE Transactions on Dielectrics and Electrical Insulation, 2009. **16**(3): p. 622-628.

106. Chang, J.-S., P.A. Lawless, and T. Yamamoto, *Corona discharge processes.* IEEE Transactions on plasma science, 1991. **19**(6): p. 1152-1166.

107. Huang, R.-T., W.-J. Sheu, and C.-C. Wang, *Heat transfer enhancement by needle-arrayed electrodes–An EHD integrated cooling system.* energy Conversion and Management, 2009. **50**(7): p. 1789-1796.

108. Yonggang, Y., H. Junping, A. Zhongliang, Y. Lanjun, and Z. Qiaogen, *Experimental studies of the enhanced heat transfer from a heating vertical flat plate by ionic wind.* Plasma Science and Technology, 2006. **8**(6): p. 697.

109. Kalman, H. and E. Sher, *Enhancement of heat transfer by means of a corona wind created by a wire electrode and confined wings assembly.* Applied Thermal Engineering, 2001. **21**(3): p. 265-282.

110. Bérard, P., D. Lacoste, and C. Laux, *Corona discharges in atmospheric air between a wire and two plates.* IEEE Transactions on Plasma Science, 2011. **39**(11): p. 2248-2249.

111. Ohkubo, T., S. Hamasaki, Y. Nomoto, J.-S. Chang, and T. Adachi, *The effect of corona wire heating on the downstream ozone concentration profiles in an air-cleaning wire-duct electrostatic precipitator.* IEEE transactions on industry applications, 1990. **26**(3): p. 542-549.

112. Awad, M. and G. Castle, *Ozone generation in an electrostatic precipitator with a heated corona wire.* Journal of the Air Pollution Control Association, 1975. **25**(4): p. 369-374.

113. Chang, J.-S., F. Pontiga, P. Atten, and A. Castellanos, *Hysteresis effect of corona discharge in a narrow coaxial wire-pipe discharge tube with gas flow.* IEEE Transactions on Industry Applications, 1996. **32**(6): p. 1250-1256.

114. Hauksbee, F., *Physico-Mechanical Experiments on Various Subjects.* Containing an Account of Several Surprizing Phaenomena Touching Light and Electricity, Producible on the Attrition of Bodies. London, 1709.

115. Newton, I., *Opticks.* 1718.

116. Faraday, M., *Experimental researches in electricity. fifteenth series.* Philosophical Transactions of the Royal Society of London, 1839. **129**: p. 1-12.

117. Maxwell, J., *Treatise in magnetism and electricity.* Vol. II, Art, 1873: p. 717-719.

118. Stuetzer, O.M., *Ion drag pressure generation.* Journal of Applied Physics, 1959. **30**(7): p. 984-994.

119. Robinson, M., *Movement of air in the electric wind of the corona discharge.* American Institute of Electrical Engineers, Part I: Communication and Electronics, Transactions of the, 1961. **80**(2): p. 143-150.

120. Yabe, A., Y. Mori, and K. Hijikata, *EHD study of the corona wind between wire and plate electrodes.* AIAA journal, 1978a. **16**(4): p. 340-345.

121. Marco, S. and H. Velkoff, *Effect of electrostatic fields on free-convection heat transfer from flat plates.* ASME Paper No. 63-HT-9, 1963.

122. Velkoff, H.R., *Investigation of the Effects of Electrostatic Fields on Heat Transfer and Boundary Layers*. 1962.

123. Maskell, B., *The effect of humidity on a corona discharge in air*, 1970, DTIC Document.

124. Hu, Q., L. Shu, X. Jiang, C. Sun, S. Zhang, and Y. Shang, *Effects of air pressure and humidity on the corona onset voltage of bundle conductors.* IET generation, transmission & distribution, 2011. **5**(6): p. 621-629.

125. Hu, Q., L. Shu, X. Jiang, C. Sun, Z. Qiu, and R. Lin, *Influence of air pressure and humidity on positive direct current corona discharge performances of the conductor in a corona cage.* International Transactions on Electrical Energy Systems, 2014. **24**(5): p. 723-735.

126. Abdel-Salam, M., A. Mizuno, and K. Shimizu, *Ozone generation as influenced by gas flow in corona reactors.* Journal of Physics D: Applied Physics, 1997. **30**(5): p. 864.

127. Allen, P. and T. Karayiannis, *Electrohydrodynamic enhancement of heat transfer and fluid flow.* Heat Recovery Systems and CHP, 1995. **15**(5): p. 389-423.

128. Ohadi, M., J. Darabi, and B. Roget, *Electrode design, fabrication, and materials science for EHD-enhanced heat and mass transport.* Annual Review of Heat Transfer, 2000. **11**(11).

129. Molki, M. and K.L. Bhamidipati, *Enhancement of convective heat transfer in the developing region of circular tubes using corona wind.* International Journal of Heat and Mass Transfer, 2004. **47**(19): p. 4301-4314.

130. Laohalertdecha, S., P. Naphon, and S. Wongwises, *A review of electrohydrodynamic enhancement of heat transfer.* Renewable and Sustainable Energy Reviews, 2007. **11**(5): p. 858-876.

131. Fylladitakis, E.D., M.P. Theodoridis, and A.X. Moronis, *Review on the history, research, and applications of electrohydrodynamics.* Plasma Science, IEEE Transactions on, 2014. **42**(2): p. 358-375.

132. Stuetzer, O.M., *Ion drag pumps.* Journal of Applied Physics, 1960. **31**(1): p. 136-146.

133. Qiu, W., L. Xia, X. Tan, and L. Yang, *The velocity characteristics of a serial-Staged EHD gas pump in air.* IEEE Transactions on Plasma Science, 2010. **38**(10): p. 2848-2853.

134. Wei, Q., X. Lingzhi, Y. Lanjun, Z. Qiaogen, X. Lei, and C. Li, *Experimental study on the velocity and efficiency characteristics of a serial staged needle array-mesh type EHD gas pump.* Plasma Science and Technology, 2011. **13**(6): p. 693.

135. Moon, J.-D., D.-h. Hwang, and S.-T. Geum, *An EHD gas pump utilizing a ring/needle electrode.* IEEE Transactions on Dielectrics and Electrical Insulation, 2009. **16**(2): p. 352-358.

136. June, M.S., J. Kribs, and K.M. Lyons, *Measuring efficiency of positive and negative ionic wind devices for comparison to fans and blowers.* Journal of Electrostatics, 2011. **69**(4): p. 345-350.

137. Komeili, B., J. Chang, G. Harvel, C. Ching, and D. Brocilo, *Flow characteristics of wire-rod type electrohydrodynamic gas pump under negative corona operations.* Journal of Electrostatics, 2008. **66**(5): p. 342-353.

138. Colas, D.F., A. Ferret, D.Z. Pai, D.A. Lacoste, and C.O. Laux, *Ionic wind generation by a wire-cylinder-plate corona discharge in air at atmospheric pressure.* Journal of applied physics, 2010. **108**(10): p. 103306.

139. Yabe, A., Y. Mori, and K. Hijikata, *Heat transfer augmentation around a downward-facing flat plate by non-uniform electric fields.* Proc. 6th Int. Heat Transfer Conf., 1978. **3**(Paper M-20): p. 171-176.

140. Owsenek, B. and J. Seyed-Yagoobi, *Theoretical and experimental study of electrohydrodynamic heat transfer enhancement through wire-plate corona discharge.* Journal of Heat Transfer, 1997. **119**(3): p. 604-610.

141. Robinson, M., *Convective heat transfer at the surface of a corona electrode.* International Journal of Heat and Mass Transfer, 1970. **13**(2): p. 263-274.

142. MIZUSHINA, T., H. UEDA, T. MATSUMOTO, and K. WAGA, *Effect of electrically induced convection on heat transfer of air flow in an annulus.* Journal of Chemical Engineering of Japan, 1976. **9**(2): p. 97-102.

143. Velkoff, H. and R. Godfrey, *Low-velocity heat transfer to a flat plate in the presence of a corona discharge in air.* Journal of Heat Transfer, 1979. **101**(1): p. 157-163.

144. Nelson, D., M. Ohidi, S. Zia, and R. Whipple. *Electrostatic effects on heat transfer and pressure drop in cylindrical geometries*. in *Proceedings of the 1991 ASME JSME thermal engineering joint conference*. 1991.

145. Tada, Y., A. Takimoto, and Y. Hayashi, *Heat transfer enhancement in a convective field by applying ionic wind.* Journal of Enhanced Heat Transfer, 1997. **4**(2).

146. Léger, L., E. Moreau, G. Artana, and G. Touchard, *Influence of a DC corona discharge on the airflow along an inclined flat plate.* Journal of Electrostatics, 2001. **51**: p. 300-306.

147. Léger, L., E. Moreau, and G.G. Touchard, *Effect of a DC corona electrical discharge on the airflow along a flat plate.* IEEE Transactions on Industry Applications, 2002. **38**(6): p. 1478-1485.

148. Moreau, E., L. Léger, and G. Touchard, *Effect of a DC surface-corona discharge on a flat plate boundary layer for air flow velocity up to 25m/s.* Journal of electrostatics, 2006. **64**(3): p. 215-225.

149. Shooshtari, A., M. Ohadi, and F.H. França. *Experimental and numerical analysis of electrohydrodynamic enhancement of heat transfer in air laminar channel flow*. in *Semiconductor Thermal Measurement and Management Symposium, 2003. Ninteenth Annual IEEE*. 2003. IEEE.

150. Ohadi, M., D. Nelson, and S. Zia, *Heat transfer enhancement of laminar and turbulent pipe flow via corona discharge.* International Journal of Heat and Mass Transfer, 1991. **34**(4): p. 1175-1187.

151. Bart, S.F., L.S. Tavrow, M. Mehregany, and J.H. Lang, *Microfabricated electrohydrodynamic pumps.* Sensors and Actuators A: Physical, 1990. **21**(1): p. 193-197.

152. Richter, A. and H. Sandmaier. *An electrohydrodynamic micropump*. in *Micro Electro Mechanical Systems, 1990. Proceedings, An Investigation of Micro Structures, Sensors, Actuators, Machines and Robots. IEEE*. 1990. IEEE.

153. Go, D.B., R. Maturana, R.K. Mongia, S.V. Garimella, and T.S. Fisher. *Ionic Winds for Enhanced Cooling in Portable Platforms*. in *Electronics Packaging Technology Conference, 2008. EPTC 2008. 10th*. 2008. IEEE.

154. Chen, Y., M.-Z. Guo, K.-S. Yang, and C.-C. Wang, *Enhanced cooling for LED lighting using ionic wind.* International Journal of Heat and Mass Transfer, 2013. **57**(1): p. 285-291.

155. Rashkovan, A., E. Sher, and H. Kalman, *Experimental optimization of an electric blower by corona wind.* Applied Thermal Engineering, 2002. **22**(14): p. 1587-1599.

156. Chang, J.-S., H. Tsubone, G.D. Harvel, and K. Urashima. *Capillary/narrow flow channel driven EHD gas pump for an advanced thermal management of micro-electronics*. in *Industry Applications Society Annual Meeting, 2008. IAS'08. IEEE*. 2008. IEEE.

157. Chang, J.-S., H. Tsubone, G.D. Harvel, and K. Urashima, *Narrow-flow-channel-driven ehd gas pump for an advanced thermal management of microelectronics.* IEEE Transactions on Industry Applications, 2010. **46**(3): p. 1151-1158.

158. Tsubone, H., G. Harvel, K. Urashima, K. Akashi, and J. Chang, *Performance Characteristics of Partially Covered Wire-Parallel Plate Electrodes Type Electrohydrodynamic Gas Pumps.* management, 2012. **1**: p. 4.

159. Schlitz, D. and V. Singhal. *An electro-aerodynamic solid-state fan and cooling system*. in *Semiconductor Thermal Measurement and Management Symposium, 2008. Semi-Therm 2008. Twenty-fourth Annual IEEE*. 2008. IEEE.

160. Shin, D.H., S.H. Baek, and H.S. Ko, *Development of heat sink with ionic wind for LED cooling.* International Journal of Heat and Mass Transfer, 2016. **93**: p. 516-528.

161. Jewell-Larsen, N., K. Honer, and G. Joseph, *Electronic system adapted for passive convective cooling and staged use of electrohydrodynamic (ehd) and*

mechanical air movers for quiet forced convection assist, 2012, Google Patents.

162. Jewell-Larsen, N., *Electrohydrodynamic (EHD) fluid mover with field shaping feature at leading edge of collector electrodes*, 2013, Google Patents.
163. Jewell-Larsen, N., Y. Zhang, M. Schwiebert, and K. Honer, *Collector-radiator structure for an electrohydrodynamic cooling system*, 2014, Google Patents.
164. Jewell-Larsen, N.E., G.G. Joseph, and K.A. Honer. *Scaling laws for electrohydrodynamic air movers*. in *ASME/JSME 2011 8th Thermal Engineering Joint Conference*. 2011. American Society of Mechanical Engineers.
165. Feng, J.Q., *Application of Galerkin finite-element method with Newton iterations in computing steady-state solutions of unipolar charge currents in corona devices.* Journal of Computational Physics, 1999. **151**(2): p. 969-989.
166. Feng, J.Q., *An analysis of corona currents between two concentric cylindrical electrodes.* Journal of Electrostatics, 1999. **46**(1): p. 37-48.
167. Townsend, J.S., *The potentials required to maintain currents between coaxial cylinders.* The London, Edinburgh, and Dublin Philosophical Magazine and Journal of Science, 1914. **28**(163): p. 83-90.
168. McDonald, J.R., W.B. Smith, H.W. Spencer III, and L.E. Sparks, *A mathematical model for calculating electrical conditions in wire-duct electrostatic precipitation devices.* Journal of Applied Physics, 1977. **48**(6): p. 2231-2243.
169. Kallio, G.A. and D.E. Stock, *Computation of electrical conditions inside wire-duct electrostatic precipitators using a combined finite-element, finite-difference technique.* Journal of Applied Physics, 1986. **59**(6): p. 1799-1806.
170. Kasayapanand, N. and T. Kiatsiriroat, *EHD enhanced heat transfer in wavy channel.* International communications in heat and mass transfer, 2005. **32**(6): p. 809-821.
171. Hoburg, J. and J. Davis, *Finite element-method of characteristics computations of self-consistent charge density-electric field structures.* Comput. Electromag., 1986: p. 217.
172. Butler, A.J., Z.J. Cendes, and J.F. Hoburg, *Interfacing the finite-element method with the method of characteristics in self-consistent electrostatic field models.* IEEE transactions on industry applications, 1989. **25**(3): p. 533-538.
173. Abdel-Salam, M. and Z. Al-Hamouz, *Finite-element analysis of monopolar ionized fields including ion diffusion.* Journal of Physics D: Applied Physics, 1993. **26**(12): p. 2202.
174. Lean, M.H. and G.A. Domoto, *Charge transport in Navier-Stokes flow*. IEEE Transactions on Magnetics, 1988. **24**(1): p. 262-265.
175. Adamiak, K., *Simulation of corona in wire-duct electrostatic precipitator by means of the boundary element method.* IEEE Transactions on Industry Applications, 1994. **30**(2): p. 381-386.

176. Jewell-Larsen, N., C. Hsu, I. Krichtafovitch, S. Montgomery, J. Dibene, and A.V. Mamishev, *CFD analysis of electrostatic fluid accelerators for forced convection cooling.* Dielectrics and Electrical Insulation, IEEE Transactions on, 2008. **15**(6): p. 1745-1753.

177. Jewell-Larsen, N.E., S.V. Karpov, I.A. Krichtafovitch, V. Jayanty, C.-P. Hsu, and A.V. Mamishev. *Modeling of corona-induced electrohydrodynamic flow with COMSOL multiphysics*. in *Proc. ESA Annual Meeting on Electrostatics, Paper E*. 2008.

178. Havet, M., *Analysis of the EHD enhancement of heat transfer in a flat duct.* IEEE Transactions on Dielectrics and Electrical Insulation, 2009. **16**(2): p. 489-494.

179. Mahmoudi, S.R., K. Adamiak, P. Castle, and M. Ashjaee, *The effect of corona discharge on free convection heat transfer from a horizontal cylinder.* Experimental Thermal and Fluid Science, 2010. **34**(5): p. 528-537.

180. Nahavandi, M. and A. Mehrabani-Zeinabad, *Numerical simulation of electrohydrodynamic effect on natural convection through a vertical enclosure channel.* Asia-Pacific Journal of Chemical Engineering, 2013. **8**(5): p. 756-766.

181. Molki, M. and T. Harirchian. *The Enhancement Effect of Corona Discharge on Natural Convection Heat Transfer in Triangular Channels*. in *ASME 2005 International Mechanical Engineering Congress and Exposition*. 2005. American Society of Mechanical Engineers.

182. Molki, M., M. Ohadi, B. Baumgarten, M. Hasegawa, and A. Yabe, *Heat transfer enhancement of airflow in a channel using corona discharge.* Journal of Enhanced Heat Transfer, 2000. **7**(6).

183. Kasayapanand, N., J. Tiansuwan, W. Asvapoositkul, N. Vorayos, and T. Kiatsiriroat, *Effect of the electrode arrangements in a tube bank on the characteristic of electrohydrodynamic heat transfer enhancement: Low reynolds number.* Journal of Enhanced Heat Transfer, 2002. **9**(5-6): p. 229-242.

184. Kasayapanand, N., *Numerical study of electrode bank enhanced heat transfer.* Applied thermal engineering, 2006. **26**(14): p. 1471-1480.

185. Esmaeilzadeh, E., A. Alamgholilou, H. Mirzaie, and M. Ashna. *Numerical Simulation of Heat Transfer Enhancement in the Presence of an Electric Field at Low Reynolds Numbers*. in *16th Australasian Fluid Mechanics Conference (AFMC)*. 2007. School of Engineering, The University of Queensland.

186. Ayuttaya, S.S.N., C. Chaktranond, and P. Rattanadecho, *Numerical analysis of electric force influence on heat transfer in a channel flow (theory based on saturated porous medium approach).* International Journal of Heat and Mass Transfer, 2013. **64**: p. 361-374.

187. Chua, B., A.S. Wexler, N.C. Tien, D.A. Niemeier, and B.A. Holmen, *Design, fabrication, and testing of a microfabricated corona ionizer.* Journal of Microelectromechanical Systems, 2008. **17**(1): p. 115-123.

188. Ongkodjojo, A., D. Li, R.C. Roberts, Q. Liu, and N.C. Tien. *Modeling and measurement of microfabricated corona discharge structures*. in *Nano/Micro*

Engineered and Molecular Systems, 2008. NEMS 2008. 3rd IEEE International Conference on. 2008. IEEE.

189. Ongkodjojo, A., A.R. Abramson, and N.C. Tien. *Optimized Ionic Wind-Based Cooling Microfabricated Devices for Improving a Measured Coefficient of Performance*. in *ASME/JSME 2011 8th Thermal Engineering Joint Conference*. 2011. American Society of Mechanical Engineers.
190. Abdel-Salam, M. and N. Allen, *Current–voltage characteristics of corona in rod–plane gaps as influenced by temperature.* IEE Proceedings-Science, Measurement and Technology, 2003. **150**(3): p. 135-139.
191. Chen, J. and J.H. Davidson, *Model of the negative DC corona plasma: comparison to the positive DC corona plasma.* Plasma chemistry and plasma processing, 2003. **23**(1): p. 83-102.
192. McDaniel, E.W. and E.A. Mason, *The mobility and diffusion of ions in gases.* 1973.
193. Liu, Y., S. Huang, and L. Zhu, *Influence of humidity and air pressure on the ion mobility based on drift tube method.* CSEE Journal of Power and Energy Systems, 2015. **1**(3): p. 37-41.
194. Karpov, S. and I. Krichtafovitch. *Electrohydrodynamic flow modeling using FEMLAB*. in *Excerpt from the Proceedings of the COMSOL Multiphysics User's Conference 2005 Boston*. 2005.
195. Castellanos, A., *Coulomb-driven convection in electrohydrodynamics.* IEEE Transactions on Electrical insulation, 1991. **26**(6): p. 1201-1215.
196. Borg, X. *Blaze Labs EHD Thrusters Research*. 2017; Available from: http://www.blazelabs.com/.
197. Peek, F.W., *Dielectric phenomena in high voltage engineering*. 1920: McGraw-Hill Book Company, Incorporated.
198. Abdel-Salam, M. and D. Wiitanen, *Calculation of corona onset voltage for duct-type precipitators.* IEEE Transactions on industry applications, 1993. **29**(2): p. 274-280.
199. Medlin, A., C. Fletcher, and R. Morrow, *A pseudotransient approach to steady state solution of electric field-space charge coupled problems.* Journal of electrostatics, 1998. **43**(1): p. 39-60.
200. Wan, C., *Electro-hydrodynamic (EHD) thruster analysis and optimization*, 2009, Master Thesis, COOPER UNION.
201. Jewell-Larsen, N., P. Zhang, C.-P. Hsu, I. Krichtafovitch, and A. Mamishev. *Coupled-physics modeling of electrostatic fluid accelerators for forced convection cooling*. in *9th AIAA/ASME Joint Thermophysics and Heat Transfer Conference*. 2006.
202. Feng, J.Q., *Electrohydrodynamic flow associated with unipolar charge current due to corona discharge from a wire enclosed in a rectangular shield.* Journal of Applied Physics, 1999. **86**(5): p. 2412-2418.
203. COMSOL Multiphysics® Modeling Software 2017; Available from: https://www.comsol.com/.

204. Levin, P.L. and J.F. Hoburg, *Donor cell-finite element descriptions of wire-duct precipitator fields, charges, and efficiencies.* IEEE transactions on industry applications, 1990. **26**(4): p. 662-670.

205. Adamiak, K., *Adaptive approach to finite element modelling of corona fields.* IEEE Transactions on industry applications, 1994. **30**(2): p. 387-393.

206. Tsubone, H., J. Ueno, B. Komeili, S. Minami, G. Harvel, K. Urashima, et al., *Flow characteristics of dc wire-non-parallel plate electrohydrodynamic gas pumps.* Journal of Electrostatics, 2008. **66**(1-2): p. 115-121.

207. Roth, J.R., *Industrial Plasma Engineering: Volume 2-Applications to Nonthermal Plasma Processing*. Vol. 2. 2001: CRC press.

208. Abdel-Salam, M., M. Nakano, and A. Mizuno, *Corona-induced pressures, potentials, fields and currents in electrostatic precipitator configurations.* Journal of Physics D: Applied Physics, 2007. **40**(7): p. 1919.

209. Chang, J., H. Tsubone, Y. Chun, A. Berezin, and K. Urashima, *Mechanism of electrohydrodynamically induced flow in a wire-non-parallel plate electrode type gas pump.* Journal of Electrostatics, 2009. **67**(2-3): p. 335-339.

210. Ghazanchaei, M., K. Adamiak, and G.P. Castle, *Predicted flow characteristics of a wire-nonparallel plate type electrohydrodynamic gas pump using the Finite Element Method.* Journal of Electrostatics, 2015. **73**: p. 103-111.

211. Go, D.B., S.V. Garimella, and T.S. Fisher. *Numerical simulation of microscale ionic wind for local cooling enhancement.* in *Thermal and Thermomechanical Phenomena in Electronics Systems, 2006. ITHERM'06. The Tenth Intersociety Conference on*. 2006. IEEE.

212. Sigmond, R. and I. Lågstad, *Mass and species transport in corona discharges.* High Temp. Chem. Processes, 1993. **2**(4): p. 5.

213. Moreau, E., *Airflow control by non-thermal plasma actuators.* Journal of Physics D: Applied Physics, 2007. **40**(3): p. 605.

214. Kibler, K. and H. Carter Jr, *Electrocooling in gases.* Journal of Applied Physics, 1974. **45**(10): p. 4436-4440.

215. Fylladitakis, E.D., A.X. Moronis, and K. Kiousis, *Design of a Prototype EHD Air Pump for Electronic Chip Cooling Applications.* Plasma Science and Technology, 2014. **16**(5): p. 491.

216. IEEE-DEIS-ENDTechnicalCommittee, *Recommended International Standard For Dimensionless Parameters Used In Electrohydrodynamics.* IEEE Transactions on Dielectrics and Elechical Insulation, 2003. **10**(1): p. 3-6.

217. Seyed-Yagoobi, J., J.E. Bryan, and J. Castaneda, *Theoretical analysis of ion-drag pumping.* IEEE Transactions on Industry Applications, 1995. **31**(3): p. 469-476.

218. Pawar, S., P. Murugavel, and D. Lal, *Effect of relative humidity and sea level pressure on electrical conductivity of air over Indian Ocean.* Journal of Geophysical Research: Atmospheres, 2009. **114**(D2).

219. Bég, O.A., M. Rashidi, M. Rastegari, T.A. Bég, S. Motsa, and A. Halim, *DTM-Padé numerical simulation of electrohydrodynamic ion drag medical*

pumps with electrical Hartmann and electrical Reynolds number effects. Journal of Advanced Biotechnology and Bioengineering, 2013. **1**(2): p. 62-79.

220. Yen, S.-C. and J.-H. Liu, *PIV measurements of exit flow field of centrifugal fans with conditional sampling.* Journal of Marine Science and Technology, 2007. **15**(3): p. 232-240.
221. Sunonwealth Electric Machine Industry Company Limited; Available from: http://www.sunon.com/index2/pro2.php?c1=10&c2=2.
222. Egan, V., J. Stafford, P. Walsh, and E. Walsh, *An experimental study on the design of miniature heat sinks for forced convection air cooling.* Journal of Heat Transfer, 2009. **131**(7): p. 071402.
223. Kim, S.J., D.-K. Kim, and H.H. Oh, *Comparison of fluid flow and thermal characteristics of plate-fin and pin-fin heat sinks subject to a parallel flow.* Heat Transfer Engineering, 2008. **29**(2): p. 169-177.
224. Teertstra, P., M. Yovanovich, and J. Culham, *Analytical forced convection modeling of plate fin heat sinks.* Journal of Electronics Manufacturing, 2000. **10**(04): p. 253-261.
225. LPTPS.com. *Best laptops Guides & Reviews*. 2017; Available from: http://www.lptps.com/best-ultra-thin-laptops/.
226. Do, T., S. Rawshdeh, and W. Shi, *ptop: A process-level power profiling tool*, 2009, HotPower.
227. NVIDIA. NVIDIA SUPPORT; Available from: http://www.nvidia.co.uk/object/support-uk.html.
228. Intel. Standard Laptops Powered by Intel Technology, October 2017; Available from: https://www.intel.co.uk/content/www/uk/en/products/devices-systems/laptops/standard.html.
229. Jewell-Larsen, N. and K.A. Honer, *Ehd device in-situ airflow*, 2012, Google Patents.
230. Jewell-Larsen, N., K.A. Honer, R. Goldman, and M.K. Schwiebert, *Electrohydrodynamic fluid mover techniques for thin, low-profile or high-aspect-ratio electronic devices*, 2014, Google Patents.
231. Lee, J.L. and R.L. Blanco Jr, *Methods and apparatus for cooling electronic devices*, 2012, Google Patents.
232. Patently Apple, Apple Reinvents the Ionic Wind Generator Cooling System 2012; Available from: http://www.patentlyapple.com/patently-apple/.